DESIGN AND IMPLEMENTATION OF AN INDUCTIVE POWER TRANSFER SYSTEM FOR WIRELESS CHARGING OF FUTURE ELECTRIC TRANSPORTATION

by

Kunwar Aditya

A Thesis
Submitted to the Faculty of Graduate Studies through
the Department of Electrical, Computer and Software Engineering
in Partial Fulfillment of the Requirements for
the Degree of Doctor of Philosophy
at the University of Ontario Institute of Technology
Oshawa, Ontario, Canada

August 2016

Design and implementation of an inductive power transfer system for wireless charging of future electric transportation

By

Kunwar Aditya

APPROVED BY SUPERVISORY COMMITTEE:

Dr. Srdjan Lucik, External Examiner
(Department of Electrical and Computer Engineering, North Carolina State University)

Dr. Sheldon S. Williamson, Thesis Supervisor
(Department of Electrical, Computer and Software Engineering, UOIT, Oshawa)

Dr. Vijay Sood, Internal Examiner
(Department of Electrical, Computer and Software Engineering, UOIT, Oshawa)

Dr. Walid M. Ibrahim, Internal Examiner
(Department of Electrical, Computer and Software Engineering, UOIT, Oshawa)

Dr. Greg Rohrauer, External to Program
(Department of Automotive, Mechanical and Manufacturing Engineering, UOIT, Oshawa)

Dr. Ying Wang, Committee Chair
(Department of Electrical, Computer and Software Engineering, UOIT, Oshawa)

[August 30, 2016]

Abstract

Design and implementation of an inductive power transfer system for wireless charging of future electric transportation

Kunwar Aditya, Ph.D.

The University of Ontario Institute of Technology, 2016

The motivation of this thesis was to formulate clear design guidelines for fabrication and control of an efficient series-series resonant inductive power transfer (SS-RIPT) system for electric vehicle battery charging application. In meeting this objective, several critical deficiencies about the field of RIPT based EV chargers specific to stationary charging have been solved. Firstly, to increase the tolerance to misalignments, use of an unsymmetrical coil pair for the charger has been proposed. An unsymmetrical coil pair, in which the outer diameter of the primary and the secondary coils are kept equal, whereas the inner diameter of the secondary is kept larger compared to the primary counterpart gives the best performance in misalignment conditions. By employing this unsymmetrical coil-pair, a charging pad which shows the horizontal tolerance to misalignment equal to 71% of the pad diameter has been presented. Secondly, a very simple yet novel analytical design procedure has been submitted, adopting which, eliminates the bifurcation issue for the entire range of load and coupling variation and therefore requires no sophisticated control. Finally, a simplified mathematical model of SS-RIPT system has been proposed for primary side control of output voltage and current. All the proposed theories and analysis have been verified by a 3.6 kW prototype of the SS-RIPT based charger fabricated in the lab. A DC-DC efficiency of 91% for rated load condition is achieved for the designed charger. For partial load conditions (less than 50% of the rated load), the efficiency is 87%.

Acknowledgements

Table of Contents

List of Figures

List of Tables

List of Symbols

V_{dc}	DC Input to Inverter
V_{AB}	Output Voltage of Inverter
v_P	Instantaneous Primary Voltage
v_S	Instantaneous Secondary Voltage
V_P	Primary Peak Voltage
V_S	Secondary Peak Voltage
V_{Prms}	RMS Value of Primary Voltage
V_{Srms}	RMS Value of Secondary Voltage
V_{CD}	Input Voltage to Rectifier
L_P	Primary Self Inductance
C_P	Primary Capacitor
L_S	Secondary Self Inductance
C_S	Secondary Capacitor
M	Mutual Inductance
C_f	Filter Capacitor
R_o	DC Load Resistance
R_L	AC Equivalent of DC Load Resistance
N_P	Primary Turn
N_S	Secondary Turn
i_P	Instantaneous Primary Current
i_S	Instantaneous Secondary Current
I_P	Primary Peak Current
I_S	Secondary Peak Current
I_{Prms}	RMS Value of Primary Current

I_{Srms}	RMS Value of Secondary Current
v_m	Instantaneous Value of Voltage across Primary Capacitor
V_m	Peak value of Voltage across Primary Capacitor
$\lvert i_S \rvert$	Rectified Current Flowing into Output Filter Network
I_o	Output Current
Vc_f	Filter Capacitor Voltage
V_o	DC Output Voltage
f_s	Switching Frequency, Hz
f_o	Resonant Frequency in Hz
ω_s	Switching Frequency in Rad/Sec
ω_o	Resonant Frequency in Rad/Sec
ω	Frequency in Rad/Sec
k	Coupling Coefficient
k_c	Critical Value of Coupling Coefficient
Sgn	Signum function
Q	Quality Factor of circuit
Q_{i_LS}	Intrinsic Quality Factor of Secondary Coil
Q_P	Primary Quality Factor
Q_S	Secondary Quality Factor
Z_{in}	Total Input Impedance
Z_r	Secondary Impedance Referred to Primary
R_r	Secondary Impedance Referred to Primary at Resonance
P_{in}	Active Power Required by Primary
P_o	Output DC power
Q_{in}	Reactive Power Required by Primary

S_{in}	Apparent Power Required by Primary
u	Normalised Frequency
η	Efficiency
D_{in}	Inner Diameter of Coils
D_{out}	Outer Diameter of Coils
S	Turn Spacing in Coils
w	Diameter of Wire in Coils
B_O	Magnetic Flux Density
δ	Skin Depth of Conductor
L_{fp}	Length of Ferrite Spoke in Primary Pad
L_{fS}	Length of Ferrite Spoke in Secondary Pad
θ_P	Angle Between Ferrite Spokes in Primary Pad
θ_S	Angle Between Ferrite Spokes in Secondary Pad
W_f	Width of Ferrite Spoke

Chapter 1   Introduction

Electric Vehicles (EVs), which are not a new concept, were developed in the mid-19th century. However, they became obsolete throughout almost entirely the 20th century mainly because of their limited driving range and high cost as compared to gasoline powered vehicles. In past the few decades, due to growing concern over increasing environmental pollution, depleting energy resources and increasing oil prices, electric propulsion has been considered as the ultimate solution since electricity can be produced by using non-polluting and continuously renewable energy sources [1]. Renewed interest in EVs has also led to increased interest in the development of charging methods for EVs. Traditionally, EVs usually use a simple plug-in charging method also known as conductive charging or plug-in charging in which a copper connected cable forms the power link. Plug-in charging is a widely accepted method on the market, and it is available for most EVs: Chevrolet Volt, Tesla Roadster, Nissan Leaf, and Mitsubishi i-MiEV. However, there are disadvantages to plug-in charging, such as safety issues caused by exposed plugs and damaged cables. To avoid the drawbacks of plug-in charging, wireless charging methods have been widely studied in recent years [2]–[5].

Wireless power transfer (WPT) has been demonstrated using various WPT systems, such as: Acoustic [6], [7]; Light [8]; Microwave [9]; Laser [10]; Capacitive [11]; and Inductive [12]. The basic layout of all WPT systems is similar. They all consist of a transmitter connected to a primary electronic circuit and a receiver connected to a secondary electronics circuit. The 'medium of power transfer' between receiver and transmitter makes them different from each other. It has been established in the literature that only an inductive WPT system has the potential to be applied for medium and high power applications, and particularly for the charging of EV batteries. In the literature, this method of power transfer has also been referred, contactless power transfer (CPT), contactless energy transfer (CET), inductively coupled power transfer

(ICPT), resonant inductive power transfer (RIPT) and inductive power transfer (IPT). For this thesis, the term RIPT will be used hereafter for consistency.

This thesis focuses on the design and control of an efficient RIPT system for charging of EV battery. In the sections to follow, a brief history of RIPT system for EV, followed by an overview of the working principle and components of an RIPT system, and commercialization activities being carried out world-wide in the field of wireless EV charging, has been presented. The final sections in this chapter will outline the objectives and contribution of this thesis and gives a brief overview of the work completed by the author.

1.1 Rationale for Adopting Wireless Charging system for EVs

The transport sector alone accounts for approximately 23% of the total energy-related emissions [13]. EVs are seen as a viable solution to the growing pollution problem. However, the major hurdle in the broad acceptance of EVs is attributed to their high battery cost and limited driving range.

The Li-Ion battery is widely used as the primary power source for the EV's drivetrain due to their high specific energy (100-265 Wh/kg) and specific power density (250-340 W/kg) compared to other battery technology. Despite its superior characteristics, it still adds considerable weight and size to the vehicle. For example, Nissan Leaf's 24 kWh battery pack weighs around 200 kg. In addition to high weight and size, the estimated cost of the battery pack is about US$700/kWh. Therefore, the price of an EV is almost double that of a gasoline counterpart with nearly half of the cost for the battery itself [14].

The limited driving range is an even greater obstacle to the market penetration of EVs than their higher cost. For example, gasoline vehicles can go over 500 km before refuelling which takes about 2-3 minutes at a filling station which are located every few kilometers. On the other hand, most EVs can only go about 100-200 km before recharging, and take a long charging time [15]. For example, Level 2 charging circuit of 9.6 kW power takes about 1.5 hrs, to fully charge the battery pack of the Chevrolet Volt [16]. Besides this, charging stations are not as readily available as fuel stations. These limitations of EVs have been termed as 'range anxiety' issue for obvious reasons.

The aforementioned limitations of EVs can be overcome by adopting wireless charging technology for EV battery charging which provides the following advantages over conventional wired charging:

(a) Range Extension: Wireless charging has the scope for 'opportunity charging' i.e. charging the vehicle little and often during the day when the EV is not in use [17]. For example, in addition for residential garage, public and private parking areas, the wireless charger can also be installed at: traffic lights; bus stops; high traffic congestion area where vehicles are slow moving; and taxis ranks that move forward as taxis are hired [18]. These opportunity charging are possible since wireless charging does not require human intervention and therefore charging can be carried out automatically. This in turn leads to significant improvements in range compared to that available from a single overnight plug-in charge.

(b) Safety and Convenience: Wireless charging provides galvanic isolation between load and source. Therefore it eliminates the disadvantages of plug-in charging technology such as: risk of electrocution, especially in wet and hostile environment from aging wiring and bad connections; failure to plug in; trip hazard from a long connecting wire; poor visual appeal due to hanging cords; contactor wear caused by excessive use and thermal cycling; and, most importantly, discomfort in handling a plug-in charger in a harsh climate that commonly has snow and where the charge point may become frozen onto the vehicle [14], [19], [20].

(c) Battery Volume Reduction: Due to the scope of opportunity charging, charging can take place more frequently. Therefore, EVs can travel the same distance with a reduced battery pack [13], [20]. This, in turn, can lower the price of EVs and make them more efficient due to the reduced weight. Frequent charging also extends the battery life by reducing the depth of discharge in the battery.

(d) Weather Proof: In a wireless charger, power transfer takes place due to an electromagnetic link, therefore charging is not affected by the presence of snow, rain, or dust storms. Besides, a transmitter is embedded underground, therefore, is safe from extreme weather condition and requires less frequent maintenance or replacement than a plug-in charger would require.

1.2 A Brief History of Development of RIPT System for EV Charging

Resonant inductive power transfer (IPT) is not a new concept, and many attempts have been made in the past to transmit power wirelessly, most notably by Nikola Tesla (1856 –1943) in the late 1800s and early 1900s. He was inspired by the work of Heinrich Hertz (1857–1984) who first confirmed the existence of electromagnetic radiation in his experiments in 1888. Tesla reported several experimental setups of his WPT study using a high-frequency oscillator for medical/therapeutic applications [21]. Figure 1.1 shows a simplified schematic of one of his experimental setup to power a light bulb wirelessly using RIPT system.
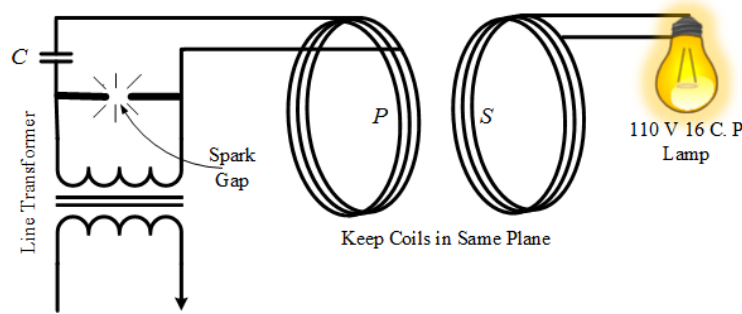
Figure 1.1 An example of RIPT setup suggested by Tesla[21], [22]

In Figure 1.1 one can see the circuit contains two loosely coupled and tuned resonant circuits: a primary (P) and a secondary (S). An external capacitor C is used to tune the primary while self-capacitance of the solenoid coil is applied to tune the secondary coil. The operating frequency used by Tesla was in the range between 20-100 kHz. Periodic spark gap discharges were used to control the power in the resonant circuit, as the modern resonant converter do today by using power electronic switches. Also, these discharges converts the mains frequency to high frequency of the resonant circuit. It is worth noting that Tesla's experiments were first to demonstrate power transfer using a resonant inductive link and forms the basis of the majority of today's modern wireless power transfer system.

In 1894, Hutin and LeBlanc submitted a patent [23] that describes a transformer system for electric railways. Although they named their system a transformer, it was basically an RIPT system for street cars. It contains a single-wire (unipolar) elongated primary track with 2 kHz alternating current and multiple resonant pick-ups at the secondary side. Ferromagnetic material and a suspension system that lowers the pick-

ups were proposed to increase mutual coupling between the track and the pick-up. Although the proposed topology has some similarities to modern solutions, its practical application was not successful, so the myth was propagated that wireless transfer of "power" over large distances was impossible. However it was possible to send "signal" and there has been significant development of the wireless communications system and inductive antennas, therefore this "Signals-yes", "power-no" categorization persisted for more than 100 years [12].

In the 1970s, due to the energy crisis and advances in materials science, semiconductors and power electronics, the temporarily suspended research in the area of EVs and inductive power supply was reinstated through academic studies. An extensive, long-term project called PATH (Partners for Advance Transit and Highways) was conducted at the University of California, Berkeley through the 1980s [24].This system was referred to as 'Dual Mode Electric Transportation' (DMET) as it considered both batteries as well as powered highways as the energy source of the EVs. For the test vehicle, a 60kW, 35-passenger bus was selected. The complete infrastructure was built for a 213 m long test track with two powered sections with a total length of 120 m. A bipolar primary track was used, and it was supplied with 1200A, 400 Hz AC. The pick-up had an area of 4.3 m^2, and a 7.6 cm distance from the primary track was used. Power control on the bus was achieved by capacitive detuning the pickup system, thereby placing a large reactive load on the generator, which the generator could easily supply at reduced efficiency. The air gap was controlled to be 50-100 mm when coupling power and 150–200 mm when not coupling power. The attained efficiency was around 60%. The results of the project have proved the substantial potential of roadway powered vehicles, but due to low efficiency and lack of economic viability project was abandoned.

In 1986, Kelly and Owens proposed powering aircraft entertainment systems using wires under the carpet in the passenger bay of a plane. It was a 38 kHz system supplying a load of 8 W for each passenger and total of 1 kW load without any controller, but the system was highly inefficient [25]. This innovation was followed by Turner and Roth (U.S. Patent 4 914 539) in 1990 using much the same infrastructure but with a controller on each parallel-tuned pickup circuit so that the VAR load on the pickup was varied to supply each entertainment system with a constant voltage. The system operated with

constant resonant voltages on all the pickups, which conserved real power but placed a large VAR load on the generator under light loading conditions.

In 1991, researchers at Auckland University, NZ led by Boys and Green focused their attention on high power applications, particularly on the inductive power supply of movable objects. Their IPT system for material handling (US Patent 5 293 308) became the cornerstone of much of the work in IPT systems over the past 20 years. This work was funded by Japanese company Daifuku Co. Ltd., so the development was compatible with Japanese regulations. Therefore, the operating frequency was constrained to be below 10 kHz. The complete system included a resonant power supply driving an elongate inductor, parallel tuned with a capacitor, and some parallel-tuned pickups, each with its decoupling controller, supplying power at nominally constant voltage to their particular load [26], [27]. Since then work in Auckland has been led by Covic and Boys. They have investigated various aspects of the IPT, such as: topologies of the primary resonant converter; compensation of the primary and pick-up circuits; the optimal control of the pick-up; the multi-phase design of the elongated primary track; and the bifurcation phenomenon. It is especially worth noting their recent achievement in designing an optimal pad for the stationary charging of EVs [28].

In 2007, a group of physicists from the Massachusetts Institute of Technology caught the world's attention by powering a 60 W of lightbulb suspended in space, 2 m away from the transmitting coil [29]. Operating frequency was 9.9 MHz and self-capacitance of the coils were used for the resonant tuning. Although the reported end-to-end efficiency of the system was only 40% [30], the media publicity and growing public interest led to the development of the spin-off company named WiTricity. WiTricity is presently offering wireless charging solutions for household electronics and EV charging systems.

In addition to stationary charging applications, in-motion charging of EVs has also been undertaken at various academic and industry research groups. Notable among them is On-Line Electric Vehicle (OLEV) project conducted at the KAIST (Korea Advanced Institute of Science and Technology) in South Korea in 2009 [31]. The high price, high weight, and limited range of electric batteries for EVs motivated researchers to develop a powered roadway system that can reduce the required amount of cells by

80%. Three generations of OLEV systems have been developed, and three different vehicles have been tested: the first generation is a light golf cart which takes power of 3 kW at an air gap of 1 cm and total efficiency of 80%; the second generation is a bus for which 6 kW power transfer at an air gap of 17cm and total efficiency of 72% has been achieved; and the third generation is an SUV for which 17 kW power transfer takes place at 17 cm air gap and efficiency of 71% [13].

1.3 Working Principle and Components of RIPT System

Although it took more than century to develop and accept the RIPT system for wireless charging of EVs and other consumer products, the basic idea is based on well-established Ampere's circuital law and Faraday's law of induction. How power transfer takes place with these two laws, can be explained with the help of Figure 1.2.
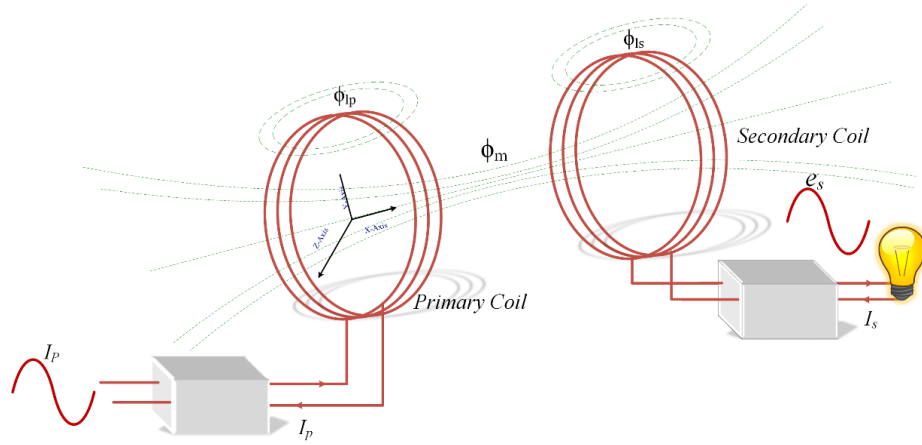
Figure 1.2 Power transfer via two mutually coupled air cored coils

Figure 1.2 shows two coils linked by inductive coupling. Here, the subscript P and S refers to primary and secondary coil, respectively. The terms ϕ_M, ϕ_{lP}, and ϕ_{lS} are mutual flux, primary leakage flux, and secondary leakage flux, respectively. Let M, L_P, L_S be mutual inductance, self-inductance of primary and self-inductance of secondary coil respectively. When a time varying current is applied to the primary coil, a time varying flux of the same frequency is produced in the region surrounding the primary. The strength of the magnetic field around a closed path is directly proportional to the current carried by the coil and is given by Ampere's law (for the case when the displacement current is neglected) by (1.1) [32].

$$\oint_l H.dl = \int_s J.ds \tag{1.1}$$

If the currents are carried by wires in a coil with N turns, then (1.1) can be simplified as:

$$\oint_l H.dl = N_P I_P \tag{1.2}$$

Here, 'H' is the magnetic field strength, N_P is number of turns while I_P is the current flowing in the primary coil, and l is the length of the circumference of the closed path. This time varying magnetic flux links the secondary coil and *emf* is induced in the secondary coil by the principle of Faraday's law of electromagnetic induction given by (1.3):

$$e_S = N_S \frac{d\phi_m}{dt} \tag{1.3}$$

Here, e_s is the emf induced in the secondary coil and ϕ_m is the flux linking the secondary coil. This emf is capable of driving a current to the load if the circuit is closed. From (1.2) one can understand that the greater the magnitude of current in the primary, the stronger will be the magnetic field strength. From (1.3) one can understand that the higher the *rate of change of mutual flux*, the greater is the magnitude of *emf* induced in the secondary. This *rate of change of mutual flux* which is equal to supply frequency signifies that a high-frequency current in the primary is needed to establish high *emf* in the secondary. However, all the flux does not link the secondary; coupling coefficient k relates common flux to total flux.

$$k = \frac{\phi_m}{\phi_m + \phi_{lP}} \tag{1.4}$$

In (1.4) $\phi_P = \phi_m + \phi_{lP}$ is the total flux produced by the primary coil. Induced emf in terms of the coupling coefficient is given by (1.5)

$$e_S = k N_S \frac{d\phi_P}{dt} \tag{1.5}$$

If all the flux link the secondary, then k is 1 and if none of the flux links the secondary k is 0 i.e. $0 \leq k \leq 1$. Based on the values of k the magnetically coupled system can be classified into two categories, namely tightly coupled systems and loosely coupled systems. In tightly coupled systems, such as transformer and induction motor, the primary is placed in proximity of secondary and flux is shaped by placing windings on the core of high magnetic permeability. Therefore, they have mutual inductance greater

than the leakage inductance. Because of tight coupling, k usually lies between 95% to 98% for the transformer and approximately 92% for the induction motor[33]. In the case of using magnetically coupled system for powering EVs, a large air gap is required to allow for inconsistency in the road surface and better clearance between the road and vehicle. Because of this large air gap, the leakage flux is very high and the coefficient of coupling is from 1% to 3% only. Such applications are classified under loosely coupled systems. Poor coupling in loosely coupled systems leads to poor transfer of power. To improve coupling and compensate leakage inductance, capacitive compensation in primary and secondary windings is required [34].

In light of the above discussion, a generalised block diagram of the RIPT system for EV battery charging can be drawn and has been shown in Figure 1.3.
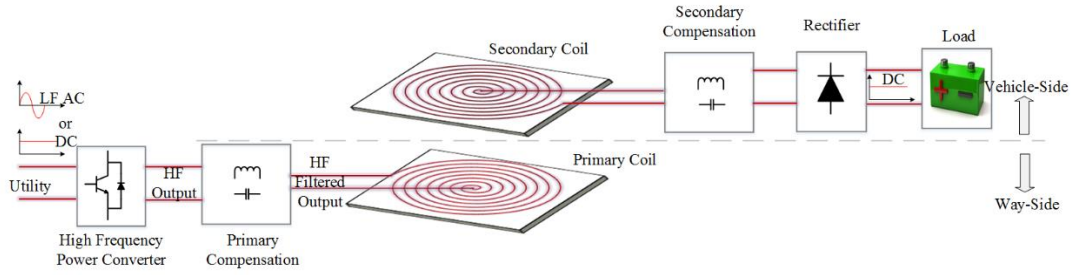
Figure 1.3 Generalized block diagram of IPT system for EV battery charging

Figure 1.3 shows the global energy chain for a typical RIPT based EV battery charger. On the way-side, power is usually provided by a utility supply that may be DC from a battery or low frequency (LF) 60 Hz AC from a grid. If the utility is supplied from a grid then a power factor correction stage may also be included in this block to reduce the harmonic pollution of the grid. A high-frequency (HF) voltage at a few tens of kHz is then generated by a high-frequency converter which is simply an inverter if the utility is DC or a power factor correction rectifier followed by an inverter if the utility is 60 Hz AC [35].

This high-frequency voltage generates energy in the form of a high-frequency current through a compensation network and primary coil. A primary compensation circuit is added so as to have the primary input voltage and the current in phase to minimize the VA-rating and thus the size of the high-frequency power converter [36]. Moreover, primary compensation also acts as a band pass filter blocking undesirable

frequency components generated from the power electronic converter feeding the primary. Therefore, an almost sinusoidal current flows in the primary coil and this enables soft switching operation of the converter feeding the primary [37].

Energy is then transferred to the vehicle side through the secondary coil which is mutually coupled to the primary coil through the flux generated in the air-gap by the primary coil current. The energy received by the secondary coil is then processed by the secondary compensation circuit which is added to improve the power transfer capability of the system [38]. Finally, the voltage thus received is rectified so as to make it exploitable by the load (batteries). Depending upon the control, an additional DC-DC converter is sometimes included between the rectifier and the load [39]. Apparently, the DC-DC converter brings in more components and corresponding losses.

Compensating networks, which are capacitors, are made to resonate with coil inductance, thus forming a resonant inductive link. Depending on the connection of the compensating capacitor in the primary and secondary coils, four types of resonant inductive links can be defined: series-series (SS), series-parallel (SP), parallel-series (PS) and parallel-parallel (PP) [40]. Primary parallel compensation such as PP and PS resonant inductive links allows using a higher primary current as only a small part of the current flows through the semiconductor. However, PP and PS have several fundamental drawbacks. First, they require an additional series inductor to regulate the inverter current flowing into the primary resonant tank. This series inductor, in turn, increases the converter size and, therefore, the total cost of the RIPT system [41], [42]. Secondly, due to the circulating current in the primary resonance tank, the partial load efficiency of parallel compensated primary system is lower [43]. Thirdly, in PP and PS resonant inductive links, the value of the primary compensation capacitor is not constant but varies with varying mutual coupling and load. Therefore, PP and PS resonant inductive links will require sophisticated control strategies to maintain unity power factor operation in the primary power supply irrespective of load and mutual coupling variation.

Primary series compensation allows canceling the significant voltage drop of a primary coil, therefore the required voltage rating of the power supply is reduced. In SS and SP resonant inductive links, no extra inductor is needed. Moreover, primary

compensation is independent of load [44]. However, in an SP resonant inductive link, primary compensation depends upon mutual coupling and, therefore, needs consideration in dynamic charging applications. The SP resonant inductive link requires a higher value of capacitance for stronger magnetic coupling, and its peak efficiency is inferior to an SS resonant inductive link [45]. Therefore, an SS resonant inductive link is theoretically the best regarding efficiency, component count, the complexity of control, and cost, and hence is the focus of this thesis.

1.4 Wireless Charging Standards for Electric Vehicle

In 2010 the Society of Automotive Engineers (SAE) assembled an international committee, known as SAEJ2954, to develop a working industry standard that establishes the interoperability, frequency band, electromagnetic compatibility, minimum performance, safety, testing criteria as well as coils definitions for wireless charging of light duty electric and plug-in electric vehicles. The international committee includes automotive equipment manufacturers (OEMs), such as GM, BMW, Ford, Nissan and Toyota; Tier 1 suppliers Delphi, Panasonic and Magna; WPT suppliers, such as Qualcomm and LG, and a collection of other organizations, such as the Argonne National Laboratory, the EPA, the DOT, UL and the University of Tennessee.

The current version of SAEJ2954 technical information report (TIR) was made available for purchase from the SAE website on May 31, 2016. The latest version addresses unidirectional charging from grid to vehicle and is intended to be used for static charging applications. Dynamic charging (charging while the vehicle is in-motion) and bidirectional power may be considered in the future based on industry feedback. This TIR specifies a common frequency band using 85 kHz band (81.39 kHz–90 kHz) for all light duty vehicle systems. In addition, it defines the power levels in four classes as shown in Table 1.1.

Table 1.1 SAE J2954 Light Duty Vehicle WPT charging classes

Classification	WPT1	WPT2	WPT3	WPT4
Power Levels	3.7 kW	7.7 kW	11 kW	22 kW
Status	Specified in TIR J2954	Specified in TIR J2954	To be Specified in TIR J2954	To be Specified in TIR J2954

SAE TIR J2954 compatible systems have been built by automakers and suppliers and are currently under test with a cross-industry team with the US Department of Energy, Idaho, and Argonne National Labs [46]. The experimental data, first in the bench and later in the vehicle, will be used to finalize the Standard by 2018 to support the roll-out of this technology.

The author would like to mention at this point that SAE TIR J2954 was made available to download only after 31st of May 2016 and the author of this thesis started working on the hardware setup in the middle of 2015. Therefore, it was not possible to follow the frequency guidelines in the TIR as it was unknown at that time. Before the release of TIR J2954, 20 kHz to 200 kHz was a very common frequency of interest in RIPT. Therefore, 40 kHz frequency was used for this thesis based on the availability of components and signal processing unit available in the lab at the time. For power level, charging standards defined by SAE J1772 for plug-in electric vehicle conductive charging [46] were followed. Therefore, for power ratings, 3.6 kW for level 2 charging was found appropriate depending on the rating of the load and power supply available in the lab. Table 1.2 gives the charging standards defined by SAE J1772 used in this thesis. However, the work presented in this thesis is scalable to all the power levels and frequency band defined by TIR J2954.

Table 1.2 Charging standard defined by SAE J1772 [46]

Charging Level		Power Level	Supply Voltage/Current	Setting
AC Level 1		1.7 kW	Single Phase 120 V/20 A AC (16 A continuous)	Residential/Parking lot
AC Level 2	Minimum	3.4 kW	Split Phase 208/240 V/20 A AC (16A continuous)	Residential/Commercial
	Maximum	19.2 kW	208/240 V/20 A AC (80 A continuous)	Commercial

DC Level	Level 1	40 kW (up to 500 V at 80 A DC)	3-Phase 208 V/480 V AC ~20 A-200 A AC	Commercial
	Level 2	100 kW (up to 500 V at 200 A DC)	500 V/200 A DC ~20A-400 A AC	Commercial

1.5 Research Goals and Objectives

The primary goal of this thesis is to design and implement a prototype of 3.6 kW of the wireless charger for static charging of Li-Ion batteries used in EVs. It is evident that the design of the entire inductive charging system includes more than one academic area such as power electronics, control system, magnetic circuit design, automation, communication system, mechanics, economics, and EMI regulations. Since it is impossible to cover all mentioned aspects, this thesis will focus on the control and magnetics design aspect of the charger. To meet this goal, several objectives are formulated:

1) To investigate the magnetic characteristics of an unsymmetrical coil pair employing Archimedean spiral, with the aim of finding the coil pair least sensitive to coupling variations

A fundamental challenge of implementing an RIPT system for wireless power transfer is a coupling variation between the primary and secondary coils due to misalignment while parking a car over the primary coil. It is well known that deviation from an optimal coupling condition degrades the power transfer efficiency. It is thus desirable to have a coil pair which is least sensitive to misalignments to ensure efficient power transfer over a wide operating area.

In the literature, different types of charging pads have been proposed such as: circular pads, bipolar pads, DD-Q pads, and H-shaped pads. Among these, circular charging pads employing Archimedean spiral is the most well-known and widely adopted pad

shape in EV battery charging application, despite its lower coupling compared to other pads. This is mainly because circular pads (CPs) are non-polarised and have the same tolerance to misalignment in all directions which makes them easier to operate. Due to their non-directional characteristics, the vehicle can approach them from any direction which ensures simplicity of use by drivers.

Due to these features the author wishes to adopt CPs for the RIPT charger. However, CPs presented in the literature employ an identically sized Archimedean spiral coil in both the primary and secondary side. For such a symmetrical coil pair, a magnetic null occurs in their coupling profile for misalignment equal to 40% of the pad diameter irrespective of separation between them. This severely limits the operation area over which power transfer takes place.

Therefore, for this thesis instead of a symmetrical coil pair, the magnetic characteristics of a CP employing unsymmetrical coil pairs have been thoroughly analysed. From the analysis, an asymmetrical coil shape which gives magnetic null at 71% of pad diameter has been derived. It is also established that the position of null, shifts with changing air-gap for unsymmetrical coil pairs.

2) To develop simple and accurate design guidelines for an SS-RIPT system considering bifurcation issue

The phenomena of existing more than one zero phase angle frequency in an RIPT system is known as the bifurcation phenomena. In an SS-RIPT system, it occurs due to an increase in the coupling coefficient above a certain critical value which is a function of load and secondary inductance. If not addressed carefully, bifurcation can cause a decreases in the voltage gain of the system, which therefore will affect the power transfer capability and overall efficiency of the system. Moreover, due to bifurcation, hard-switching of the primary side inverter semiconductor occurs if operating close to the resonant frequency. Some authors handle this issue by adopting a sophisticated variable frequency control strategy [47]–[50] which increases the overall complexity and the cost of the system. For these reasons, bifurcation is best avoided by the design process. Design steps to eliminate bifurcation have not yet been reported in the literature. In addition to this, missing from the literature is a complete step by step design procedure addressing issues, such as: calculation of electrical parameters for a

given load profile; selecting the number of turns in coils; and air-gap between coils. Some authors use three-dimensional (3-D) finite element simulation for coil design. However, finite element simulations are complicated and may require a significant number of iterations before achieving the final design goals and therefore are time-consuming.

In this thesis, a design guideline for creating an SS-RIPT system employing a circular Archimedean spiral has been developed. Formulated design guidelines use simple analytical expressions for calculating the electrical parameters (self-inductance and mutual inductance) to achieve the desired load profile and use FEA analysis only for the verification purposes. Electrical parameters of the system are calculated in such a way that bifurcation does not occur for the entire load and coupling variations. This thesis has also covered analytical expressions for calculating the physical parameters of the coils, such as: number of turns; turn spacing; and outer and inner diameter.

The literature, always emphasizes on having a coupling coefficient value as high as possible. Evolution of polarised pads is evidence of this mindset. However, through the research for this thesis, it has been established that a coupling value lower than a critical value is desirable and sufficient for the efficient operation of the charger for an entire range of load variations. Circular coil geometry can easily provide this critical value of coupling and thus complicated polarised pad designs are not required at least not for stationary charging application.

3) To derive a simplified mathematical model for SS-RIPT system for primary side control

In most RIPT systems, power flow regulation is implemented on the secondary side, which requires extra switching circuits and controllers between the rectifier and the load. Introducing an additional power converter is advantageous in cases where multiple secondary systems exist, with varying loads. However, in the case of static charging where only one secondary is coupled to the primary, it is preferable to achieve power flow regulation from the primary side converter itself, by varying the voltage magnitude of the HF inverter. Eliminating an additional power converter stage is important for having an efficiency figure close to those of plug-in charger value.

For the above reasons, in this thesis primary side control has been preferred. To control the power flow from the primary side, a suitably designed closed-loop controller is consistently needed, to improve tolerance to misalignments and parameter variations. For the design of control loops, a small-signal model of the system is required for calculating the appropriate value of the phase and gain margins of the system to guarantee a robust control.

However, small-signal modelling for an RIPT system has not been reported extensively in the literature and mainly covers the steady state model which is not useful for designing the control loops. Only a few research papers have reported the dynamic model of an SS-RIPT system. The extended describing function (EDF) is a well-known method for modelling resonant converters, due to its high accuracy. However, it requires complex mathematical formulation effort, evident from the small-signal model presented by some authors. Presented models in the literature are 9th order system.

For this thesis, a reduced dynamic model of an SS-RIPT system has been derived considering the soft-switching in the primary side inverter. From this reduced dynamic model, a small-signal model of the SS-RIPT system has been derived. The derived model is a 5th order system and requires less computational effort than other presented models in the literature.

The derived model accurately predicts the frequency response of the system in low-frequency regions (up to one tenth of the resonant frequency). In the high-frequency region, the frequency response of derived model doesn't match the actual system frequency response but maintains the similar trend of variations. Since the derived model accurately predicted low-frequency behaviour, therefore it was found useful for the design of the output voltage and current controller. The current and voltage controllers derived from the small-signal model were tested on experimental setup for different dynamic conditions and were found to give robust performance.

Chapter 2 Design Considerations for Resonant Inductive Link

2.1 Brief Overview of Different Coil Shapes Employed In Wireless Charger

Resonant inductive power transfer (RIPT) has gained popularity for electric vehicle (EV) battery charging in the past few years. The most important part of an RIPT system is the charging pads which form the wireless links. Extensive research studies have been conducted and published over time concerning the optimization of charging pads by employing different core shapes. Conventional design uses E-cores [51], U-cores [51], [52] and pot cores [53]–[56]. However, these were incompatible with EV applications since a greater thickness of the core is required to achieve the desired flux path. In turn, they compromise the ground clearance of the EV or require extensive chassis modification. Moreover, these designs are fragile, weighty, expensive and highly sensitive to horizontal misalignments [57], [58]. To overcome these demerits of a conventional design, different planar coil structures having more visual appeal and enhanced tolerance to misalignment are widely used for the stationary charging of EVs.

Planar coils are broadly classified into two categories namely polarized pads (PPs) and non-polarized pads (NPPs) as shown in Figure 2. 1. NPPs (including circular pads and square pads) are single coil pads which can couple and generate only perpendicular components of the flux. PPs are multiple coil pads which can couple and create the parallel, perpendicular or both the component of flux [59]. The initially polarized pad was an H-shaped ferrite bar with double-sided winding [60]. The height of the flux generated in such a pad is twice the height generated by the PP of the same size and gives better tolerance to horizontal misalignments. However, it also generates flux out the back of the pad, therefore when an aluminium backing plate is added it generates more loss, in the form of eddy current than that usually expected for an EV charging system [61]. To overcome the aforesaid limitations of the H-shaped pad, single-sided multiple coil polarized pads were developed such as: double-D pad (DDP), double-D quadrature pad (DDQP) and bipolar pad (BP) [62].
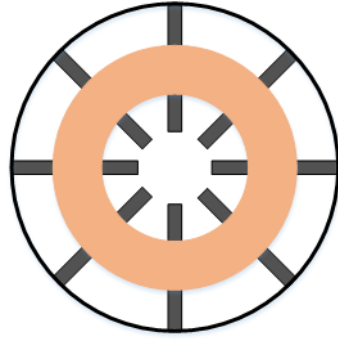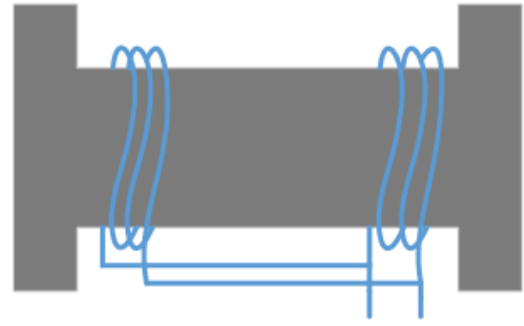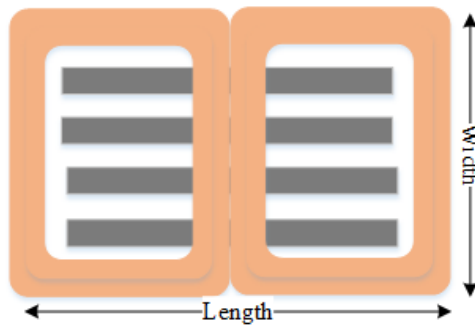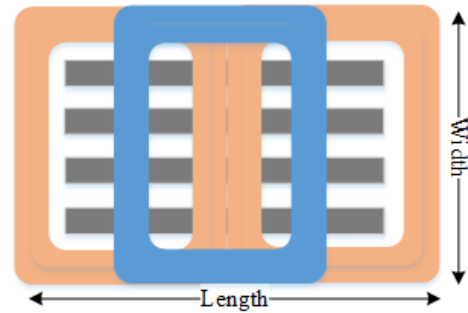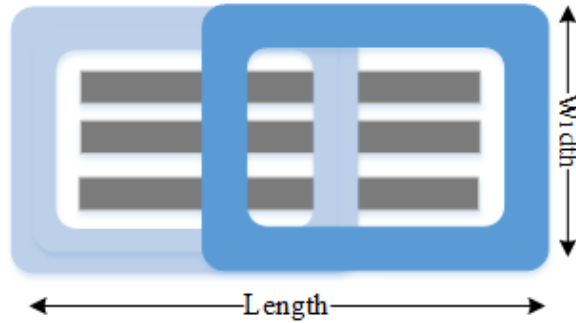
Figure 2.1 Different charging pads (i) Non-Polarized pad: (a) CP (ii) Polarized Pad: (b) H-Shaped Pad (c) DD Pad (d) DDQ Pad (e)Bipolar Pad

The DDP generates a single-sided flux path with extremely low leakage flux out of the back which allows the addition of aluminium shielding without affecting the efficiency by a significant amount [28]. It also has a higher tolerance to misalignment in a horizontal direction compared to the non-polarised pad while height of the flux path is the same as the H-shaped pad. However, this higher tolerance exists only along the

width of the pad. This is due to the existence of a coupling null when the horizontal offset is ~34% of the pad length [63], moreover it generates only the parallel component of the flux which makes this pad non-interoperable with non-polarised pads. To solve this problem, a quadrature coil is added to the DDP to form the DDQP. This pad can couple and generate both horizontal and vertical components of the flux and have high tolerance to misalignments in both lateral and horizontal directions. Similar advantages are obtained with the BP with a less amount of copper than the DDQP. Both the the DDQP and BP are interoperable with other types of pads. In spite of the features such as greater tolerance to misalignment and ability to interoperate with other pads types, both the DDQP and BP require two synchronized inverters if used as the primary pad and two synchronized rectifiers if used as a secondary pad. They are sensitive to angular misalignments and coupling can drops over 13% with a growing angular misalignments up to 30 degree [64]. They also require location or flux sensor and complicated control strategy [63]. This, in turn, increases the overall cost and complexity of the charger. For static charging of personal EVs, the driver can park their vehicle within the accepted misalignment. Moreover, EVs are often equipped with a navigational system which can assist the driver in parking their EV. Due to these reasons, the author firmly believes that while multiple coil pads may be necessary for dynamic charging application, for static charging application simple non-polarised pads can be used.

Circular pads (CPs) are non-polarised pads and have the same tolerance to misalignment in all directions, and are easier to operate. They are non-directional, i.e. a vehicle can approach them from any direction. Despite having lower coupling than other similarly sized coil geometries over identical air gaps and misalignment, for static EV charging applications, the circular geometry is still the most widely used [42]. Therefore, in ongoing research by the author a CP has been adopted for designing the wireless charger for EVs.

It was established in [28] and [57] that regardless of how optimized the design is, the fundamental height of the flux path in a circular pad is about 1/4 of the pad's diameter and it exhibits a null in their mutual coupling profile when offset horizontally by approximately 40% of the pad diameters. However, these magnetic characteristics were established for pads in which the primary and secondary sides are identical in shape and size. Hence, unsymmetrical shapes should also be thoroughly analyzed before

coming to a conclusion on the coupling performance of CPs. CPs have coils in the form of Archimedean spirals. It is the characteristics of the coil that sets the position of the null, not the housing of the coil with consists of ferrite spokes and an aluminium shielding backplane [65]. Therefore, it is logical and much easier to investigate the magnetic characteristics of Archimedean spirals instead of the whole pad.

In this chapter, simplified, easy to follow design guidelines for a series-series (SS) resonant inductive link for EV battery charger will be presented, which the author believe is missing from the literature. In [66]–[68], design procedures have been given, but there still remain many design decisions that depend on the actual case and the experience of the designer. Some authors use three-dimensional (3-D) finite element simulations for coil design. However, finite element simulations are complicated and time-consuming, and so are more appropriate for design verification. Therefore, coil parameters (electrical, circuit and geometric) should be analytically calculated.

The author presents a design procedure which calculates the parameters of coils, such as self and mutual inductance, for the desired power transfer, in such a way that the bifurcation issue can be avoided at the design level. After calculating the electrical and circuit parameters of coils, geometric parameters, such as size, numbers of turns, turns spacing have been analytically computed. The importance of the quality factor which is an important figure of merit for an RIPT system as well as the significance of bifurcation phenomena has been explained. In addition to this, magnetic characteristics of all the possible unsymmetrical coil shapes will be investigated in order to identify the shape which is least sensitive to misalignment. Following the design guidelines and design consideration for an Archimedean spiral, a 3.6 kW wireless charging pad will be designed for the SS-RIPT system.

2.2 Electrical Equivalent Circuit for Series-Series Compensated RIPT System

Figure 2.2 shows the equivalent circuit of a series-series compensated resonant inductive power transfer (SS-RIPT) system. The primary side of the SS-RIPT link is fed from the voltage-sourced full-bridge inverter which converts the DC voltage V_{dc} into high-frequency AC voltage V_{AB}. On the secondary side, a rectifier with a capacitive filter C_f converts the high-frequency voltage into DC voltage V_o and DC current I_o

required by the load, R_o. SS topology acts as a current source when the primary is fed from the voltage-source at ideal resonant condition [69]. Therefore, a simple capacitive filter is sufficient.
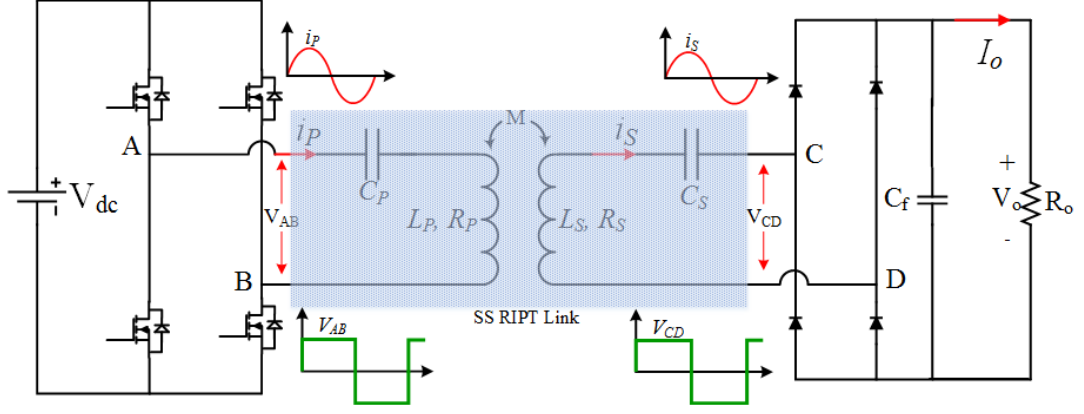
Figure 2.2 Series-series compensated RIPT system

A full bridge inverter produces a square wave voltage V_{AB}, which contains an infinite number of harmonics. However, the SS-RIPT link acts as a band-pass filter blocking undesirable frequency components generated from the power electronic converter feeding the primary. Therefore, the current flowing through the RIPT link is almost sinusoidal. This allows the first harmonic approximation (FHA) method [70] to be used for calculating the parameters of the SS-RIPT link. Figure 2.3 shows the simplified equivalent model of the circuit illustrated in Figure 2.2.
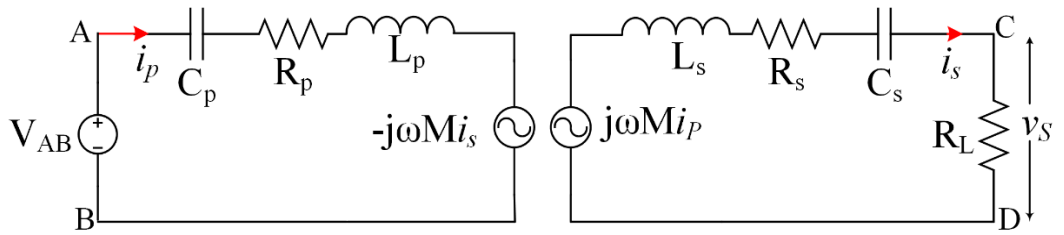
Figure 2.3 Simplified equivalent circuit of SS-RIPT system

In Figure 2.3, C_P, C_S, R_P, R_S, L_P, L_S, M and ω represents the primary compensation capacitor, secondary compensation capacitor, primary coil resistance, secondary coil resistance, primary coil self-inductance, secondary coil self-inductance, the mutual inductance between the coils and operating frequency, respectively. The primary coil is compensated (made to resonate with self-inductance of the primary coil) to minimize

the VA rating of the supply hence improving the power factor whereas the secondary winding is compensated to enhance the power transfer capability of the system [71]–[79]. The value of the primary and secondary capacitor for an SS-RIPT system is given by (2.1):

$$C_S = \frac{1}{\omega_o^2 L_S} \tag{2.1}$$

In (2.1), ω_o represents the resonant frequency of the circuit. Since the primary capacitor is made to resonate with the self-inductance of the primary coil, it acts as the sharply tuned band-pass filter, and therefore, the primary current i_P is almost sinusoidal. Due to transformer action, secondary current i_S is also nearly sinusoidal.

For a rectifier with a capacitive output filter, a square wave of voltage appears at the input to the rectifier. Therefore, the voltage across the CD terminal V_{CD} is a square wave similar to the inverter output [80], [81]. If continuous conduction of the diode bridge rectifier is considered, then the load resistance R_o as seen from the CD terminal can be given by (2.2) [82]:

$$R_L = \frac{8}{\pi^2} R_o \tag{2.2}$$

At this stage, it is important to introduce two important concepts of the RIPT system namely: the quality factor and the bifurcation phenomena. These two concepts need to be considered while designing coils for an RIPT system and have been discussed below in Subsections 2.2.1 and 2.2.2.

2.2.1 Quality Factor of an SS-RIPT System

Quality factor Q is an important figure of merit in the RIPT system. It has been defined differently in the literature [83]. As per the author's knowledge there are at least four ways in which it can be defined as described below:

1) The quality factor can be defined as the ratio of the reactive power of either the inductor or the capacitor to the average power of the resistor at resonance, that is:

$$Q = \frac{Reactive\ power}{Average\ power} \tag{2.3}$$

2) The quality factor is also an indication of how much energy is placed in storage (continual transfer from one reactive element to the other) compared to that dissipated. Therefore, it can be defined in terms of energy ratio as:

$$Q = 2\pi \frac{Maximum\ energy\ stored}{Total\ energy\ lost\ per\ period} \qquad (2.4)$$

3) The quality factor is used to represent a measure of the number of times voltage across the reactive element is greater than the supply voltage and can be defined as the ratio of voltage across the inductor or the capacitor in a series resonant circuit to the voltage across resistance in the circuit, that is:

$$Q = \frac{Voltage\ across\ inductor\ or\ capcaitor}{Voltage\ across\ resistor} \qquad (2.5)$$

4) Finally, the quality factor is used to represent the sharpness of the frequency response around the resonant frequency and can be defined as the ratio of a system's resonant frequency to its bandwidth, that is:

$$Q = \frac{Resonant\ frequency\ of\ the\ circuit}{Bandwidth\ of\ the\ circuit} \qquad (2.6)$$

The definition given by (2.6) is useful for laboratory measurement since it is possible to measure both the resonant frequency and the bandwidth of a resonant circuit using variable frequency source and an oscilloscope.

It should be noted that the quality factor can be assigned to an individual component or to a complete circuit. When assigned to the individual component, it is used to represent the purity of the reactive element and is known as the intrinsic quality factor Q_i. For example in Figure 2.3, the intrinsic quality factor of the secondary coil is given by:

$$Q_{i-Ls} = \frac{\omega_o L_S}{R_S} \qquad (2.7)$$

From (2.7), it can be seen that the intrinsic quality factor is inversely proportional to the self-resistance of the coil. It is used to represent 'the goodness of a reactive component'. A low self-resistance of the coil, or in other words the high intrinsic quality factor of the coil is desirable for low power dissipation in the form of copper loss.

When the quality factor is assigned to a complete circuit, it is nearly always assumed to mean 'the quality factor of the circuit at resonance'. This thesis, deals with the quality factor of the entire circuit. For the RIPT system the quality factor of the primary and secondary are defined separately. Equations (2.3) - (2.6) will yield the same value of the quality factor. Applying any one of the four definitions, the value of the quality factor for the secondary side and the primary side in an SS-RIPT system can be given by (2.8) and (2.9) respectively [84]:

$$Q_S = \frac{\omega_o L_S}{R_S + R_L} = \frac{1}{\omega_o C_S (R_L + R_S)} \qquad (2.8)$$

$$Q_P = \frac{\omega_o L_P}{R_P + R_r} = \frac{1}{\omega_o C_P (R_P + R_r)} \qquad (2.9)$$

In (2.9), R_r is the impedance of the secondary side reflected to the primary side at resonant condition and is given by (2.10):

$$R_r = \frac{\omega_o^2 M^2}{R_S + R_L} \qquad (2.10)$$

From (2.3), (2.4), (2.8) and (2.9), it can be observed that for a given value of the reactance in the circuit, the lower the self-resistance of the coil, the greater the quality factor and lower the power dissipation. Therefore, a high value of the quality factor is desirable for any circuit to keep the losses minimum. The same conclusion can be made from (2.6) which indicates that a smaller bandwidth leads to a higher selectivity of a resonant circuit. This would mean that it only allows the resonant frequency component to pass and block (or significantly reduces) other frequency components from entering the circuit. Therefore, losses in the circuit will be minimum and the current flowing through the circuit will be close to sinusoidal.

From the above discussion, it appears that the higher value of the quality factor is a desirable characteristic of a series resonant circuit. However, (2.5) indicates that a high-quality factor can lead to a dangerously high voltage across the insulation and may result in electrical breakdown if not handled carefully. For example in Figure 2.3, if the voltage across the load resistance is 400 V and the voltage drop across the self-resistance of the coil is neglected, then for Q_S of value 10, the voltage across the inductor and capacitor terminal would be about 4000 V. Therefore, a component of higher ratings would be required. In addition the cable joining these components together will also

require extra insulation. Moreover, (2.6) indicates that the higher the quality factor, the steeper the slope of the gain curve and therefore the circuit becomes difficult to tune and control [39], [85].

From the above discussion, it can be concluded that the selection of the quality factor requires a trade-off between complexity of control, component ratings, and losses in the system. In practical applications, a value of 2 to 10 is usually selected for Q [66], [73], [75].

2.2.2 Bifurcation Phenomena In an SS-RIPT System

The resonant inductive power transfer system is a double tuned circuit [86] i.e. two capacitors are added to form two resonant tanks with primary and secondary coil inductances. The primary capacitor is so chosen that the high frequency inverter which acts as the primary power source has minimum possible VA rating, i.e., the primary voltage and current are in the phase. In such a double tuned circuit, it is very common to have more than one zero phase angle (ZPA) frequency. This phenomenon where more than one ZPA frequency exists is known as bifurcation or pole splitting [86]–[89]. Identifying the real ZPA frequency is crucial for system efficiency and power transfer capability. To understand bifurcation phenomena, consider Figure 2.3. The equation of input complex power i.e. input VA rating S_{in} for the SS-RIPT system can be given by (2.11):

$$S_{in} = \frac{V_{Prms}^2}{Z_{in}^*} \tag{2.11}$$

In (2.11), Z_{in} is the total input impedance seen from terminal AB and is given by (2.12):

$$Z_{in} = \frac{1}{j\omega C_P} + j\omega L_P + R_P + Z_r \tag{2.12}$$

In (2.22), Z_r is reflected impedance from the secondary side to the primary side and is given by (2.13):

$$Z_r = \frac{\omega^2 M^2}{R_L + R_S + j\omega L_S + \frac{1}{j\omega C_S}} \tag{2.13}$$

Putting (2.13) in (2.12) and rearranging the real and complex terms, one can get obtain:

$$Z_{in} = R_P + \frac{\omega^2 M^2 (R_L + R_S)}{(R_S + R_L)^2 + \left(\omega L_S - \frac{1}{\omega C_S}\right)^2} + j\left(\omega L_P - \frac{1}{\omega C_P} - \frac{\left(\omega L_S - \frac{1}{\omega C_S}\right)\omega^2 M^2}{(R_S + R_L)^2 + \left(\omega L_S - \frac{1}{\omega C_S}\right)^2}\right)$$

$$\triangleq R_{in} + jX_{in} \tag{2.14}$$

Putting (2.12) - (2.14) in (2.11), one can obtain the complex power in terms of reactive power and active power as shown below:

$$S_{in} = \frac{|V_{Prms}|^2 R_{in}}{R_{in}^2 + X_{in}^2} + j\frac{|V_{Prms}|^2 X_{in}}{R_{in}^2 + X_{in}^2}$$

$$\triangleq P_{in} + jQ_{in} \tag{2.15}$$

In (2.15), P_{in} represents the total real power input into the SS-RIPT link and Q_{in} represents total reactive power input into the SS-RIPT link shown in Figure 2.3. V_{Prms} is the RMS value of the fundamental component of V_{AB} or RMS value of primary voltage. R_{in} is the total resistance and X_{in} is the total reactance seen from terminal AB.

For input VA ratings to be minimum and unity power factor operation, Q_{in} should be zero, that is:

$$\frac{|V_{Prms}|^2 X_{in}}{R_{in}^2 + X_{in}^2} = 0 \tag{2.16}$$

Equation (2.16) implies $X_{in} = 0$, that is:

$$\omega L_P - \frac{1}{\omega C_P} - \frac{\left(\omega L_S - \frac{1}{\omega C_S}\right)\omega^2 M^2}{(R_S + R_L)^2 + \left(\omega L_S - \frac{1}{\omega C_S}\right)^2} = 0 \tag{2.17}$$

For simplifying the analysis, normalized frequency u as defined by (2.18) is considered.

$$\frac{\omega}{\omega_o} = u \tag{2.18}$$

In (2.18), ω_o is the resonant frequency, given by (2.19):

$$\omega_o = \frac{1}{\sqrt{L_P C_P}} = \frac{1}{\sqrt{L_S C_S}} \tag{2.19}$$

Putting (2.18) in (2.17), one can obtain:

$$(u^2 - 1)[\omega^2 C_S^2 (R_S + R_L)^2 + (u^2 - 1)^2] - (u^2 - 1)\omega^4 M^2 C_S C_P = 0 \tag{2.20}$$

Putting (2.7) in (2.20), one can obtain:

$$(u^2 - 1)\left[\frac{u^2}{Q_S^2} + (u^2 - 1)^2\right] - (u^2 - 1)u^4 k^2 = 0 \qquad (2.21)$$

In (2.21), k is the coefficient of coupling, given by (2.22):

$$k = \frac{M}{\sqrt{L_S L_P}} \qquad (2.22)$$

$$(u^2 - 1)\left[\frac{u^2}{Q_S^2} + (u^2 - 1)^2 - u^4 k^2\right] = 0 \qquad (2.23)$$

Equation (2.23) has two parts. Solving each of them separately gives all the zero phase angle frequency for the SS-RIPT system. This has been presented below.

The first part:

$$u^2 - 1 = 0 \qquad (2.24)$$

$$u = 1 \qquad (2.25)$$

This gives, $\omega = \pm\omega_o$ \qquad (2.26)

The negative value of ω is ignored since it is physically unrealized.

The second part:

$$\frac{u^2}{Q_S^2} + (u^2 - 1)^2 - u^4 k^2 = 0 \qquad (2.27)$$

Solving (2.27) gives:

$$u^2 = \frac{(2 - Q_S^{-2}) \pm \sqrt{(Q_S^{-2} - 2)^2 - 4(1 - k^2)}}{2(1 - k^2)} \qquad (2.28)$$

$$u = \pm\left[\frac{(2 - Q_S^{-2}) \pm \sqrt{(Q_S^{-2} - 2)^2 - 4(1 - k^2)}}{2(1 - k^2)}\right]^{0.5} \qquad (2.29)$$

Neglecting negative roots, (2.29) gives two additional value of ω for ZPA frequency as shown below:

$$\omega = \left[\frac{(2-Q_S^{-2})\pm\sqrt{(Q_S^{-2}-2)^2-4(1-k^2)}}{2(1-k^2)}\right]^{0.5} \omega_o$$

$$\triangleq \left[\frac{(2-Q_S^{-2})\pm\sqrt{\Delta}}{2(1-k^2)}\right]^{0.5} \omega_o \tag{2.30}$$

If $\Delta=0$, then there are two values of ω for ZPA:

$$\omega = \omega_c = \left[\frac{2-Q_S^{-2}}{2(1-k^2)}\right]^{0.5} \omega_o \quad \& \quad \omega = \omega_o$$

If $\Delta>0$, then there are three values of ω for ZPA:

$$\omega = \omega_o, \omega = \omega_H = \left[\frac{(2-Q_S^{-2})+\sqrt{(Q_S^{-2}-2)^2-4(1-k^2)}}{2(1-k^2)}\right]^{0.5} \omega_o$$

$$\&$$

$$\omega = \omega_L = \left[\frac{(2-Q_S^{-2})-\sqrt{(Q_S^{-2}-2)^2-4(1-k^2)}}{2(1-k^2)}\right]^{0.5} \omega_o$$

If $\Delta<0$, then (2.30) will have two complex conjugate roots that are physically unrealized and there will be only one value of ω for ZPA:

$$\omega = \omega_o$$

From $\Delta=0$, the critical value of the coupling coefficient k_c can be derived as follows:

$$(Q_S^{-2} - 2)^2 - 4(1 - k^2) = 0 \tag{2.31}$$

$$k = k_c = \frac{1}{Q_S}\sqrt{1 - \frac{1}{4Q_S^2}} \tag{2.32}$$

In the literature the critical coupling has been defined as $k_c = \frac{1}{Q_S}$ [90]–[92]. Equation (2.32) shows the greater the value of Q_S, the smaller the difference between the critical couplings defined in the literature and derived in this thesis.

Putting value of k_c in ω_c, one can obtain the value of the frequency at the critical coupling coefficient. Its value is given by (2.33):

$$\omega_{c\_kc} = \left(1 - \frac{1}{2Q_S^2}\right)^{-0.5} \omega_o \tag{2.33}$$

From the above analysis, it is clear that for a bifurcation free operation, i.e. for single ZPA frequency, k should be less than k_c. For k, greater than k_c, there are three values of ZPA frequency: ω_o, ω_L, ω_H. A simple calculation shows that: $\omega_L < \omega_o < \omega_{c\_kc} < \omega_H$. It is important to note that ω_L and ω_H are related to k and R_L. On the other hand ω_o is independent of k and R_L.

When the coupling start decreasing, ω_L will increase and ω_H will decrease. Finally, at a coupling equal to k_c, ω_H and ω_L start merging and becomes equal to ω_{c_kc}, i.e. $\omega_L = \omega_{c\_kc} = \omega_H$. Therefore, there will be two ZPA frequencies ω_o and ω_c. However, at a significant value of Q_S, difference between ω_c and ω_o is negligibly small. For example for $Q_S = 4$, $\omega_c = 0.984\omega_o$.

If k is decreased further such that $k < k_c$, then ω_L and ω_H disappears. There will be only one ZPA frequency ω_o. Moreover, the peak magnitude of the voltage gain curve also starts increasing as k decreases. Therefore, for higher gain and bifurcation free operation, k should be less than k_c. These points will be illustrated later in the thesis using designed coil parameters.

The bifurcation phenomenon is undesirable as it affects the control, efficiency and stability of the overall system. This can be understood in terms of types of control strategy used for the power flow regulation. All the primary side control strategies for a static RIPT system can be broadly classified into three types:

(a) Fixed Frequency Control: In this type of control, the inverter is operated at constant switching frequency which is slightly deviated from the true resonant frequency to accommodate soft-switching operation. To regulate the power flow, phase/duty cycle of the inverter switches is varied. This allows producing an inverter output voltage with a variable pulse width at fixed frequency and hence allow the regulation of output voltage and current. This is the simplest of all control strategies. However, due to sudden change in load and coupling, soft switching is not guaranteed

in the vicinity of the resonant frequency if bifurcation occurs. Due to loss of soft-switching, switching losses will increase. Additionally, reduction of voltage gain due to bifurcation requires a higher current to deliver the same amount of power to the load. This results in increased copper losses in the coils and conduction losses in the switches.

(b) Variable Frequency Control: In this type of control scheme, the duty cycle of the pulses driving the inverter switches is kept constant at 50% and the switching frequency is varied to regulate the output power. To guarantee the soft-switching operation, operating frequency is selected higher than all the three ZPA frequencies. Such a large deviation from true resonant frequency will cause large circulating current in the resonant tank and therefore will cause a drop in overall efficiency of the system due to large conduction losses in switches as well as copper losses in the coils. Moreover, due to sudden change in load and coupling system could still bifurcate and it becomes difficult to guarantee soft switching operation [92], [93].

(c) Dual Control: In this type of control both frequency and duty cycle is varied for output power regulation. A variable frequency controller tracks the zero phase angle between the primary voltage and primary current, with a phase-locked-loop (PLL) controller, in order to minimize the VA rating of the supply [92], [93]. However, as derived earlier, an SS-RIPT system can have three ZPA frequencies. Therefore, due to sudden change in load and coupling it may uncontrollably switch between the three available ZPA frequencies. In turn, the operating frequency of the power supply will drift away from the true resonant frequency and the system might become unstable. Consequently power transfer will drop significantly. To deal with uncertainty in bifurcation region, sophisticated variable frequency control strategies which quickly adapt to instantaneous parameters variations have been proposed in [5], [47]-[50]. In [5], [47]-[50] instead of tracking the ZPA between primary voltage and current, the ZPA between primary voltage and secondary current has been tracked. The ZPA frequency between primary voltage and secondary current depends upon the instantaneous parameters of the RIPT system, but is unique for a set of these parameters, thus avoiding any instability issues caused by bifurcation.

From above discussion it can be concluded that bifurcation should be avoided at design level itself to ensure a simple control as well as an efficient and stable operation

of the system. The next subsection presents bifurcation free design guidelines for calculating the parameters of the SS-RIPT system for a given load.

2.3 Calculation of Electrical Parameters for Bifurcation Free Operation

Figure 2.4 shows the block diagram and components of an SS-RIPT based wireless charger. The aim is to calculate the parameters of the SS-RIPT link (shown in the red dotted box) for a given load (battery pack).
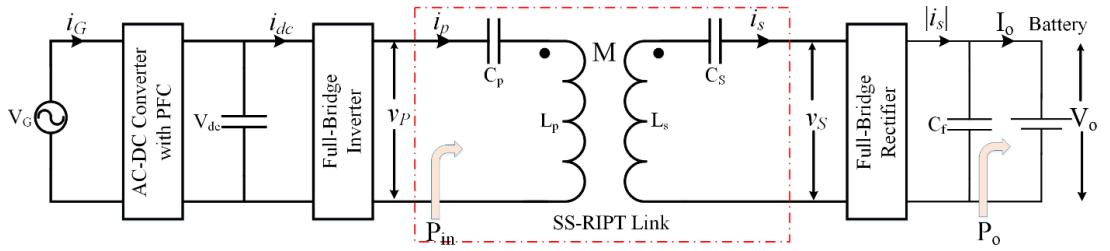
Figure 2.4 SS-RIPT based wireless charger

For simplifying the calculation of the parameters of the SS-RIPT link, the following assumptions are made:

(1) The efficiency of the SS-RIPT link is assumed to be 100%. This assumption is valid since the value of coil resistance is unknown before the design of the link, and therefore it is assumed to be negligible.

(2) Only the fundamental component (first harmonic) of the input voltage v_P and output voltage v_s of the SS-RIPT link is considered and higher order harmonics are neglected. In other words, the quality factor of the primary and the secondary circuit are deemed to be high to obtain sinusoidally varying primary and secondary currents.

(3) All the switching elements are considered ideal with zero commutation time (i.e. instantaneous turn on and off) and zero on-resistance (i.e., when conducting they present neither voltage drop nor losses). In other words, all converters are assumed to be 100% efficient.

(4) The magnitude of input voltage to the SS-RIPT link, i.e. V_P, is considered to be equal to the grid (supply) voltage magnitude V_G. This assumption is valid since there is usually a power factor correction stage between grid supply and full

bridge inverter. This PFC stage can adjust the *DC* link voltage, V_{dc}, of full bridge inverter to give V_P equal to the grid voltage.

(5) Ideal resonance in the primary and the secondary side is assumed.

Let the desired output power be P_o. Since the load is a battery pack, therefore the charging voltage is known, as defined by the manufacturer of the battery pack. Let V_o be the nominal charging voltage or the output voltage. Battery can then be represented by DC resistance R_o as:

$$R_o = \frac{V_o^2}{P_o} \tag{2.34}$$

According to [80] and [93], the AC equivalent of a DC resistive load with a diode rectifier and a capacitive output filter can be given by (2.35). This is the value of resistance seen by the secondary of the SS-RIPT link.

$$R_L = \frac{8}{\pi^2} \frac{V_o^2}{P_o} \tag{2.35}$$

The secondary voltage v_s is a square wave due to the capacitive output filter. The RMS value of the fundamental component of v_s can be given by (2.36). And RMS value of secondary current i_S can be given by (2.37):

$$V_{Srms} = 2\sqrt{2}\frac{V_o}{\pi} \tag{2.36}$$

$$I_{Srms} = \frac{V_{Srms}}{R_L} \tag{2.37}$$

From assumption (1), P_o is equal to P_{in}. Since V_P has been assumed equal to the grid voltage V_G, the RMS value of primary current can be given by (2.38):

$$I_{Prms} = \frac{P_{in}}{V_{Prms}} \tag{2.38}$$

Once the value of the primary and the secondary current are known, the value of the mutual inductance for the desired amount of output power can be derived by applying the KVL equation on the secondary side of the SS-RIPT link.

From Figure 2.3, at resonant frequency, $\omega_o = \frac{1}{\sqrt{L_S C_S}}$, the following equation can be written:

$$|j\omega_o M i_P| = R_L |i_S| \tag{2.39}$$

The secondary inductance is calculated from the secondary quality factor Q_S. As discussed earlier, the value of Q_S should be selected between 2 to 10 as a higher value can make the system difficult to tune, and a lower value will generate harmonics in the current and the voltage waveform. Equation (2.40) gives the value of the required secondary inductance.

$$L_S = \frac{Q_S R_L}{\omega_o} \tag{2.40}$$

The value of the coupling-coefficient k can be obtained using the equation of the critical coupling derived in section (2.2.2) in this thesis. To avoid the bifurcation, value of k should be selected to be less than k_c, that is:

$$k < \frac{1}{Q_S} \sqrt{1 - \frac{1}{4Q_S^2}} \tag{2.41}$$

Equation (2.41) will decide the minimum air-gap between the primary and the secondary coils. It also tells that there is a maximum value of the coupling-coefficient, exceeding which will let the system into the bifurcating mode and therefore having a coupling-coefficient as high as possible is not a good design practice and should be avoided. This is an important difference between a loosely coupled system such as the SS-RIPT system and a closely coupled system such as power transformers in which it is desirable to have a coupling as high as possible. Once the value of k is decided, the primary inductance can be calculated using (2.42):

$$L_P = \frac{M^2}{L_S k^2} \tag{2.42}$$

After calculating the parameters for the SS-RIPT link. The next stage is physically building the coils from the calculated values.

2.4 Analytical Design of Archimedean Spiral Coils

This section presents analytical formulas for calculating electrical parameters such as the self-inductance and the mutual inductance of the coil as well as the geometric parameters such as: inner diameter, outer diameter, inter-turn spacing and distance between the coils.

2.4.1 Analytical Model of Self-Inductance of Coils

Accurate physical modeling of the Archimedean spiral (inductor) is important since, once built, it is difficult to modify the spiral. In [94], [95], Wheeler presented several formulas for planar spiral inductors, which were intended for the discrete inductors. In [96], a modified expression of Wheeler formulas was given for spiral, square, hexagonal and octagonal planar coils but it relies on lookup tables. For this thesis, an amended form of the original Wheeler formula for an Archimedean spiral coil has been used to calculate the geometric parameters of the spiral coil from the estimated value of self-inductance. Figure 2.5 shows the representation of an Archimedean spiral.
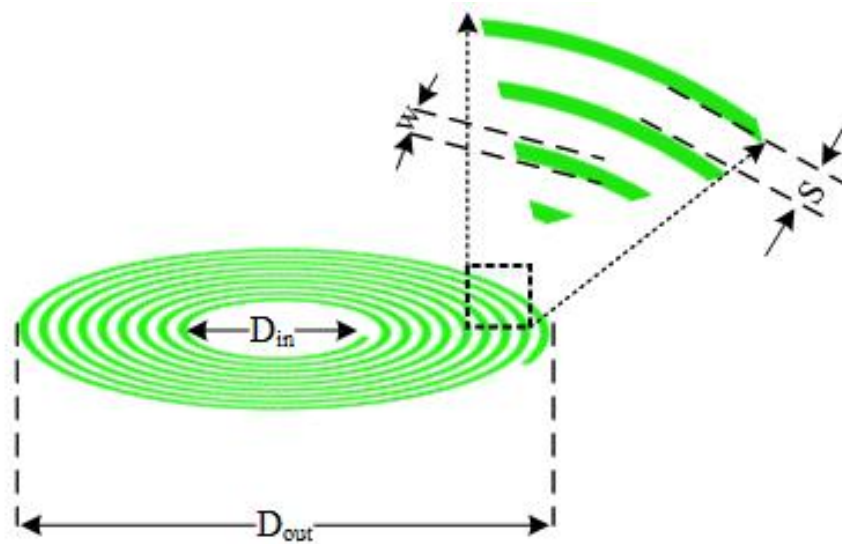
(a) 3-D view of Archimedean spiral
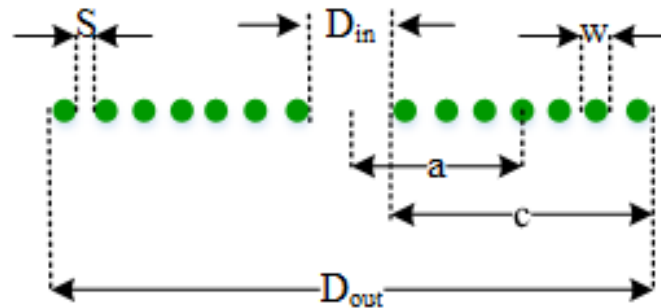
(b) Cross-sectional View of Archimedean spiral

Figure 2.5 Physical representation of Archimedean spiral

From Figure 2.5 it is obvious that D_{out} is the outer diameter; D_{in} is inner diameter; S is the spacing between turns; and w is the diameter of the wire used for making the coil. Equation (2.43) gives the original Wheeler expression for calculating the inductance of spiral coils [94].

$$L = \frac{a^2 N^2}{8a + 11c} \tag{2.43}$$

Equation (2.43) gives the inductance value in µH when all the dimensions are in inches. 'N' is the number of turns. With the help of Figure 2.5(b), c and a can be given by (2.44) and (2.45), respectively.

$$c = \frac{d_{out} - d_{in}}{2} \tag{2.44}$$

$$a = \frac{d_{out} - c}{2} = \frac{d_{out} + d_{in}}{4} \tag{2.45}$$

Putting (2.44) and (2.45) in (2.43) a modified and more usable version of the Wheeler formula can be derived as shown in (2.46):

$$L = \frac{N^2 (D_{out} + D_{in})^2}{8(15 D_{out} - 7 D_{in})2.54} \tag{2.46}$$

Equation (2.46) gives the inductance value in µH when all the dimension are in cm. For the design of coils, this modified Wheeler formula will be used throughout the thesis. Equation (2.47) gives the relation between D_{out} and D_{in}.

$$D_{out} = D_{in} + 2w + (S + w)(2N - 1) \tag{2.47}$$

Using (2.46) and (2.47), all the geometric characteristics of coils can be derived from the given value of inductance.

The design process starts by selecting the value of D_{out}. D_{out} can be decided from the air-gap required between the primary and the secondary coil. It has been established in the literature that the fundamental height of the flux path in a circular pad (or even circular Archimedean spiral) is about 1/4 of the coil diameter [97]. Therefore, it gives an idea about the how large the primary coil should be. If air-gap does not matter then D_{out} can be decided from the available foot-print on the place where the primary coil needs to be put. Once D_{out} is selected, then (2.46) can be used to calculate N and D_{in} for the known value of L by a numerical iteration process (trial and error method).

In (2.47), w is calculated from the selected value of the current density for the coils. Once w is calculated, the only remaining unknown is S, and it can be derived from (2.47). However, there can be more than one combination of N and D_{in} for the given value of L and D_{out}. Therefore, different values of S for the same L can be achieved. Therefore, one can obtain a series of coil geometry for the same L. This, in turn, leads to a number of primary and secondary coils for the given value of L. The coil-pair that is least sensitive to misalignment should be selected for the SS-RIPT link.

2.4.2 Analytical Model of Mutual Inductance between Coils

Most researchers rely on 3-D finite element analysis software for the calculation of mutual inductance between the two coils used in the wireless charger for EVs. This is due to the arbitrarily shaped coils (e.g. DD, DDQ) being used in such an application. The analytical solution of the magnetic field for such an arbitrary shaped coil is mathematically intractable and sometimes not possible. However, for a spiral shaped coils, the analytical solution of the magnetic field and therefore mutual inductance can be obtained due to its symmetrical shape and symmetrical coupling profile.

A few authors have presented the analytical expressions for mutual inductance between spiral coils using Neumann's formula [97], [120]. Neumann's formula [98] can provide an analytical equation for the mutual inductance between two coils of any shape. However, its solution is tedious due to the presence of double integral.

For this thesis, a rather simple approach based on Bio-Savart law [99] has been utilised to achieve the same final expression presented in [97], [120] for coaxial coils. The derived model calculates the mutual inductance from the geometric parameter of the coil-pair and does not require the solution of Neumann's formula. Consider the mutually coupled coils shown in Figure 2.6.
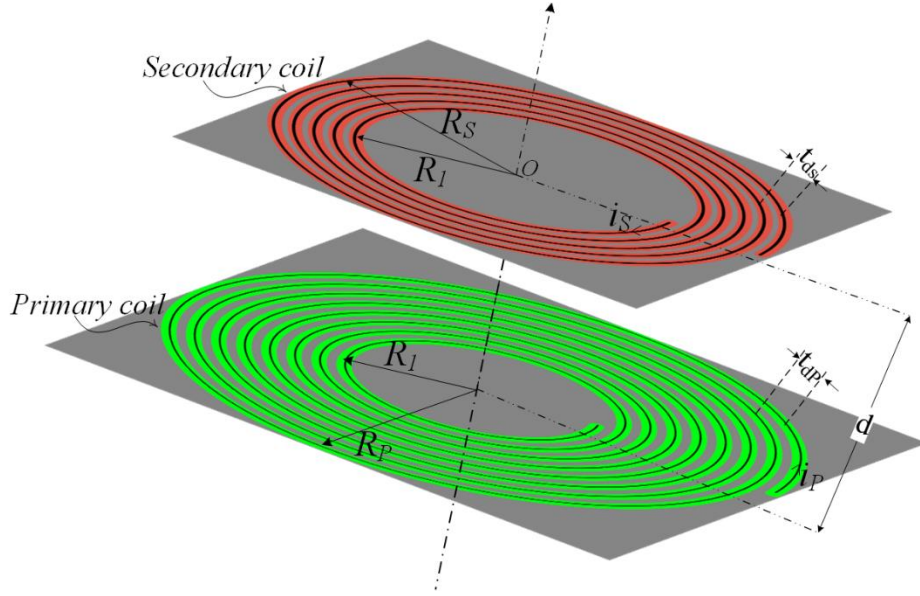
Figure 2.6 Mutually coupled coaxial coils

For the derivation of mutual inductance, it is assumed that coil turns are constant current carrying filaments. Let N_P and N_S represent the number of turns in the primary and the secondary coils, respectively. Let R_p and R_s represent the radius of the current filaments in the primary and the secondary coils respectively. Here, the subscript '*P*' and '*S*' are integers '1, 2, 3…..' such that N_1 represents the inner most turn (first turn) and R_1 represents the radius of the innermost filament and so on. Let *d* be the distance between the coaxial coils. Let I_P and I_S be the current in the primary and secondary coils.

Using Bio-Savart's law, the magnetic flux density B_o (RMS value) at the center of the secondary coil due to each primary current-carrying filament can be given by (2.48):

$$B_o = \frac{\mu_o}{4\pi} I_{Prms} \frac{2\pi R_P^2}{\left(R_P^2 + d^2\right)^{\frac{3}{2}}} \tag{2.48}$$

The total flux density at the center of the secondary coil due to all the primary current-carrying filaments is given by the summation of flux density by each primary current carrying filament, that is:

$$B_o = \frac{\mu_o}{4\pi} I_{Prms} \sum_{P=1}^{N_p} \frac{2\pi R_P^2}{\left(R_P^2 + d^2\right)^{\frac{3}{2}}} \tag{2.49}$$

Mutual inductance M between the primary and secondary coils' innermost turn, i.e. $N_s = N_I$, then can be given by the flux linkage in the secondary turn divided by the current flowing in primary coil, that is:

$$M = \frac{B_o A_S}{I_{Prms}} \tag{2.50}$$

In (2.50) A_S represents the area covered by each secondary filament and is given by (2.51):

$$A_S = \pi R_S^2 \tag{2.51}$$

Putting (2.49) and (2.51) in (2.50) gives the value of M between the primary coil and one of the secondary turns as shown below:

$$M = \frac{\mu_o}{2} \pi R_S^2 \sum_{P=1}^{N_P} \frac{R_P^2}{\left(R_P^2 + d^2\right)^{\frac{3}{2}}} \tag{2.52}$$

The total mutual inductance between the primary and the secondary coil can then be finally given by the superposition of the individual M between the primary coil and each secondary filament, that is:

$$M = \frac{\mu_o}{2} \pi \sum_{S=1}^{N_S} R_S^2 \sum_{P=1}^{N_P} \frac{R_P^2}{\left(R_P^2 + d^2\right)^{\frac{3}{2}}} \tag{2.53}$$

Equation (2.53) can be used to calculate the distance between two coaxial coils for the given value of mutual inductance.

2.5 Finding Coil-Pair Least Sensitive to Misalignment

As discussed in section (2.4.1) there could be several possible geometries for the primary and the secondary coils for given value of L. Therefore, one can have more than one coil-pair for the SS-RIPT link. To find the coil-pair which is the least sensitive to misalignment, a design example using 500 W setup has been presented in this section. A rating of 500 W was selected since building the coils are expensive and therefore a low power rating has been chosen to save money on prototypes. The design steps are presented in the following subsections:

2.5.1 Calculation of Electrical Parameters for 500 W setup.

The electrical parameters were calculated for 48 V output at 500 W and 40 kHz resonant frequency. Input was considered to be 120 V (regular household single phase supply in North America). In the lab, Litz wire 90/38 SPN SN (90 strands, 38 AWG each strand) was available and therefore the author intended to use this wire for building the prototypes of the coils. Due to the limited current carrying capacity of the wire, V_{srms} was kept at 48 V instead of V_o. Using the steps shown in section 2.3, the electrical parameters are calculated as follows:

$$R_L = \frac{V_{Srms}^2}{P_O} = \frac{48 \times 48}{500} = 4.608 \ \Omega \tag{2.54}$$

Q_S was selected to be 4, then L_S is given by (2.55):

$$L_S = \frac{Q_S R_L}{\omega_o} = \frac{4 \times 4.608}{2 \times \pi \times 40000} = 73.33 \ \mu H \tag{2.55}$$

$$I_{Srms} = \frac{V_{Srms}}{R_L} = \frac{48}{4.608} = 10.416 \ A \tag{2.56}$$

$$I_{Prms} = \frac{P_O}{V_{Prms}} = \frac{500}{120} = 4.16 \ A \tag{2.57}$$

$$M = \frac{I_{srms} R_L}{I_{Prms} \omega_o} = \frac{10.416 \times 4.608}{4.16 \times 2 \times \pi \times 40000} = 46 \ \mu H \tag{2.58}$$

$$k < \frac{1}{Q_S}\sqrt{1 - \frac{1}{4Q_S^2}} \triangleq k < \frac{1}{4}\sqrt{1 - \frac{1}{4 \times 16}} \triangleq k < 0.248 \tag{2.59}$$

Therefore k_c is 0.248. Value of k was selected to be 0.2. Then L_P is given by (2.60):

$$L_P = \frac{M^2}{L_S k^2} = \frac{46 \times 46 \times 10^{-6}}{73.33 \times 0.2 \times 0.2} = 721.39 \ \mu H \tag{2.60}$$

The values of compensation capacitors were calculated from (2.19). All the calculated (ideal) electrical and circuit parameters for 500 W have been shown in Table 2.1. To verify the calculated parameters, the SS-RIPT link was simulated in PLECS. The simulation was performed for ideal conditions, i.e. R_P and R_s were considered equal to zero and an ideal resonance (perfect tuning) in both the primary and the secondary side was assumed. The results obtained are shown in Figure 2.7, where it can be seen

that the simulation results closely matches the calculated values shown in Table 2.1. Figure 2.8 shows the simulation circuit used in PLECS 3.7.5.

Table 2.1 Electrical and circuit parameters of 500 W setup

Parameters	Values
V_{srms}	48 V
I_{Srms}	10.41 A
V_{Prms}	120 V
I_{Prms}	4.16 A
R_L	4.61 Ω
L_P	721.39 µH
L_S	73.33 µH
M	46 µH
C_P	219.46×10^{-4} µF
C_S	215.89×10^{-3} µF
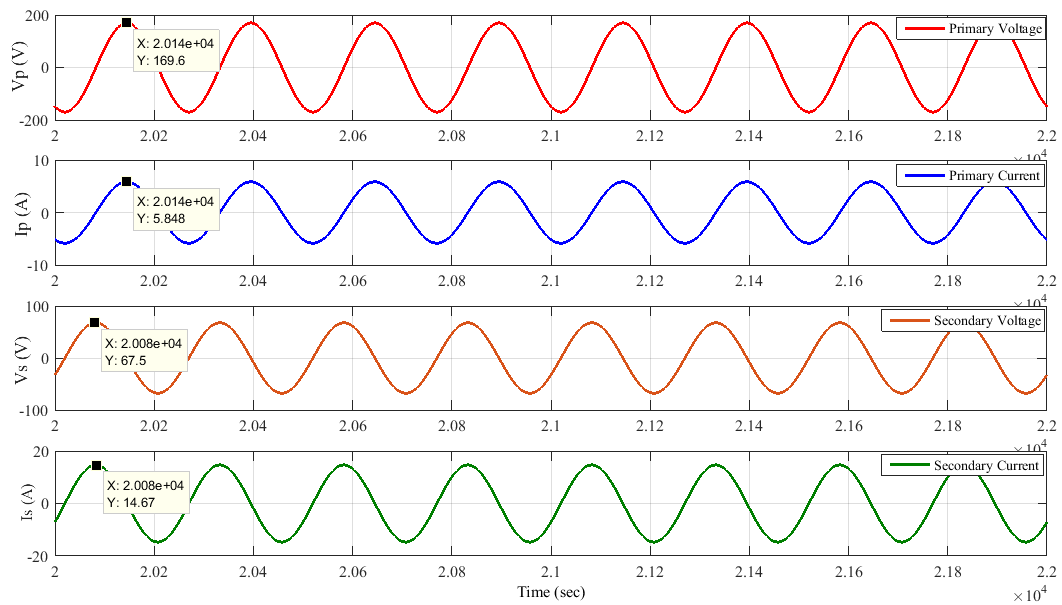
Figure 2.7 Simulation results for 500 W setup under ideal condition
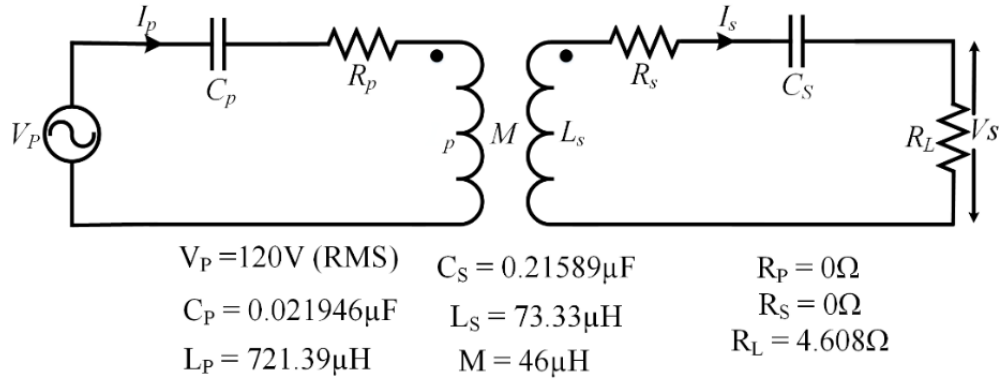
Figure 2.8 Circuit diagram for simulation of 500 W setup under ideal condition

To verify that a bifurcation free design has been achieved, the input phase angle of the SS-RIPT link was plotted against the frequency for different values of coupling coefficient k as shown in Figure 2.9. Table 2.2 lists all the zero crossing frequencies in Figure 2.9 for the different values of k.
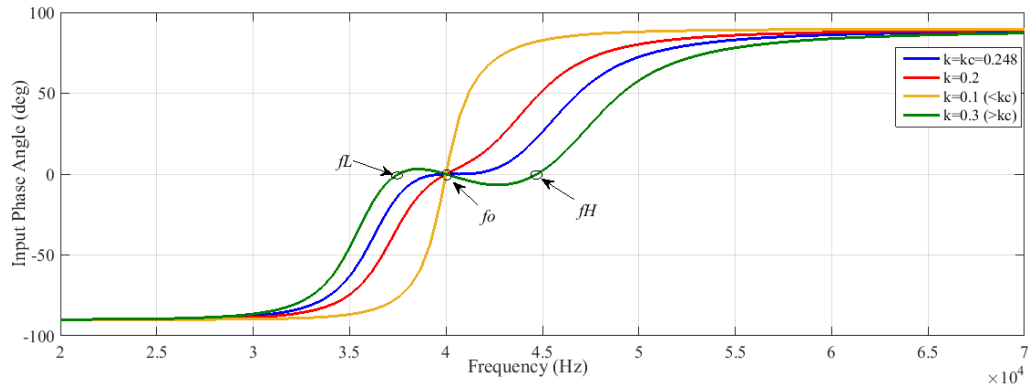
Figure 2.9 Input phase angle Vs frequency for 500 W setup under ideal condition

Table 2.2 Values of ZPA frequencies for different k

k	$f_o = \omega_o/2\pi$ (Hz)	$f_H = \omega_H/2\pi$ (Hz)	$f_L = \omega_L/2\pi$ (Hz)
0.100	40000	39835+4604.3i	39835-4604.3i
0.200	40000	40296+3033.6i	40296+3033.6i
0.248	40000	40640	40640
0.300	40000	44722	37504

From Figure 2.9 and Table 2.2, it is clear that for $k>k_c$ (0.248), there are three distinct ZPA frequencies: f_o, f_H, and f_L. At critical coupling (k=0.248), there are only two ZPA frequencies as f_L and f_H become equal to ω_{c_kc} given by (2.33). As k decreases below the critical coupling value of 0.248, there is only one ZPA frequency equal to f_o since f_H and f_L become imaginary. It can also be observed that $\omega_L < \omega_o < \omega_H$.

These results are in close agreement with the analysis presented in Section 2.2.2. Voltage gain (V_S/V_P) has been plotted against frequency variation in Figure 2.10.
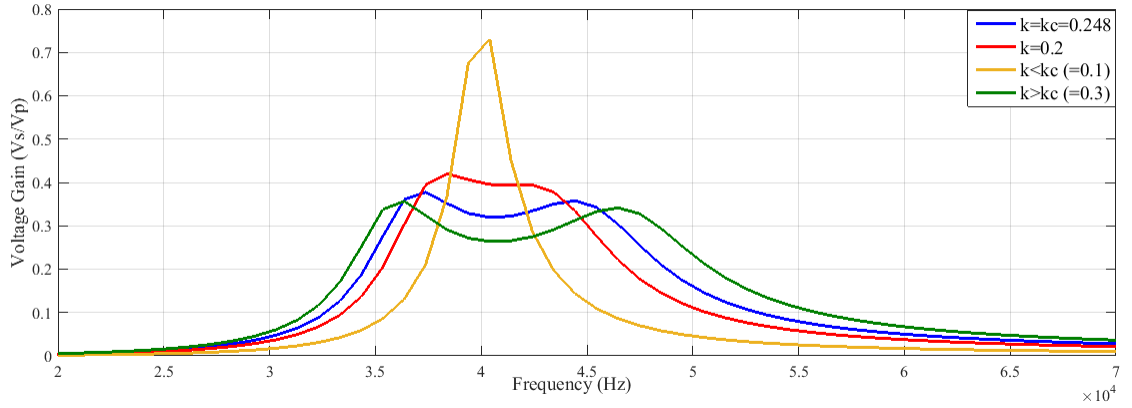
Figure 2.10 Voltage gain Vs frequency for 500 W setup under ideal condition

In Figure 2.10, there are two distinct peaks for values of k less than k_c. However, as k starts decreasing below k_c, the distance between the two peaks starts decreasing until finally they merge into a single distinct peak. One can also see that gain increases as the coupling decreases. The existence of double peak characteristics is known as pole-splitting or frequency-splitting phenomenon [100]–[105]. Although some authors [93] prematurely regard the pole-splitting phenomenon to be the same as bifurcation phenomenon, they are not entirely the same.

Frequency-splitting is related to the output characteristics of the system and determines the frequencies at which peak voltage gain, or in other words, peak power transfer, occurs. Bifurcation, on the other hand, describes input characteristics and determines the frequencies at which minimum input VA ratings can be satisfied. This can be understood from the plot shown below in Figure 2.11.
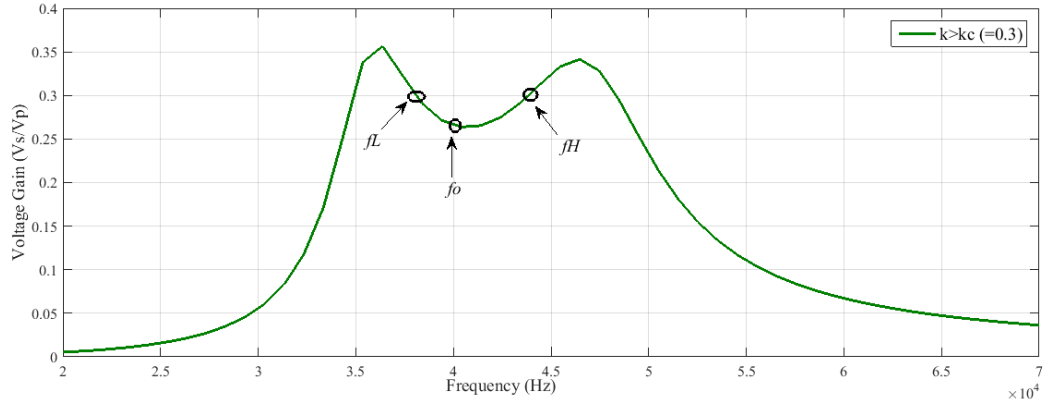
Figure 2.11 Voltage gain curve for *k*=0.3 under ideal condition

From Figure 2.11, one can observe that the peaks in the voltage gain curve occur at frequencies other than bifurcation frequencies. Therefore, the bifurcation phenomenon is not the same as the frequency-splitting phenomenon. In fact, the conditions for frequency-splitting can be derived using equation $\frac{dP_{in}}{d\omega} = 0$ as opposed to bifurcation conditions which are obtained using equation $Q_{in} = 0$. Detailed analysis of frequency-splitting phenomena is beyond the scope of this thesis hence has not been presented.

Nevertheless, both phenomena, although not exactly the same, show similar characteristics and under certain conditions, they can become exactly the same [106]. Therefore, it is safe to say here that coupling should be less than critical coupling to achieve a higher gain and hence greater power transfer.

2.5.2   Calculation of Geometric Parameters for 500 W setup.

As discussed earlier, more than one combination of primary and secondary coils can be designed from given parameters. Five coil-pair combinations were considered for finding the topology least sensitive to misalignment. The primary coil was kept the same in all five coil pairs since mutual coupling is a bilateral circuit property. A description of coil pairs is given below:

(i) Coil-pair P-S_1: For this coil-pair, the outer and the inner diameter of the primary and secondary coils are kept the same.

(ii) Coil-pair P-S_2: For this coil-pair, the outer diameter of the secondary coil is kept less than the outer diameter of the primary coil and the inner diameter of the secondary coil is kept bigger than the inner diameter of primary coil.

(iii) Coil-pair P-S_3: For this coil-pair, the inner diameter, as well as the outer diameter of the secondary coil, is kept smaller than their primary coil counterparts.

(iv) Coil-pair P-S_4: For this coil-pair, the inner diameter of the secondary coil is kept larger than the inner diameter of the primary coil and the outer diameter of the secondary coil is kept the same as the outer diameter of the primary coil.

(v) Coil-pair P-S_5: For this coil-pair, the inner diameter of the secondary coil is kept the same as the inner diameter of the primary coil and the outer diameter of the secondary coil is kept less than the outer diameter of the primary coil.

In all coil-pairs 'P' represents the primary coil and 'S' represents the secondary coil. A 'number' subscript has been used with 'S' to differentiate the secondary coils. For clarity, five coil-pairs are illustrated in Figure 2.12.

(a) P-S$_1$

(b) P-S$_2$

(c) P-S$_3$

(d) P-S$_4$

(e) P-S$_5$
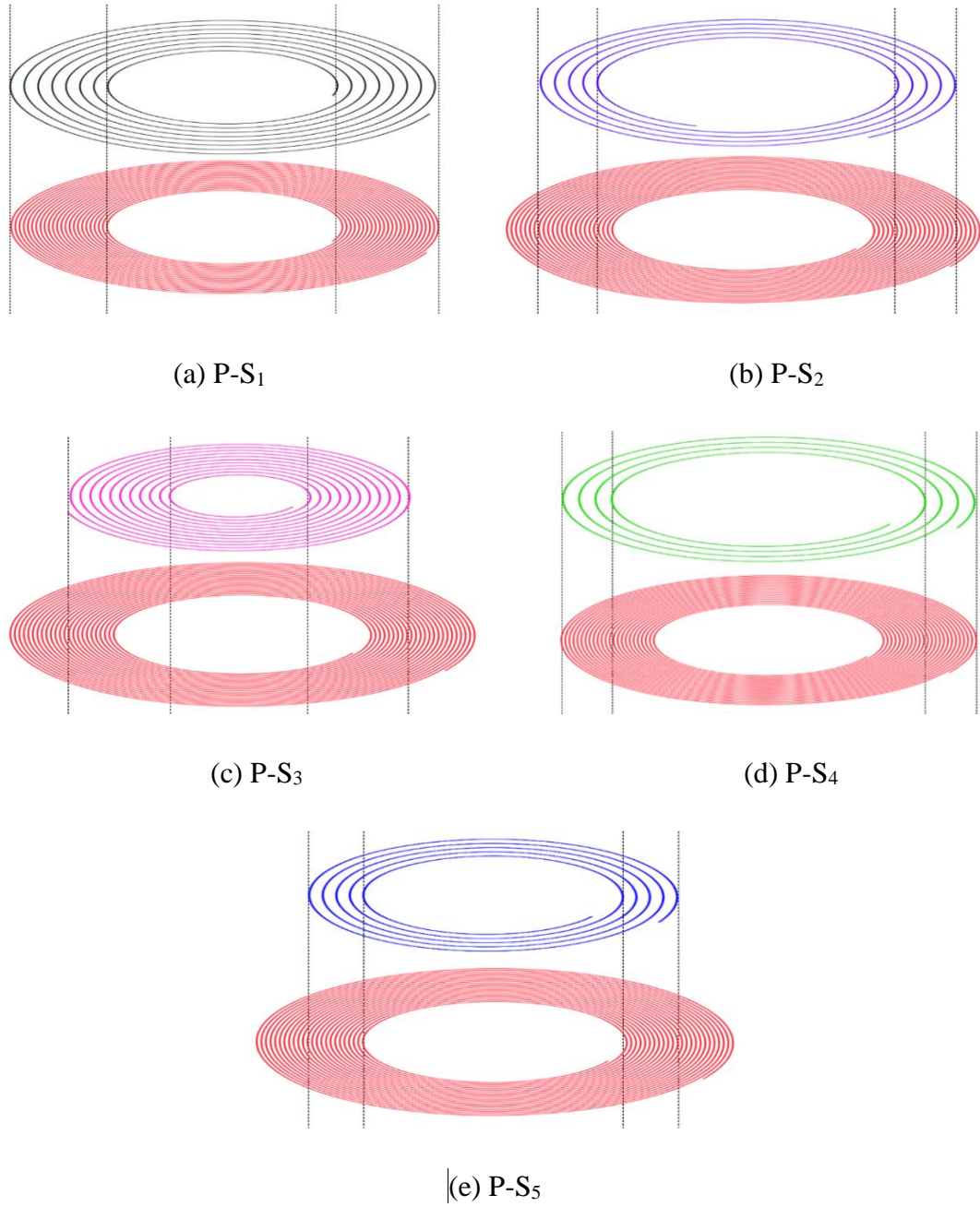
Figure 2.12 Different coil-pairs

Equations (2.46) and (2.47) were used to calculate the geometric parameters of coils to achieve an inductance value as close as possible to the calculated values. For the primary coil, an outer diameter of 28cm was found appropriate to satisfy all five coil geometries. Since the accuracy of the Wheeler formula degrades with the increasing inter-turn spacing [94], and because it has been shown in [58] that increasing the pitch decreases the mutual coupling, therefore inter-turn spacing was maintained zero for the

primary coil. Figure 2.13 shows the fabricated coils. Geometric parameters of all the coils are given in Table 2.3.
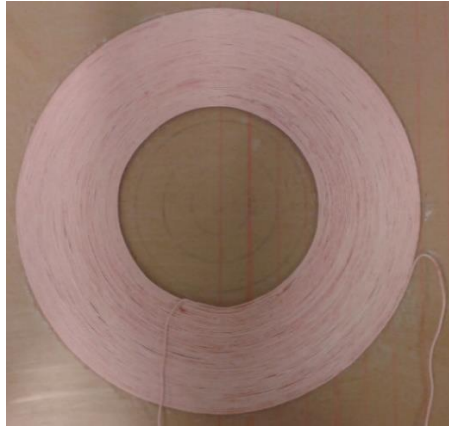
(a) Primary Coil *P*
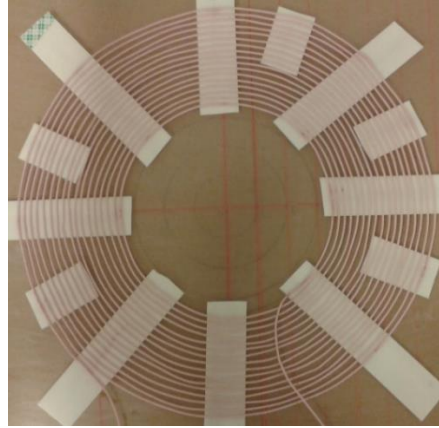
(b) Secondary coil S_1
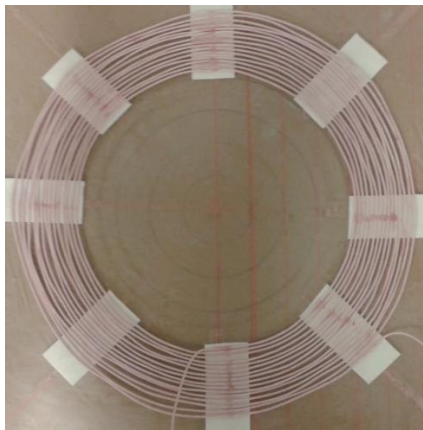
(c)Secondary Coil S_2
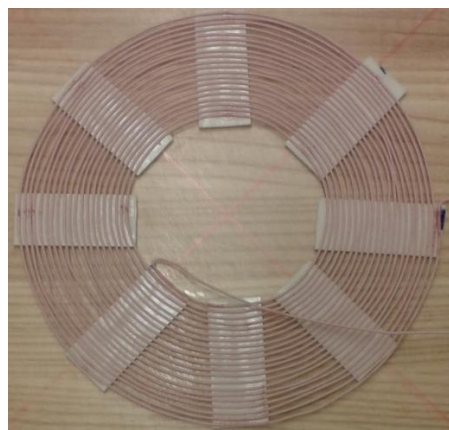
(d)Secondary Coil S_3
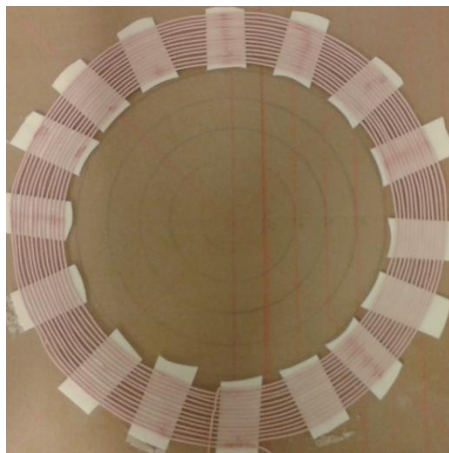
(e)Secondary Coil S_4
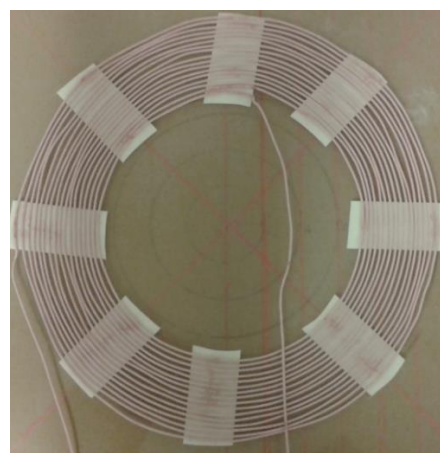
(f)Secondary Coil S_5

Figure 2.13 Fabricated coils for 500 W setup

Table 2.3 Geometric parameters of designed coils

Coils	N	D_{out} (cm)	D_{in} (cm)	S (mm)	W (mm)
P	52	28	14	0	124.46×10^{-2}
S_1	16.4	28	14	3	124.46×10^{-2}
S_2	15	24	16.6	124.46×10^{-2}	124.46×10^{-2}
S_3	20	19.6	9.6	124.46×10^{-2}	124.46×10^{-2}
S_4	13	28	21.4	124.46×10^{-2}	124.46×10^{-2}
S_5	16.4	22	14	124.46×10^{-2}	124.46×10^{-2}

2.5.3 Verification of Analytical Expressions

The resistance and self-inductance of the fabricated coils were measured using a Keysight E4980AL precision LCR meter. Table 2.4 gives the resistance and the inductance of the coils measured using the LCR meter and compares them against the analytically calculated values.

Table 2.4 Verification of self-inductance model

Coils	R (ohm) (Measured)	L (µH) (Measured)	L (µH) (Analytical)
P	1	722.56	721
S_1	32.43×10^{-2}	75.91	72.51
S_2	27.90×10^{-2}	75.50	74.8
S_3	0.29	74.24	73.99
S_4	0.28	75.44	75.11
S_5	28.65×10^{-2}	74.61	73.33

From Table 2.4, one can observe that the calculated values of the self-inductance of the coils match closely to the measured values. This, in turn, shows the effectiveness of the analytical expression for the inductance presented in Subsection 2.4.1.

The analytical expression for the mutual inductance derived in section (2.4.2) was tested on all of the coil-pairs at different air-gaps. The results obtained were compared with those obtained using the LCR meter. Figure 2.14 show the measured values,

analytical values and the percentage error between the measured and the analytical values for each coil-pair.
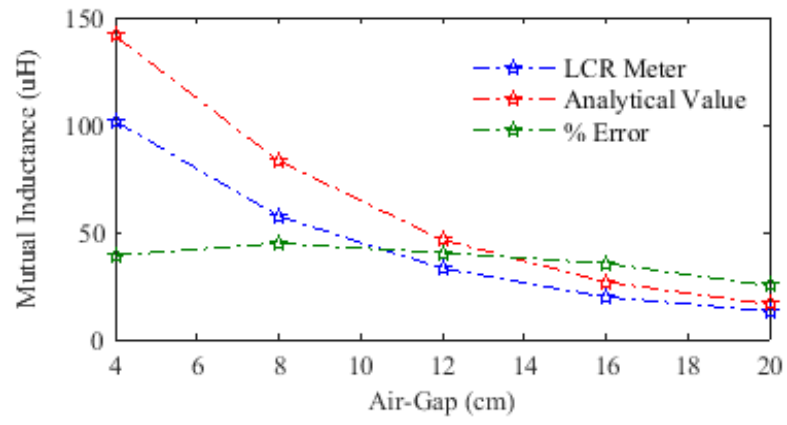
(a) Coil-Pair P-S$_1$
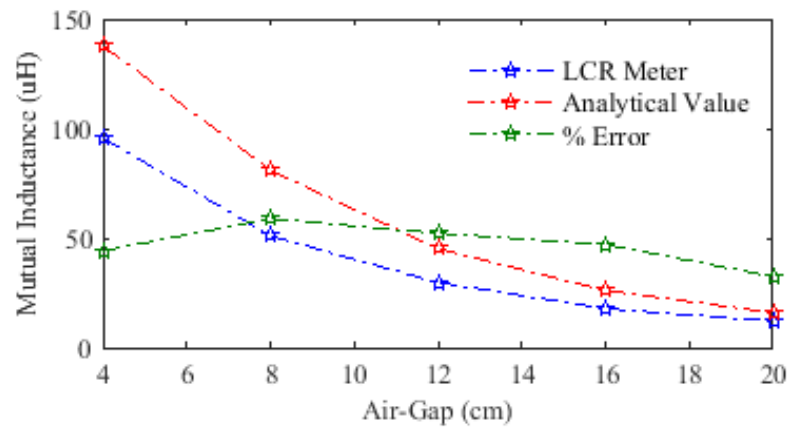
(b) Coil-Pair P-S$_2$
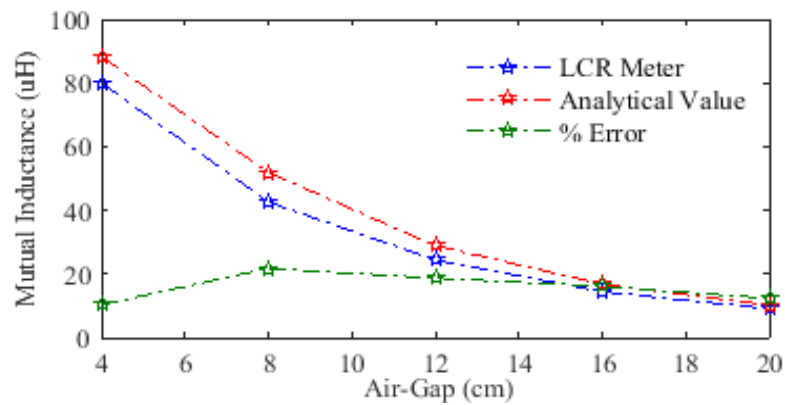
(c) Coil-Pair P-S$_3$
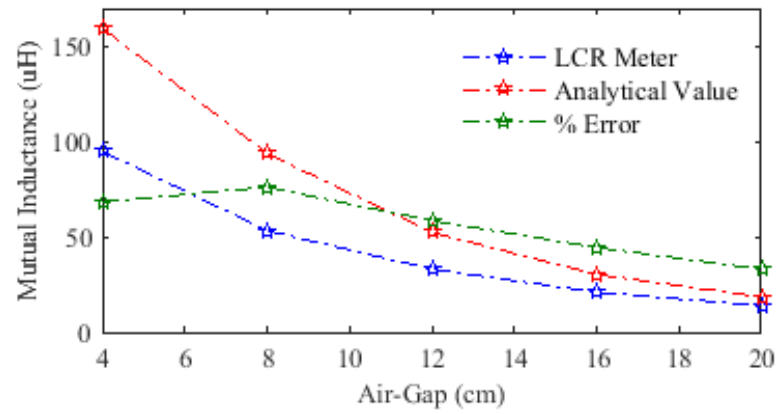
(d) Coil-Pair P-S₄
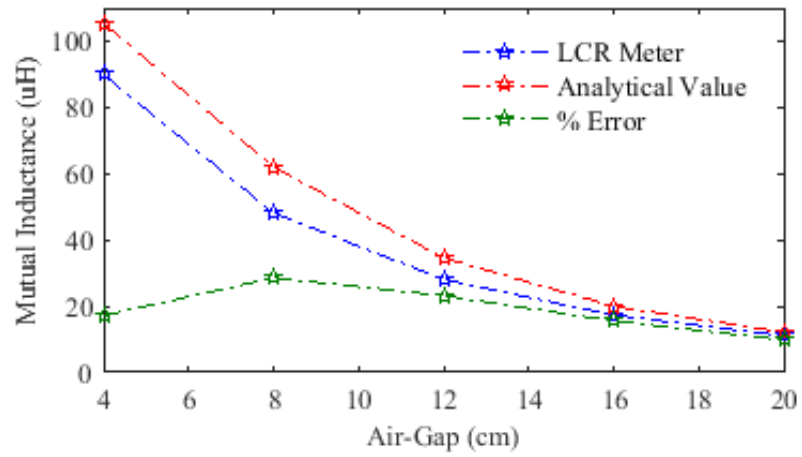
(e) Coil-Pair P-S₅
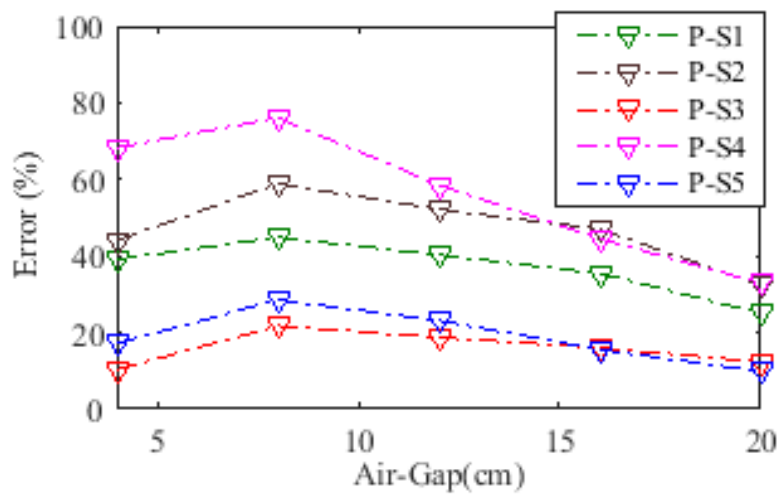
(f) % Error for each coil-pair

Figure 2.14 Verification of mutual inductance model

From the plots, the following observations can be made:

(i) There is a significant error between the LCR values and the analytical values for all the coil-pairs. Error decreases with the increasing distance between the coils in each coil-pair. This trend, in turn, concludes that (2.53) can be used for the case where there is a significant distance between coils. As pointed out in [98], [99] analytical expression is highly accurate if the distance between the coils is greater than the minimum size of the either coil in the coil-pair under test.

(ii) Out of all the geometric characteristics, the inner diameter most affects the accuracy of the analytical expression. If two coils have the same inner diameter, then the coil having the smaller outer diameter will give a more accurate result from the analytical expression. For example, in all the coil-pairs, the primary is common. However, the secondary coil is of a different size with S_3 having a minimum inner diameter (9.6mm). Next is the S_5 and S_1 (14cm), next to that is S_2 (16.6cm) and the largest is S_4 (21.4cm). In between S_5 and S_1, S_1 is considered larger in size due to its outer diameter being larger than that of S_5. Then this order of the size of the coil-pair can then be compared as:

$$P\text{-}S_3 < P\text{-}S_5 < P\text{-}S_1 < P\text{-}S_2 < P\text{-}S_4$$

Therefore, the order of accuracy of the analytical expression is $P\text{-}S_3 > P\text{-}S_5 > P\text{-}S_1 > P\text{-}S_2 > P\text{-}S_4$ with $P\text{-}S_3$ being the highest accurate case and $P\text{-}S_4$ being the least accurate case. The same trend has been obtained in Figure 2.14 (f).

(iii) Although the accuracy of the analytical expression is poor, the trend of variation of the mutual inductance with the air-gap predicted by the analytical expression is similar to the pattern obtained using the LCR meter.

From the above discussion, it can be concluded that the derived analytical expression for the mutual inductance should be used for applications where coil spacing is very large compared to the size of coils. Examples of such applications are printed circuit board transformers [107], [108]; wireless battery chargers for biomedical applications [109]–[111]; and electronic and printed circuit board design [112]. For an EV battery charger, the distance between the coils is less than the coil diameter, therefore this expression cannot be used.

Since the analytical expression did not predict the correct results for coaxial coils, there was no point in deriving the expression for the non-coaxial coils. Therefore, in the section to follow, the LCR meter has been used to calculate the distance between the coils for the given value of the mutual inductance. Simulations using a 3-D FEA package, called JMAG, has been used to verify the obtained results.

2.5.4 Mutual Inductance Profile of Coil-Pairs

To find the mutual-inductance profile of each coil pair under air-gap variations and misalignment conditions, two types of tests were performed: (a) changing the misalignment at the fixed air-gap, (b) changing the air-gap at zero misalignments. Figure 2.15 shows a concept diagram explaining the difference between misalignment and air-gap variation. All the results obtained for test (a) and test (b) are plotted in Figure 2.16.
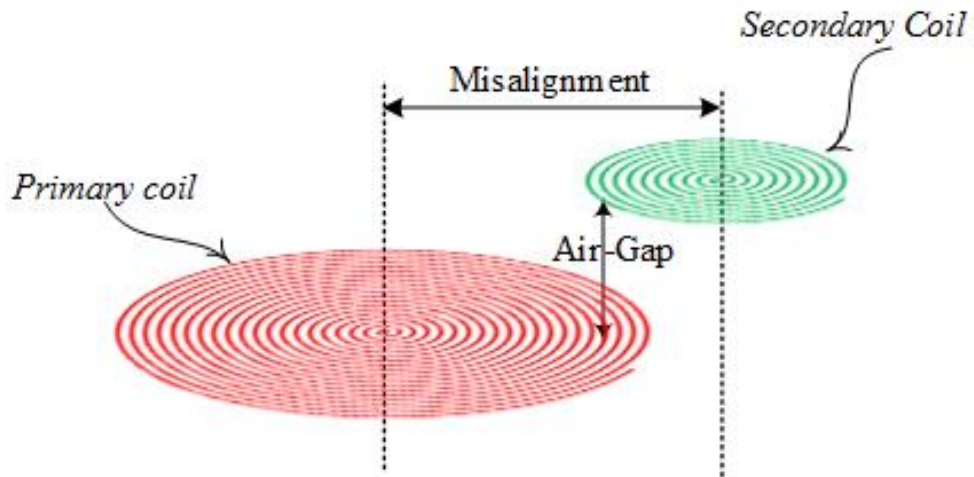
Figure 2.15 Concept of misalignment and air-gap
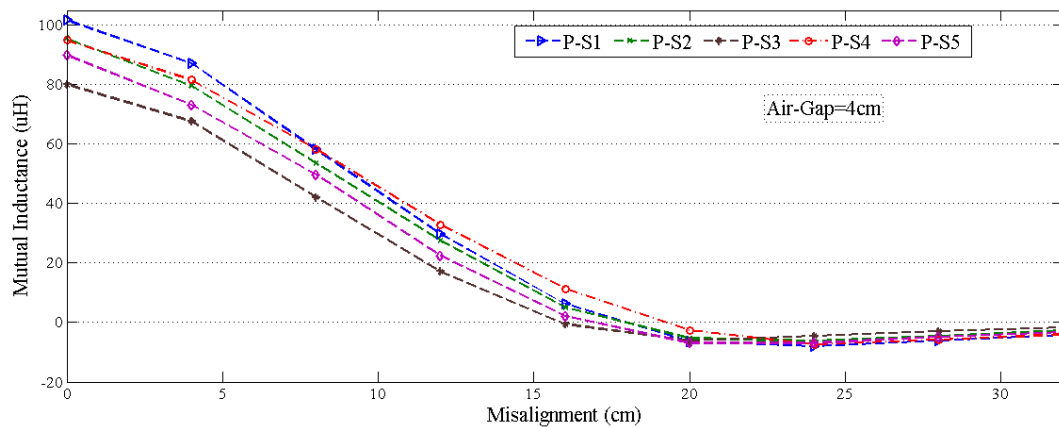
(a) Misalignment at 4cm air-gap
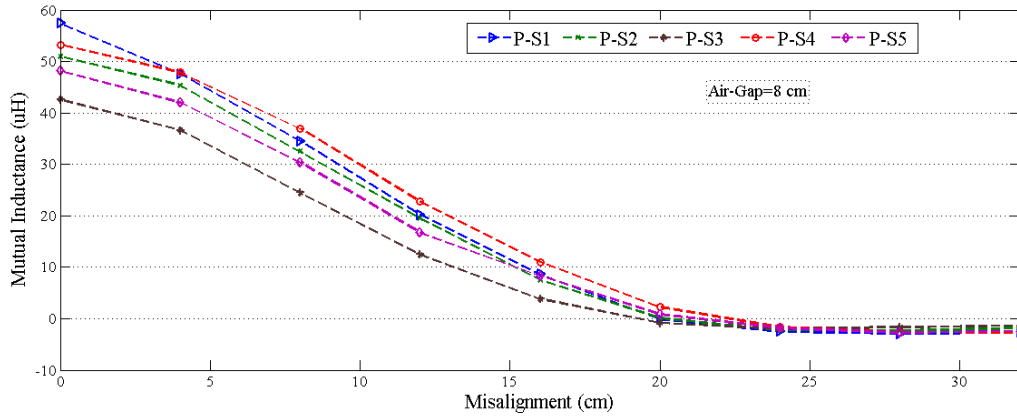
(b) Misalignment at 8cm air-gap
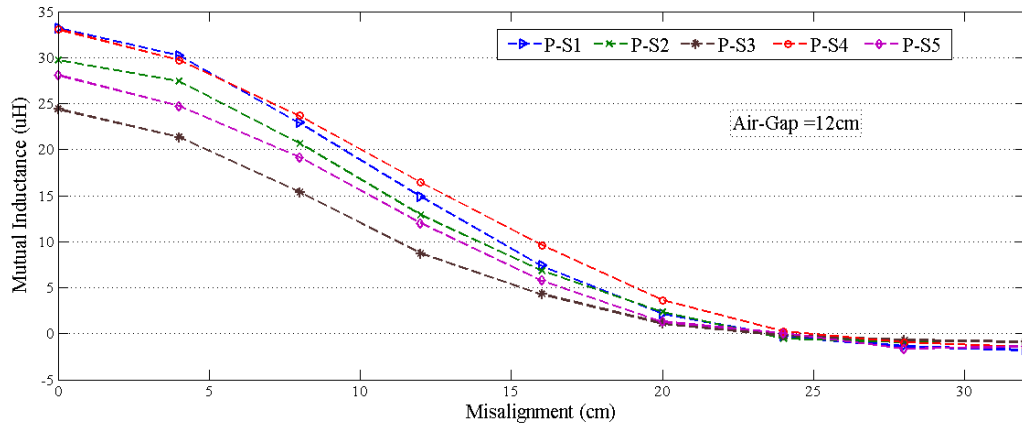
(b) Misalignment at 12cm air-gap

Figure 2.16 Performance of coil-pairs under misalignment at fixed air-gap

From the plots shown in Figure 2.16, one can observe that coil-pair P-S4 gives the best performance under a misalignment situation at all the air-gaps. Coil-pair P-S3 gives the worst performance under misalignment and air-gap variations. Mutual inductance profile at the different air-gap is also the superior for the coil-pair P-S4. Only at a perfectly aligned condition, i.e. 0 cm misalignment, does P-S1 give mutual inductance greater than P-S4. However, this difference decreases as the air-gap increases. To clarify this point, the mutual inductance versus air-gap at 0cm misalignment has been plotted in Figure 2.17.
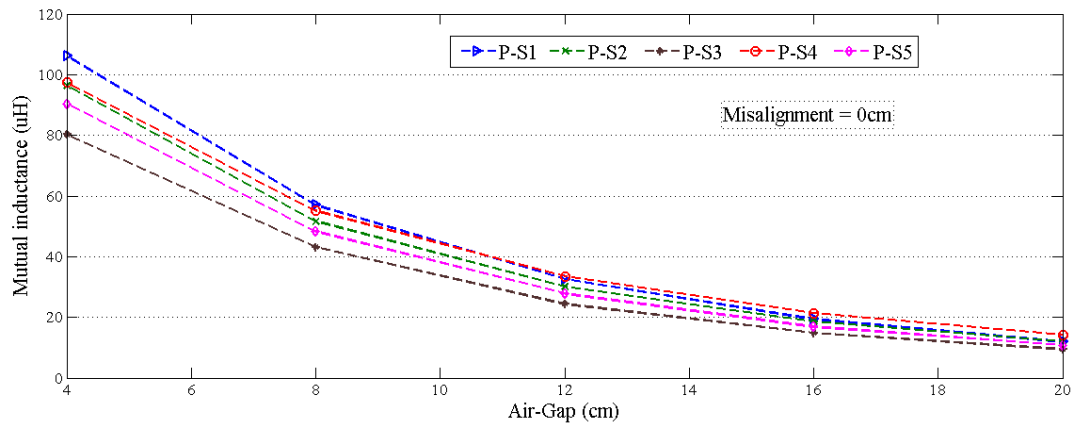
Figure 2.17 Performance of coil-pairs under gap variation but perfect alignment

From Figure 2.16 and Figure 2.17, it can be firmly claimed that P-S$_4$ is the best coil-pair to be adopted for the SS-RIPT link.

The coils were fabricated manually in the lab. Therefore, maintaining uniform turn spacing was not possible as is evident from Figure 2.18 and therefore some discrepancies in dimensions also crept in. Hence, it was felt necessary to verify the performance shown in Figure 2.16 using FEA analysis. For this purpose, 3-D models of the coil-pairs were modeled in the JMAG-Designer. Mutual inductance for all coil-pairs at misalignments but fixed an air-gap of 4cm was calculated and is shown in Figure 2.19.
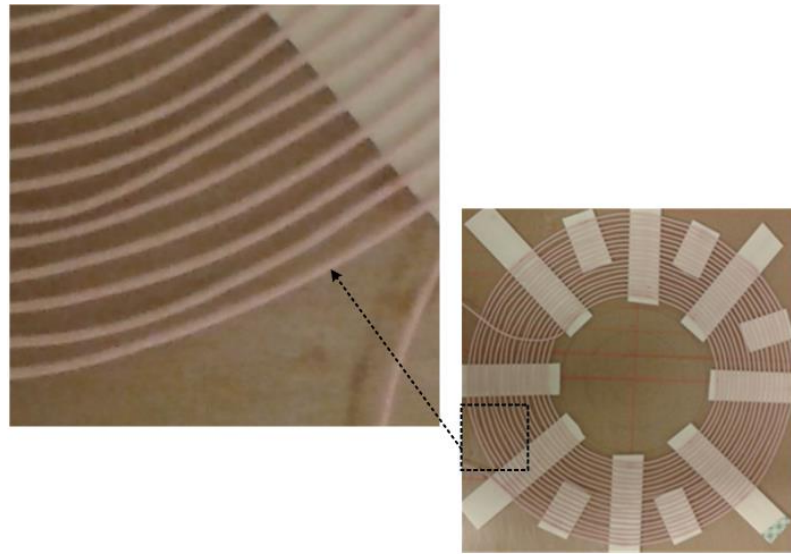
Figure 2.18 Nonuniform turn spacing in S$_4$
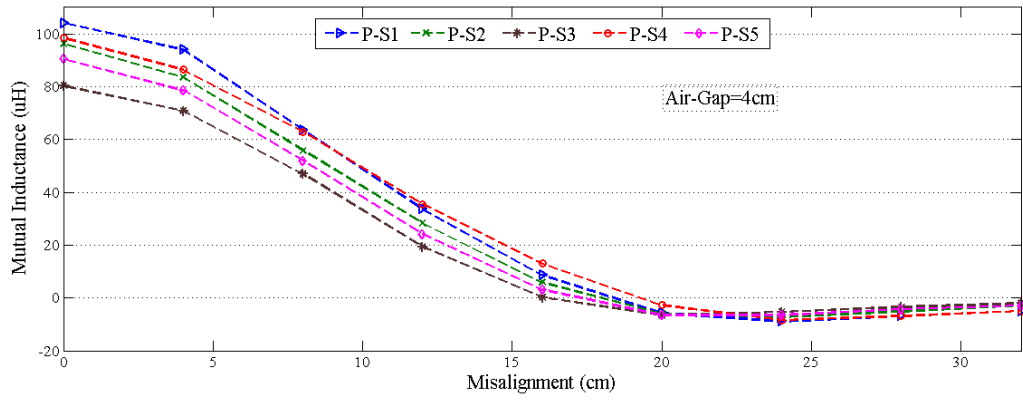
Figure 2.19 Results obtained using JMAG for misalignments at 4cm air-gap

The results shown in Figure 2.19, obtained using 3-D FEA analysis in the JMAG-Designer, match closely to the result illustrated in Figure 2.16 (a). Since 3-D simulations are computationally intensive and require long run times, therefore only one case (misalignment at fixed air-gap of 4 cm) was simulated. This is sufficient to verify the performance of coil-pairs obtained in Figure 2.16 due to the matching performance achieved.

Figures 2.20-2.24 shows the 3-D models of the coil-pair created in the JMAG-Designer for calculating mutual inductance.

(a) Misalignment=0cm, Air-gap=8cm   (b) Misalignment=4cm, Air-gap=4cm
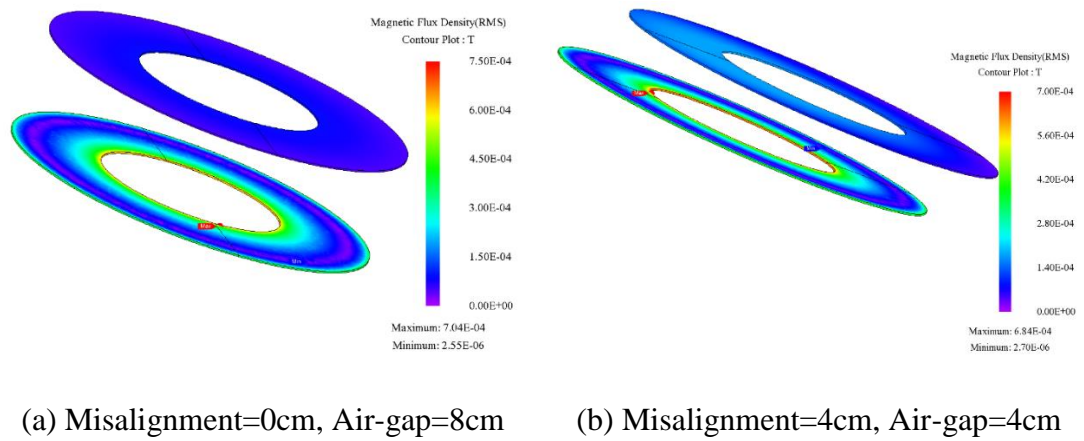
Figure 2.20 3-D FEA model of P-S$_1$

(a) Misalignment=0cm, Air-gap=8cm   (b) Misalignment=4cm, Air-gap=4cm
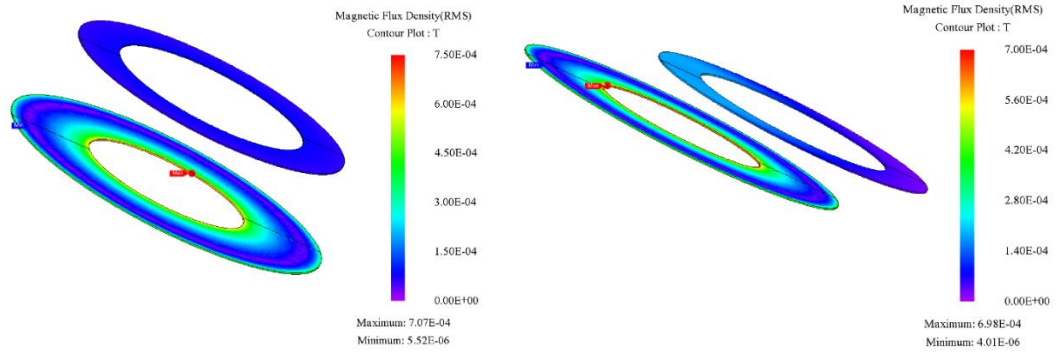
Figure 2.21 3-D FEA model of P-S$_2$

(a) Misalignment=0cm, Air-gap=8cm   (b) Misalignment=8cm, Air-gap=4cm
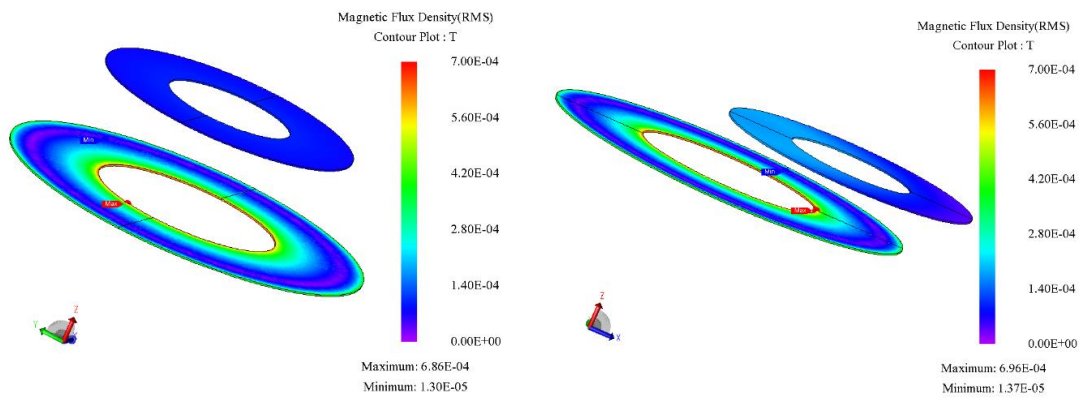
Figure 2.22 3-D FEA model of P-S$_3$

(a) Misalignment=0cm, Air-gap=8cm   (b) Misalignment=8cm, Air-gap=4cm
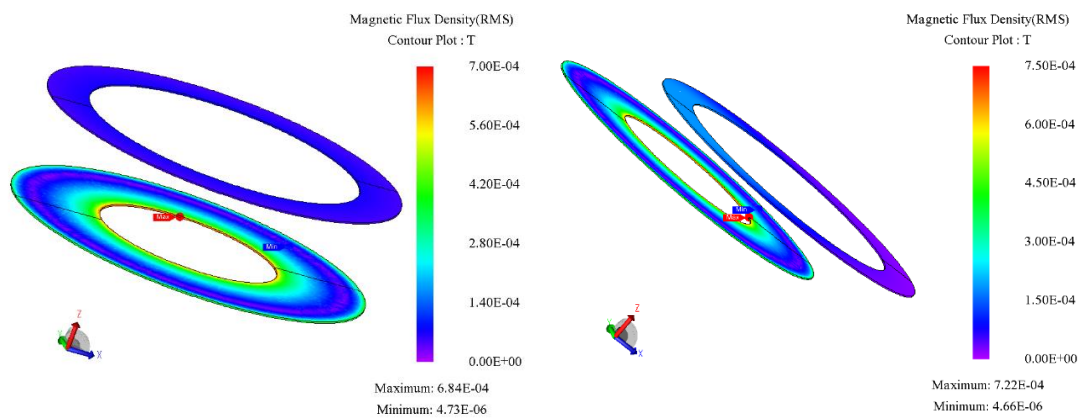
Figure 2.23 3-D FEA model of P-S$_4$
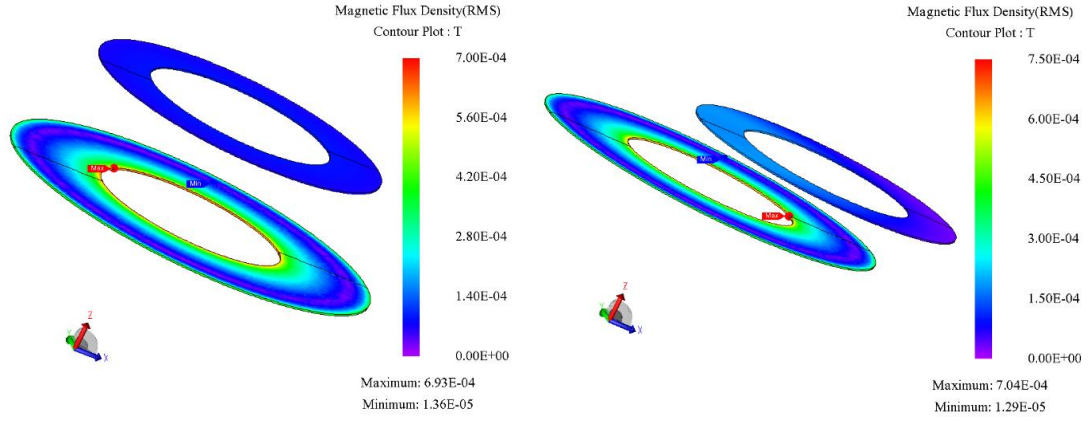
(a) Misalignment=0cm, Air-gap=8cm   (b) Misalignment=8cm, Air-gap=4cm

Figure 2.24 3-D FEA model of P-S$_5$

2.6   Summary of Chapter 2

This chapter presents the design considerations for a series-series resonant inductive link employing coils in the shape of the Archimedean spiral. The importance of quality factor and bifurcation free design has been explained.

Novel and easy to follow bifurcation free design guidelines for calculating the electrical parameter of the SS-RIPT link have been presented. The analytical expression to decide the geometric characteristics such as the number of turns in the coil and the outer and inner diameter of the coils has been presented and verified to give accurate results.

It was found that a series of coil-pairs can be designed from the given value of the circuit parameters. Since a greater charging zone is desired in the EV battery charging applications, all the coil-pair were tested to find the one which is least sensitive to misalignment and air-gap variation.

For testing purposes, coil-pairs of 500 W output power were designed following the design steps presented in this chapter. It was found the outer radius of the secondary coil should be kept equal to the outer radius of the primary coil, and inner radius of the secondary coil should be maintained greater than the inner radius of the primary coil to obtain the best coupling profile.

Chapter 3 Design of 3.6 kW Wireless Charger

3.1 Calculation of Electrical Parameters

The electrical parameters are calculated for a nominal charging voltage i.e. output voltage V_o of 168 V. Since a 3.6 kW charger falls into the category of an AC level 2 charger according to SAE J1772 charging standards (Table 1.2), the RMS value of the fundamental component of the primary voltage V_P is assumed to be 240 V. A resonant frequency f_o of 40 kHz and secondary quality factor Q_S equal to 4 are considered. A value of 4 for Q_S gives critical coupling k_c equal to 0.248. To eliminate bifurcation, nominal coupling k is assumed to be 0.2 for bifurcation free operation. Table 3.1 gives the calculated (ideal) electrical and circuit parameters.

Table 3.1 Ideal electrical and circuit parameters of 3.6 kW charger

Parameters	Values
V_o	168 V
I_o	21 A
V_{Prms}	240 V
I_{Prms}	15 A
V_{Srms}	151 V
I_{Srms}	23 A
R_o	7.84 Ω
L_P	398.58 μH
L_S	101.06 μH
M	40.14 μH
C_P	39.72×10^{-3} μF
C_S	156.65×10^{-3} μF

Since an operating frequency of 40 kHz is used, increase in resistance of the wire due to eddy currents needs to be considered. Eddy current is caused by two mechanisms known as skin effect and proximity effect [113]–[116]. Braided enamelled conductors

known as Litz wire have been found very effecting in mitigating these two high frequency effect [117], [118] .

A Litz wire consists of many thin strands, each individually insulated, wound into a wire. Each strand is no thicker than the skin depth [119], which ensures an efficient use of the conductive area. The strands are then woven together so that the location of each strand alternates between the centre of the wire and the edge of the wire. This ensures that the proximity effect will affect each strand the same, and thus carry the same current. The next section discusses the selection of the number of strand, the overall gauge, and the construction of the Litz wire used in making the coils for the 3.6 kW charger.

3.2   Design of Litz Wire for the Coils

From Table 3.1, one can observe that the maximum value of RMS current flowing in the SS-RIPT link is 21.43 A. However, for the design of Litz wire the maximum current of 30 A (RMS) was considered to allow for some safety margin and future expansion of this work.   Following steps were followed to calculate the required number of strands and overall gauge of the wire.

a) Calculate the Overall Gauge of the Required Wire: The design of the Litz wire starts by selecting an appropriate value of current density for the wire. From the literature review, it is found that the recommended value of the average current density for a given continuous power level and temperature rise over ambient temperature for convention cooling lies between 2 to 6 A/mm^2 [68], [120]. For this thesis, the value of 4 A/mm^2 is considered. Therefore, for a given value of the current, the overall area of the cross section of the wire is given by (3.1).

$$Area\ of\ cross\ section\ of\ wire = \frac{current}{current\ desnity} \qquad (3.1)$$

Equation (3.1) gives the value of 7.5 mm^2. According to the table of American wire gauge (AWG) sizes, available online, an 8 or 9 AWG overall cross-section of wire is required. 8 AWG is selected.

b) Calculate Number of Strands: The skin depth for a round conductor is given by (3.2) [113]

$$\delta = \sqrt{\frac{\rho}{\pi f \mu}} \qquad (3.2)$$

In (3.2), δ is the skin depth in m, f is the frequency in Hz, μ is the magnetic permeability of the conductor in H/m, ρ is the resistivity of the conductor in Ω-m. Value of f here is 40000 Hz, μ for copper is $4\pi \times 10^{-7}$ Ω-m. The value of resistivity of copper is 1.72×10^{-7} Ω-m at 20°C and 2.3×10^{-7} Ω-m at 100 °C [121]. Since the resistivity of copper increases with increasing temperature and from (3.2) it can be seen that as resistivity increases, skin depth increases, it is better to calculate the skin depth for a worst case scenario, i.e. room temperature (20 °C). Putting all these values in (3.2), skin depth is calculated to be 0.33 mm.

The diameter of a selected strand should be less than the skin depth. A good design uses a strand diameter smaller than the skin depth by a factor of 4 or more [122]. Therefore, a strand of 38 AWG (0.101mm) diameter is selected. The number of strands can then be given by (3.3).

$$Number\ of\ strands = \frac{area\ of\ cross\ section\ of\ overall\ wire}{area\ of\ cross\ section\ of\ each\ strand} \qquad (3.3)$$

Equation (3.3) gives value of 1044.7~ 1045.

c) *Decide the Construction of the Litz Wire*: In the Litz wire, skin and proximity effects can be further divided into strand level and bundle-level effects [119]. Simple twisting is adequate to eliminate the bundle level proximity effect but to avoid bundle level skin effect, multiple levels of twisting, also known as true Litz construction are required [122], [123]. First *n1* number of strands are twisted together, followed by twisting *n2* of those sub-bundles; additional stages are followed if required. The value of *n*1 is given by (3.4) [113].

$$n1 = \frac{4(sink\ depth)^2}{(diameter\ of\ single\ strand)^2} \qquad (3.4)$$

Equation (3.4) gives *n*1 equal to 42.7; a value of 42 is selected. The first level of twisting is 42 strands together. This will eliminate the bundle level skin effect at the first level. For the second level 3, 4 or 5 sub-bundles are selected. Here a value of 5 was used. Therefore, the second level of twisting gives 5×42= 210 strands. Finally, for the last level, 5 bundles of the second level will give 1050 strands.

The final construction is designated as 5/5/42 if each level of twisting is in the same direction (also known as a bunching operation) or as 5×5×42 if the direction of the twisting alternates at each level (also known as cabling operation).

The cabling operation is more effective in eliminating high-frequency effects. Therefore, 8 AWG 5×5×42/32 with single Nylon served was ordered from a cable manufacturing company named New England Wire Technologies. The overall dimeter of the purchased Litz wire with nylon covering was measured as 4.6 mm.

3.3   Fabrication of Coils for 3.6 kW Charger

Coils were fabricated based on the P-S$_4$ coil-pair. For the 3.6 kW charger, the outer diameter 'D_{out}' was selected to be 47 cm. The diameter of the wire 'w' is known to be 4.6 mm. Inter-turn spacing 'S' was kept the minimum possible, since it has been established in the literature that an increase in turn spacing decreases mutual inductance [28], [58]. Mutual inductance decreases with turn spacing because flux collapses in between the spacing, thereby reducing coil's overall magnetomotive force (MMF). Since S, w and D_{out} are fixed, the inner diameter 'D_{in}' and number of turns 'N' are adjusted using (2.46) and (2.47) to achieve inductance value as close as possible to the ideal value. Table 3.2 gives the ideal geometric parameters for the ideal self-inductance values.

Table 3.2 Ideal geometric parameter for 3.6 kW charger

Coils	N	D_{out} (mm)	D_{in} (mm)	S (mm)	W (mm)
Primary	39.97	470	98	0	4.6
Secondary	11.70	470	356	7.8×10^{-2}	4.6

The coils were fabricated manually and therefore some discrepancies in geometric parameters crept in during the fabrication process. Therefore, there is some difference between the actual parameters of the assembled coils and ideal parameter values. Figure 3.1 shows the assembled coil and Table 3.3 gives the actual geometric and self-inductance value achieved.
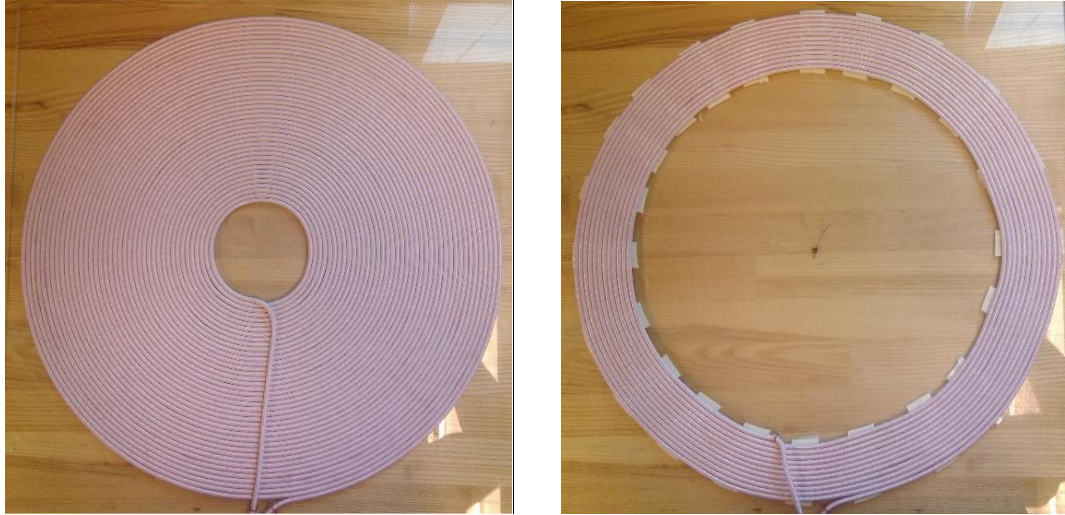
(a) Primary Coil   (b)Secondary Coil

Figure 3.1 Fabricated coils

Table 3.3 Actual parameter of fabricated coils

Coils	N	D_{out} (mm)	D_{in} (mm)	L (µH)	R (Ω)
Primary	40	470	95.4	397.16	0.16
Secondary	12	470	356	105.77	0.08

Since the analytical expression for the mutual inductance derived in Subsection 2.4.2 was not useful, the LCR meter was used to achieve mutual inductance of value 40.14 µH by manually adjusting the air-gap. An air-gap of 16.5 cm was found to give an M value of 40.14 µH.

3.4   Addition of Ferrites to the Fabricated Coils

Due to the presence of large air-gap, leakage flux is very high in an RIPT system. At the power level of kW, it is necessary to limit the value of the leakage magnetic field in the region accessible to humans and animals [124]. For this purpose ferrite cores along with copper or aluminium plate, collectively known as shielding, is added to the coils for minimising the leakage flux [28], [125].

From the literature reviews it is known that adding a flat plate of ferrite sheet to the back of an Archimedean spiral is very effective in minimising the leakage flux. However, using a solid piece of ferrite plate adds weight, is fragile and is very expensive.

Therefore, the new design uses ferrite cores in the shape of spokes to reduce weight and cost. Besides this, spacing between the ferrites act as a shock absorber. Figure 3.2 shows the coil circular coil with ferrite spokes.
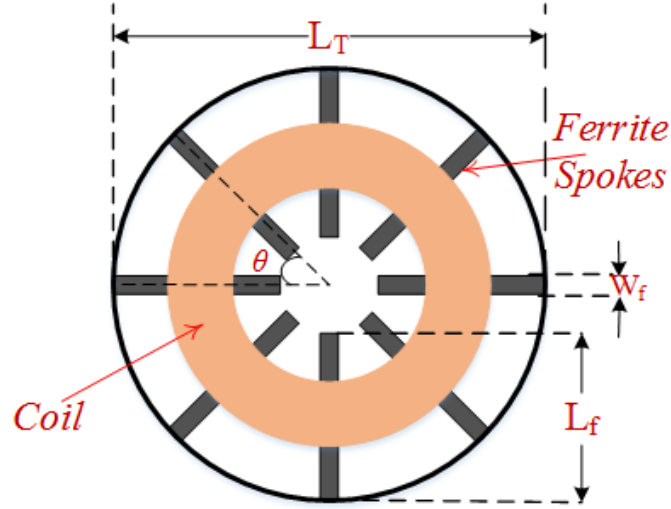
Figure 3.2 Circular charging pads

In Figure 3.2, L_f is the length of the ferrite spoke, L_T is the total length of the pad, W_f is the width of the ferrite spoke, θ is the angle between the two ferrite spokes. PC95 cores from the TDK Ferrite Company, which can operate in the frequency range 0 to 500 kHz and have low power losses from 25 to 100 °C, were therefore considered for this thesis. The MH&W International Corporation had available PC95 cores in I shape. 50 pieces of the PC95 core of dimension 55.9X19.3X6.6 mm were ordered.

However, it is found that the addition of cores increases the self-inductance of the coils. The original value of self-inductances is achieved by adjusting the turns of the original coils by unwinding the inner turns of the primary and secondary coils (so that the outer diameter is not affected).

The coil with ferrite backing is referred to as 'pad' in this thesis. Figure 3.3 shows the picture of the final coils with ferrite cores. The electrical attributes and physical of the primary and secondary pad are provided in Table 3.4 and Table 3.5, respectively.
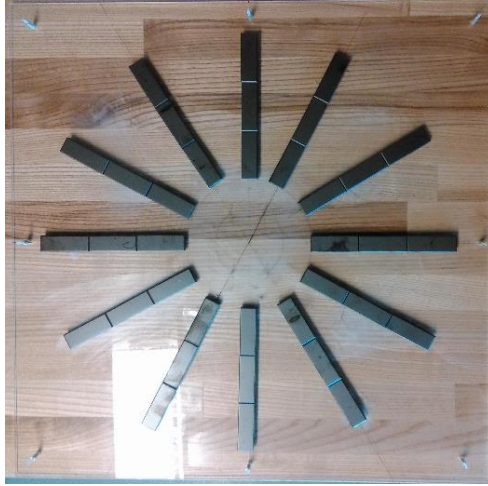
(a) Ferrite spokes for Primary pad   (b) Primary coil with ferrite spoke
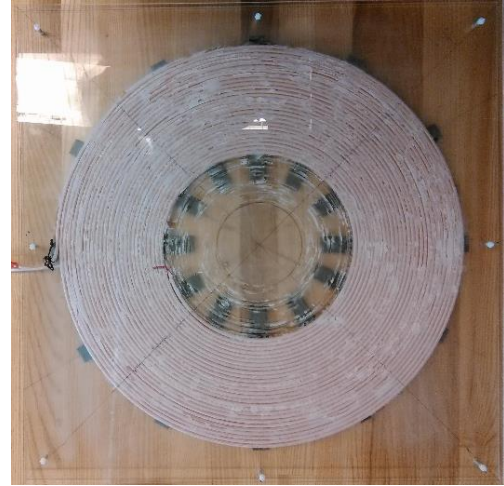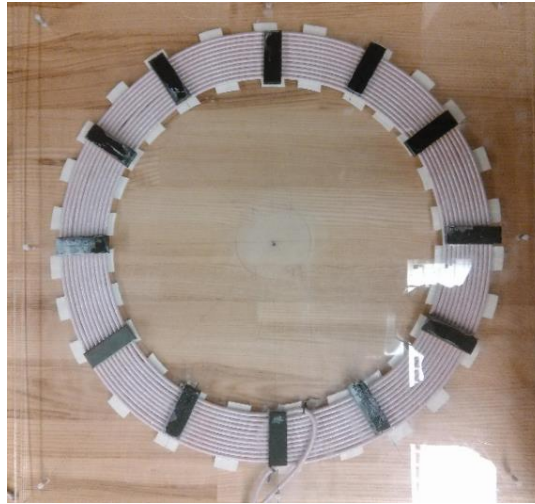
(c) Secondary Coil with ferrite

Figure 3.3 Final primary and secondary pads

Table 3.4 Electrical parameters of charging pad at 16cm air-gap

Electrical Parameters	Values
Primary Resistance, R_P (Ω)	0.13
Secondary Resistance, R_S (Ω)	0.06
Primary Inductance, L_P (μH)	400.65
Secondary Inductance, L_S (μH)	101.10
Mutual Inductance, M (μH)	40.14

Table 3.5 Physical attributes of the charging pad

Charging Pad Attributes	Value/Dimension/Material
Primary Turns, N_P	26
Secondary Turns, N_S	11
L_f for Primary pad (mm)	167.7
L_f for Secondary pad (mm)	55.9
D_{in} for Primary coil (mm)	223.6
D_{in} for Secondary coil (mm)	360
D_{out} for Primary coil (mm)	470
D_{out} for Secondary coil (mm)	470
L_T for Primary pad (mm)	490
L_T for Secondary pad (mm)	470
θ for Primary and secondary	30°
Litz wire	Type II 8 AWG 5×5×42/32
Ferrite Material	TDK PC95

It is worth pointing out here that the number of ferrites added was not sufficient for completely shielding the coils. From the FEA analysis in JMAG, the appropriate number of ferrites required for complete shielding was calculated. However, due to the two months of supplier lead time in shipping the additional ferrites, it was decided to use the designed charging pads for the experimental validation. A study of shielding has been done separately in JMAG and has been presented in Chapter 6 in detail.

3.5   Verification of Designed Pads

3.5.1   Verification of Magnetic Saturation in Ferrites

Before using the designed charging pad for the experimental setup, it is necessary to verify that magnetic saturation does not occur in the ferrite spokes for 3.6 kW of power transfer at an operating frequency of 40 kHz.

For this purpose, a 3-D magnetic field frequency analysis was created in JMAG. PC95 material at different temperatures is present in the material database library of the JMAG-Designer. PC95 core at 60 degrees is selected for analysis considering the

temperature rise in a practical situation. Due to its complicated structure (multiple levels of twisting) it is practically impossible to model the individual strands of the Litz wire. Therefore, it is modelled as a single solid region, and uniform current density is applied throughout the cross-section of the Litz wire in the software setting.

In 'edit circuit' settings of JMAG, the primary power supply of 240 V (RMS) at 40 kHz was used. The load on the secondary was kept at 6.35 Ω (AC equivalent of DC resistance load of 7.84 Ω) for 3.6 kW power output. The values of the capacitors were selected based on the inductance values calculated in the JMAG at a16 cm air-gap. Table 3.6 gives the value of inductance calculated at a 16 cm air-gap in the JMAG. Figure 3.4 shows the circuit created in the JMAG for obtaining the flux density distribution in the charging pads at resonance condition and 3.6 kW output power.

Table 3.6 Circuit parameters at 16 cm air-gap in JMAG

L_P (µH)	L_S (µH)	M (µH)
400.6	99.3	41.42
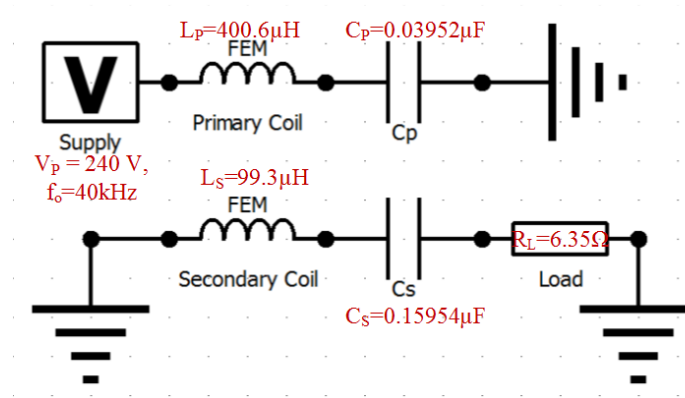
Figure 3.4 Circuit created in JMAG

One can observe that the value of the primary and secondary inductance obtained using FEA analysis matches closely to the actual values shown in Table 3.5. This, in turn, verifies that the primary and the secondary pads were modelled correctly in the JMAG. Figure 3.5 shows the magnetic flux density distribution in the primary and secondary pads for an air-gap of 16 cm.
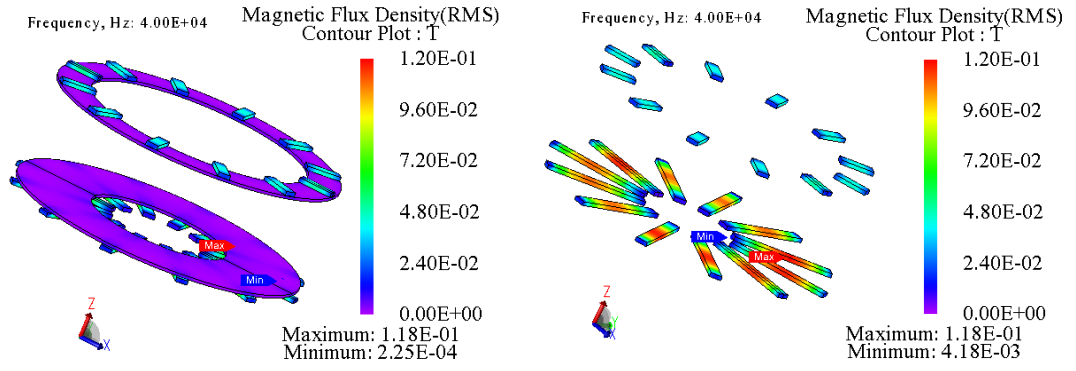
(a) Charging pads at 16 cm air gap   (b) Primary and secondary ferrites spokes

Figure 3.5 Magnetic flux density distribution

It can be confirmed from Figure 3.5 that the maximum value of the flux density in the core is 120 mT which is significantly lower than the saturation flux density of the PC95 material shown in Figure 3.6.
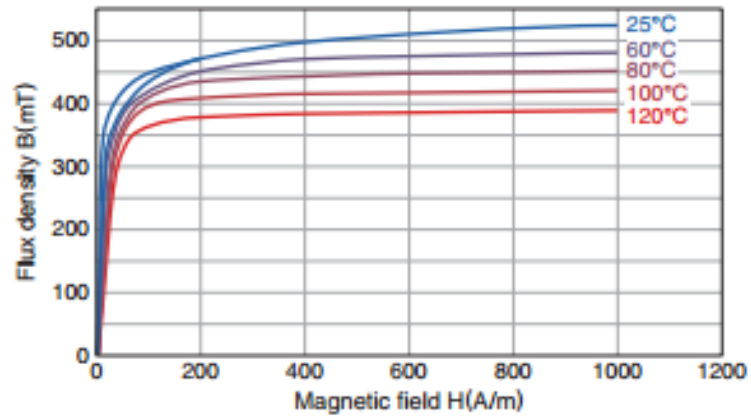
Figure 3.6 B-H temperature characteristics of PC95 material [126]

3.5.2   Verification of Bifurcation Free Design

To verify that the parameters shown in Table 3.5 will ensure the bifurcation free operation, the input phase angle of the SS-RIPT link was plotted against the frequency for three different values of coupling coefficient k as shown in Figure 3.7. In Figure 3.7, ideal tuning (the same value of resonant frequency as in primary tuning) at 40 kHz has been assumed.
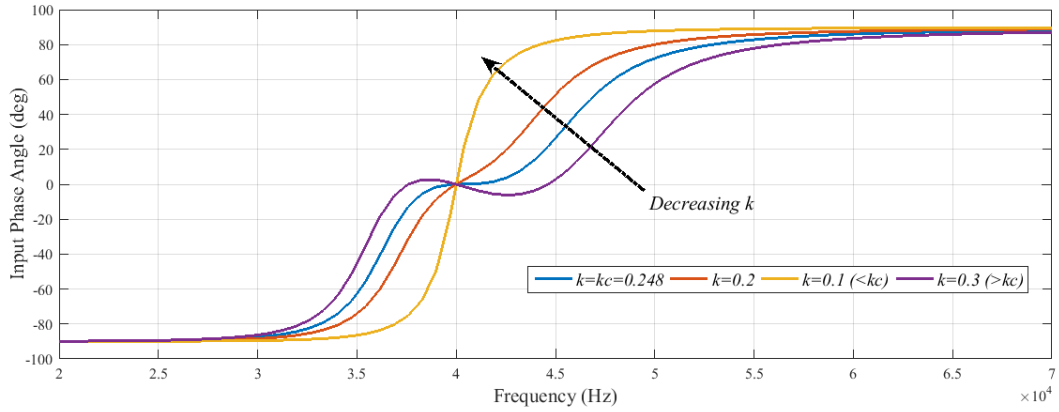
Figure 3.7 Input phase angle Vs frequency for 3.6 kW

From the plot shown in Figure 3.7, one can observe that for the value of a coupling coefficient less than the critical value of 0.248, bifurcation free operation is achieved. If the value of the coupling coefficient is increased above the critical value, then there will be two values of ZPA frequency. Operating above the value of critical coupling will ultimately lead to a decrease in the output power at the resonant frequency. This is evident from the voltage transfer ratio (V_S/V_P) versus frequency plot shown in Figure 3.8.
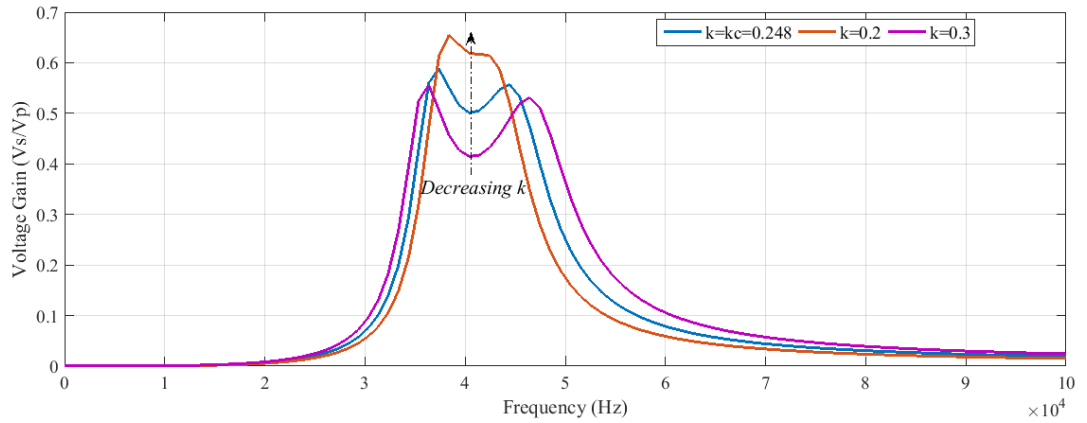
Figure 3.8 Voltage transfer ratio Vs frequency for 3.6 kW

It is evident from Figure 3.8 that it is necessary to maintain coupling below critical coupling to obtain higher output voltage and therefore higher output power.

3.6   Sensitivity Analysis of Designed Pads

A key challenge of implementing a wireless power transfer system is the variation in the mutual coupling profile due to the change of the air-gap and alignment between the primary and secondary pads. The reason is that the efficiency and the power transfer is directly affected by the mutual coupling variations (see Appendix A). Therefore, proper alignment is required for optimum power transfer and efficient operation of the charger. For an EV battery charging application, the secondary pad is fixed underneath the car, and the primary pad is set on the ground. Therefore, in a practical situation vertical separation is fixed as shown in Figure 3.9 (a). There is a possibility of slight change in vertical air-gap due to the change in the tyre pressure but for most of the time, it can be assumed to be constant. However, the coupling can still vary widely due to the misalignment issue while parking the car over the primary pad, as shown in Figure 3.9 (b). To assist the driver in parking the car, EVs are often equipped with a guidance system such as: Magnetic coupling positioning system; triangulated radio frequency identification (RFID) positioning system; special mechanical or electronic maneuver of charging pads. [127], [128].

(a) Vertical Air-gap   (b) Misalignment
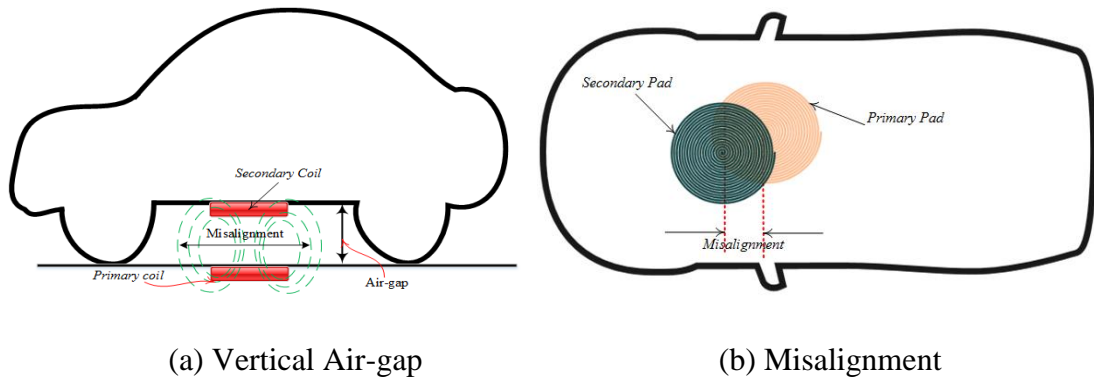
Figure 3.9 Parking car over primary pad

To measure the mutual inductance profile in a misalignment scenario, a test bench emulating vehicle behaviour was fabricated in a lab as shown in Figure 3.10. The secondary pad was placed on a movable trolley while the primary was kept on a stationary table. A nominal air-gap between the primary and secondary pads was maintained at 16 cm. Figure 3.10 shows a picture of the test bench. Mutual inductance

at fixed air-gap and varying alignment between primary and secondary was measured using the LCR meter. The results obtained have been plotted in Figure 3.11.

Self-inductance of the primary and the secondary pads was also measured at different air-gaps but were found to remain almost constant. For example self-inductance of the primary pad at 0 cm misalignment and 45 cm misalignment for a fixed air-gap of 16 cm are measured to be 400.65 µH and 399.90 µH, respectively. Knowing the parameter variations at an air-gap of 16 cm is of prime importance here, since, as discussed above for EV charging, vertical air-gap is highly unlikely to change. However, assuming a 5 mm variation in vertical air-gap due to change in tyre pressure, self-inductance of pads was measured, and found to be almost constant. This, in turn, makes the selection of compensation capacitors for the primary and the secondary pads very easy.
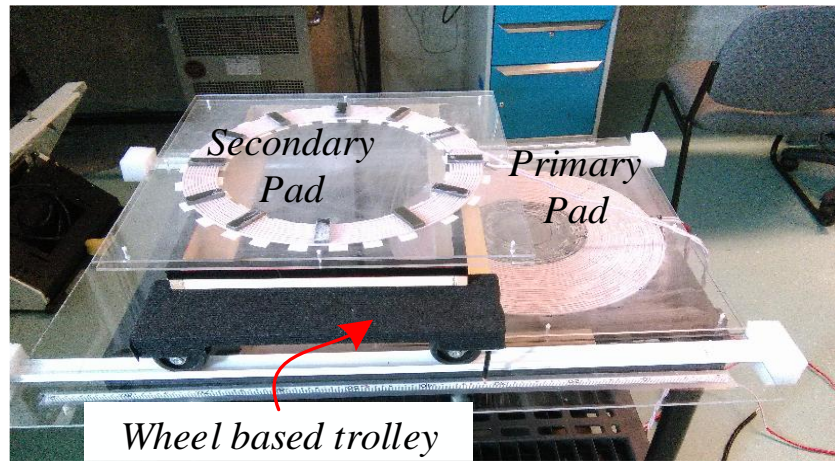
(a)
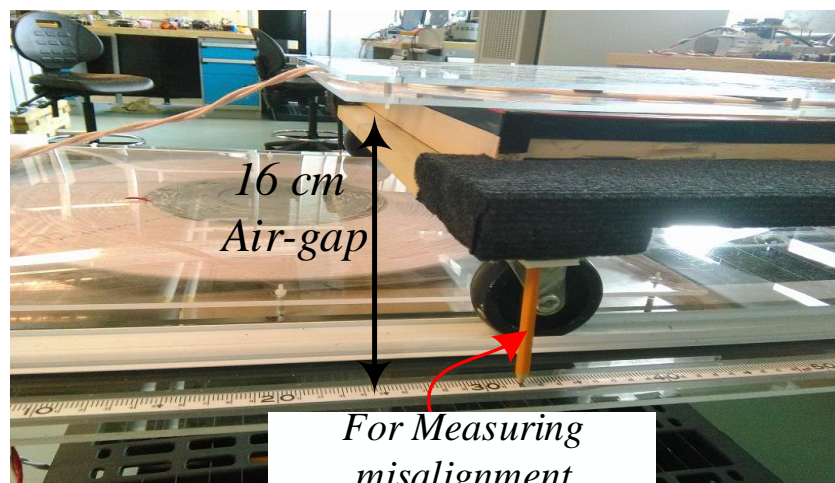
(b)

Figure 3.10 Test bench for measuring misalignment
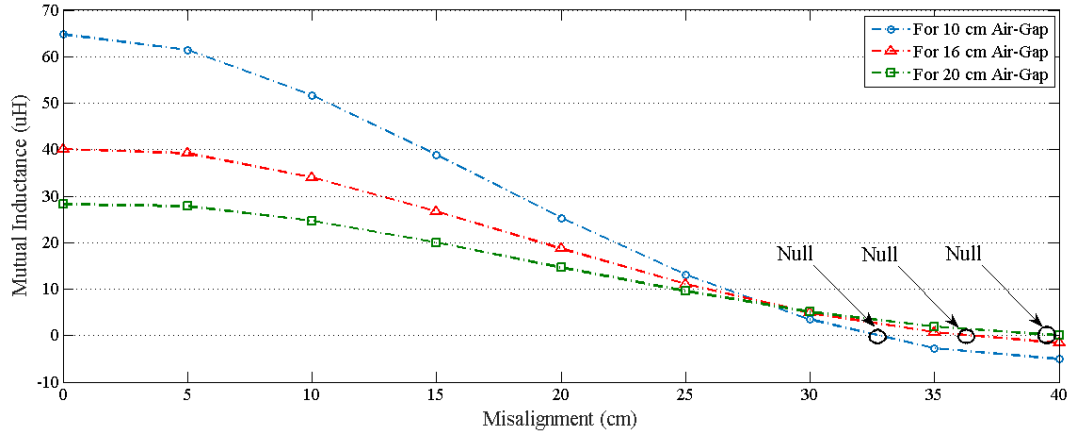
Figure 3.11 Mutual inductance Vs misalignment at fixed air-gap

For a nominal air gap of 16 cm, it can be seen that the mutual inductance remains almost constant until 5 cm misalignment, after which it decreases gradually. Magnetic null in mutual inductance profile at a 16 cm air-gap occurs at a misalignment of 37 cm, which is 78% of the pad size (outer diameter). Another important observation which could be made from Figure 3.11 is that the position of the magnetic null does not occur at the same position but changes with the changing air-gap. This is an important characteristic of a non-symmetrical coil pair and has been discussed in detail in Appendix B.

The parameters of the primary and secondary pads (shown in Figure 3.3) were measured using the LCR meter at different frequencies. The results obtained are plotted in Figure 3.12. The parameters of the primary and secondary coils (without ferrite spokes), shown in Figure 3.1, were also measured using the LCR meter at different frequencies and are plotted in the same graph for comparison purposes.
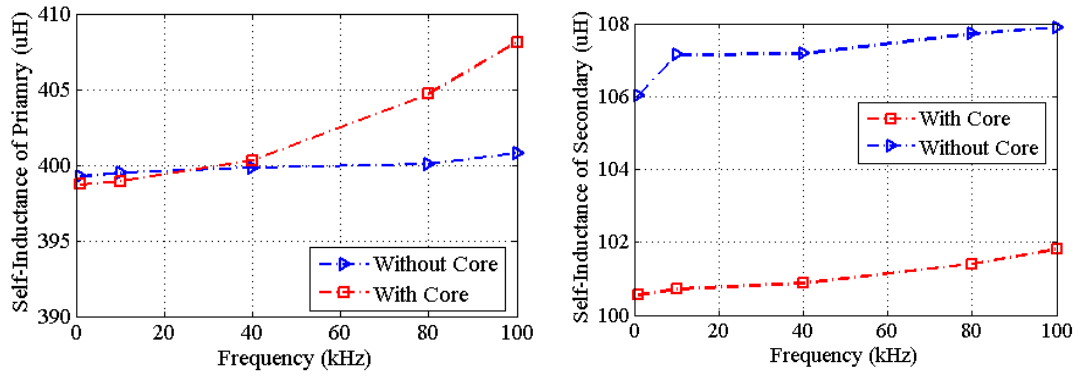
(a) Primary self-inductance Vs frequency (b) Secondary Self-inductance Vs frequency
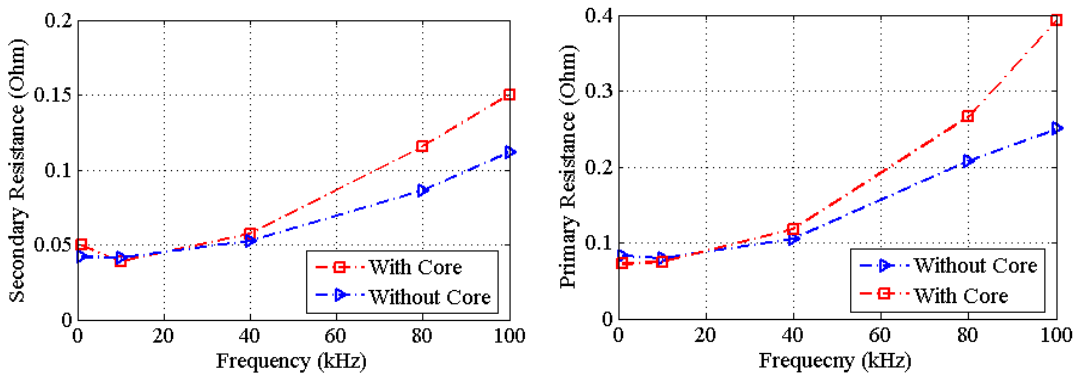
(a) Secondary resistance Vs frequency   (b) Primary resistance Vs frequency

Figure 3.12 Parameters variation with respect to frequency

From the plots shown in Figure 3.12, the following observations can be made:

(a) Resistance is more affected by the frequency variations compared to self-inductance.

(b) Between 'with core' and 'without core' cases, 'with core' parameters are more affected by the change in frequency. This is because flux becomes more concentrated near the pad due to field shaping provided by the ferrites cores. Eddy current in both ferrites and wires increases with increasing frequency.

(c) Maximum change in self-inductance of the primary pad is 2.5% for an increase in frequency from 0 to 100 kHz. For the secondary pad, the maximum change is 1.8%. Self-inductance of coils without a core remains almost unaffected.

(d) Since the change in self-inductance is very low, for frequency variations centred around a resonant frequency (in the present case 40 kHz), it can be assumed

constant. This, in turn, helps to select switching frequency slightly beyond the resonant frequency for adopting soft-switching in the inverter switches.

3.7 Summary of Chapter 3

In this chapter, charging pads for 3.6 kW output have been designed following the design considerations presented in Chapter 2. Since the shielding becomes imperative in a high power application to limit the exposure of humans and animals to the time varying magnetic field, ferrite spokes were added to the back of the coils. The designed pads were simulated in the JMAG for verifying that magnetic saturation of ferrite cores does not occur. The sensitivity of the designed pads with respect to misalignment and frequency variations was also presented. The fundamental horizontal tolerance limit for the designed charging pad is found to be 78% of the pad diameter for a nominal air-gap of 16 cm.

Chapter 4 Mathematical Model and Controller Design

For the efficient power transfer between the primary and the secondary pads, the value of the nominal coupling should be maintained for which the pads were designed initially. This requires the vehicle to be parked in a specific position [129], [130]. However, while parking the vehicle over the primary coil, misalignments could always occur; hence the coils could deviate from the nominal coupling scenario. Moreover, the parameters of the system could vary, due to: fluctuation in supply voltage; misalignments; and variation of load, due to varying states of the charge of the EV battery pack. These issues can lead to the deviation of output voltage and current from the desired operating points.

A suitably designed closed-loop controller is consistently needed, in order to improve tolerance to misalignments and parameter variations. For the design of control loops, dynamic analysis of the RIPT system is essential [131]. An RIPT system is a typical higher-order resonant circuit, and consists of one slow moving pole, due to the output filter (rectifier + capacitor) and fast moving poles, due to the resonant tank elements. This causes a difference in frequency between the resonant network and the filter network. This relegates the usage of modelling techniques typically used for PWM DC/DC converters [132]. Therefore, in due course, various specialised techniques have been developed for the dynamic analysis of such resonant systems. Some of the popular techniques include: Generalised state-space averaging (GSSA) method [132], sampled data modelling (SDM) [133], extended describing function (EDF) method [134], and general unified phasor transformation (GUPT) [135].

For this thesis, the EDF method has been preferred over other methods. This is mainly due to its reputation for generating a highly accurate mathematical model of resonant converters. The EDF technique was first introduced by Yang *et al.* in 1991 [136]. More recent work and advancement on the EDF method has been presented in [137], [138]. This modeling technique works on the fundamental principle of first harmonic approximation of state variables. This, in turn, provides a set of modulation functions that relate the state variable with the input and control variables, which are

both in time-domain and frequency-domain [138]. Although the EDF method is highly accurate it requires higher order representation and therefore more complex formulation effort. For instance, a small signal model of the SS-RIPT system has been derived in [139]–[142] and the derived model is either an 8th or 9th order system.

The aim of this chapter is to derive a simplified small-signal model of the SS-RIPT system using the EDF method. The derived model has been used to design voltage and current control loops for battery charging.

4.1 A Reduced Dynamic Model for an SS-RIPT system

In most RIPT systems, power flow regulation is implemented on the secondary side, which requires extra switching circuits and controllers between the rectifier and the load [12], [143], [144]. Introducing an additional power converter is advantageous in cases where multiple secondary systems exist, with varying loads. However, in the case of only one secondary pickup, the additional converter only adds size and weight to the pickup circuit, while also generating supplementary losses. Therefore, it is preferable to achieve power flow regulation from the primary side converter itself, by varying the voltage magnitude of the high-frequency inverter [36], [88], [145]. Figure 4.1 shows the circuit representation of the SS-RIPT system under primary side control. Figure 4.1 will be referred to as *full model* of the SS-RIPT system in this chapter.
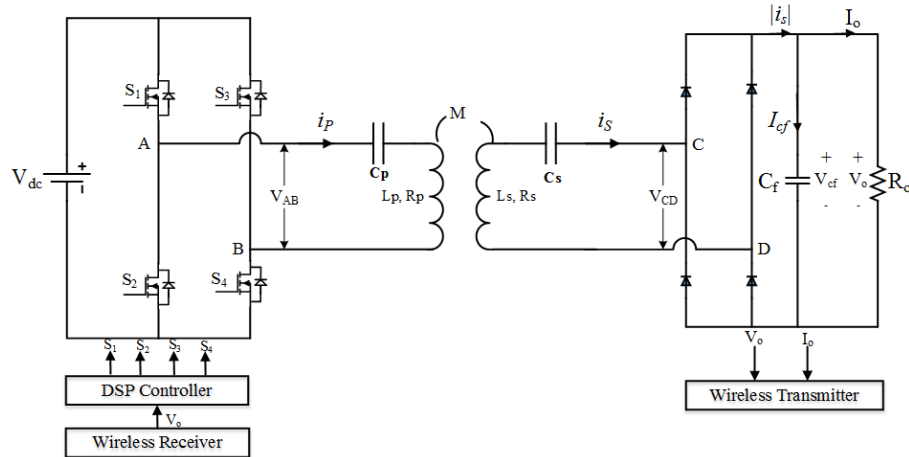
Figure 4.1 Circuit representation of an SS-RIPT system for primary side control

In Figure 4.1, $|i_S|$ is the rectified value of the current flowing into the output filter network. The secondary circuit is operated at resonant frequency to improve the power

transfer capability of the system, while the primary circuit is operated at resonant frequency to ensure power transfer at unity power factor. However, at resonant frequency, hard switching of the inverter will occur. Thus, in order to minimize switching losses, switching frequency needs to be deviated from resonant frequency, to accommodate soft switching techniques, such as zero voltage switching (ZVS) or zero current switching (ZCS). Soft switching not only reduces losses in the switching circuit, but also prohibits non-permitted switching actions from occurring, which otherwise can destroy the   IGBTs/MOSFETs [146]. In this thesis, ZVS has been considered, since the DC/AC inverter was built using MOSFET switches; ZVS is ideal for MOSFETs [136]. To derive the small-signal model an equivalent circuit of the SS-RIPT system needs to be derived. For the derivation of the small-signal model, following steps are implmented:

Due to the non-linear nature of the AC/DC rectifier (with the filter capacitor C_f), the resistance seen at the input of the rectifier is not the same as the load resistance [80]. If continuous conduction of diode bridge rectifier is considered, then the load resistance as seen from the CD terminal can be given by (4.1):

$$R_L = \frac{8}{\pi^2} R_o \tag{4.1}$$

Using (4.1), equivalent circuit of Figure 4.1 can be redrawn as in Figure 4.2.
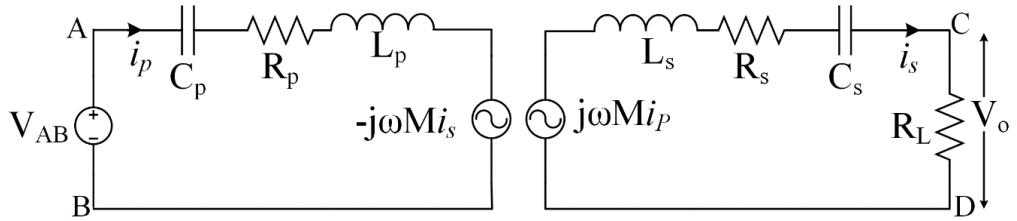
Figure 4.2 Equivalent circuit of Figure 4.1

Let the switching frequency be ω_s, given by (4.2):

$$\omega_s = \frac{1}{\sqrt{L_s C_s}} \tag{4.2}$$

Then,

$$j\omega M i_P = i_s (R_S + R_L) \tag{4.3}$$

$$\left|\frac{i_S}{i_P}\right| = \frac{\omega M}{R_S + R_L} = n \tag{4.4}$$

Equation (4.2) will ensure resonance in the secondary coil. Therefore, the power transfer capability of the secondary will remain unaffected. This also ensures that reflected impedance seen by the primary will be purely resistive. Let resonant frequency be ω_o, given by:

$$\omega_o = \frac{1}{\sqrt{L_P C_P}} \tag{4.5}$$

In (4.5) C_P is selected such that switching frequency (ω_s) should be greater than resonant frequency (ω_o) [147]. This will ensure ZVS in the primary inverter switches. The circuit shown in Figure 4.2 can be further reduced to Figure 4.3, by reflecting the secondary impedance to the primary side, by a scaling factor of $\frac{\omega^2 M^2}{|Z_{22}|^2}$. Here, Z_{22} is the impedance of the secondary, which is now equal to $(R_S + R_L)$.
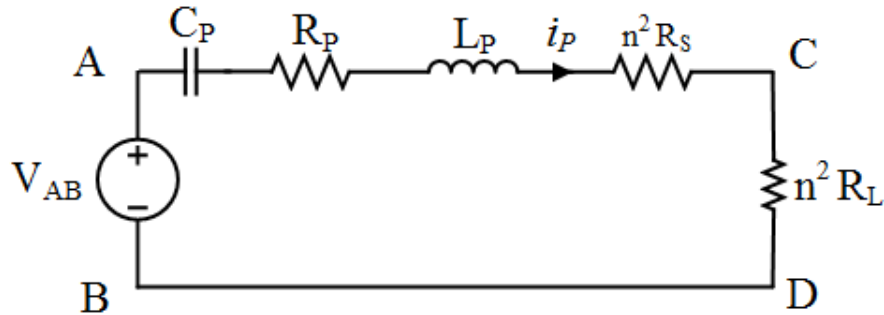
Figure 4.3 Equivalent circuit referred to primary

The voltage drop across CD can be given by (4.6):

$$V_{CD} = i_P n^2 R_L = \frac{\omega^2 M^2}{(R_S + R_L)^2} i_P R_L \tag{4.6}$$

Using (4.4) in (4.6), it can be further written as:

$$\frac{\omega^2 M^2}{(R_S + R_L)^2} i_P R_L = \frac{\omega M}{R_S + R_L} i_S R_L$$

$$\triangleq \frac{\omega M}{R_S + R_L} V_o \tag{4.7}$$

Using (4.7), the final equivalent circuit can be drawn as shown in Figure 4.4.
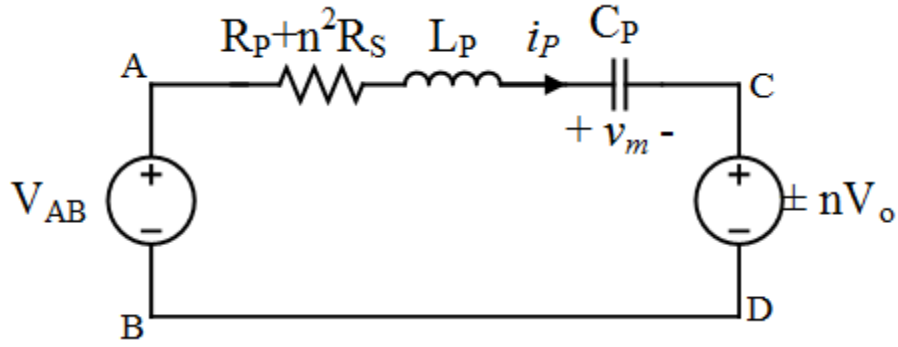
Figure 4.4 Final equivalent circuit of series-series topology

The equivalent circuit shown in Figure 4.4 is a greater simplification over the equivalent circuit derived in [141], [148]. This equivalent circuit is similar to the equivalent circuit of series-loaded resonant DC/DC converter [149], [136]. However, in the derivation of the final equivalent circuit, secondary side dynamics were neglected, therefore this model will be referred to as '*a reduced dynamic model*' of the SS-RIPT system. The impact of oversimplification of the actual physical model and usefulness of the reduced dynamic model will be made clear in the controller design section presented in the later part of this thesis.

4.2 Derivation of Small-Signal Model from Reduced Dynamic Model

The following assumptions are made before deriving the small-signal model from the reduced dynamic model of the SS-RIPT system:

a) All switches are considered to be ideal in nature and dead-time between switches has been neglected.

b) The quality factor of the inductance is considered to be high, in order to obtain sinusoidal varying current, i_P.

c) Parasitic inductance and resistance of the compensation capacitors as well as filter capacitor is neglected.

Based on the above assumptions, a step-by-step derivation of the small-signal model is presented below.

A. Non-linear State Equation:

Applying KVL to the circuit shown in Figure 4.4:

$$V_{AB} = L_P \frac{di_P}{dt} + v_m + \left(R_p + n^2 R_S\right)i_P + sgn(i_P)nV_0 \qquad (4.8)$$

$$C_P \frac{dv_m}{dt} = i_P \qquad (4.9)$$

where, $sgn(x)$ is a symbol function, given by:

$$Sgn(x) = \begin{cases} 1, x > 0 \\ 0, x = 0 \\ -1, x < 0 \end{cases}$$

Applying KCL to the rectifier network of Figure 4.1:

$$c_f \frac{dV_o}{dt} + \frac{V_o}{R_L} = |i_S|$$

$$\triangleq \frac{2}{\pi} I_S \qquad (4.10)$$

The output equation is given by:

$$V_o = V_{cf} \qquad (4.11)$$

Equations (4.8)-(4.11) gives the non-linear state space model of the *reduced dynamic model*. This model contains both the linear (inductor current and capacitor voltage) and the non-linear terms (inverter output and rectifier input). The linear terms can be approximated to be sinusoidal, while the nonlinear terms can be approximated by some describing functions.

B. Harmonic Approximation:

The resonant networks connected to the output of the inverter have significant filtering capability, due to their sharply tuned band-pass frequency response, which is nominally centered at resonant frequency. Thus, the primary current i_P and the voltage across the primary capacitor v_m are approximately sinusoidal. This enables an approximation of the magnitude of i_P and v_m by their fundamental terms, using Fourier series expansion. This is called harmonic approximation [149]. Therefore:

$$v_m(t) = V_x \cos(\omega_s t) + V_y \sin(\omega_s t) \qquad (4.12)$$

$$i_P(t) = I_x \cos(\omega_s t) + I_y \sin(\omega_s t) \qquad (4.13)$$

Here, V_x and I_x represent the magnitude of the co-sinusoidal part of v_m and i_p whereas V_y and I_y represent the magnitude of the sinusoidal part of v_m and i_P. They are slowly time varying quantity and hence the dynamic behaviour of these terms can be investigated [136].

C. Derivation of Extended Describing Functions:

For ZVS, switching frequency should be greater than the resonant frequency. However, deviation from the resonant frequency will cause a decrease in the power transfer capability of the SS-RIPT system [44]. This will also result in higher conduction and turn-off losses since the current need to be higher to transfer the same amount of power. Therefore, power saved by ZVS might be lost in the conduction losses and turn-off losses. Thus, a control strategy that can vary the voltage without deviating much from resonant frequency and yet maintain ZVS is required. There are mainly three narrow frequency-range control techniques used for the control of resonant converters, namely: asymmetrical duty cycle (ADC) control also known as asymmetrical PWM control; symmetrical clamped mode (SCM) control, also known as phase shift control; and asymmetrical clamped mode (ACM) control [150], [151]. It has been shown in [147], [152] that, only ACM control has the best performance in terms of the least losses in the inverter switches as compared to the other two control strategies. It also has the lowest switching frequency for ZVS under all load conditions. Therefore, ACM control has been considered for this thesis. Figure 4.5 shows the switching scheme and the voltage waveform of the ACM control. The dashed wave-form represents the fundamental component of V_{AB}, which can be described by (4.14) using the Fourier series expansion.
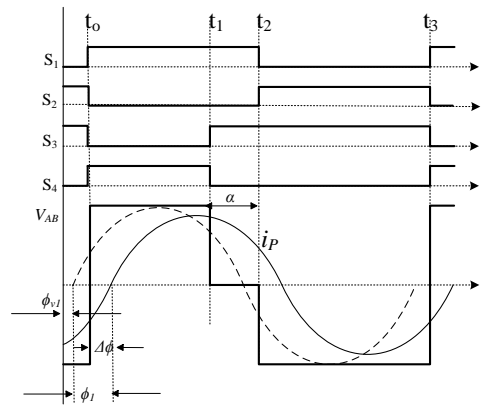
Figure 4.5 Switching scheme and voltage waveform of ACM control

$$V_{AB} = -\frac{V_{dc}\alpha}{2\pi} + \frac{V_{dc}}{n\pi}\sin n\alpha \sum_{n=1}^{\infty}\cos n\omega_s t + \frac{V_{dc}}{n\pi}[2 - \cos n(\pi - \alpha) -$$

$$\cos n\pi] \sum_{n=1}^{\infty}\sin n\omega_s t \tag{4.14}$$

Since in EDF only the first harmonic is of prime importance. Therefore, neglecting the DC term and higher harmonic components of the inverter output, V_{AB} can be given by (4.15):

$$V_{AB} = \frac{V_{dc}}{\pi}\sin\alpha\cos\omega_s t + \frac{V_{dc}}{\pi}(3 + \cos\alpha)\sin\omega_s t \tag{4.15}$$

The duty cycle, d is given by:

$$d = \frac{t_{on}}{T} = \frac{2\pi - \alpha}{2\pi} \quad \therefore \alpha = 2\pi(1 - d) \tag{4.16}$$

In terms of duty cycle d (4.15) can be replaced by (4.17):

$$V_{AB} = -\frac{V_{dc}}{\pi}\sin 2\pi d\cos\omega_s t + \frac{V_{dc}}{\pi}(3 + \cos 2\pi d)\sin\omega_s t$$

$$\triangleq f_1(d, V_{dc})\sin\omega_s t + f_2(d, V_{dc})\cos\omega_s t \tag{4.17}$$

The output voltage V_o is reflected across the rectifier input as V_{CD}, where $V_{CD} = V_o$ if i_p is positive and $V_{CD} = -V_o$ if i_p is negative. Therefore, from Figure 4.4, V_{CD} can be given mathematically as:

$$V_{CD} = sgn(i_P)nV_0 \tag{4.18}$$

Using EDF, non-linear term $V_{CD} = sgn(i_P)nV_0$ is written as a function of i_P and V_{cf}. Hence:

$$V_{CD} = \frac{4n}{\pi}V_{cf}\frac{I_y}{I_P}\sin\omega_s t + \frac{4n}{\pi}V_{cf}\frac{I_x}{I_P}\cos\omega_s t \tag{4.19}$$

$$\triangleq f_3(I_x, I_y, V_{cf})\sin\omega_s t + f_4(I_x, I_y, V_{cf})\cos\omega_s t$$

In (4.17) and (4.19), functions f_1, f_2, f_3 and f_4 are called extended describing functions and magnitude of i_P is given by (4.20):

$$|i_P| = I_P = \sqrt{I_x^2 + I_y^2} \tag{4.20}$$

D. Harmonic Balance:

Inserting (4.12), (4.13), (4.17) and (4.19) in (4.8) and (4.9), and by equating the coefficients of DC, sine and cosine terms respectively, we obtain:

$$L_P \frac{dI_y}{dt} = L_P I_x \omega_s - V_y - (R_P + n^2 R_S)I_y - \frac{4n}{\pi} V_{cf} \frac{I_y}{I_P} + \frac{V_{dc}}{\pi}(3 + \cos 2\pi d)$$

$$(4.21)$$

$$L_P \frac{dI_x}{dt} = -L_P I_y \omega_s - V_x - (R_P + n^2 R_S)I_x - \frac{4n}{\pi} V_{cf} \frac{I_x}{I_P} - \frac{V_{dc}}{\pi}\sin 2\pi d \quad (4.22)$$

$$C_P \frac{dV_x}{dt} = I_x - V_y C_P \omega_s \tag{4.23}$$

$$C_P \frac{dV_y}{dt} = I_y + V_x C_P \omega_s \tag{4.24}$$

$$C_f \frac{dV_{cf}}{dt} = \frac{2nI_P}{\pi} - \frac{V_o}{R_o} \tag{4.25}$$

Equations (4.21)-(4.25) give the large-signal model of the SS-RIPT system in terms of state variables. The large-signal model is composed of the steady-state model and the small-signal model. One can observe that the large signal model is constructed of 5 state variables as opposed to the 8 or 9 variables presented in [139]–[142].

E. Steady State Analysis:

Under steady state condition, state variables do not change with time. Therefore, setting all the derivatives in the large-signal model to zero, one obtains:

$$L_P I_x \omega_s - V_y - (R_P + n^2 R_S)I_y - \frac{4n}{\pi} V_{cf} \frac{I_y}{I_P} + \frac{V_{dc}}{\pi}(3 + \cos 2\pi d) = 0 \quad (4.26)$$

$$-L_P I_y \omega_s - V_x - (R_P + n^2 R_S)I_x - \frac{4n}{\pi} V_{cf} \frac{I_x}{I_P} - \frac{V_{dc}}{\pi}\sin 2\pi d = 0 \tag{4.27}$$

$$I_x - V_y C_P \omega_s = 0 \tag{4.28}$$

$$I_y + V_x C_P \omega_s = 0 \tag{4.29}$$

$$\frac{2nI_P}{\pi} - \frac{V_o}{R_o} = 0 \tag{4.30}$$

Put (4.29) and (4.30) in (4.27) one can get:

$$L_P I_y \omega_s = \frac{I_y}{\omega_s C_P} - (R_P + n^2 R_S)I_x - \frac{4n}{\pi} V_{cf} \frac{I_x}{I_P} - \frac{V_{dc}}{\pi}\sin 2\pi d \tag{4.31}$$

$$I_y \left(L_P \omega_s - \frac{1}{\omega_s C_P}\right) = -\frac{V_{dc}}{\pi}\sin 2\pi d - (R_P - n^2 R_S)I_x - \frac{4n^2}{\pi}\frac{2I_P}{\pi}\frac{I_x}{I_P} R_o \tag{4.32}$$

$$I_y \left(L_P \omega_s - \frac{1}{\omega_s C_P} \right) = -\frac{V_{dc}}{\pi} \sin 2\pi d - \left(R_P + n^2 R_S + \frac{8n^2}{\pi^2} R_o \right) I_x \qquad (4.33)$$

$$I_y alpha = -\frac{V_{dc}}{\pi} \sin 2\pi d - Beta I_x \qquad (4.34)$$

Here, *Beta* is the effective resistance offered to the inverter in ohm, i.e.:

$$Beta = R_P + n^2 R_S + \frac{8n^2 R_o}{\pi^2} \qquad (4.35)$$

And:

$$alpha = \left(L_P \omega_s - \frac{1}{\omega_s C_P} \right) \qquad (4.36)$$

Inserting (4.28) and (4.30) in (4.26) one obtains:

$$L_P I_x \omega_s - \frac{I_x}{C_P \omega_s} - (R_P + n^2 R_S) I_y - \frac{8n^2}{\pi^2} I_y R_o + \frac{V_{DC}}{\pi} (3 + \cos 2\pi d) = 0 \quad (4.37)$$

$$I_x(-alpha) = \frac{V_{DC}}{\pi} (3 + cos 2\pi d) - I_y Beta \qquad (4.38)$$

Using (4.34) and (4.38, one obtains I_x and I_y in terms of circuit parameters as follows:

$$I_x = -\frac{V_{dc}}{\pi} \frac{(3 + cos 2\pi d) + \frac{Beta}{alpha} sin 2\pi d}{(alpha^2 + Beta^2)} alpha \qquad (4.39)$$

$$I_y = -\frac{V_{dc}}{\pi} \frac{sin 2\pi d}{alpha} + \frac{V_{DC}}{\pi} \frac{alpha * Beta}{(alpha^2 + Beta^2)} \left(3 + cos 2\pi d + \frac{beta}{alpha} sin 2\pi d \right) \quad (4.40)$$

F. Perturbation and Linearization:

The state variable vector and control/input variables vector can be expressed as:

$$\vec{X} = [I_x \quad I_y \quad V_x \quad V_y \quad V_{cf}]^T \qquad (4.41)$$

$$\vec{U} = [V_{dc} \quad d \quad \omega_s]^T \qquad (4.42)$$

The small-signal model can be derived by introducing ac perturbation, represented by '~' in the input variable vector and state variable vector resulting in:

$$x = \vec{X} + \tilde{x}, \quad v_{dc} = V_{dc} + \tilde{V}_{dc}, \quad d = d + \tilde{d}, \quad \omega_s = \omega_s + \tilde{\omega}_s$$

Separating perturbation from DC and very small signals gives the small-signal model of SS-RIPT system:

$$\frac{d\tilde{x}}{dt} = A\tilde{x} + B\tilde{u} \qquad (4.43)$$

$$\tilde{y} = C\tilde{x} + D\tilde{u} \qquad (4.44)$$

Here, A is the state matrix which gives the relation between derivatives of the states and the state variables. B is the input matrix which provides the relation between the derivatives of the state variables with input/control variables. C is the output matrix which relates the state variables with the output variables and D is the direct transmission matrix which represents those elements which directly transmit input to the output of the SS-RIPT system.

A

$$= \begin{bmatrix} \frac{-1}{L_P}\left(\frac{4n}{\pi I_P}V_{cf} + R_P + n^2 R_s\right) & -\omega_s & \frac{-1}{L_P} & 0 & \frac{-4nI_x}{\pi I_P L_P} \\ \omega_s & \frac{-1}{L_P}\left(\frac{4n}{\pi I_P}V_{cf} + R_P + n^2 R_s\right) & 0 & \frac{-1}{L_P} & \frac{-4nI_y}{\pi I_P L_P} \\ \frac{1}{C_P} & 0 & 0 & -\omega_s & 0 \\ 0 & \frac{1}{C_P} & \omega_s & 0 & 0 \\ \frac{nI_P}{\pi I_x C_f} & \frac{nI_P}{\pi I_y C_f} & 0 & 0 & \frac{-1}{R_o C_f} \end{bmatrix}$$

$$B = \begin{bmatrix} -\frac{\sin 2\pi d}{\pi L_P} & -\frac{2V_{dc}}{L_P}\cos 2\pi d & -I_y \\ \frac{1}{\pi L_P}(3 + \cos 2\pi d) & -\frac{2V_{dc}}{L_P}\sin 2\pi d & I_x \\ 0 & 0 & -V_y \\ 0 & 0 & V_x \\ 0 & 0 & 0 \end{bmatrix}$$

$$\tilde{u} = \begin{bmatrix} \tilde{V}_{dc} \\ \tilde{d} \\ \tilde{\omega}_s \end{bmatrix} \qquad \tilde{x} = \begin{bmatrix} \tilde{\iota}_x \\ \tilde{\iota}_y \\ \tilde{v}_x \\ \tilde{v}_y \\ \tilde{v}_{cf} \end{bmatrix}$$

$$\tilde{y} = \tilde{V}_{cf}, \quad C = \begin{bmatrix} 0 & 0 & 0 & 0 & 1 \end{bmatrix} \quad \& \quad D = 0 \qquad (4.45)$$

Equation (4.45) gives the small-signal model of the reduced dynamic model of the SS-RIPT system. The derived small-signal model has duty cycle (d), input voltage (V_{dc}), and switching frequency (ω_s) as control variables, and load voltage as the output

variable. It should be noted that (4.45) represents the small-signal model of the reduced dynamic model and not the actual physical model, i.e. full model shown in Figure 4.1.

4.3 Piecewise-Linear Model of Li-Ion Battery Pack

A Li-Ion battery pack used in EVs is required for testing the designed charging pad and controller (controller design is discussed later in this chapter). However, the actual battery pack was not available in the lab. Therefore, DC electronic load was used to emulate battery charging profile. For a Li-Ion battery, the charging process usually consists of two main stages: constant current (CC) charging and constant voltage (CV) charging stage [153]–[159]. During the CC charging stage, the battery is charged at constant current until the specified peak voltage of the battery cell is reached. At the end of the CC mode, the battery cell voltage is at the specified peak value, and this voltage is maintained across the battery cell throughout the CV charging stage. Figure 4.6 shows the typical charging profile for a single Li-Ion battery cell [154].
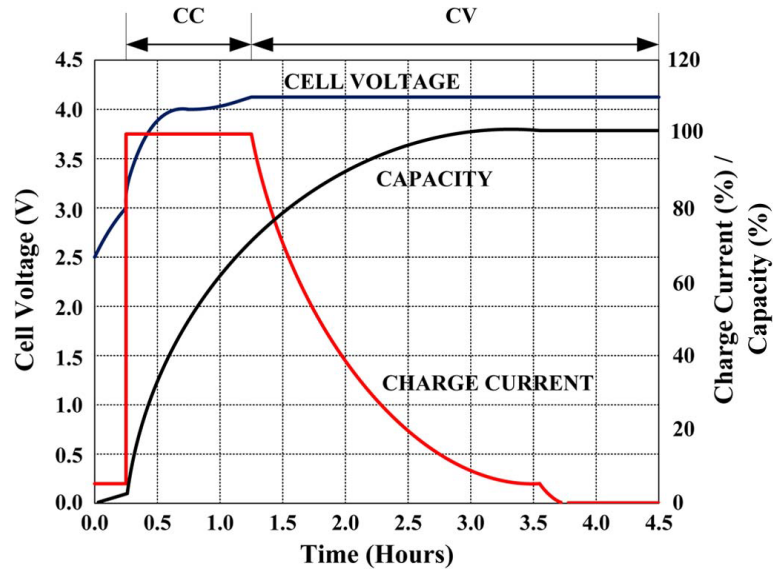
Figure 4.6 Charging Profile of a Li-Ion Cell [154]

The battery pack employed in EVs consists of several individual Li-Ion cells connected in series and parallel combinations to meet the charging voltage and current ratings, as shown in Figure 4.7 [160].
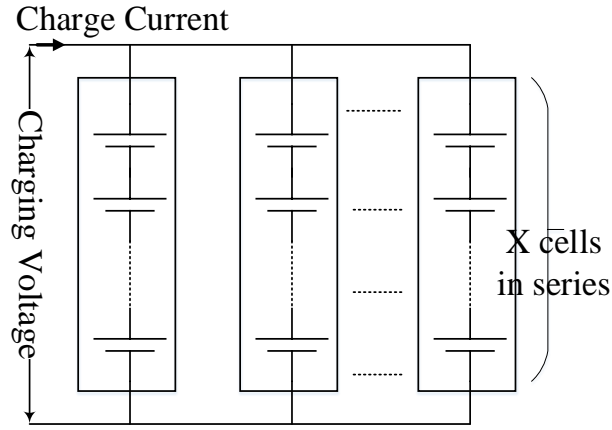
Figure 4.7 Li-Ion battery pack structure

As presented in Chapter 3, the SS-RIPT system was designed for the output voltage of 168 V. Therefore, a charging voltage of 168 V was considered for the CV mode. For the CC mode, a current of 19 A was considered. A battery pack of capacity 6.1 kWh was considered. 6.1 kWh rating was selected from the rating of the battery pack used in an electric car named Renault Twizy. For 19 A of current in CC mode, the charge rate (C rate) of the battery pack can be calculated by (4.46):

$$C = \frac{6100}{168 \times 19} = 0.523 \tag{4.46}$$

For 168 V, the number of cells connected in the series is given by (4.47):

$$x = \frac{168}{4.2} = 40 \tag{4.47}$$

The advised charge rate of a Li-Ion cell is between 0.5C and 1C to prolong the battery life [157]. The higher the C rate the faster the cell reaches the peak voltage of 4.2 V (CV stage). However, in a Li-Ion battery, terminal voltage is not an indication of the state of charge (SOC) of the battery. Therefore, increasing the C rate does not hasten the full-charge state by much. Although the cell reaches CV mode quicker, the CC mode will take longer accordingly. Besides this, a rapid charging to 4.2 V results in a lower battery capacity at the end of the CC stage compared to slower charging. Due to these reasons, the C rate of 0.523 seems an appropriate value as it falls within the recommended charging practices. Charging is terminated when the current drops to 2% of the rated current [161]. Based on the these information, the charging parameters of the designed battery pack can be calculated by extrapolating the values at different

stages on the charging profile of the Li-Ion cell as shown in Figure 4.6. Table 4.1 shows the calculated parameters.

Table 4.1 Charging parameters of designed battery pack

Charging Current, I_o (A)	Charging Voltage, V_o (V)	Equivalent Resistance, R_o (Ω)
19 (0.523C)	120 (3x)	6.31
19 (0.523C)	140 (3.5x)	7.36
19 (0.523C)	156 (3.9x)	8.21
19 (0.523C)	160 (4x)	8.42
19 (0.523C)	168 (4.2x)	8.842
14.524 (0.4C)	168 (4.2x)	11.56
10.893(0.3C)	168 (4.2x)	15.42
7.262(0.2C)	168 (4.2x)	23.13

Using data presented in Table 4.1, the piecewise-linear charging profile of 6.1 kWh battery pack can be plotted as shown in Figure 4.8.
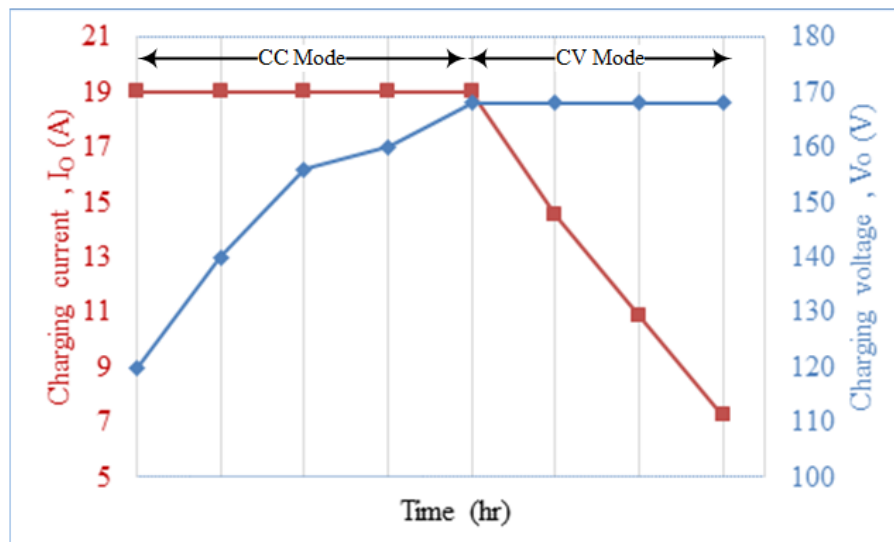
Figure 4.8 Piecewise-linear model of Li-Ion battery charging profile

The values of equivalent resistance calculated in Table 4.1 will be used as the load for the simulation and experimental validation of the designed charger.

4.4 Selecting the Compensation Capacitors for ZVS Tuning

Referring to Figure 4.5, the condition to achieve ZVS operation in all switches of the primary inverter is given by (4.48) [147], [152], [162]:

$$\Delta\phi = \phi_1 - \phi_{v1} > 0 \tag{4.48}$$

Here,

$$\phi_1 = \tan^{-1}\left(Q_P\left(\omega_n - \frac{1}{\omega_n}\right)\right) \tag{4.49}$$

In (4.49), Q_P is the primary quality factor given by (2.9) and ω_n is the normalised switching frequency given by (4.50).

$$\omega_n = \frac{\omega_s}{\omega_o} \tag{4.50}$$

Equation (4.48) can be satisfied either by increasing ϕ_1 or by decreasing ϕ_{v1}. ϕ_1 can be increased by raising the switching frequency, which is not recommended due to the reasons previously mentioned. Therefore, a better approach will be to decrease ϕ_{v1}.

From (4.15), the amplitude of the fundamental component of V_{AB} is given by (4.51) and the value of ϕ_{v1} is given by (4.52).

$$V_{AB1} = \frac{V_{dc}}{\pi}\sqrt{10 + 6\cos\alpha} \tag{4.51}$$

$$\phi_{v1} = \tan^{-1}\frac{\sin\alpha}{3+\cos\alpha} \tag{4.52}$$

Using (4.48), (4.49) and (4.52), the minimum value of ω_n for AVC at critical point $\Delta\phi = 0°$ is given by (4.53).

$$\omega_n = \frac{(3-\cos\alpha)\sin\alpha+\sqrt{(\cos^2\alpha-6\cos\alpha+9)\sin^2\alpha+(256+64\sin^2\alpha+4\sin^4\alpha)Q_P^2}}{(16+2\sin^2\alpha)Q_P} \tag{4.53}$$

From Table 4.1, the load resistance varies from 6.315 Ω to 23.13 Ω for the entire charging period of the battery. The load resistance of 6.315 Ω corresponds to Q_P equal to 5.1540 and 23.13 Ω corresponds to Q_P equal to 18.3911. To find the minimum value

of the normalised switching frequency, α was plotted against ω_n for two extreme values of load resistance and is presented in Figure 4.9.
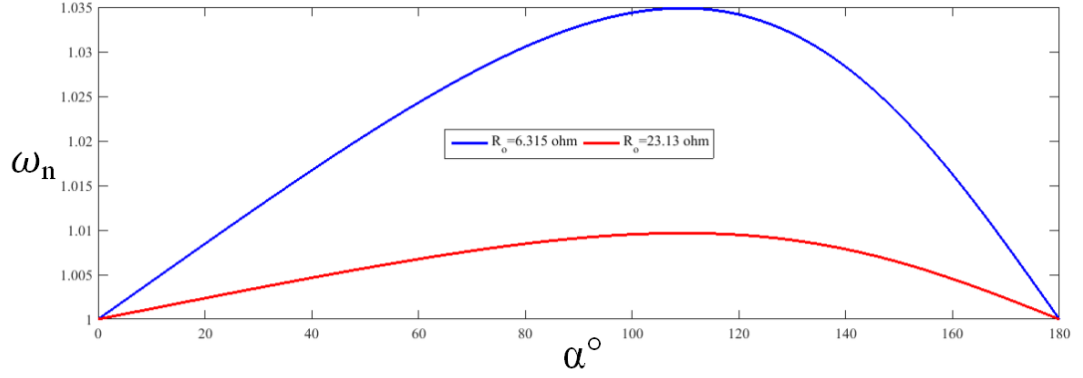
Figure 4.9 ω_n Vs α for ZVS at different load

From Figure 4.9, one can see that the minimum value of ω_n is 1.035 for the entire load range. However, due to the practical availability of capacitors, the switching frequency was selected to be 41.426 kHz and the primary was tuned to the resonant frequency of 39.031 kHz. This, in turn, gives the value of ω_n equal to 1.0613. Table 4.2 and Table 4.3 show the final parameters of the SS-RIPT system for simulation and experimental measurements. The minimum value of V_{dc} required for 3.6 kW output power at the nominal load resistance of 7.84 Ω was calculated to be 337.13 V. Therefore, a round figure of 340 V was used. The value of the filter capacitor C_f for 1% ripple in the output voltage at the switching frequency of 41.426 kHz and load resistance 7.84 Ω was calculated to be 154 µF. However, due to the practical availability of capacitor, a value of 220 µF was used.

Table 4.2 Variable parameters for experimental setup

Parameters	Nominal Values
Load Resistance, R_o	7.84 Ω
Mutual Inductance, M	40.23 µH
Air-gap	16 cm
Coupling Coefficient, k	0.20
Output Power, P_o	3.60 kW

Table 4.3 Fixed circuit parameters for experimental setup

Parameters	Values
V_{dc} (V)	340
L_p (μH)	400.65
L_s (μH)	101.10
R_p (Ω)	0.13
R_s (Ω)	0.06
C_p (nF)	41.50
C_s (nF)	146
f_o (kHz)	39.03
fs (kHz)	41.42
C_f (uF)	220

Since the primary and secondary are now tuned to a different value of resonant frequency (to achieve ZVS), this type of tuning will be referred to as 'ZVS tuning' in this thesis. To show the impact of ZVS tuning on the system performance, *input phase angle versus frequency* for 'ideal tuning' and 'ZVS tuning' has been plotted in Figure 4.10(a) and Figure 4.10(b), respectively.

Here, ideal tuning refers to the same value of resonant frequency (40 kHz) in the primary and secondary coils.
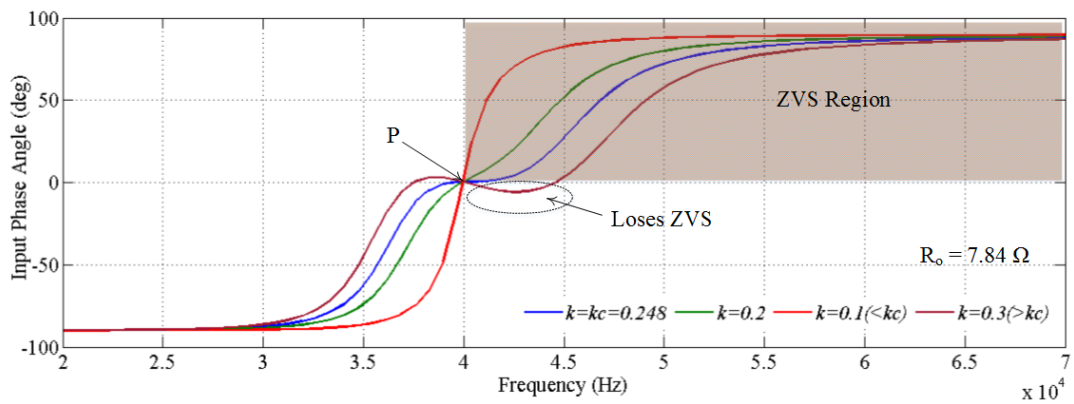
(a) Input phase angle Vs frequency for ideal tuning
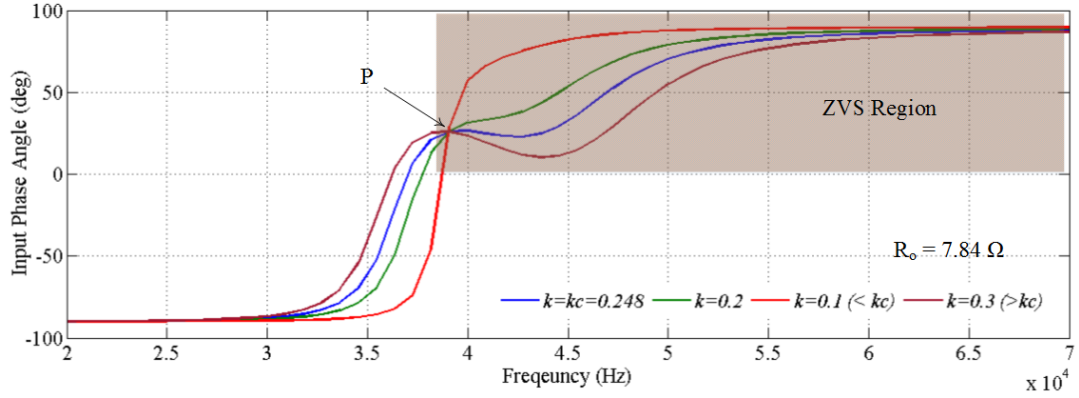
(a) Input phase angle Vs frequency for ZVS tuning

Figure 4.10 Impact of ZVS tuning on input phase angle plot

In Figure 4.10, the shaded portion represents the ZVS region. From Figure 4.10 (a), one can observe that for 'ideal tuning' condition, the inverter switches will leave ZVS if the value of coupling coefficient k increases beyond the critical value (k_c). To achieve ZVS for all values of k, the switching frequency needs to be greater than 4.5 kHz. Due to the significant deviation from the original resonant frequency of 40 kHz, the entire system parameters will be affected, and the designer will not achieve the output for which he/she may have originally designed the system.

As compared to the 'ideal tuned', the 'ZVS tuned' system maintains ZVS in inverter switches for all values of the coupling coefficient beyond point 'P'. Here point P on the curve represents the coupling independent point. Besides this, point P shifts slightly to the left of 40 kHz; therefore, it gives a wider range of frequency in which ZVS will occur. In other words, ZVS is ensured even if the system parameters vary due to variations in temperature and ageing effect.

Further to ensure that ZVS occurs in the inverter switches for the entire load range, *input phase angle versus frequency* was plotted for the minimum and the maximum value of the load resistance as shown in Table 4.1. The plot was obtained for the three different value of coupling coefficient, considering ZVS tuning. The result is shown in Figure 4.11.
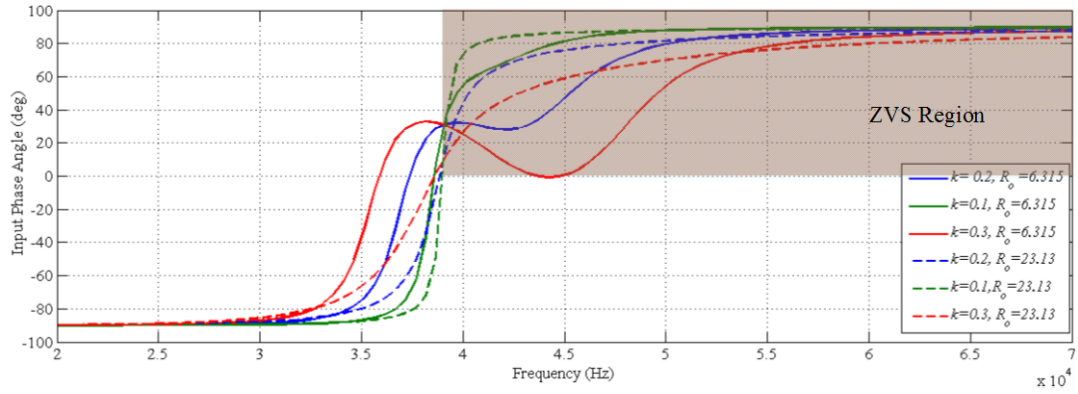
Figure 4.11 Input phase angle versus frequency for ZVS tuning and entire load
variation

From Figure 4.11, one can observe that ZVS will be maintained for the entire
variation of load resistance at each coupling coefficient, for the selected switching
frequency of 41.426 kHz.

4.5 Design of Voltage Control Loop

Using the derived small-signal model, a voltage control loop was designed for the
fixed frequency and variable duty cycle control. The following subsection discusses the
step by step procedure for the derivation of the voltage controller:

4.5.1 Bode Plot of Open-Loop System

To design the control loop, transfer function of the plant being controlled is required.
Here, the plant represents the transfer function of the output variable to the control
variable. This can be obtained from the derived small-signal model, i.e. (4.45) by
solving (4.54):

$$G_P(s) = C(sI - A)^{-1}B + D \qquad (4.54)$$

Since the output variable is V_o and the control variable is d, $G_P(s)$ represents the plant,
$\frac{\tilde{V}_0}{\tilde{d}}$. Figure 4.12 shows the open-loop Bode plot of $G_P(s)$ for 0.8 duty cycle obtained
using MATLAB.
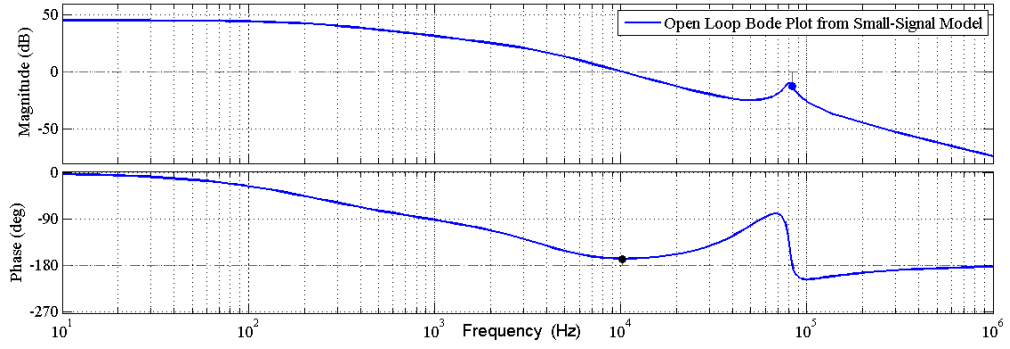
Figure 4.12 Open loop Bode plot of $G_P(s)$ for 0.8 duty cycle

The Bode plot of $G_P(s)$ has a phase margin of 12° at a crossover frequency of 10.2 kHz. Both the gain margin (GM) and phase margin are positive which indicates that the open loop system is stable. To verify the accuracy of the derived small-signal model, the frequency response of the *full model* is required. Some software such as PSIM, SIMPLIS, and PLECS, can perform frequency responce analysis of resonant converters. For this thesis, PLECS 3.7.5 was used.

To verify the accuracy of the mathematical steps taken in deriving the small-signal model from the *reduced dynamic model*, an *AC sweep* was performed on the *reduced dynamic model* (Eq. 4.8 – Eq. 4.11) in PLECS. Figure 4.13 compares the result shown in Figure 4.12 with the *AC sweep* results obtained for the *reduced dynamic model* in open loop simulated in PLECS for the duty cycle of 0.8.
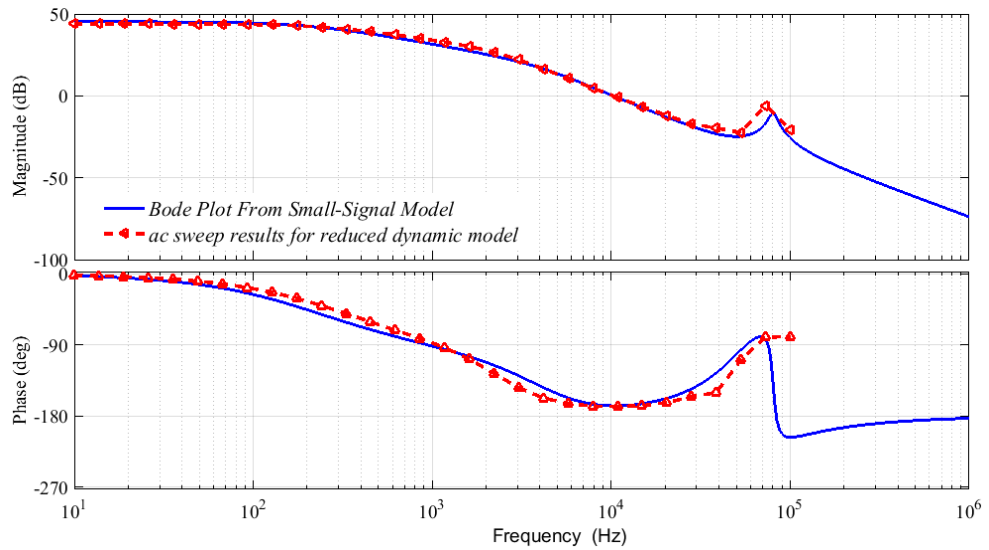
Figure 4.13 Open loop AC sweep results for the reduced dynamic model simulated in PLECS

In PLECS, the *AC sweep* was performed for a few discrete points to reduce simulation time. From Figure 4.13, one can observe that the *AC sweep* result of the *reduced dynamic model* closely follows the Bode plot of the small-signal model. This, in turn, validates that the mathematical derivation of the small-signal model from the *reduced dynamic model* is accurate.

Since the small-signal model was derived by oversimplification of the full model (Figure 4.1), it is necessary to verify whether the derived small-signal model can predict the actual physical system behaviour. For this purpose, the open loop Bode plot of the *full model* at 0.8 duty cycle was obtained using the *AC sweep* in PLECS. Figure 4.14, compares the Bode plot obtained using *AC sweep* on the *full model* and the Bode plot of the small signal model $G_P(s)$ shown in Figure 4.12.
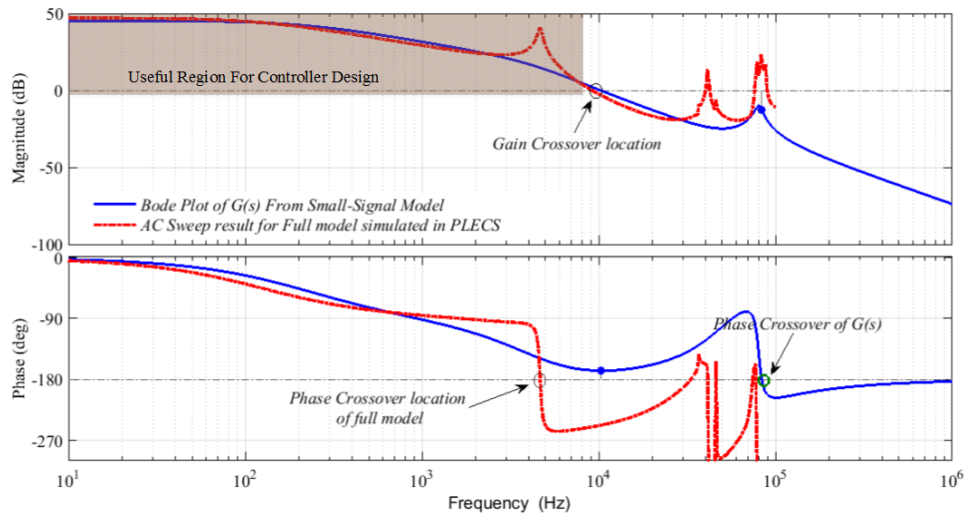
Figure 4.14 Open loop AC sweep results for the full model simulated in PLECS

From Figure 4.14, one can observe that the derived small-signal model can predict the full model (actual system) behaviour for up to 4 kHz frequency. Beyond the 4 kHz frequency, the small signal model starts deviating from full model behaviour but maintains a very similar trend of variation. In fact, for the actual system, phase-crossover frequency lies to the left of the gain crossover frequency. Therefore, the actual system will be unstable for the small disturbances in load, duty cycle or input voltage.

Figure 4.14 shows that the derived small-signal model is not suitable for predicting the actual system behaviour for frequencies beyond 4 kHz. However, here the aim is to design the control loop for output voltage and current control, which is DC. As a rule

of thumb, a closed loop system bandwidth is selected, five to ten times the highest frequency being controlled. In Figure 4.14, one can observe that low-frequency behaviour of the *full model* is accurately predicted by the derived small signal model. This makes the derived model useful for the design of the voltage and current loops. This point will become clearer from the analysis presented in next subsection. Appendix C shows the picture of the *reduced model* and the *full model* simulated in PLECS for obtaining *AC sweep* results.

4.5.2 Derivation of Closed-Loop Controller

The design of the voltage loop, shown in Figure 4.15, involves defining the voltage loop quantitatively and should meet the design criteria of both the phase margin (PM) and the bandwidth (BW) also known as crossover frequency f_c.
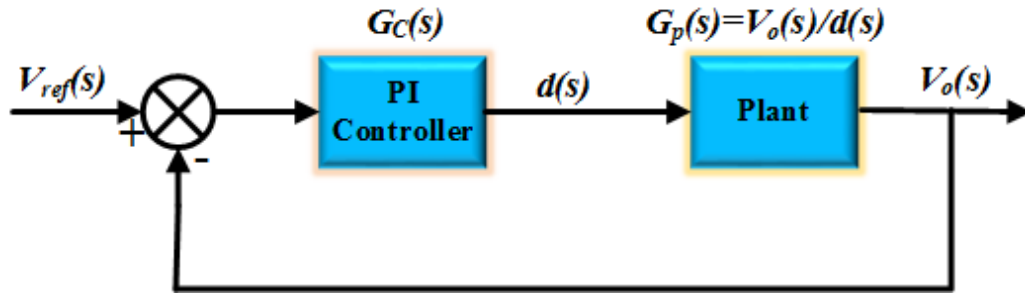
Figure 4.15 Voltage control loop

Here, $G_c(s)$ is the transfer function of the PI regulator. The voltage loop transfer function (LTF) is then given by $LTF(s) = G_c(s) \, G_p(s)$.

The following steps were used for deriving the transfer function of the controller:

1. Select Phase Margin, Cross-Over Frequency and Type of Controller:

The PI controller is designed to increase the low-frequency gain and reduce the steady state error be-tween the desired and the actual output voltage while maintaining a positive PM at the selected crossover frequency. For the choice of controller, one should see the slope of the gain curve at the selected crossover frequency. If the gain is constant, then a simple PI controller is selected. If the slope is -20 dB/dec, then a PI type 2 should be chosen. If the slope is -40 dB/dec, then PI type 3 should be selected.

Here, the aim is to control the output voltage, which is DC. Therefore, a bandwidth (f_c) of 40 Hz is selected. On the gain curve of $G_P(s)$, 40 Hz lies on the flat region. This indicates the use of a simple PI as the controller choice. The phase margin (PM) of 85° is selected to provide adequate damping to a closed-loop system for sudden a change in the duty cycle. The transfer function of the PI controller is given by (4.55):

$$G_c(s) = K_{PI}\frac{1+s\tau}{s\tau} \qquad (4.55)$$

2. Calculate the Needed Phase Boost:

From the Bode plot of the plant, $G_P(s)$, $|G_P(f_c)| = 45\ dB$ and $\angle G_s(f_c) = -11°$

The controller has to present a phase lead of ϕ and a gain of 45 dB. Here:

$$\phi = PM - (180 + \angle G_s(f_c)) = \text{-84°} \qquad (4.56)$$

The required phase boost at the crossover frequency is given by (4.57):

$$boost = \phi + 90 = 6° \qquad (4.57)$$

3. Calculate the Time Constant, τ:

$$\tan^{-1} 2\pi f_c\tau = boost \qquad (4.58)$$

$$\therefore \tau = 4.182 \times 10^{-4}$$

4. Calculate the Controller Gain at the Crossover Frequency:

At the desired crossover frequency, the *LTF* should cross *0 dB* line, i.e.:

20log (LTF)$_{fc}$ = 0dB $\qquad (4.59)$

20log G$_c$(f$_c$)+20log G$_P$(f$_c$) = 0

$\therefore K_{PI} = 0.00054$

Therefore, the PI controller becomes:

$$G_c(s) = 0.00054\frac{1+0.0004182s}{0.0004182s} \qquad (4.60)$$

Figure 4.16 shows the Bode diagram of the designed PI controller.
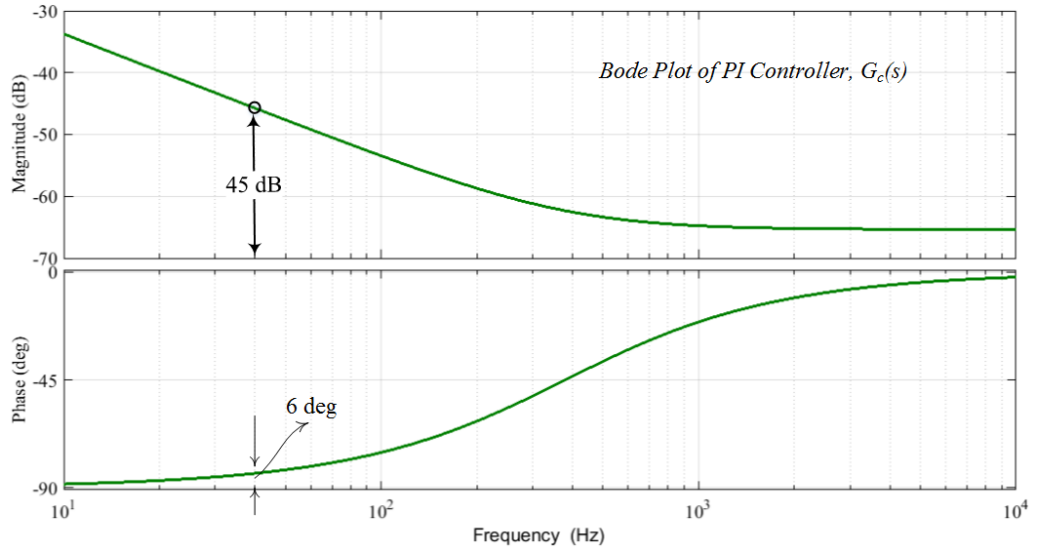
Figure 4.16 Bode plot of the designed PI controller, Gc(s)

From Figure 4.16, one can observe that at 40 Hz the phase boost provided by the controller is 6°. Moreover, a gain of -45 dB provided by the controller will make the gain of LTF zero at 40 Hz, i.e. a crossover frequency of 40 Hz is achieved.

Figure 4.17 shows the Bode plot of LTF, i.e. $G_c(s)*G_p(s)$ and the Bode plot of the *full model* with PI controller obtained using an *AC sweep* in PLECS.
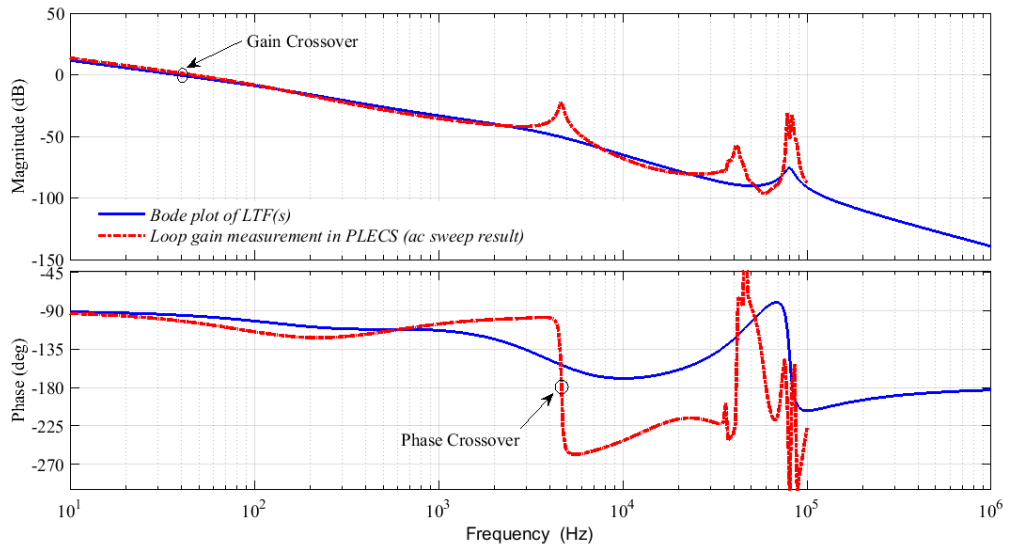
Figure 4.17 Bode plot of LTF and closed-loop system implemented in PLECS

From Figure 4.17, one can observe that a gain crossover frequency of 40 Hz and PM of 85° have been obtained for the derived small-signal model as well as for the *full model*. Moreover, for the closed-loop system, the location of the gain crossover

frequency is to the left of the phase crossover frequency for both the derived model as well as for the *full model*. Therefore, the closed loop system is stable.
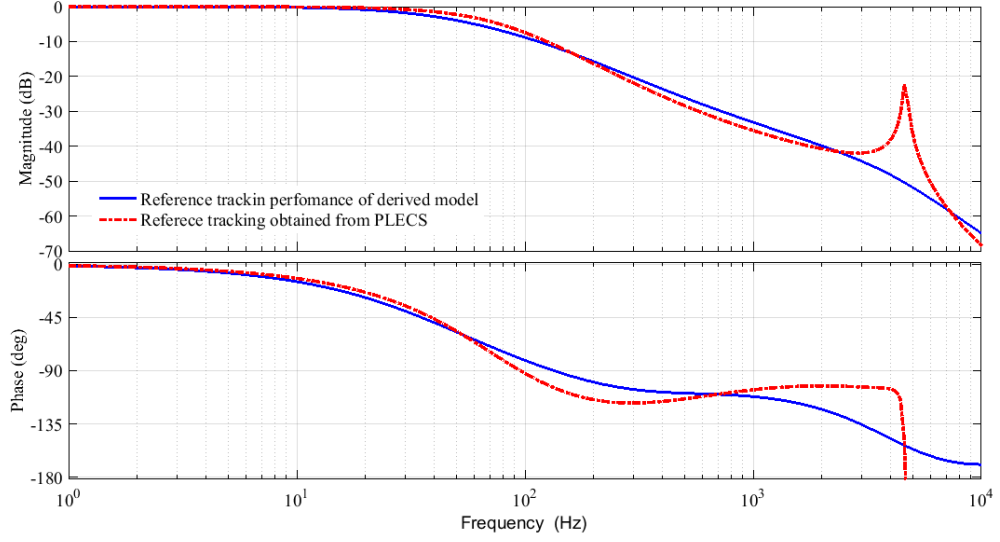
Figure 4.18 Reference tracking performance of derived model and actual model

Figure 4.18 shows the reference tracking performance for the derived small-signal model and the *full model* simulated in PLECS. Reference tracking performance is represented by transfer function $\frac{V_o(s)}{V_{ref}(s)}$. From the plot, one can see that the output voltage V_o will follow the reference voltage V_{ref} very closely until 40 Hz, i.e. until the crossover frequency. After crossover frequency of the closed-loop system, the gain drops rapidly and simply follows the open loop gain, which indicates excellent high-frequency noise rejection characteristics of the designed closed-loop system.

4.6 Design of Current Control Loop

To design the current controller, a small signal model is required, setting the output current as the output variable. For this purpose, the output voltage V_o in the non-linear equation (4.8 - 4.11) can be replaced by the product of output current I_o and load resistance R_o to obtain the small-signal model in terms of load current, as the output variable. The modified small signal model is given by (4.61) and (4.62) below.

$$\frac{d\tilde{x}}{dt} = A\tilde{x} + B\tilde{u} \tag{4.61}$$

$$\tilde{y} = C\tilde{x} + D\tilde{u} \tag{4.62}$$

Here,

A

$$= \begin{bmatrix} \dfrac{-1}{L_P}\left(\dfrac{4n}{\pi I_P}V_{cf} + R_P + n^2 R_s\right) & -\omega_s & \dfrac{-1}{L_P} & 0 & \dfrac{-4nR_O I_x}{\pi I_P L_P} \\[3mm] \omega_s & \dfrac{-1}{L_P}\left(\dfrac{4n}{\pi I_P}V_{cf} + R_P + n^2 R_s\right) & 0 & \dfrac{-1}{L_P} & \dfrac{-4nR_O I_y}{\pi I_P L_P} \\[3mm] \dfrac{1}{C_P} & 0 & 0 & -\omega_s & 0 \\[3mm] 0 & \dfrac{1}{C_P} & \omega_s & 0 & 0 \\[3mm] \dfrac{nI_P}{\pi I_x R_O C_f} & \dfrac{nI_P}{\pi I_y R_O C_f} & 0 & 0 & \dfrac{-1}{R_O C_f} \end{bmatrix}$$

$$B = \begin{bmatrix} -\dfrac{\sin 2\pi d}{\pi L_P} & -\dfrac{2V_{dc}}{L_P}\cos 2\pi d & -I_y \\[3mm] \dfrac{1}{\pi L_P}(3 + \cos 2\pi d) & -\dfrac{2V_{dc}}{L_P}\sin 2\pi d & I_x \\[3mm] 0 & 0 & -V_y \\[2mm] 0 & 0 & V_x \\[2mm] 0 & 0 & 0 \end{bmatrix}$$

$$\tilde{u} = \begin{bmatrix} \tilde{V}_{dc} \\ \tilde{d} \\ \widetilde{\omega}_s \end{bmatrix} \qquad \tilde{x} = \begin{bmatrix} \tilde{\imath}_x \\ \tilde{\imath}_y \\ \tilde{v}_x \\ \tilde{v}_y \\ \tilde{I}_O \end{bmatrix}$$

$$\tilde{y} = \tilde{I}_O\,, \quad C = \begin{bmatrix} 0 & 0 & 0 & 0 & 1 \end{bmatrix} \quad \& \quad D = 0 \tag{4.63}$$

   The current controller was designed for the PM of 75° at the crossover frequency of 80 Hz. The derived PI controller is given by (4.46). Figure 4.19 shows the current control loop. Figure 4.20 compares the Bode plot of LTF, for the current control, obtained using the derived model and the loop gain measurements in PLECS.

$$G_c(s) = \frac{0.0114 + 7.421e^{-6}s}{0.0004182s} \tag{4.64}$$
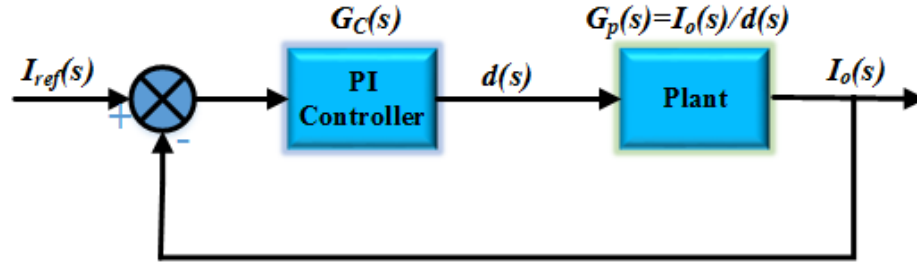
Figure 4.19 Current control loop
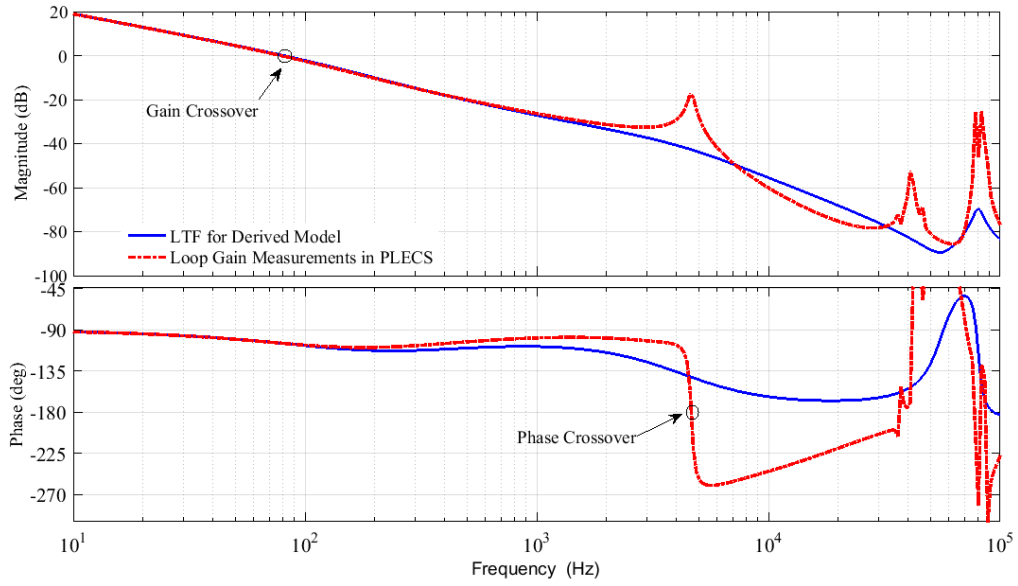
Figure 4.20 Bode plot of LTF and closed-loop system implemented in PLECS

From Figure 4.19, one can see that the PM of 75° is achieved at the crossover frequency of 80Hz. Both the derived loop transfer function as well as the *full model* are stable.

4.7   Summary of Chapter 4

In this chapter, a small-signal model of the SS-RIPT system has been derived. For the derivation of the small-signal model, a reduced dynamic model of SS-RIPT system was first derived. This, in turn, gives a fifth order system as compared to the 9th order system presented in the literature by other authors. The derived small-signal model was verified using an *AC sweep* method in PLECS.

The derived model accurately predicts the frequency response of the actual system in low frequency regions. In high frequency regions, the frequency response of the derived model does not match the actual system frequency response but maintains a

similar trend of variations. Since the low-frequency behaviour was accurately predicted, the derived model was found useful for the design of the output voltage and current controller.

This chapter also presents a piecewise-linear model of a Li-Ion battery pack to be used for simulation and experimental setup. In addition to this, the selection of compensation capacitors to achieve ZVS in inverter switches at all the loading and coupling variations, has been presented.

Chapter 5 Simulation and Experimental Validation

5.1 Description of Hardware Setup

The designed controller was implemented on the SS-RIPT system, the parameters of which have been mentioned in Table 4.2 and Table 4.3. All the simulation and experimental results were performed for the load profile specified in Table 4.1. For the experimental results, the closed-loop voltage controller was implemented in real-time using dSPACE® ControlDesk 5.3. LEM sensor LV20-P was used to sense the output voltage and LA 55-P was used to sense the current. A 63800 series programmable AC/DC electronic load from Chroma System Solutions was used as the load. XR Series power supplies from Magna-Power Electronics was used as the programmable DC power supply. The inverter was built using full-bridge MOSFET power module (APTM120H29FG) from Microsemi. For the rectifier, low loss fast recovery diode module from IXYS (DSEI2X101-06A) was used. Figure 5.1 shows a picture of the setup. Figure 5.2 shows each component and its place in the circuit for more clarity. Table 5.1 provides the ratings and supplier information for each component used for building the hardware setup.
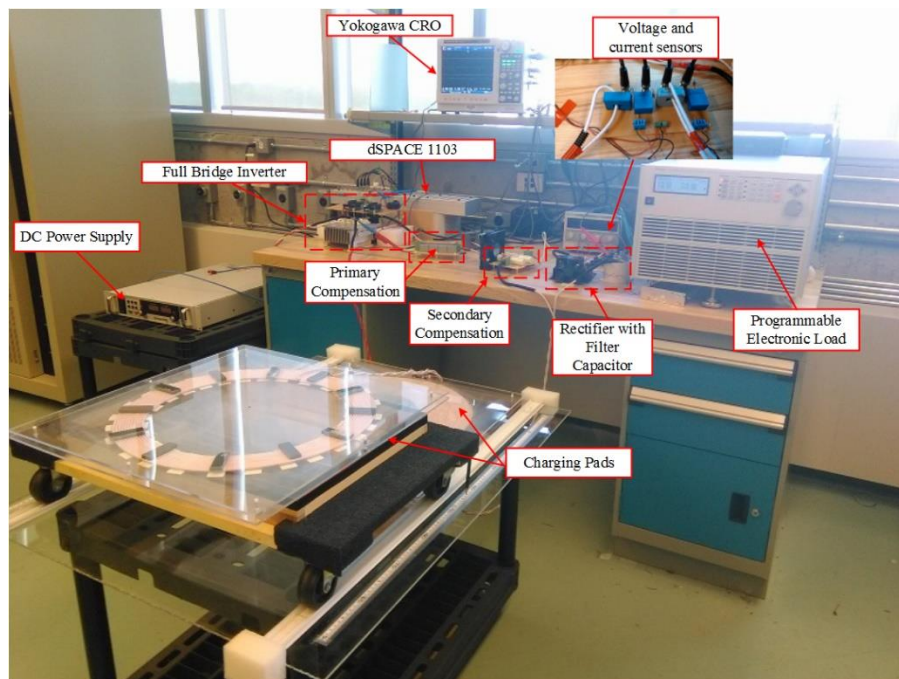
Figure 5.1 Photograph of the experimental setup
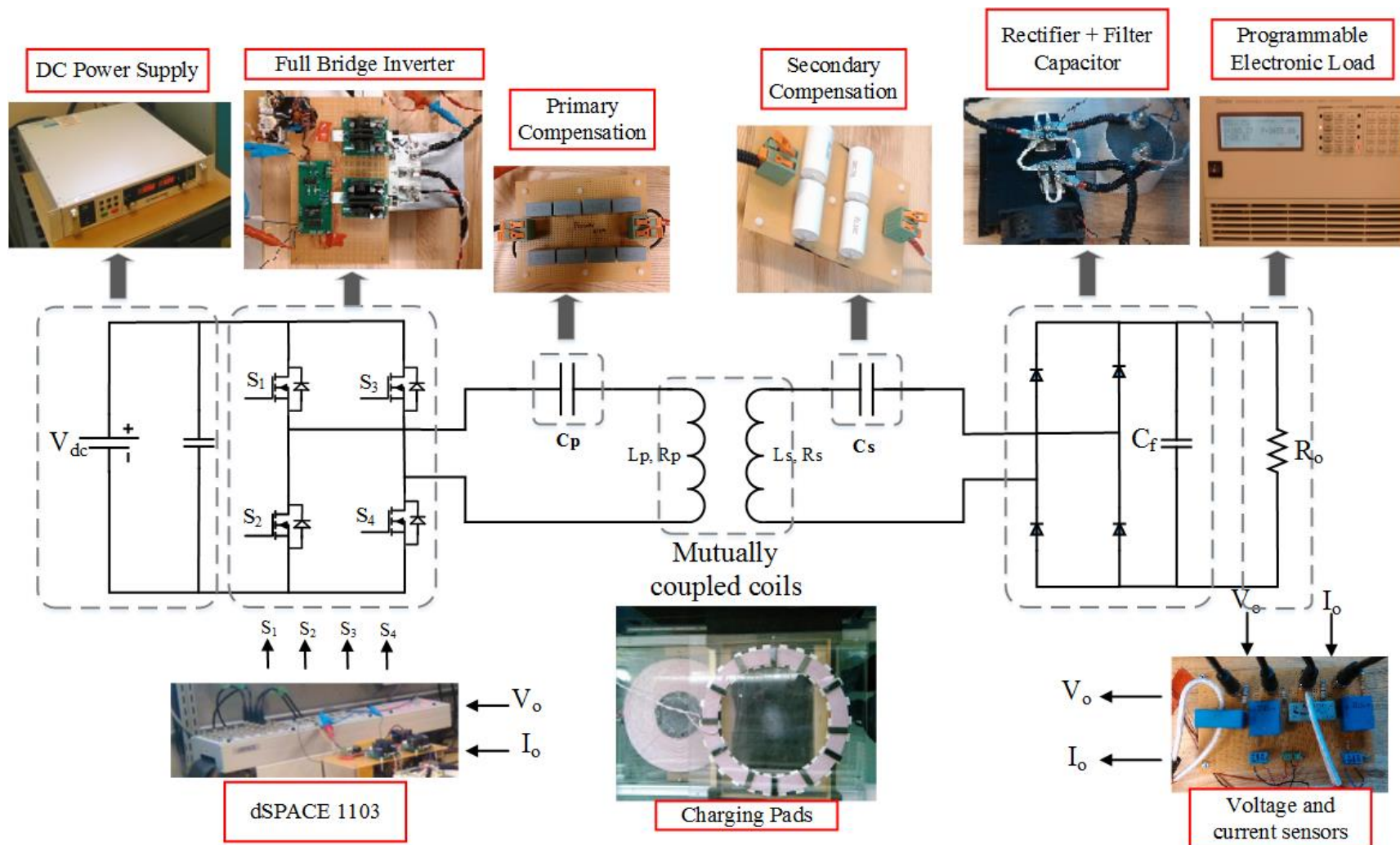
Figure 5.2 Picture showing the place of each equipment/components in the circuit

Table 5.1 Components and their technical specifications for 3.6 kW charger

Circuit Configuration	Component/Quantity	Manufacturer Part No.	Ratings
Full-Bridge inverter	Full-Bridge Mosfet Power Module/1	Microsemi APTM120H29FG	1200 V, 34 A @ 25°C R_{DSon} =290 mΩ @ 25°C
Full-Bridge Rectifier	Fast Recovery Epitaxial Diode/2	IXYS DSEI2x101-06A	600 V, 96 A, t_{rr}=35 ns
Primary Compensation Capacitors	Metallized Polypropylene Film Capacitors /4	Cornell-Dubilier-Electronics 940C30P15K-F	0.15 µF±10%, ESR=8 mΩ 500 V (AC), 3 kV (DC)
Secondary Compensation Capacitors	Metallized Polypropylene Film Capacitors /8	Vishay BFC238350823	0.082µF±5%, 550 V (AC), 100 V (DC)
Rectifier Filter Capacitor	Metallized Polypropylene Film Capacitors/1	Kemet C4DEHPQ6220A8TK	220 µF±10% 600 V (DC) ESR= 1 mΩ
Gate Drivers for inverter switches	Universal Gate Driver Evaluation Board/2	Powerex Inc. BG2C-5015	Peak Drive current ±5A Minimum R_G=2 Ω
Voltage Sensor	Closed-Loop Voltage Transducer/2	LEM LV 20-P	Voltage Sensing 10 to 500V DC~25 kHz
Current Sensor	Closed-Loop Current Transducer/2	LEM LA 55-P	Current Sensing 50 A DC~200 kHz

5.2 Simulation and Experimental Results for Open Loop

To verify the calculated parameters of the 3.6 kW design, the SS-RIPT link was simulated in PLECS for the fixed circuit parameters shown in Table 4.2 and nominal circuit parameters as shown in Table 4.3. The obtained results are compared with the experimental result for the nominal load resistance of 7.84 Ω and air-gap of 16 cm. Results obtained for the simulation and the experiment are shown in Figure 5.3 and Figure 5.4, respectively. The simulation and experiment were performed under open loop condition and 0.5 duty in inverter switches.
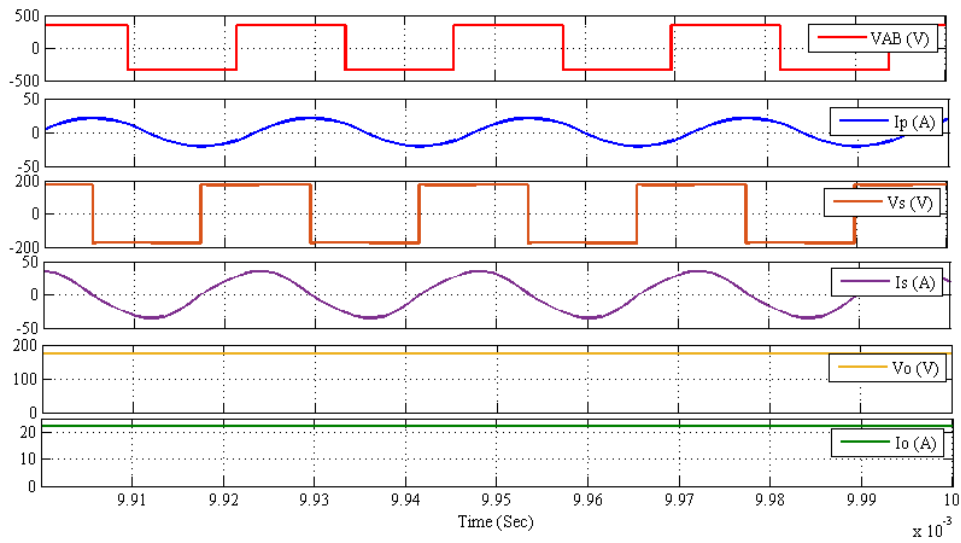
Figure 5.3 Simulation results for V_{dc}=340 V, R_o=7.84 Ω and k=0.2 in open loop

In simulation, ideal mosfet and diodes were used. The output voltage of 174.5 V and output current of 22.25 A, i.e output of 3.882 kW is obtained for the coupling coefficient k of 0.2. This is slightly above the designed value, and is due to the following reasons:

(a) The design of the SS-RIPT link for 3.6 kW was conducted based on the ideal resonant condition in both the primary and secondary coils. However, in the simulation, ZVS tuning was used.

(b) The parameters of the SS-RIPT link were calculated based on the first harmonic equivalent circuit, i.e. primary input voltage was assumed to be perfect sinusoidal. However, in the simulation, input voltage was square wave due to the inverter stage which generates additional harmonics in the circuit.

(c) The analytical calculation was performed by neglecting winding resistance; in the simulation resistance was included.
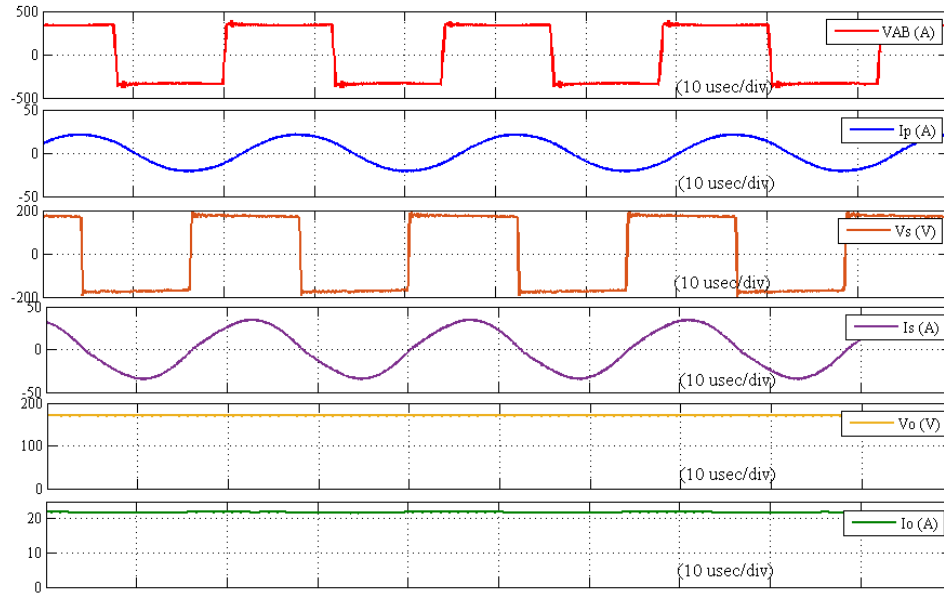
Figure 5.4 Experimental results for V_{dc}=340 V, R_o=7.84 Ω and air-gap =16 cm in open loop

In the experimet, an output current of 21.6 A, and output voltage of 169.8 V was obtained. The slight difference between the simulation and experimental results is due to the following reasons:

(a) In the simulation, core loss was not included; however, in experimental result it was present.

(b) In the simulation, ideal diode and MOSFET switches were used; however in the experimental results, losses in the switching element will affect the output power.

(c) Simulation parameters are ideal values while experimental values are plagued by the non-idealities of the hardware circuit, such as equivalent series resistance of the compensating capacitors, parasitic resistance and inductance of the connectors and soldered joints.

Nevertheless, in both the simulation and experiment, the results obtained are very close to the analytical design value. This, in turn, validates the designed parameters.

5.3 Simulation and Experimental Results for Current Control

To test the performance of the designed charger and the closed loop controller in CC mode of battery charging, the following case studies were performed:

Case I: Change in load at fixed reference current

Case II: Change in reference current at fixed load

Case III: Fluctuations in input DC supply

Case IV: Change in mutual coupling at fixed load

All the case studies have been performed for the value of the load resistance for the CC charging mode mentioned in Table 4.1. The vertical air-gap was kept at 16 cm for all cases. The ensuing subsections discuss these cases in detail.

5.3.1 Case I: Change in Load at Fixed reference Current

To test the dynamic performance of the designed controller, step change in the DC load was performed at the fixed reference current. For this purpose, the reference current was fixed at 19 A and the load resistance R_o was stepped from 6.315 Ω (2279.71 W) to 8.31 Ω (3 kW). Figure 5.5 and Figure 5.6 shows the transient performance of the simulated results and experimental results, respectively.
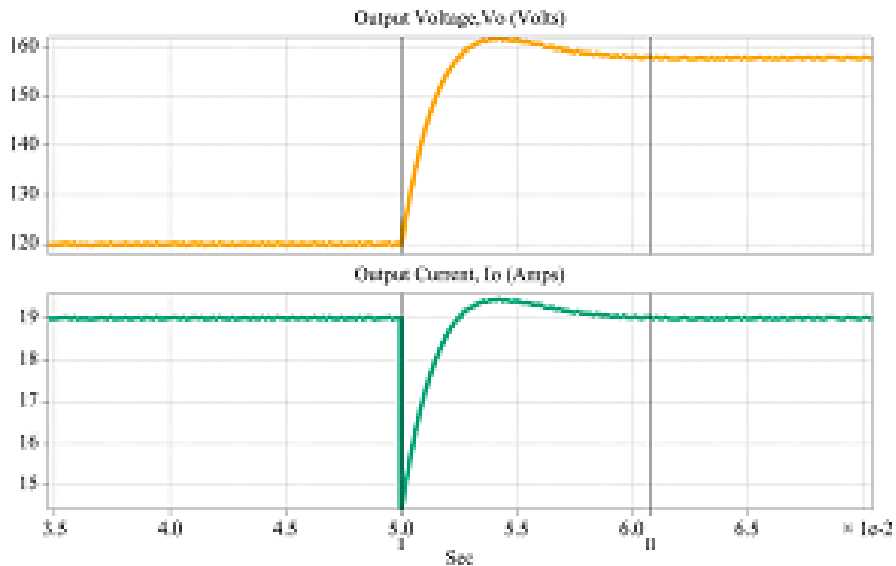
Figure 5.5 Simulation results for V_{dc}=340 V, with step change in R_o from 6.315 Ω to 8.31 Ω, and I_{ref} = 19 A
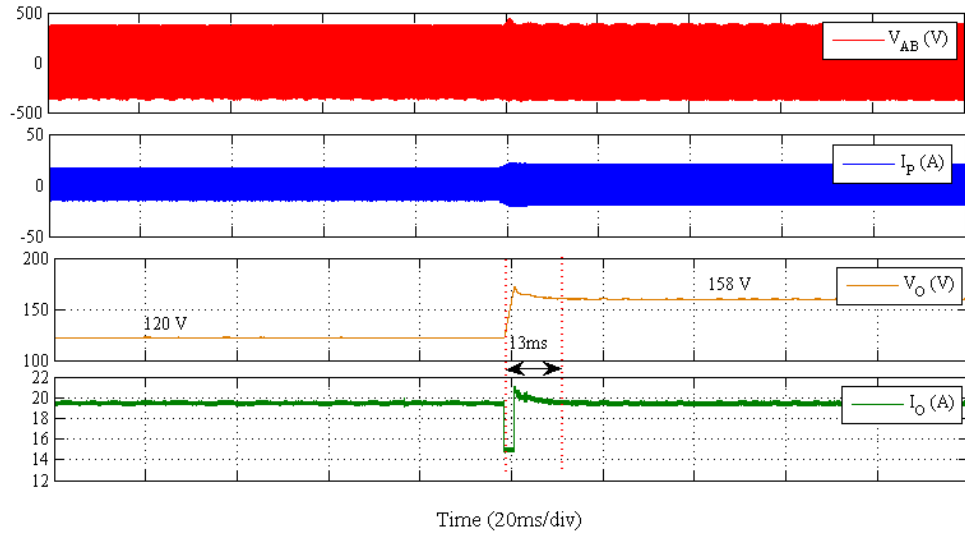
Figure 5.6 Experimental results for V_{dc}=340 V, with step change in R_o from 6.315 Ω to 8.31 Ω, and I_{ref} = 19 A

From the results, it can be observed that when a step increase in the load resistance is applied, the output current undershoot and controller takes corrective action to bring it back to 19 A in about 13 ms in experimental result and about 11 ms in simulation result. The current undershoot in the simulation and experimental result is 4.4 A and 4 A, respectively.
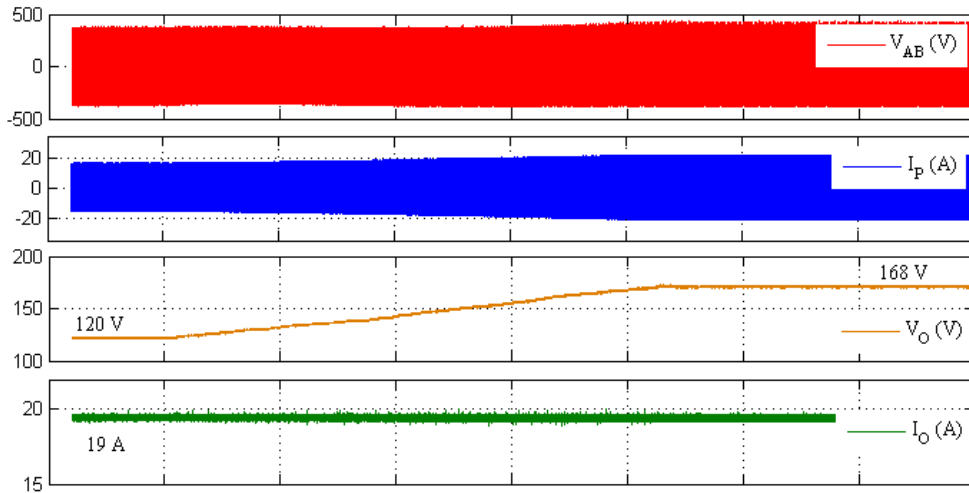
Figure 5.7 Experimental results for V_{dc}=340 V, with gradual increase in R_o from 6.315 Ω to 8.31 Ω, and I_{ref} = 19 A

The actual battery takes hours to charge thus, it acts as a high inertia load; as a result, step change in load resistance will not occur in real situations and only a gradual change in load resistance is expected. Therefore, load resistance R_o was gradually increased from 6.31 Ω to 8.84 Ω at a reference current of 19 A to test the tracking performance of the designed current controller. The results obtained are shown in Figure 5.7.

From the result, one can observe that the current remains constant and the load voltage smoothly increases for increasing load.

5.3.2 Case II: Change in Reference Current at Fixed Load

The reference current was stepped down from 19 A to 14 A at a fixed load resistance R_o of value 8.21 Ω Figure 5.8 shows the transient performance of the simulated results, while the experimental results are shown in Figure 5.9.

From the results, it can be observed that the controller takes approximately 10 ms to reach a steady state for both the simulation and the experimental results. No transient undershoot/overshoot occurs due to the damping provided by the high PM (85°) of the controller.
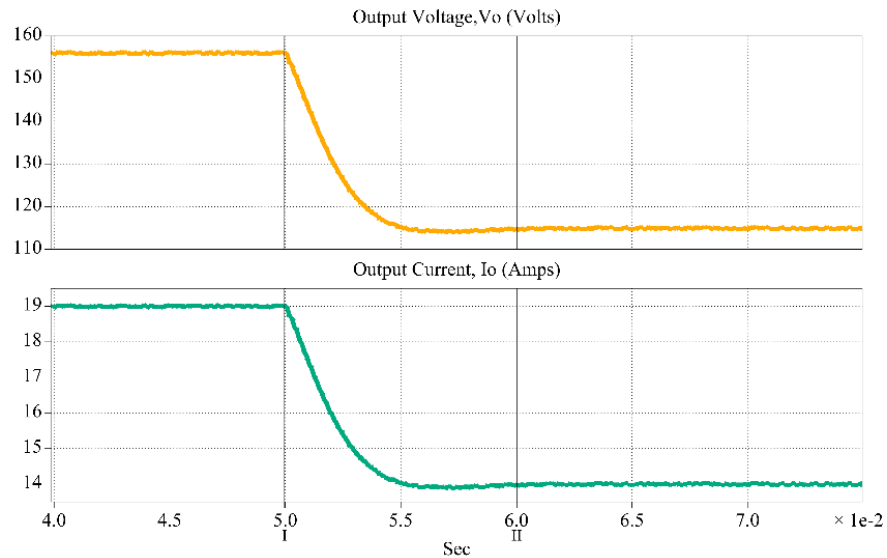
Figure 5.8 Simulation results for V_{dc} = 340 V, with step change in reference current from 19 A to 14 A, for R_o = 8.21 Ω
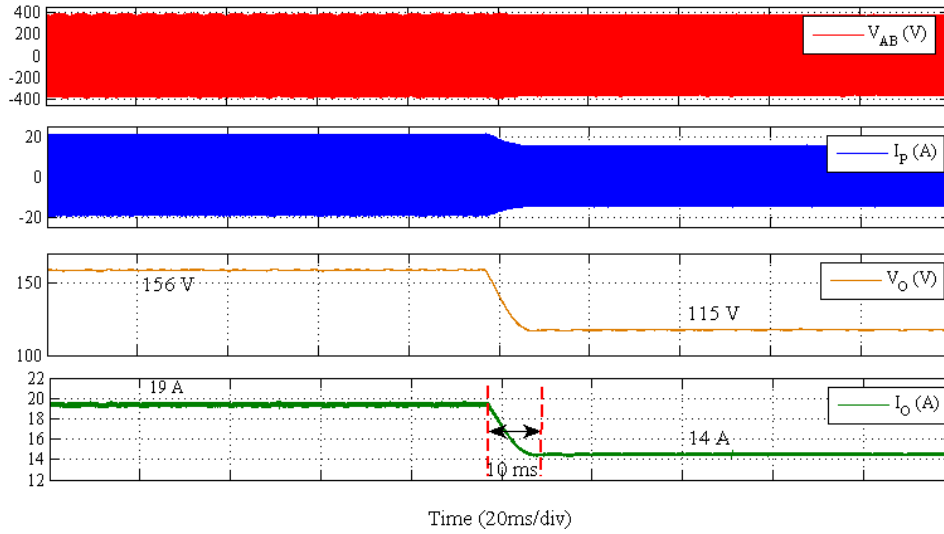
Figure 5.9 Experimental results for $V_{dc} = 340$ V, with step change in reference current from 19 A to 14 A, for $R_o = 8.21$ Ω

5.3.3 Case III: Fluctuation in Input DC supply

To test the robustness of the designed controller for the variations in DC input voltage, the reference voltage was kept 19 A at 6.315 Ω load, and ±10% variation in DC input voltage (340 V) was introduced by varying the DC supply voltage. Chroma XR series DC power supply only has a stepless rotary knob on its front panel to set the voltage/current. Therefore, a step change in DC input to the inverter was not possible and as a result, input voltage was gradually changed from the front panel rotary knob. The results obtained are shown in Figure 5.10.
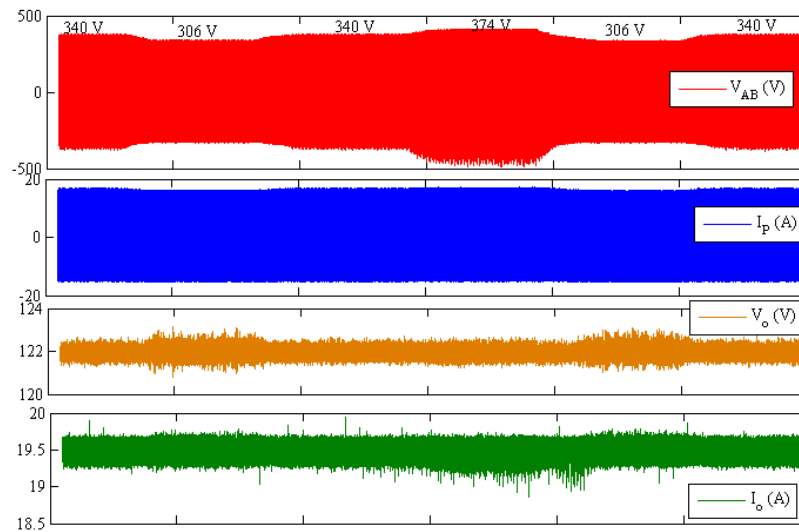
Figure 5.10 Reference tracking performance of for ±10% fluctuation in DC power supply, I_{ref} is kept 19 A and $R_o = 6.315$ Ω

From Figure 5.10, it can be seen that the controller keeps the output current fixed at the reference value in spite of the variations in the DC input voltage. Since the load is fixed, the output voltage also remains constant.

5.3.4 Case IV: Change in Mutual Coupling at Fixed Load

To test the controller performance during variation in mutual coupling between the primary and secondary, alignment of secondary with respect to primary was manually varied in the sequence [5 cm -10 cm -15 cm -20 cm -15 cm -0 cm]. The reference current and the load was kept 19 A and 7.36 Ω, respectively. The results obtained are shown in Figure 5.11.
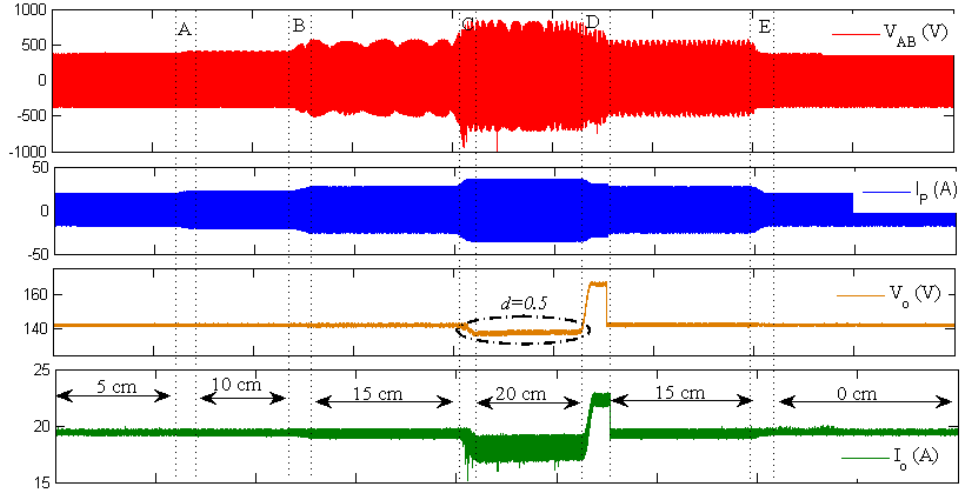
Figure 5.11 Tracking performance of controller for change in misalignment for V_{dc}=340 V, I_{ref}=19 A and R_o =7.36 Ω

In Figure 5.11, regions (A, B, C, D, and E) between the dotted lines indicate the transition period during which the alignment is changed from the previous value to the next steady value. During the transition from 5 to 10 cm (region A) and from 10 to 15 cm (region B), the controller correctly tracks the reference current. While transitioning from 15 cm to 20 cm (region C), the controller fails when misalignment is 20 cm (i.e. system is operating in open loop) and the output current decreases below the reference current value. When reducing the misalignment from 20 cm to 15 cm, the controller starts working again and correctly tracks the reference current. Figure 5.12 shows the inverter output voltage at different misalignment values.
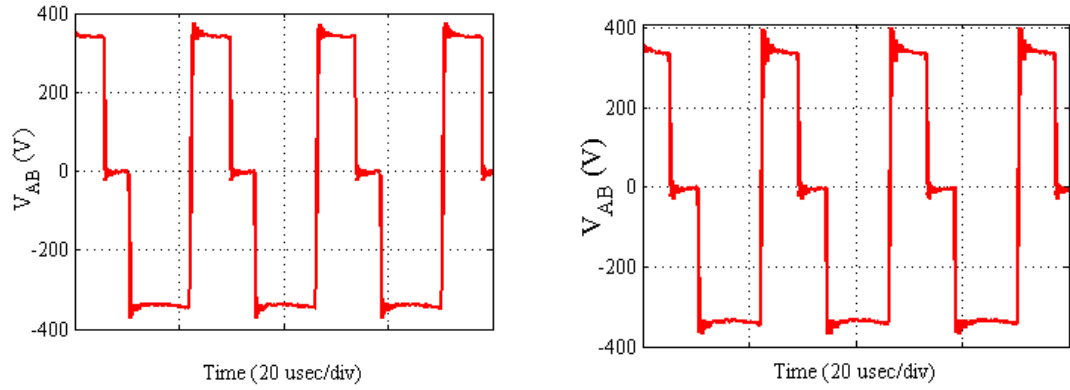
(a) Inverter output at 5 cm misalignment (b) Inverter output at 10 cm misalignment
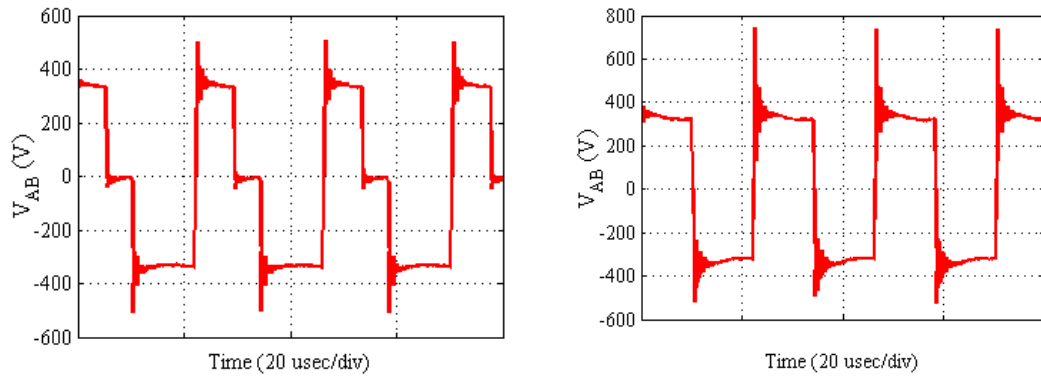
(a) Inverter output at 15 cm misalignment (b) Inverter output at 20 cm misalignment

Figure 5.12 Inverter output voltage at different value of misalignment value, with I_{ref} =19 A and R_o=7.36 Ω

In Figure 5.12, one can observe that the controller manages to control the switching of the inverter until 15 cm of misalignment. At a misalignment value of 20 cm, the controller fails to follow the reference current, i.e. the system behaviour corresponds to that of an open loop circuit, and the inverter operates at a duty cycle of 0.5. This happens due to reason outlines in following paragraph:

Due to the decrease in mutual inductance value, the magnitude of the current drawn from the supply will increase. This is also evident from Figure 5.11 and Figure 5.13 in which one can observe that the magnitude of the primary current keeps increasing with the increasing value of misalignment. For a misalignment equal to 20 cm, the increase in primary current is not met by the selected power supply rating, therefore the controller saturates and switching occurs at 0.5 duty cycle.
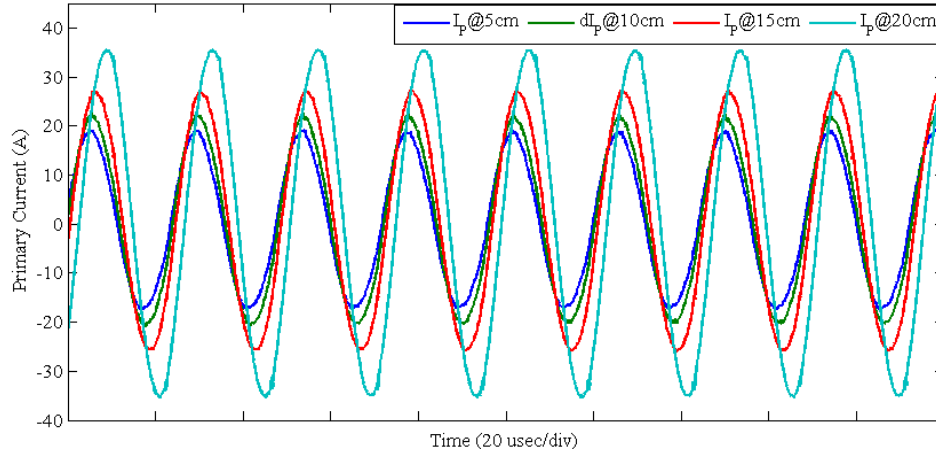
Figure 5.13 Primary current at different values of misalignment

Note: The increase in the primary current due to the increase in misalignment indicates the usefulness of the design in which the primary turns are kept higher than the secondary turns. Taking into consideration the misalignment condition, the current rating of wires in symmetrical coils needs to be oversized for both the primary and secondary pads. However, for the design in which the number of turns in the primary pad is greater than the secondary pad, no oversizing of the conductor is required. This, in turn, makes the overall system cheaper and lighter compared to the system employing a symmetrical coil pair.

5.4   Simulation and Experimental Results for Voltage Control

All the case studies performed for current control were repeated for voltage control. All the case studies (except case II) were conducted for the value of load resistance corresponding to the CV charging mode mentioned in Table 4.1. Vertical air-gap was kept at 16 cm for all cases. The ensuing subsections discuss these cases in detail.

5.4.1   Case I – Change in Load at Fixed Reference Voltage

To test the dynamic performance of the designed controller, a step change in DC load was performed at fixed reference voltage. For this purpose, the reference voltage was set at 168V and the load was stepped down from 8.84 Ω (3192.76 W) to 11.56 Ω (2441.5 W). Figure 5.14 shows the transient performance of the simulated results, while the experimental results are shown in Figure 5.15. From the results, it can be observed that when the step increase in load is applied, the output voltage overshoot and controller takes corrective action to bring it back to 168 V in about 12 ms in

experimental result and 11 ms in simulation result. Voltage overshoot in the simulation and experimental results is 15 V and 24 V, respectively.
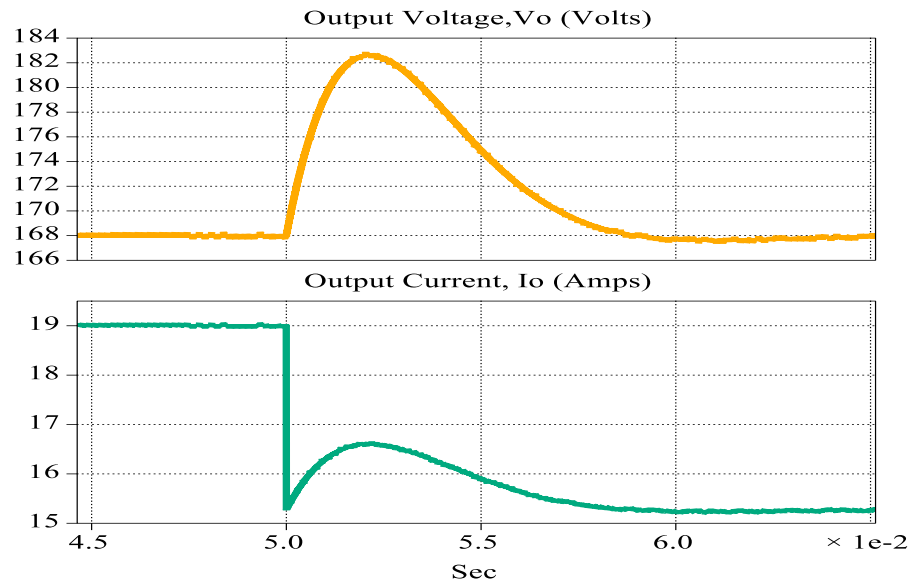
Figure 5.14 Experimental results for V_{dc}=340 V, with step change in R_o from 8.84 Ω to 11.56 Ω, and V_{ref} =168 V
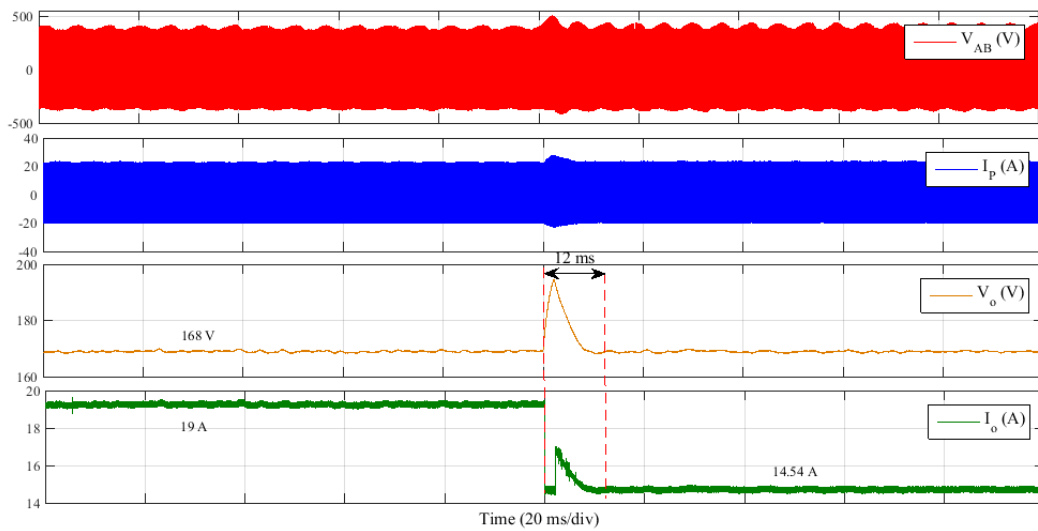
Figure 5.15 Experimental results for V_{dc}=340 V, with step change in R_o from 8.84 Ω to 11.56 Ω, and V_{ref} =168 V

5.4.2   Case II – Change in Reference Voltage at Fixed Load

The reference voltage was stepped down from 168 V (rated voltage) to 92 V at 7.84 Ω load resistance. Figure 5.16 shows the transient performance of the simulated results, while the experimental results are shown in Figure 5.17.
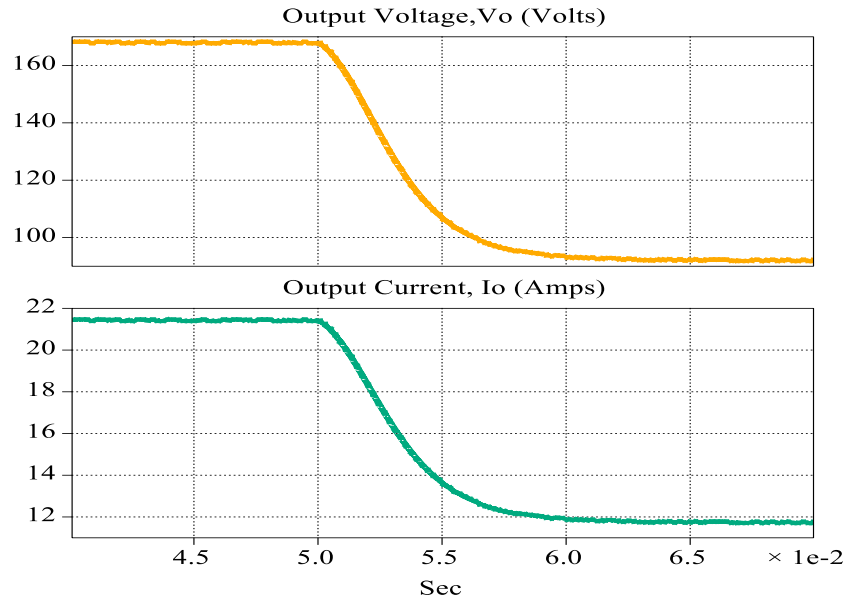
Figure 5.16 . Simulation closed-loop response for step change reference voltage from 168 V to 92 V, with R_o equal to 7.84 Ω
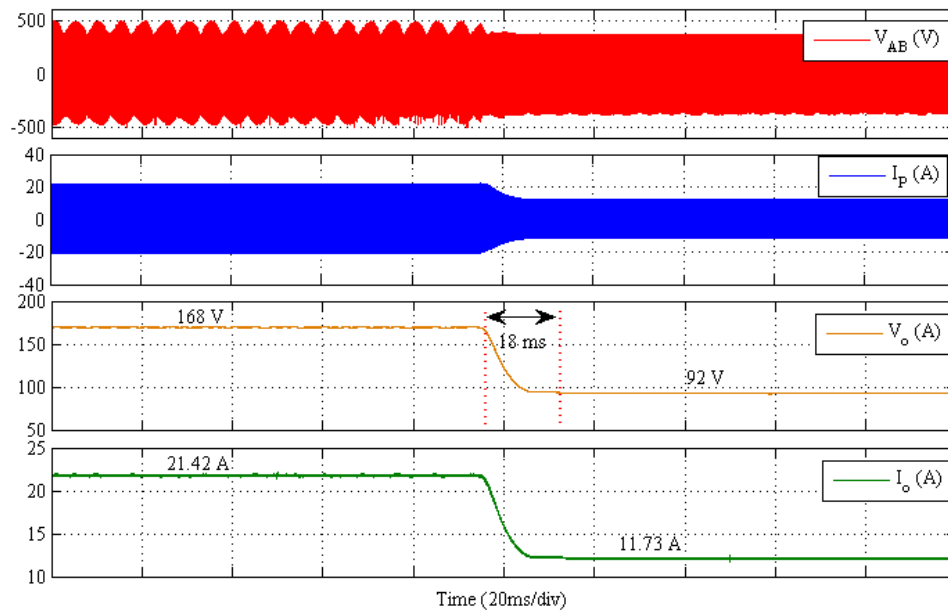
Figure 5.17 Experimental closed-loop response for step change reference voltage from 168 V to 92 V, with R_o equal to 7.84 Ω

From the results, it can be observed that the controller takes approximately 14 ms to reach steady state for the simulation and 18ms for the experimental results. No transient undershoot/overshoot occurs due to damping provided by the high PM (85°) of the controller.

5.4.3 Case III – Tracking Performance of Controller for Variation in DC Input Voltage

To test the robustness of the designed controller for the variations in DC input voltage, reference voltage was kept 160 V at 10 Ω load and ±10% variation in DC input voltage (340 V) was introduced. The results obtained are shown in Figure 5.18.
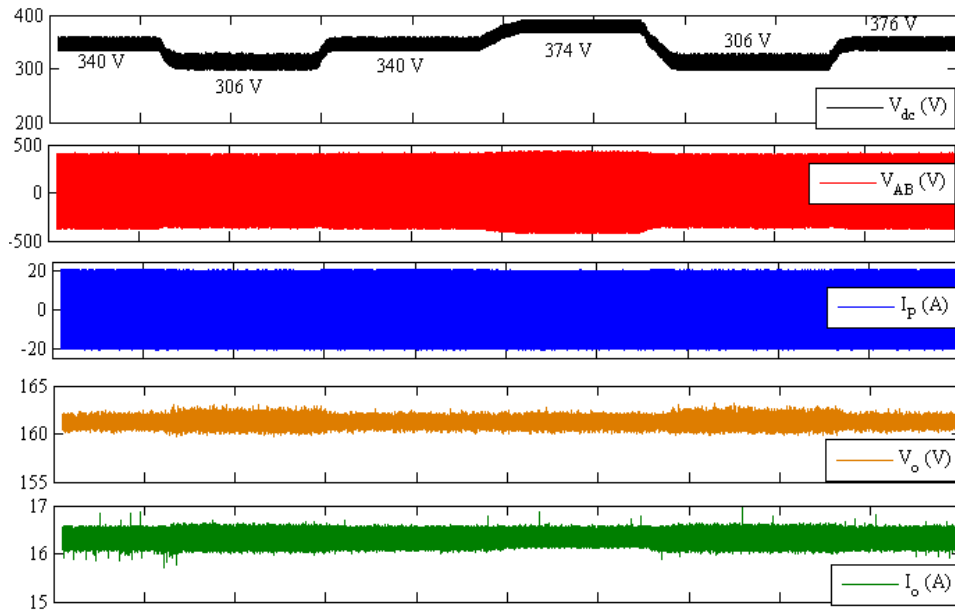
Figure 5.18 Experimental results for variation in DC input voltage

From Figure 5.18, it can be seen that the controller keeps the output voltage fixed at the reference voltage in spite of variations in the DC input voltage. Since the load is fixed, the output current also remains constant.

5.4.4 Case IV – Tracking Performance of the Controller for Variation in Mutual Coupling

To test the controller performance during variation in mutual coupling between the primary and the secondary, alignment of the secondary with respect to the primary was manually varied in the sequence [0 cm -5 cm -10 cm -15 cm -20 cm - 0 cm]. Reference

voltage and load was kept 168 V and 12 Ω, respectively. The results obtained are shown in Figure 5.19.
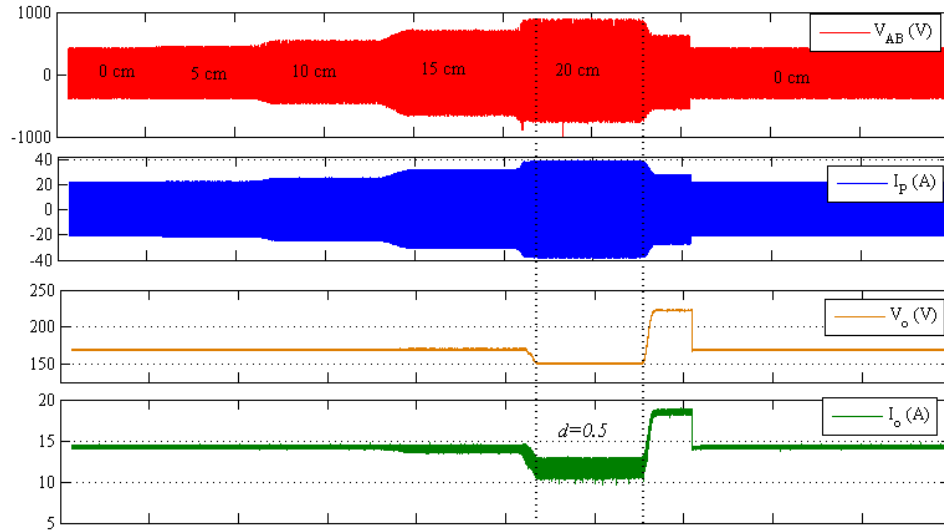
Figure 5.19 Tracking performance of controller for change in misalignment for V_{dc}=340 V, with V_{ref} =168 V and R_o =12 Ω

Similar to the current control case, the voltage controller could not track the output voltage for misalignment greater than 15 cm. This is due to the similar explantion for the current controller results and is again explained below for more clarity:

At misalignment of 20 cm and a vertical air gap of 16 cm, the value of mutual inductance is measured to be 19 µH. An output voltage of 168 V at the load resistance of 12 Ω corresponds to 2.352 kW of output. To supply output power of 2.352 kW at mutual inductance value of 19 µH (k is 0.0944), the minimum DC input voltage required will be 410 V. Value of 410 V is calculated based on first harmonic approximation, therefore for the actual setup, this value will be slightly more. Since V_{dc} is fixed to 340 V for experimental setup, the current requirement of the primary winding, for misalignment of 20 cm, is not supported by the DC power supply.Therefore, the voltage controller saturates to the maximum value of 0.5 duty, and the system behaves as an open loop system.

Since maximum voltage rating of XR series Magna power supply present in our lab is 375 V, the above point was illustrated using simulation in PLECS, as shown in Figure 5.20.
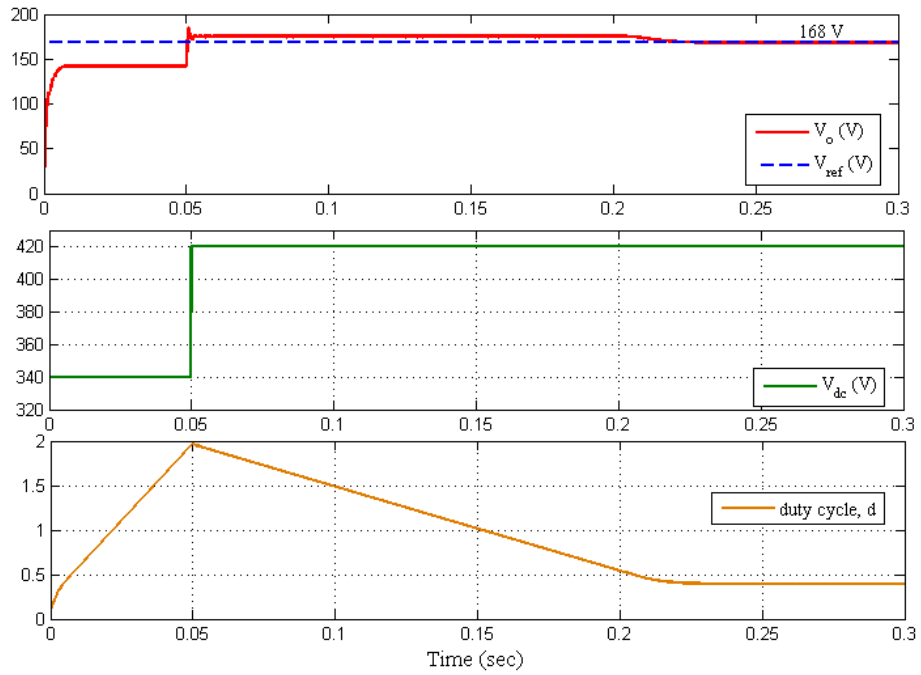
Figure 5.20 Simulation result for M=19 μH, V$_{ref}$=168 V and Ro = 12 Ω, with step change in DC input from 340 V to 420 V

From the simulation results, one can observe that for V_{dc} of 340 V, the output voltage does not follow the reference voltage command. When V_{dc} is stepped-up to 420 V at 0.05 sec, output voltage overshoots and settles to 168 V of reference after about 0.17 sec.

Although the operating range of the controller can be increased by increasing the V_{dc} input, this is not recommended due to the following reasons:

(a) As misalignment increases, the current drawn from the supply increases as can be seen from Figure 5.19. Therefore, for a particular value of misalignment, the current in the winding may exceed its current carrying capacity and this, in turn, will damage the system.

(b) Even if the coil is designed to carry such an amount of current, it is not advisable to continue charging under such misalignment. This is because the large current flowing in the winding overall charging efficiency will be very poor and will not bring any advantage from the perspective of power saving.

5.5 Verification of ZVS in Inverter Switches

To verify that the inverter operates under ZVS condition, the method described in [150] has been used. According to [150], the polarity of current at four switching instances (t_0, t_1, t_2, t_3) can be observed to confirm ZVS in switches. These instances are shown in Figure 5.21 and the polarity of the current at these instances are defined by (5.1) for achieving ZVS.
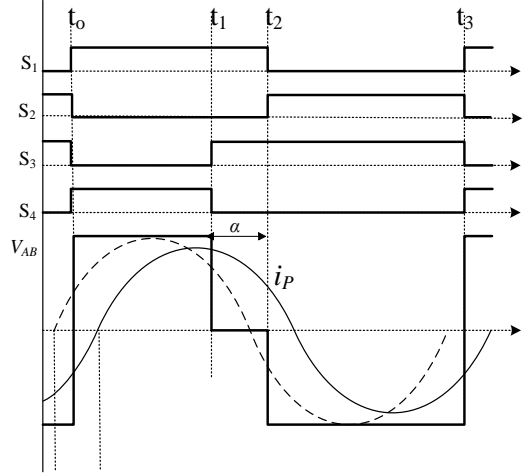
Figure 5.21 Verification of ZVS in inverter switches

$i_P(t_0) < 0$ For S1

$i_P(t_1) > 0$ For S3

$i_P(t_2) > 0$ For S2

$i_P(t_3) < 0$ For S4 (5.1)

Since it is not possible to verify ZVS for each load condition, only the following three load conditions were considered:

(a) Beginning the CC charging mode: In this mode, load resistance is 6.315 Ω and output power is 2.28 kW, which is 63.3% of rated power of 3.6 kW.

(b) Beginning of the CV mode (or end of the CC mode): In this case, load resistance is 8.842 Ω and output power is 3.192 kW (88.6% of rated power).

(c) End of the CV mode: In this case, load resistance is 23.13 Ω and the output power is 1.22 kW (33.8% of rated power)

The experimental results for the above three load conditions were plotted in MATLAB and are shown in Figure 5.22.

(a) R_L=6.315 Ω, I_o=19 A

(b) R_L=8.842 Ω, I_o =19 A

(c) R_L =23.13 Ω, V_o= 168 V
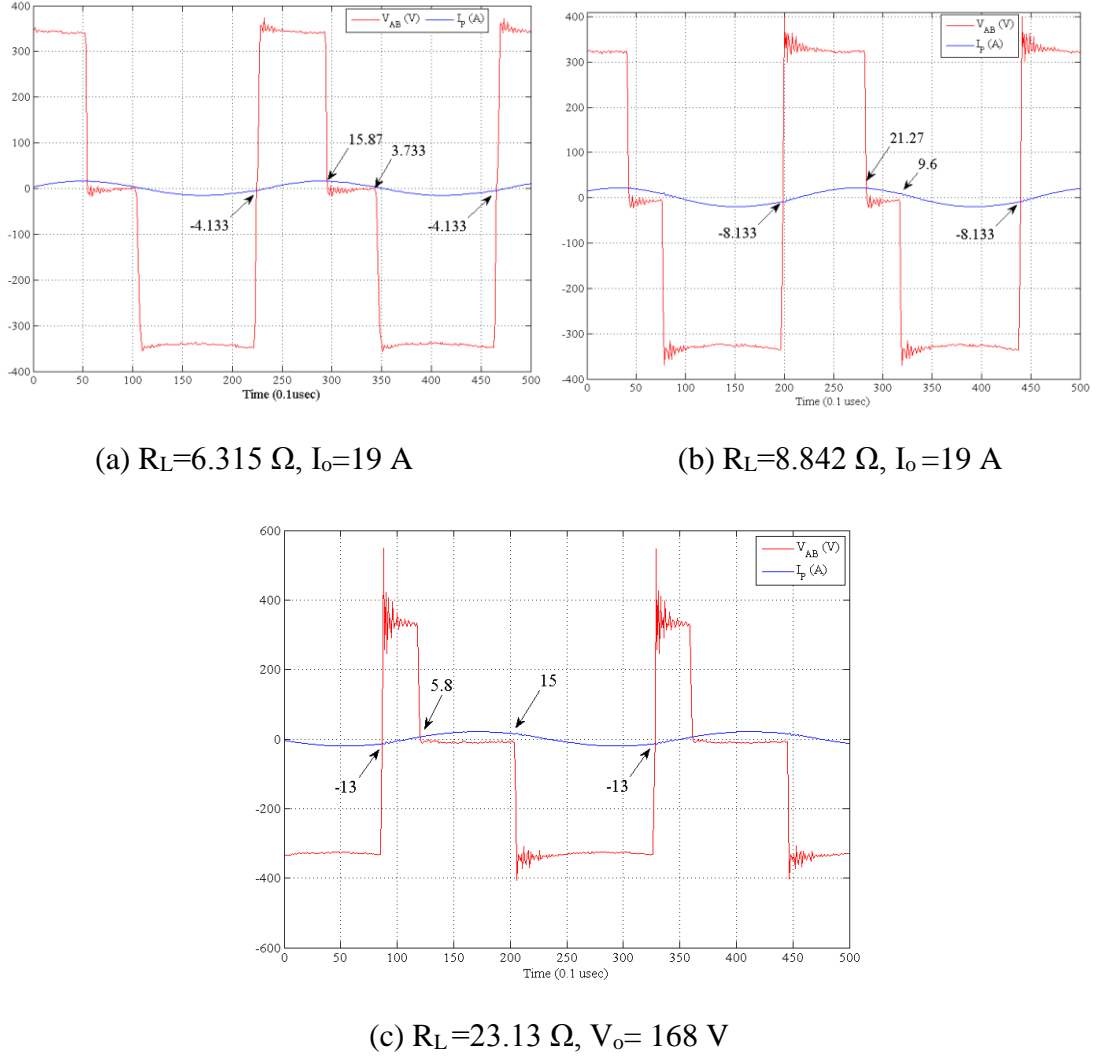
Figure 5.22 Verification of ZVS in inverter switches for charging under perfect aligned condition

In Figure 5.22, one can observe that the polarity of the current for each load profile fulfils the condition given by (5.1). Even at a partial load condition of 33%, ZVS is maintained. Therefore, it can be said that the designed charger will operate under ZVS condition for the entire charging profile. The results shown in Figure 5.22 were obtained at perfect alignment and fixed air-gap of 16 cm, i.e. mutual inductance was constant.

It is also necessary to verify the ZVS operation for the change in coupling coefficient during the charging process. For this purpose, the reference voltage was kept 168 V at 7.84 Ω and alignment between the primary and the secondary coils was varied at a fixed

air gap of 16 cm. The results obtained for 5 cm, 10 cm and 15 cm of misalignment are shown in Figure 5.23.
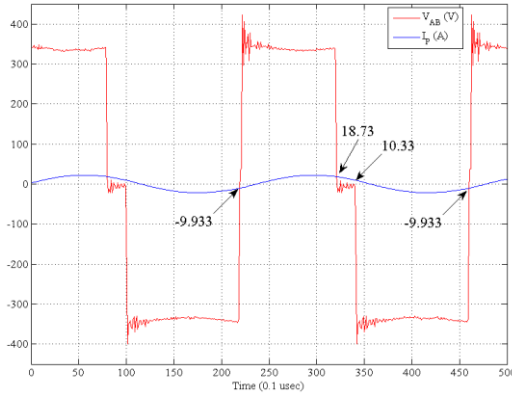
(a) Waveform for Misalignment =5 cm   (b) Waveform for Misalignment =10 cm
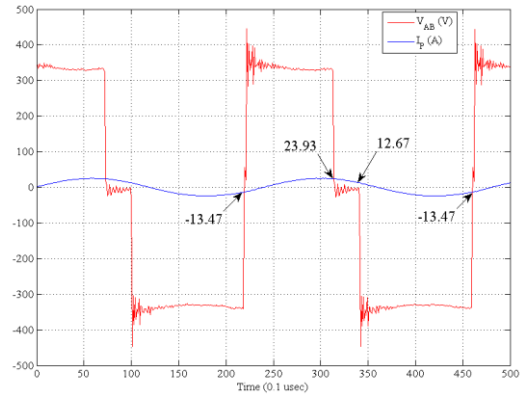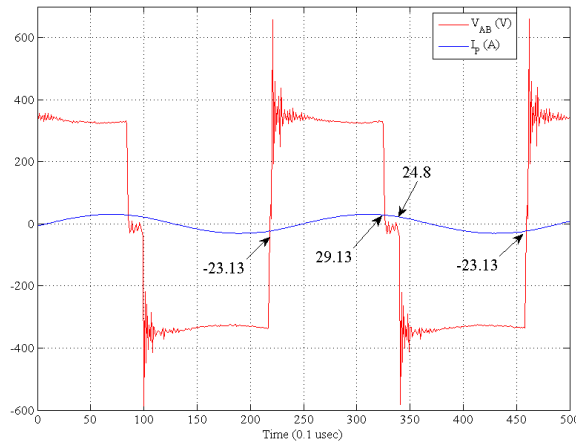
(c) Waveform for Misalignment =15 cm

Figure 5.23 Verification of ZVS in inverter for V_o=168 V and R_o=7.84 Ω at different misalignment values

In Figure 5.23, waveform satisfies the condition for achieving ZVS for all the three case.

5.6 DC-DC Efficiency of the Designed Charger

DC to DC efficiency of the designed SS-RIPT charger was calculated for all the cases presented for constant current and constant voltage control. The result are shown in Table 5.2.

Table 5.2 DC-DC efficiency calculation for different cases

Cases		Pin=$V_{DC}*I_{DC}$ (Watts)	Pout=V_o*I_o (Watts)	η (%)
CC-Case I. I_{ref} =19 A	R_o= 6.315 Ω	340*7.5=2550	120*19=2280	89.41
	R_o= 8.31 Ω	340*9.8=3332	157.89*19=3000	90.03
CC-Case II. R_o= 8.21 Ω	I_{ref} =19 A	340*9.8=3332	156*19=2964	88.96
	I_{ref} = 14 A	340*5.4=1836	115*14=1610	87.70
CC-Case III. R_O= 6.315 Ω I_{ref} =19 A	V_{DC} =306V	306*8.36=2558.16	120*19=2280	89.12
	V_{DC} =340V	340*7.52=2556.8	120*19=2280	89.17
	V_{DC} =374V	374*6.84=2558.16	120*19=2280	89.12
CC-Case IV. I_{ref}=19 A R_o = 7.36 Ω	Misalign.=5 cm	340*8.78=2985.2	139.84*19=2656.96	89.00
	Misalign.=10 cm	340*8.88=3019.2	139.84*19=2656.96	88.00
	Misalign.=15 cm	340*9.2=3128	139.84*19=2656.96	84.94
CV-Case I. V_{ref} =168 V	R_O= 8.84Ω	340*10.32=3508.8	168*19=3192	90.97
	R_o= 11.56Ω	340*8=2720	168*14.53=2441.04	89.76
CV-Case II. R_o= 7.84 Ω	V_{ref} =168V	340*11.6=3944	168*21.42=3598.56	91.2
	V_{ref} = 92V	340*3.54=1203.6	92*11.73=1079.16	89.66
CV-Case III. R_o= 10 Ω V_{ref}=160V	V_{DC} =306V	306*9.24=2827.44	160*16=2560	90.54
	V_{DC} =374V	374*7.54=2819.96	160*16=2560	90.78
	V_{DC} =374V	340*8.3=2822	160*16=2560	90.71
CV-Case IV. V_{ref}=168V R_o = 12 Ω	Misalign.=5 cm	340*7.78=2645.2	168*14=2352	88.91
	Misalign.=10 cm	340*7.94=2699.6	168*14=2352	88.79
	Misalign.=15 cm	340*8.40=2856	168*14=2352	82.35

From Table 5.2, it can be noted that the efficiency at rated load condition (168 V and 7.84 Ω) is 91.2%. Even at 1610 W (44.7% of rated load), light load condition efficiency is 87.70%. Efficiency decreases with increasing misalignment. The worst efficiency obtained is 82.35 % for the CV-Case IV at a misalignment value of 15 cm. However, in this case the load on the charger is 2352 W, which is 63% of rated load. If misalignment occurs for the load near to the rated load, the efficiency will not deteriorate to 81%. This is evident from CC-Case IV in which loading on the charger is about 74% of rated load, and the efficiency at 15 cm is 84%. Figure 5.24 shows the

efficiency of the designed charger for the entire charging period calculated for 0 cm, 5 cm and 10 cm of misalignment, with a constant air-gap of 16 cm.
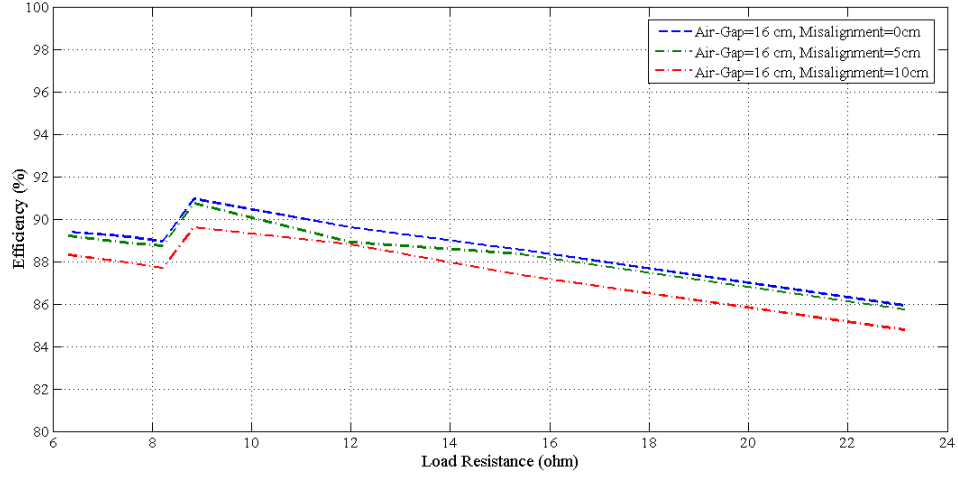
Figure 5.24 Efficiency Vs load plot for different value of misalignment and fixed air-gap of 16 cm.

5.7   Summary of Chapter 5

In this chapter, the simulation and experimental results for output current control and output voltage control for different cases have been presented. The designed controller shows the excellent tracking capability for both output voltage and output current changes. Transient performance of simulation and experimental results match very well. Moreover, the designed charger operates under ZVS condition for all loading and coupling variation. This indicates the effectiveness of the proposed model outlined in Chapter 4.

Moreover, it was established that the designed charger (close-loop system) could meet the load demand for lateral misalignment up to 15 cm at a fixed air-gap of 16 cm. DC-DC efficiency of the designed charger for the rated load condition and the nominal coupling coefficient (3.6 kW at 168 V) is found to be 91%.

Chapter 6   Safety and Shielding Issues

6.1   Safety Considerations of Wireless Charger for Electric Vehicles

Due to the presence of a large air-gap between the primary and the secondary pads, the leakage flux is very high. Exposure to the leakage flux could cause adverse effects on health. Therefore the frequency and amplitude of the leakage magnetic field should be elaborately controlled to meet the safety regulations [163]. The designer should ensure that the magnetic flux density should meet safety guidelines. There are two international groups that set standards/Guidelines for Human Exposure to electromagnetic field (EMF) [164]: one is the International Committee on Electromagnetic Safety (ICES) under the Institute of Electrical Electronic Engineers (IEEE) [165], and the other is the International Commission on Non-ionizing Radiation Protection (ICNIRP) [166] [164].

The guideline published by ICNIRP is the most referenced standard to ensure human safety [20]. There are two versions of the ICNIRP standard: 1998 version and 2000 version. According to ICNIRP 1998, the general public should not be exposed to average flux densities greater than 6.25 µT for switching frequencies in the range of 0.8-150 kHz [167]. In the ICNIRP 2010 guidelines, the reference level for the general public is relaxed to 27 µT [20].The increase in the reference level is because the former guidelines were too conservative.

As compared to ICNIRP, the guidelines published by the IEEE International Committee on Electromagnetic Safety are more relaxed. In IEEE Std. C95.1-2005, the maximum permissible exposure of the head and torso is 205 µT for the general public. The maximum permissible exposure for the limbs is even higher, at 1130 µT [161].

A car is usually made of steel, which is an excellent shielding material [20]. People sitting inside the car are shielded from the leakage flux. However, people standing next to the car are at risk of exposure to the leakage magnetic field. Therefore, it is necessary to determine the magnitude of flux density in the region surrounding the vehicle.

As shown in Figure 6.1(a), assuming that the width of the vehicle is 1.6m and the secondary pad is installed such that it is centered under the vehicle body, the user will

be exposed to the flux density levels occurring at and beyond the vehicle chassis, i.e. at point P (a distance of 0.8 m from the centre of the coil). For this purpose, magnetic flux density, at 800 mm from the centre of the primary coil under perfect alignment at 16 cm air-gap and rated load condition, was measured using FEA analysis in JMAG. The result obtained is shown in Figure 6.2 which shows that the magnitude of flux density at coordinates (x=800mm, -0.284mm, z=81.5mm) is 14.5 µT. This value is within the safety guidelines recommended by ICNIRP 2010 and IEEE.
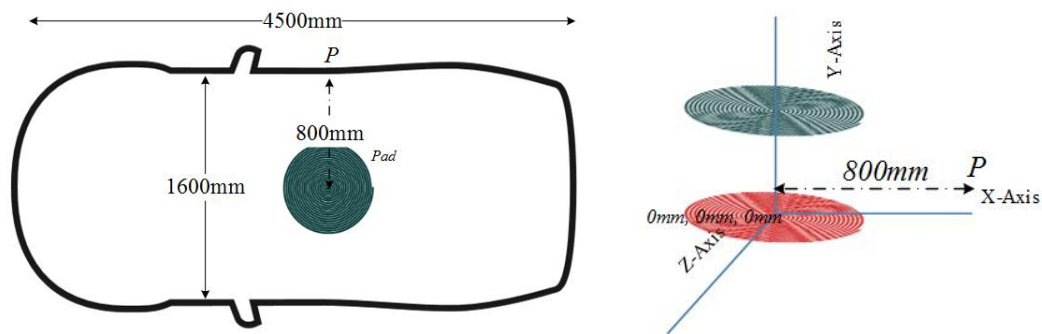
Figure 6.1 Position of the leakage flux measurement point (*P)* demonstrated with the sketch of top view of an RIPT powered EV.
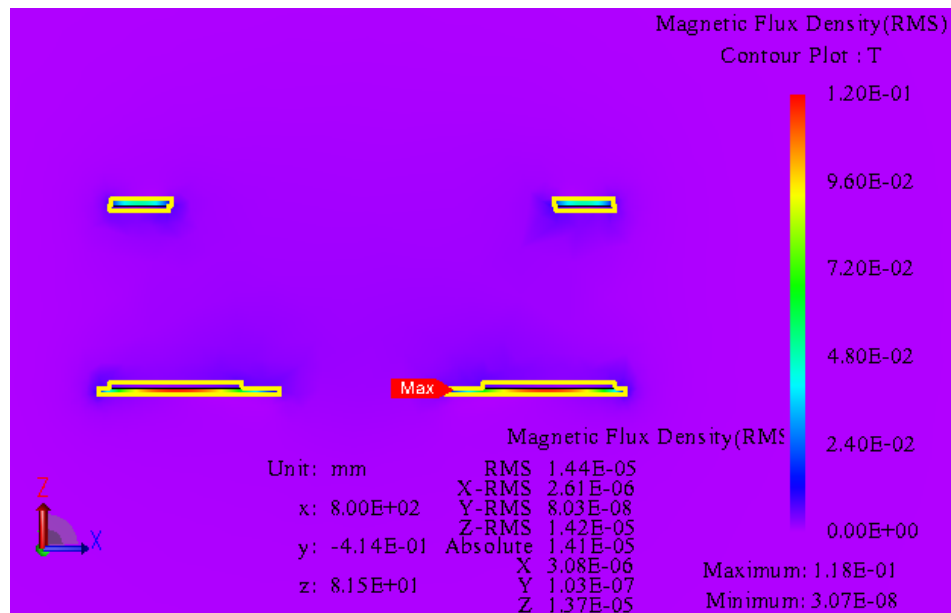
Figure 6.2 Magnetic flux density at distance 800 mm from the center of the coil

6.2   Effect of shielding on leakage flux

It was observed in Chapter 3 that, due to the addition of ferrite spokes, the value of self-inductance of the coils is modified. This happens because the flux path is changed by the presence of magnetic materials in its vicinity. Since the EV chassis is made of steel, similar magnetic phenomena is expected. Due to the change in the originally designed inductance value, the charger will not perform as desired. In addition, the EV chassis acts as an undesirable load to the charging pads and power is lost in the form of heat due to an eddy current generated in the chassis by time varying flux [169].

To handle the aforesaid issues, leakage flux above the plane of secondary pad needs to be shielded so that it does not interact with the vehicle body. Since the primary is embedded on the ground, it can be made sure that no magnetic material exists in the fundamental flux path existing below the primary pad, hence no shielding is necessary. Figure 6.3 shows the magnetic flux line distribution of the designed coil operating under a nominal air-gap of 16 cm and output power of 3.6 kW, using JMAG analysis.
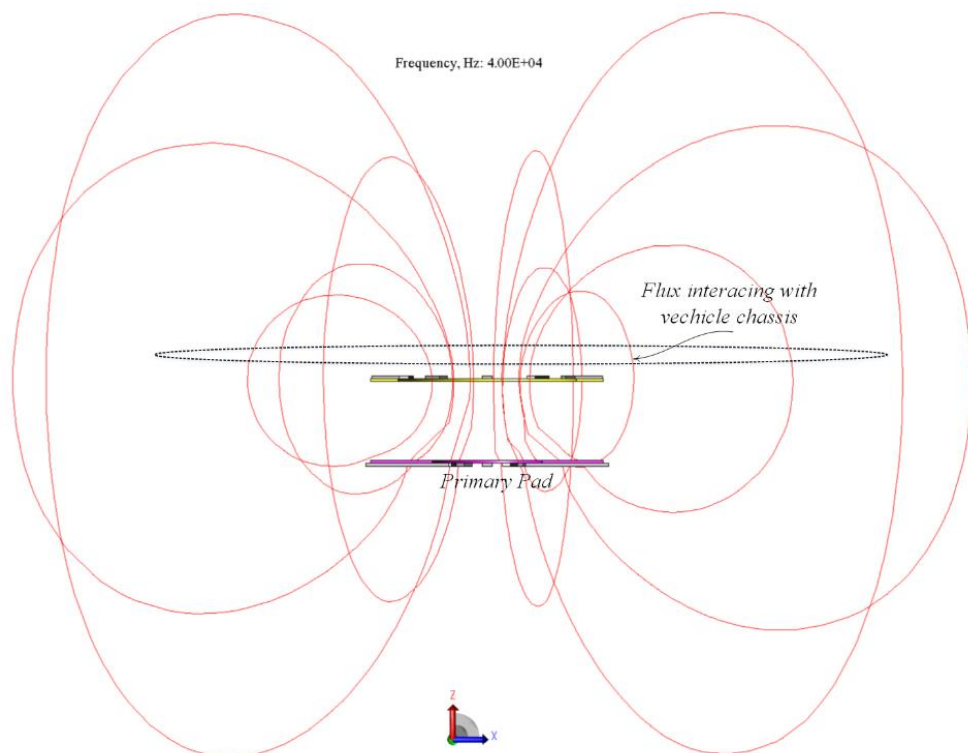
Figure 6.3 FEA result showing magnetic flux lines of designed charger operating at 16 cm air-gap without shielding

As shown in Figure 6.3, the flux out of the secondary ferrites needs to be suppressed. The Auckland University published studies in which an aluminium backing plate was used to contain the leakage flux out of the ferrite side [12], [39], [28], [53]. Therefore, an aluminium sheet of thickness 2 mm and diameter equal to the diameter of the secondary pad was added above the secondary ferrite to study the behaviour of flux lines in the presence of the shielding. Between the secondary ferrite and the aluminium sheet an air-gap of 5mm was kept since the original pad was contained inside the acrylic sheet of thickness 5mm. The result obtained is shown in Figure 6.4.
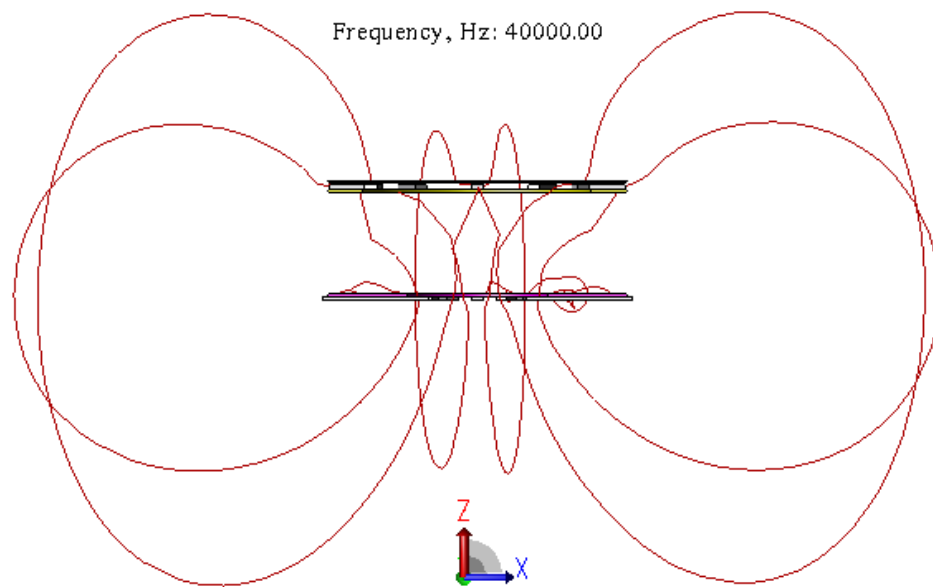
Figure 6.4 FEA result showing magnetic flux lines of designed charger operating at 16 cm air-gap with shielding added to secondary side

The effect of the addition of the shielding is clearly visible in Figure 6.4. The flux lines existing above the secondary pad have been considerably reduced because a suitable conductive material with low permeability, such as copper or aluminium, when exposed to a time-varying magnetic field will induce an eddy current in them. This eddy current produces a magnetic field in the opposite direction of the external field. This in turn causes the external field to bend off instead of entering the material [170]. Therefore, instead of coming out of the secondary ferrites, the flux lines are diverted and contained in the plane below the shielding plate. This can be seen in the JMAG using a current density vector plot. Figure 6.5 shows the direction of the instantaneous

current in primary coil and the eddy current induced in the aluminium shield when the supply phase is 45° and 135°.
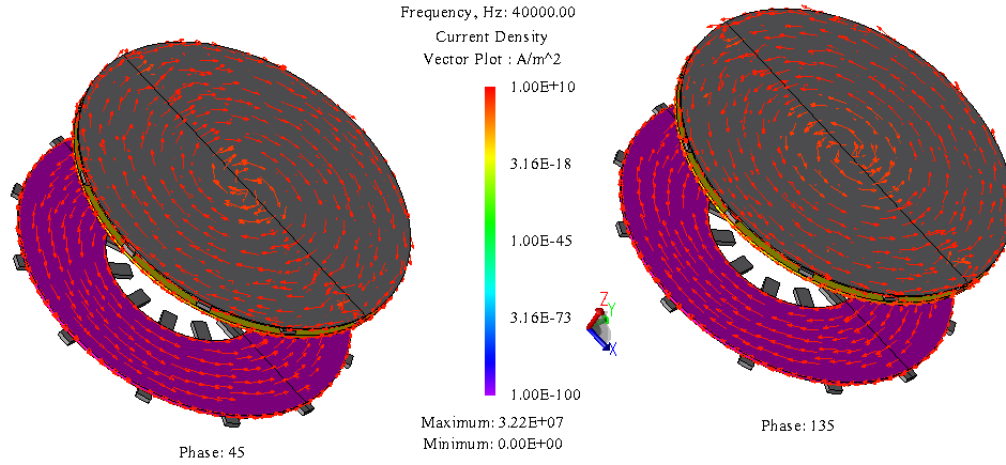
Figure 6.5 current density vector plot in designed pad with shield when supply phase is 45° and 135°.

In Figure 6.5 one can observe that the eddy current direction is opposite to that of the primary current for both the 45° phase (i.e. when the primary current is rising) and 135° phase (i.e. when the primary current is falling).

The addition of an aluminium plate proves to be an effective shield. However, since the flux linkage to the secondary pad is diverted, the value of inductance is changed. In the presence of the shield, the value of the self-inductance of the secondary pad decreases to 51.60 μH as opposed to the original value of 99.30 μH shown in Table 3.6. The value of the self-inductance of the primary pad also falls to 384 μH. Mutual inductance decreases to 15.27 μH. This issue can be solved by adding more ferrites between the coil and the aluminium plate.

6.3 Design of Shielding for Coils

To completely shield the charging pads, more ferrites were required than originally used in the fabricated charging pads. Since the analytical formulation of shielding is not possible, its successful implementation calls for an iterative approach. For this purpose, two variables were adjusted: angle θ between two ferrite spokes and inner diameter D_{in} of the coils as shown in Figure 6.6. The outer diameter, as well as turn spacing, was not

varied. While adjusting the D_{in}, it was ensured that unsymmetrical configuration of coil-pair P-S4 remains intact.
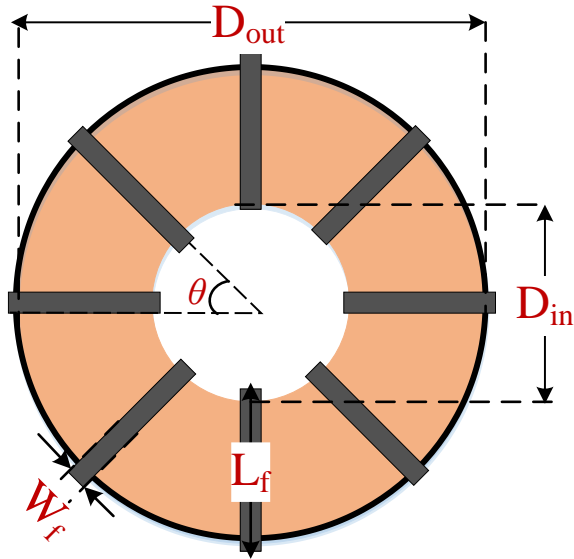
Figure 6.6 Reference figure for designing the shielding

These iterations were performed in JMAG Designer. For all iterations, eddy current loss in aluminium shield as well as the iron loss in ferrites spokes was included. For the 40 kHz operation, considering skin depth, an aluminium sheet of thickness less than 0.3 mm is required. This requires an element size of 0.1 or less to be defined for the aluminum part in the JMAG, for allowing the creation of a fine mesh across its cross-section. This is essential for the accuracy of the analysis. However, the simulation was taking too much time to converge, therefore an aluminium sheet of 1 mm was used instead, and an element size of 0.5 mm was defined for the aluminium part.

Ferrites spokes were modelled based on I core of material PC95 and dimension 55.9X19.3X6.6 mm. Litz wire was modelled as a single solid region, and a uniform current density was applied throughout the cross-section of wire in a software setting. Table 6.1 gives the results of each iteration.

Table 6.1 FEA results of each iteration for nominal air-gap of 16 cm in perfect alignment

Description of Iterations	Parameters with ferrites (μH)	Parameters with ferrite+Aluminum shield (μH)
1. $\theta_P = \theta_S = 30°$, N_P=26, N_S=11 L_{fP} =166.5mm, L_{fS} =55.5mm	L_P=400.6, L_S =99.3, M=41.42	L_P=384.06, L_S =51.60, M=15.27
2. $\theta_P = \theta_S$=15°, N_P=24.2, N_S=10.6 L_{fP} =166.5mm, L_{fS} =55.5mm	L_P=397.8, L_S =100.86, M=42.61	L_P=382.32, L_S =64.45, M=19.74
3. θ_P= 15°, θ_S= 7.5°, N_P=23.6, N_S=10, L_{fP} =166.5mm, L_{fP} =55.5mm	L_P=398.74, L_S =103.09, M=42.49	L_P=383.6, L_S =75.6, M=23.03
4. θ_P= 15°, θ_S= 7.5°, N_P=23.6 N_S=9.5, L_{fP}=166.5mm, L_{fS} =55.5*2mm	L_P=408.97, L_S =115.15, M=49.94	L_P=399.75, L_S =101.89, M=39.51

In Table 6.1, L_{fp} represents the length of the ferrite spoke in the primary pad and L_{fS} represents the length of the ferrite spokes in the secondary pad. θ_P and θ_S represents the angle between the radially placed ferrites in the primary and secondary sides, respectively. Iteration number 4 with shielding gives values matching the original value and therefore is considered for the final design. It will be referred to as 'final charging pad' in this thesis for the sake of distinguishing it with the 'pad used in hardware setup'.

Figure 6.7 shows the final charging pad modeled in JMAG. Figure 6.8 gives the dimension of each part of the final charging pad. (JMAG models for first three iterations are shown in Appendix D. Iteration 1 without aluminium shield was used in the experimental setup).
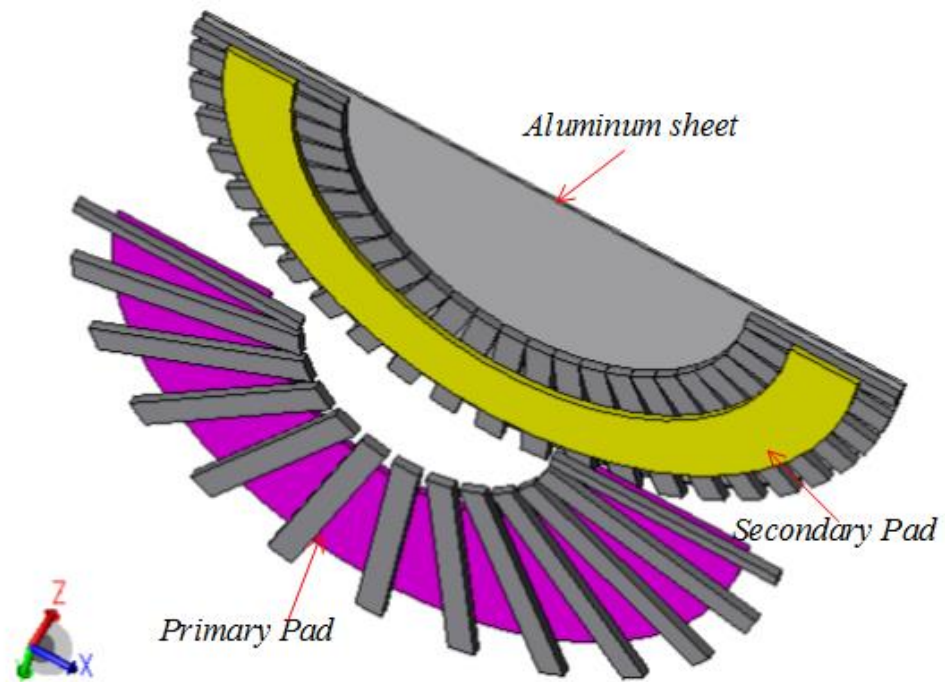
Figure 6.7 3D (1/2) model of final charging pad created in JMAG
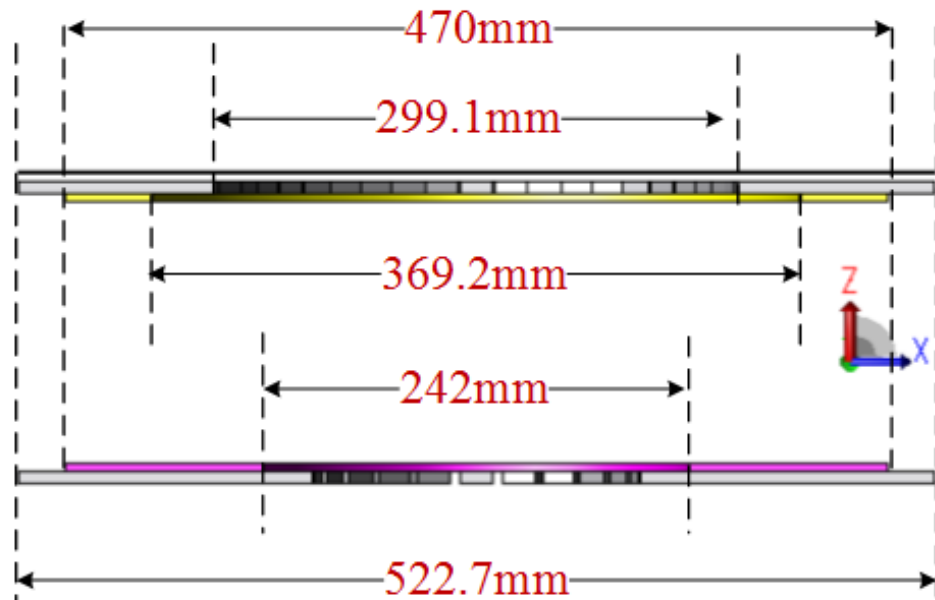
Figure 6.8 Dimensions of final charging pad created in JMAG

6.4 Performance Analysis of Final Charging Pad

(a) **Mutual Coupling Profile**: Figure 6.8 compares the mutual inductance profile of the 'final charging pad' and the 'pad used in experimental setup' for increasing air-gap

under perfect alignment using JMAG analysis. From the plot, one can observe that the final charging pad gives a higher value of mutual inductance at low air-gap. However, its roll-off rate is higher compared to the charging pad used in the experimental setup.
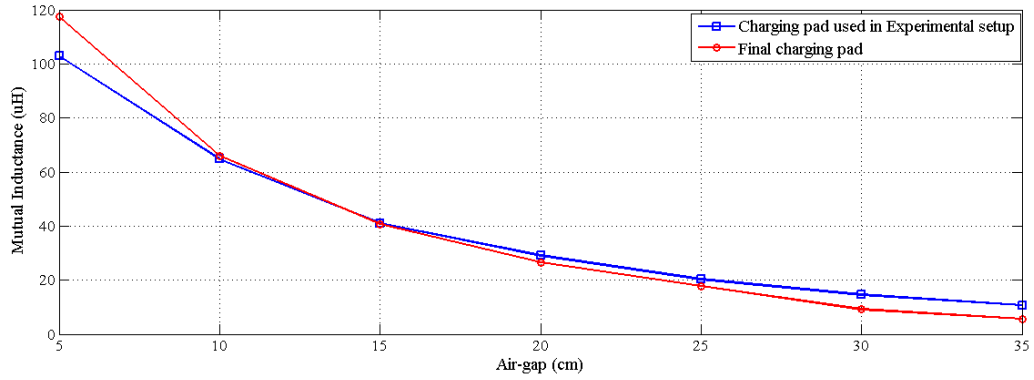
Figure 6.9 Mutual inductance profile for increasing air-gap: comparison of 'final charging pad' with 'pad used in hardware setup'
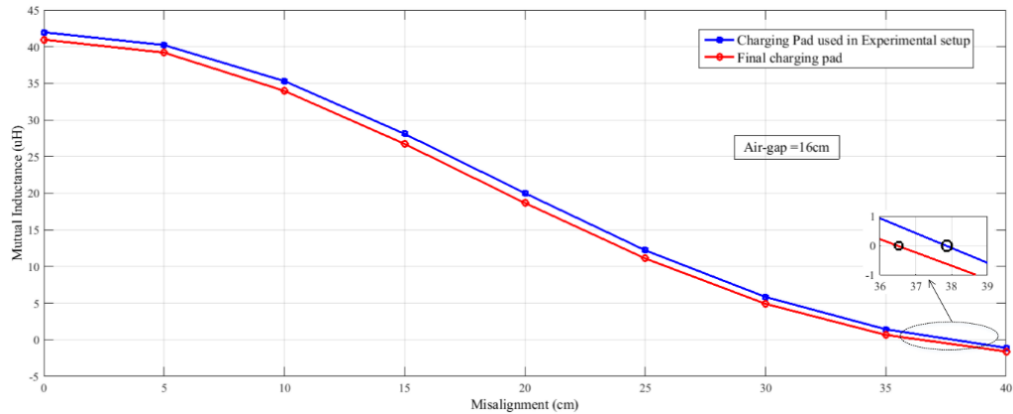
Figure 6.10 Mutual inductance profile for misalignments at 16 cm air-gap: comparison of 'final charging pad' with 'pad used in hardware setup'

Figure 6.10 compares the mutual inductance profile of both pads for a fixed air-gap and varying alignment conditions. From the plot, one can observe that the performance of the final charging pad is only slightly inferior to the pad used in the experiment. Magnetic null still occurs at approximately 37 cm of misalignment, which is 71% of the overall pad diameter.

(b) Loss Estimation: Losses in each part of the final charging pad were calculated using FEA analysis. For this purpose, the magnetic resonance analysis model was

created in JMAG. Supply voltage of 240 V at 40 kHz was applied to the primary side, and the load resistance of 6.31 Ω was kept on the secondary side. Tuning capacitors for 40 kHz resonance were calculated based on the inductance values obtained at 16cm air-gap in JMAG. The eddy current in the ferrites and shield were allowed in the material property settings. The results obtained for each part have been shown in Table 6.2 and compared with the results obtained for the pad used in the experimental setup.

Table 6.2 Loss calculations from JMAG

Parts	Charging pad used in experimental setup	Final charging pad
Primary Coil	25. 67 W	19.21 W
Secondary Coil	31.38 W	25.31 W
Air Region	0.00 W	0.00 W
Primary Core	2.45W	2.16 W
Secondary Core	0.16 W	0.91 W
Aluminium shield	NA	15.27 W
Total	59.66 W	62.86 W

From Table 6.2, one can observe that the difference in losses in both chargers is very low. Copper loss forms the significant percentage of the total loss in both chargers. The loss in the cores is very small due to their high resistivity. In final charging pad, there is 15.27 W of additional loss due to eddy current loss in the aluminium plate. However, since the number of turns is reduced in the final charging pad, copper loss value is low. Therefore, the total loss is approximately the same for both chargers. The total efficiency of the resonant circuit calculated in JMAG is 98.25% for the final charger and 98.47% for the charger used in the experimental setup. From this analysis, the same value of DC-DC efficiency can be expected for the final charging pads.

(C) Safety Regulations: The FEA result for the magnetic field measurements at a distance of 800mm from the center of the final charging pad is shown in Figure 6.11.
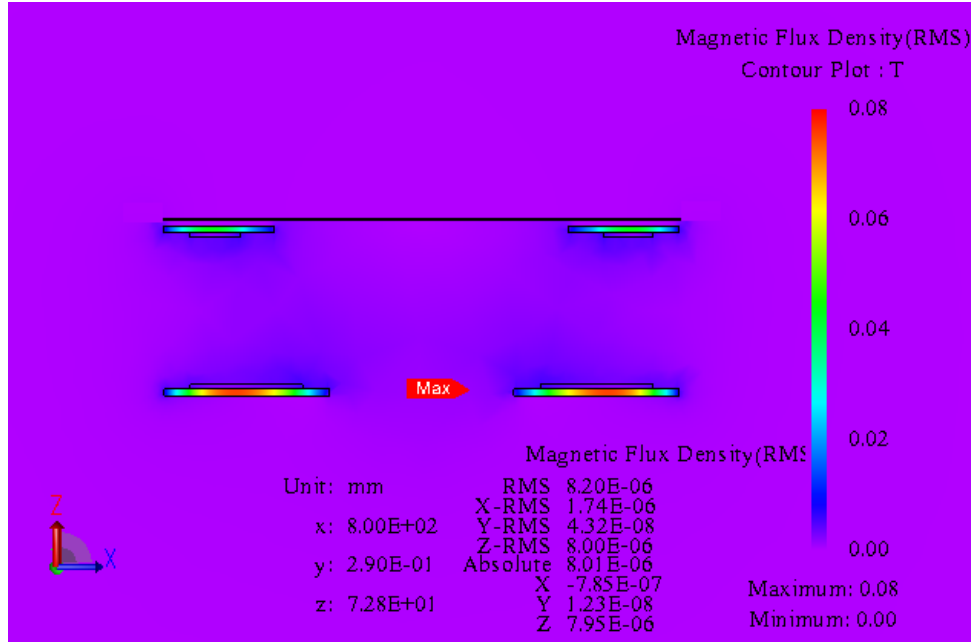
Figure 6.11 Magnetic flux density at distance 800 mm from the center of the coil

From Figure 6.11 one can see that the magnitude of the flux density at coordinates (X=800mm, Y=-0.290mm, Z=72.8mm) is 8.2 µT. This value is within the safety guidelines recommended by ICNIRP 1998, ICNIRP 2010 and IEEE. This value is almost half of the flux density value obtained for the pad used in the experimental setup. Moreover, the maximum flux density has also decreased from 0.12 T to 0.08 T. This is due to an increase in the volume of ferrite cores and a decrease in mmf due to decrease in the number of turns.

6.5 Summary of Chapter 6

In this chapter, the safety considerations associated with wireless chargers have been addressed. Leakage flux density of the designed charger used in experimental setup was measured using JMAG. It was found that leakage flux density in the region outside the vehicle chassis is within the standard defined by IEEE and ICNIRP. Therefore, the designed charger is safe for the general public. However, since an EV chassis is made of steel, it acts as an undesirable load to the charging pads. This, in turn, causes a change in the mutual coupling and self-inductance values of the original pad. Therefore, to tackle this issue, shielding of the charging pad is required.

Using an iterative approach, a final charging pad with shielding has been designed using JMAG. Due to the addition of shielding, the mutual coupling profile for

misalignment conditions is slightly degraded. For the 'final charging pad', the magnetic null was found to occur at a misalignment distance equal to 71% of the pad diameter as compared to the previous value of 78%.

FEA measurements show that the magnetic field strength meets the stringent International Commission on Non-Ionizing Radiation Protection (ICNIRP) guidelines for human safety.

Chapter 7 Comparison with SAE J2954

This chapter compares the work presented in this thesis with the standards recommended by SAE J2954 taskforce. Work covered in this thesis as well work not covered has been documented as per SAE J2954.

7.1 WPT Classification

7.1.1 WPT Power Classes with Efficiency Targets

Wireless power transfer (WPT) classes in TIR SAE J2954 [127] are defined in terms of the maximum input VA to primary side or ground assembly (GA) electronics. Power class WPT1 and WPT2 have been defined to align with the maximum power requirements defined in SAE J1772 for AC Level 1 and Level 2 charging, respectively. Power classes WPT3 and WPT4 have been defined provisionally and are still under development. Table 7.1 shows the power classes that have been defined for WPT and identifies the preliminary efficiency performance targets for the classes.

Table 7.1 WPT power classification for light duty vehicles

	WPT Power Class			
	WPT1	**WPT2**	**WPT3**	**WPT4**
Maximum input VA	3.7 kVA	7.7 kVA	11.1 kVA	22 kVA
Minimum target efficiency	>85%	>85%	>85%	TBD
Minium target efficiency at offset position	>80%	>80%	>80%	TBD

As discussed in Chapter 5, DC-DC efficiency of designed charger is 91% under rated load condition. The efficiency figure does not include the front-end power factor and correction stage, but with recent publications [171], it can be shown that the efficiency

of this stage can reach as high as 98%. Factoring this component, the grid to battery efficiency of 89% is expected from the designed charger. From the experimental results, it was verified that charger efficiency under misalignment remains greater than 80%. Since charger has been designed for 3.6 kW of rated load. Therefore, according to Table 7.1, designed charger can be classified into WPT1 category.

7.1.2 WPT Z Classes

The vertical distance over which power has to be transferred is an important parameters for WPT system specification. For that purpose, three Z-classes are defined to classify the WPT systems.The Z classification is based on the secondary side or vehicle assembly (VA) coil ground clearance and has been mentioned in Table 7.2. The VA coil ground clearance is the vertical distance between the ground surface and the lower surface of the VA coil as shown in Figure 7.1.
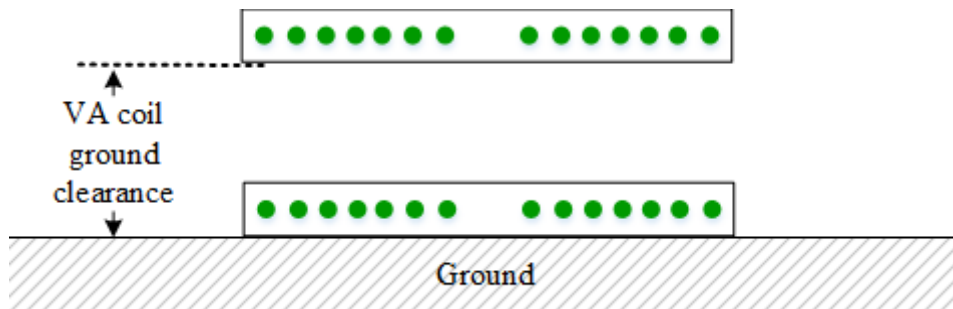
Figure 7.1 Definition of the VA coil ground clearance

Table 7.2 Specification of Z-classes

Z-Class	VA Coil ground clearance range (mm)
Z1	100-150mm
Z2	140-210mm
Z3	170-250mm

Charger presented in this thesis was developed for nominal air-gap of 16 cm. This 16 cm of air-gap was measured between top of primary coil and bottom of secondary coil. Therefore, according to Table 7.2, it can be classified as Z2 class WPT system.

7.2 General System Requirements and Interface

7.2.1 Functional/Physical Requirement

According to SAE J2954, the wireless charging system consists of a utility interface, high-frequency power inverter, coupling coils, rectifier, filter, optional regulator and communication between the battery and the inverter.

Because the focus of this thesis was the development of DC-DC power transfer stage and magnetics design aspects, and the development of communication interface between source and load has the potential of being a separate Ph.D. topic, therefore, has not been covered in this thesis. For the same reason utility interface was not developed and off-the-shelf DC power supply was used for the DC link of the high-frequency inverter.

7.2.2 Frequency Range and Tuning

SAE J2954 TIR specifies a common frequency band using 85 kHz band (81.39 kHz–90 kHz) for all light duty vehicle systems. In this thesis 40 kHz was used since work presented in the thesis was completed before the date of the publication of TIR J2954.

However, work presented in this thesis is scalable to all the frequency range de-fined by SAE J2954. Before the release of TIR J2954, 20 kHz to 200 kHz was a very common frequency of interest in RIPT. For the same power level, if the current work is extended for 85 kHz then according to (2.39) to (2.41) the value of self-inductance and mutual inductance between the coils are expected to be half of the values calculated for 40 kHz. Therefore, overall size of coils will also reduced by almost half.

7.2.3 Nominal Position and Offset

The nominal position in the XY-plane of a VA with respect to an GA is specified by describing the misalignment between the centre of the primary coil and centre of the secondary coil.

Developed charger must operate over a range in X and Y direction to account for expected misalignment in actual use. A complaint GA-VA pair must be able to meet the requirements of this TIR as given in Table 7.3.

Table 7.3 Positioning tolerance requirements for VAs

Offset direction	Value (mm)
ΔX	± 75
ΔY	± 100
ΔZ	$Z_{nom}-\Delta_{low} \rightarrow Z_{nom}-\Delta_{low}$

In this thesis circular coil was used, therefore it has same tolerance in X and Y direction. From experimental results it was found that it is capable of operating within ± 15 cm of misalignment. This value is greater than the minimum requirement imposed by SAE J2954 in Table 7.3. Tolerance was not tested in Z direction and has been left for the future work.

7.3   Interoperability

SAE J2954 allows the coil to be built in any shape. The only restriction is that the coil shape used should allow the flux to exist only on the one side of the assembly by ensuring the appropriate use of ferrites and aluminium backing. To approve the interoperability of GA and VA products, they shall comply with the interoperability performance requirements mentioned in SAE J2954.

Interoperability of designed coil in this theis has not been tested and has been left for the future work.

7.4   EMF Exposure to Human and Implanted Medical Devices

For EMF emissions in the standard operating frequency of band of 81.38 to 90 kHz, the general public reference level are given by Table 7.4.

Table 7.4 EMF exposure standard: reference levels defined by ICNIRP 2010

Quantity	RMS Level	Peak Level
Magnetic Field	27 µT or 21.4 A/m	38.2 µT or 30.4 A/m
Electric Field	83 V/m	117 V/m
Contact current	17 mA @ 85 kHz	24 mA @ 85 kHz

EMF exposure limit was measured using FEA analysis software JMAG. For the charger presented in this thesis, FEA measurements show that the magnetic field strength meets the stringent International Commission on Non-Ionizing Radiation Protection (ICNIRP) guidelines for human safety.

Measurement of electric field induced in human tissue due to external electric or magnetic field is not straightforward and requires human body models to be created in FEA tool. This also requires knowledge of human anatomy and modelling of tissue permittivity. Such kind of research is out of the scope of this thesis and hence has not been covered.

7.5 Safety Testing

According to TIR J2954, the system must be able to determine if there are any object in the close proximity to the system that would cause an unsafe condition at any time during the charging operation and take appropriate action by alerting operation or powering down when needed. Different testing needs to be performed as mentioned in TIR J2954 such as : Object detection, temperature rise testing, ignition testing. This testing requires dedicated lab and development of appropriate communication hardware and software interface. Since the development of communication system was out of the scope of this thesis, therefore this work has been left for the future developments.

Besides this development of alignment system as well as EMI/EMC testing has also been not covered in this thesis but needs to be investigated as per guidelines mentioned in SAE J2954 TIR before using the developed charger for practical implementation.

Chapter 8   Conclusion

8.1   Achieved results

(a) Finding Coil-Pair Least Sensitive to Misalignment: Compared to symmetrical circular coil-pairs, use of unsymmetrical circular coil-pair increases tolerance to horizontal misalignments. Due to its unsymmetrical shape, the position of the magnetic null in the coupling profile shifts with the change in separation between the coils. By operating the primary and secondary pads at distinct separation, a position of null can be shifted further away from the centre of the coils. This, in turn, increases the effective area, over which a given amount of power can be transferred to the load. After investigating several unsymmetrical coil-pairs, it was found that the outer radius of the secondary coil should be kept equal to the outer radius of the primary coil, and inner radius of the secondary coil should be maintained greater than the inner radius of the primary coil to obtain the best coupling profile.

A 3.6 kW charging pad was fabricated based on the proposed unsymmetrical coil-pair. The designed charging pad shows magnetic null in its coupling profile at about 78% of the overall pad diameter. With the addition of shielding this magnetic null was found to occur at 71% of the overall diameter of the charger. This is a significant improvement over the symmetrically shaped circular charging pad presented in the literature in which magnetic null position occurs at about 38-40% of the overall diameter [12], [167]. Due to increased tolerance of circular charging pad, it can now be implemented in dynamic charging application as well.

(b) Development of Bifurcation Free Design Guidelines: A set of novel and easy to follow bifurcation free design guidelines for calculating the electrical parameter of SS-RIPT link has been presented. A SS-RIPT link designed using this analytical approach was found to operate without any bifurcation phenomena for the entire load range and coupling variations. Therefore, sophisticated control strategies are not required for the operation of the charger in varying load and misalignment conditions. To fabricate the coils based on the calculated electrical parameters, accurate and straightforward analytical expressions have been formulated based on wheelers formula. Proposed design guidelines reduces the complexity of the controller and therefore overall cost of the system.

(c) Derivation of a Simplified Small-Signal Model for SS-RIPT System: A simplified mathematical model was derived for designing the voltage and current control loops for the primary side control. A mathematical model is of fifth order as compared to the ninth order model existing in the literature. This model has been derived assuming a reduced dynamic model of the SS-RIPT system suitable for the control of power flow from the primary side. The model was verified using a frequency sweep performed in the PLECS simulation tool. The derived model very accurately predicts the low-frequency behaviour, and therefore was found useful for designing the output voltage and current control loops. Designed control loops were implemented on a lab built 3.6 kW prototype of the SS-RIPT based wireless charger. Both the current control loop and the voltage control loop were found to give optimum performance for different dynamic case studies.

The experimental results are in good agreement with the analysis presented in this thesis. A DC-DC efficiency of 91 % is achieved for the designed charger for rated load conditions. Even at a partial load condition (less than 50% of rated load), the efficiency is 87%. For the experimental setup, shielding was not designed. Therefore, the impact of adding shielding to the efficiency was analysed using FEA analysis in JMAG. The inclusion of aluminium shielding generates eddy current loss in them. However, due to the decrease in the number of turns in shielded charger, the overall efficiency remains almost constant. The efficiency of the SS-RIPT link was measured using JMAG and is found to be 98.47% for the unshielded design and 98.25% for the shielded design. Therefore, the final charger with shielding is expected to give the same value of DC-DC efficiency under the same experimental setup conditions. Moreover, all the experiments were performed in a non-ideal environment. The table used for equipments, such as CRO and DC load, was made of steel and therefore acts as an undesirable load to the unshielded charger which was kept in the proximity to the measuring equipment due to limited lab space. Since the equipments themself contains metal, they acts as a passive load to the leakage flux. For the completely shielded charger, DC-DC efficiency is expected to be slightly better.

The efficiency figure does not include the front-end power factor and correction stage, but with recent publications [171], it can be shown that the efficiency of this stage

can reach as high as 98%. Factoring this component, the grid to battery efficiency of 89% is expected from the designed charger.

Further, under the ICNIRP 2000 and IEEE Std. C95.1-2005 guideline, the safety evaluation for the designed 3.6 kW SS-RIPT based charger was conducted in JMAG. The average magnetic flux density at 0.8 m from the center of the pad is 14.5 μT. This value is within the safety guidelines recommended by both ICNIRP 2010 as well as the IEEE.

8.2   Future Developments

For making the system more useful for practical implementation, the following improvements are suggested:

1. For the successful integration of the charger into the vehicle, shielding of the secondary pad is required. For this purpose, the final charging pad presented in Chapter 6 should be implemented for hardware testing to examine its usefulness in practical situations.

2. Asymmetric coil-pairs increases the tolerance to misalignment. However, no systematic relationship between different dimensions of the asymmetric coils has been presented in this thesis. It would be very helpful for a designer, if a generally applicable rule of null point as function of coil dimension could be developed for the coil-pair P-S_4.

3. As observed from the experimental results, the efficiency decreases with increasing misalignment. Therefore, for efficient charging of EVs, it is necessary to park the secondary pad in close alignment with the primary pad. This requires the development of a coil positioning system to assist drivers in parking the car over the primary pad.

4. For the hardware setup, BNC cable was used to transfer the sensed voltage and current to the DSP module. However, for practical implementation, development of an infrared communication (as it is fast and immune to the electromagnetic interference) and associated signal conditioning would be required for sending the information from the load side to the primary side.

5. Bidirectional power transfer can be investigated by replacing the rectifier on the load side with the active rectifiers to increase the overall efficiency of the system. More importantly, it allows for the scope of dual side control, therefore can provide more controlling options.

References

[1] L. Chen, G. R. Nagendra, J. T. Boys and G. A. Covic, "Double-Coupled Systems for IPT Roadway Applications," *IEEE Journal of Emerging and Selected Topics in Power Electronics*, vol. 3, no. 1, pp. 37-49, March 2015.

[2] J. G. Hayes, M. G. Egan, J. M. D. Murphy, S. E. Schulz and J. T. Hall, "Wide-load-range resonant converter supplying the SAE J-1773 electric vehicle inductive charging interface," *IEEE Trans. on Industry Applications*, vol. 35, no. 4, pp. 884-895, Jul/Aug 1999.

[3] G. A. Covic, J. T. Boys, M. L. G. Kissin and H. G. Lu, "A Three-Phase Inductive Power Transfer System for Roadway-Powered Vehicles," *IEEE Trans. on Industrial Electronics*, vol. 54, no. 6, pp. 3370-3378, Dec. 2007.

[4] U. K. Madawala and D. J. Thrimawithana, "A Bidirectional Inductive Power Interface for Electric Vehicles in V2G Systems," *IEEE Trans. on Industrial Electronics*, vol. 58, no. 10, pp. 4789-4796, Oct. 2011.

[5] K. Yan, Q. Chen, J. Hou, X. Ren and X. Ruan, "Self-Oscillating Contactless Resonant Converter With Phase Detection Contactless Current Transformer," in *IEEE Trans. on Power Electronics*, vol. 29, no. 8, pp. 4438-4449, Aug. 2014.

[6] M. G. L. Roes, J. L. Duarte, M. A. M. Hendrix and E. A. Lomonova, "Acoustic Energy Transfer: A Review," *IEEE Trans. on Industrial Electronics*, vol. 60, no. 1, pp. 242-248, Jan. 2013.

[7] Y. Hu, X. Zhang, J. Yang and Q. Jiang, "Transmitting electric energy through a metal wall by acoustic waves using piezoelectric transducers," *IEEE Trans. on Ultrasonics, Ferroelectrics, and Frequency Control*, vol. 50, no. 7, pp. 773-781, July 2003.

[8] A. Sahai and D. Graham, "Optical wireless power transmission at long wavelengths," in *Proc. International Conference on Space Optical Systems and Applications*, Santa Monica, CA, 2011, pp. 164-170.

[9] S. Sasaki, K. Tanaka and K. i. Maki, "Microwave Power Transmission

Technologies for Solar Power Satellites," in *Proc. of the IEEE*, vol. 101, no. 6, pp. 1438-1447, June 2013.

[10] L. Summerer and O. Purcell, "Concepts for Wireless Energy Transmission via Laser," 2008.

[11] J. Dai and D. C. Ludois, "A Survey of Wireless Power Transfer and a Critical Comparison of Inductive and Capacitive Coupling for Small Gap Applications," *IEEE Transactions on Power Electronics*, vol. 30, no. 11, pp. 6017-6029, Nov. 2015.

[12] G. a. Covic and J. T. Boys, "Inductive Power Transfer," *Proc. IEEE*, vol. 101, no. 6, pp. 1276–1289, 2013.

[13] J. Huh, W. Lee, G. H. Cho, B. Lee and C. T. Rim, "Characterization of novel Inductive Power Transfer Systems for On-Line Electric Vehicles," in *Proc. IEEE Applied Power Electronics Conference and Exposition (APEC),* Fort Worth, TX, 2011, pp. 1975-1979.

[14] H. H. Wu, A. Gilchrist, K. Sealy, P. Israelsen, and J. Muhs, "A review on inductive charging for electric vehicles," in *Proc. IEEE International Electric Machines and Drives Conference,* 2011, pp. 143–147.

[15] Y. Kondo, H. Kato, R. Ando, T. Suzuki and Y. Karakama, "To what extent can speed management alleviate the range anxiety of EV?," in *Proc. IEEE Electric Vehicle Symposium and Exhibition (EVS27), 2013 World*, Barcelona, 2013, pp. 1-8.

[16] S. M. Lukic, M. Saunders, Z. Pantic, S. Hung and J. Taiber, "Use of inductive power transfer for electric vehicles," in *Proc. IEEE PES General Meeting*, Minneapolis, MN, 2010, pp. 1-6.

[17] S. A. Birrell, D. Wilson, C. P. Yang, G. Dhadyalla, and P. Jennings, "How driver behaviour and parking alignment affects inductive charging systems for electric vehicles," *Transportation Research Part C Emerging Technololgy*, vol. 58, no. PD, pp. 721–731, 2015.

[18] T. M. Fisher, K. B. Farley, Y. Gao, H. Bai, and Z. T. H. Tse, "Electric vehicle

wireless charging technology: a state-of-the-art review of magnetic coupling systems," in *Wireless Power Transfer*, vol. 1, no. 2014, pp. 87–96, 2014.

[19] A. Khaligh and S. Dusmez, "Comprehensive Topological Analysis of Conductive and Inductive Charging Solutions for Plug-In Electric Vehicles," *IEEE Trans. on Vehicular Technology*, vol. 61, no. 8, pp. 3475-3489, Oct. 2012.

[20] S. Li and C. C. Mi, "Wireless Power Transfer for Electric Vehicle Applications," *IEEE Journal of Emerging and Selected Topics in Power Electronics*, vol. 3, no. 1, pp. 4-17, March 2015.

[21] N. Tesla, "High frequency oscillators for electro-therapeutic and other purposes," in *Proc. IEEE*, vol. 87, no. 7, pp. 1282–1292, 1999.

[22] S. Y. R. Hui, "Magnetic Resonance for Wireless Power Transfer [A Look Back]," *IEEE Power Electronics Magazine*, vol. 3, no. 1, pp. 14-31, March 2016.

[23] Patent US527857-Hutin-google patents [online] available at http://www.google.com/patents/US527857.

[24] PATH team, "Roadway powered electric vehicle project parametric studies: phase 3D final report," *California partner for advanced transit and highway research report*, Oct 1996.

[25] A. W. Kelly and W. R. Owens, ''Connector less power supply for an air-craft passenger entertainment system,'' *IEEE Trans. on Power Electron.*, vol. 4, no. 3, pp. 384–354, Jul. 1989.

[26] J. T. Boys, G. A. Covic and A. W. Green, "Stability and control of inductively coupled power transfer systems," in *IEE Proceedings - Electric Power Applications*, vol. 147, no. 1, pp. 37-43, Jan 2000.

[27] A. W. Green and J. T. Boys, "10 kHz inductively coupled power transfer-concept and control," in *Proc. IEEE International Conference on,Power Electronics and Variable-Speed Drives,* London, 1994, pp. 694-699.

[28] M. Budhia, J. T. Boys, G. A. Covic and C. Y. Huang, "Development of a Single-Sided Flux Magnetic Coupler for Electric Vehicle IPT Charging Systems,"

in *IEEE Transactions on Industrial Electronics*, vol. 60, no. 1, pp. 318-328, Jan. 2013.

[29] M. Kesler, "Highly Resonant Wireless Power Transfer: Safe, Efficient, and over Distance," *WiTricity Corp*, 2013.

[30] H. Nguyen and J. I. Agbinya, "Splitting Frequency Diversity in Wireless Power Transmission," in *IEEE Transactions on Power Electronics*, vol. 30, no. 11, pp. 6088-6096, Nov. 2015.

[31] S. Lee, J. Huh, C. Park, N. S. Choi, G. H. Cho and C. T. Rim, "On-Line Electric Vehicle using inductive power transfer system," *in Proc. IEEE Energy Conversion Congress and Exposition*, Atlanta, GA, 2010, pp. 1598-1601.

[32] D. K. Cheng, "Field and Wave Electromagnetics," *IEEE Antennas and Propagation Society Newsletter*, vol. 28, no. 2. pp. 27–28, 1986.

[33] A. Zaheer, M. Budhia, D. Kacprzak and G. A. Covic, "Magnetic design of a 300 W under-floor contactless Power Transfer system," in *Proc. Annual Conference on IEEE Industrial Electronics Society*, Melbourne, VIC, 2011, pp. 1408-1413.

[34] H. H. Wu, A. Gilchrist, K. D. Sealy, and D. Bronson, "A high efficiency 5 kW inductive charger for EVs using dual side control," *IEEE Trans. Ind. Informatics*, vol. 8, no. 3, pp. 585–595, 2012.

[35] S. Lukic and Z. Pantic, "Cutting the Cord: Static and Dynamic Inductive Wireless Charging of Electric Vehicles," in *IEEE Electrification Magazine*, vol. 1, no. 1, pp. 57-64, Sept. 2013.

[36] W. Chwei-Sen, O. H. Stielau, and G. A. Covic, "Design considerations for a contactless electric vehicle battery charger," *IEEE Trans. on. Industrial Electronics*, vol. 52, no. 5, pp. 1308–1314, 2005.

[37] T. Diekhans, F. Stewing, G. Engelmann, H. van Hoek and R. W. De Doncker, "A systematic comparison of hard- and soft-switching topologies for inductive power transfer systems," in *Proc. IEEE Electric Drives Production Conference, 2014 4th International*, Nuremberg, 2014, pp. 1-8.

[38] X. Qu, S. C. Wong, C. K. Tse and G. Zhang, "Design consideration of a current-source-output inductive power transfer LED lighting system," *in Proc. IEEE Energy Conversion Congress and Exposition*, Pittsburgh, PA, 2014, pp. 3607-3611.

[39] G. A. Covic and J. T. Boys, "Modern Trends in Inductive Power Transfer for Transportation Applications," *IEEE Journal of Emerging and Selected Topics in Power Electronics*, vol. 1, no. 1, pp. 28-41, March 2013.

[40] Y. H. Sohn, B. H. Choi, E. S. Lee, G. C. Lim, G. H. Cho, and C. T. Rim, "General Unified Analyses of Two-Capacitor Inductive Power Transfer Systems: Equivalence of Current-Source SS and SP Compensations," *IEEE Trans. on Power Electronics*, vol. 30, no. 11, pp. 6030–6045, 2015.

[41] A. J. Moradewicz and M. P. Kazmierkowski, "Contactless energy transfer system with FPGA-controlled resonant converter," *IEEE Trans. on Industrial Electronics*, vol. 57, no. 9, pp. 3181–3190, 2010.

[42] B. Esteban, M. Sid-Ahmed, and N. C. Kar, "A Comparative Study of Power Supply Architectures in Wireless EV Charging Systems," *IEEE Trans. on Power Electronics*, vol. 30, no. 11, pp. 6408–6422, 2015.

[43] R. Bosshard, J. Mühlethaler, J. W. Kolar and I. Stevanović, "The η-α-Pareto front of inductive power transfer coils," in *Proc. Annual Conference on IEEE Industrial Electronics Society*, Montreal, QC, 2012, pp. 4270-4277.

[44] K. Aditya and S. S. Williamson, "Design considerations for loosely coupled inductive power transfer (IPT) system for electric vehicle battery charging - A comprehensive review," in *Proc. IEEE Transportation Electrification Conference and Expo,* Dearborn, MI, 2014, pp. 1-6.

[45] M. Bertoluzzo, M. K. Naik and G. Buja, "Preliminary investigation on contactless energy transfer for electric vehicle battery recharging," *in Proc. IEEE 7th International Conference on Industrial and Information Systems,* Chennai, 2012, pp. 1-6.

[46] S. International, "SAE Electric Vehicle and Plug in hybrid electric vehicle

Conductive Charge Coupler," *SAE J1772 Stand.*, 2001.

[47]   R. Chen *et al*., "Analysis and parameters optimization of a contactless IPT system for EV charger," in *Proc. IEEE Applied Power Electronics Conference and Exposition,* Fort Worth, TX, 2014, pp. 1654-1661.

[48]   Y. H. Chao and J. J. Shieh, "Series-parallel loosely coupled battery charger with primary-side control," in *Proc. International Conference on Control, Automation and Information Sciences,* Ho Chi Minh City, 2012, pp. 226-230.

[49]   E. Gati; G. Kampitsis; S. Manias, "Variable Frequency Controller for Inductive Power Transfer in Dynamic Conditions," in *IEEE Transactions on Power Electronics* , vol.PP, no.99, pp.1-1.

[50]   E. Gati, G. Kampitsis, I. Stavropoulos, S. Papathanassiou and S. Manias, "Wireless Phase - Locked Loop control for inductive Power Transfer Systems," *in Proc. IEEE Applied Power Electronics Conference and Exposition*, Charlotte, NC, 2015, pp. 1601-1607.

[51]   C. G. Kim, D. H. Seo, J. S. You, J. H. Park, and B. H. Cho, "Design of a contactless battery charger for cellular phone," *IEEE Trans. on Industrial Electronics*, vol. 48, no. 6, pp. 1238–1247, 2001.

[52]   D. A. G. Pedder, A. D. Brown, and J. A. Skinner, "A contactless electrical energy transmission system," *IEEE Trans. on Industrial Electronics,* vol. 46, no. 1, pp. 23–30, 1999.

[53]   R. Laouamer, M. Brunello, J. P. Ferrieux, O. Normand, and N. Buchheit, "A multi-resonant converter for non-contact charging with electromagnetic coupling," in *Proc. IEEE International Conference on Industrial Electronics, Control, and Instrumentation (Cat. No.97CH36066)*, 1997, vol. 2, pp. 792–797.

[54]   S. Valtchev, B. Borges, K. Brandisky, and J. Ben Klaassens, "Resonant contactless energy transfer with improved efficiency," *IEEE Trans. on Power Electronics*, vol. 24, no. 3, pp. 685–699, 2009.

[55]   H. Sakamoto, K. Harada, S. Washimiya, K. Takehara, Y. Matsuo, and F. Nakao, "Large air-gap coupler for inductive charger," *IEEE Trans. on Magnetics*, vol.

35, no. 5 PART 2, pp. 3526–3528, 1999.

[56] J. Hirai, T.-W. Kim, and a Kawamura, "Study on intelligent battery charging using inductive transmission of power and information," *IEEE Trans on Power Electronics*, vol. 15, no. 2, pp. 335–345, 2000.

[57] M. Budhia, G. A. Covic, and J. T. Boys, "Design and optimization of circular magnetic structures for lumped inductive power transfer systems," *IEEE Trans. on Power Electronics*, vol. 26, no. 11, pp. 3096–3108, 2011.

[58] M. Budhia, G. Covic and J. Boys, "A new IPT magnetic coupler for electric vehicle charging systems," *in Proc. Annual Conference on IEEE Industrial Electronics Society*, Glendale, AZ, 2010, pp. 2487-2492.

[59] A. Zaheer, H. Hao, G. A. Covic, and D. Kacprzak, "Investigation of multiple decoupled coil primary pad topologies in lumped IPT systems for interoperable electric vehicle charging," *IEEE Trans. on Power Electronics*, vol. 30, no. 4, pp. 1937–1955, 2015.

[60] T. Fujita, T. Yasuda, and H. Akagi, "A moving wireless power transfer system applicable to a stationary system," in *Proc. IEEE Energy Conversion Congress and Exposition,* Montreal, 2015, pp. 4943–4950.

[61] J. T. Boys and G. A. Covic, "Inductive power transfer systems (IPT) fact sheet: no. 1 – basic concepts," *http://www.qualcomm.com/media/documents/*.

[62] J. T. Boys and G. A. Covic, "Inductive power transfer systems (IPT) fact sheet: no. 2 – Magnetic circuits for powering electric vehicles," *http://www.qualcomm.com/media/documents/ipt-fact-sheet*.

[63] N. Liu and T. G. Habetler, "Design of a Universal Inductive Charger for Multiple Electric Vehicle Models," *IEEE Trans. on Power Electronics*, vol. 30, no. 11, pp. 6378–6390, 2015.

[64] W. Ni, I. B. Collings, X. Wang, R. P. Liu, A. Kajan, M. Hedley, and M. Abolhasan, "Radio alignment for inductive charging of electric vehicles," *IEEE Trans. on Industrial Informatics*, vol. 11, no. 2, pp. 427–440, 2015.

[65]   B. Esteban, N. Stojakovic, M. Sid-Ahmed, and N. C. Kar, "Development of mutual inductance formula for misaligned planar circular spiral coils," in *Proc. IEEE Energy Conversion Congress and Exposition*, pp. 1306–1313, 2015.

[66]   O. H. Stielau and G. A. Covic, "Design of loosely coupled inductive power transfer systems," in *Proc. IEEE International Conference on Power System Technology,* Perth, WA, 2000, pp. 85-90.

[67]   Byung-Song Lee and Kyung-Hee Han, "Modeling and analysis of IPT system used for PRT," *in Proc. International Conference on Electrical Machines and Systems*, 2005, pp. 839-842.

[68]   J. Sallan, J. L. Villa, a. Llombart, and J. F. Sanz, "Optimal Design of ICPT Systems Applied to Electric Vehicle Battery Charge," *IEEE Trans.on Industrial Electronics*, vol. 56, no. 6, pp. 2140–2149, 2009.

[69]   K. Aditya and S. S. Williamson, "Comparative study of Series-Series and Series-Parallel compensation topologies for electric vehicle charging," *in Proc. IEEE International Symposium on Industrial Electronics,* Istanbul, 2014, pp. 426-430.

[70]   C. Zheng *et al.*, "High-Efficiency Contactless Power Transfer System for Electric Vehicle Battery Charging Application," *IEEE Journal of Emerging and Selected Topics in Power Electronics*, vol. 3, no. 1, pp. 65-74, March 2015.

[71]   C.-S. Wang, G. A. Covic, and O. H. Stielau, "Power transfer capability and bifurcation phenomena of loosely coupled inductive power transfer systems," *IEEE Trans. on Industrial Electronics*, vol. 51, no. 1, pp. 148–157, 2004.

[72]   C. Zheng, R. Chen and J. S. Lai, "Design considerations to reduce gap variation and misalignment effects for inductive power transfer system," in *Proc. Annual Conference of the IEEE Industrial Electronics Society*, Dallas, TX, 2014, pp. 1384-1390.

[73]   Chwei-Sen Wang, O. H. Stielau and G. A. Covic, "Load models and their application in the design of loosely coupled inductive power transfer systems," in *Proc. IEEE International Conference on Power System Technology,* Perth, WA, 2000, pp. 1053-1058 vol.2.

[74] M. Ibrahim, L. Pichon, L. Bernard, A. Razek, J. Houivet and O. Cayol, "Advanced Modeling of a 2-kW Series–Series Resonating Inductive Charger for Real Electric Vehicle," in *IEEE Transactions on Vehicular Technology*, vol. 64, no. 2, pp. 421-430, Feb. 2015.

[75] W. Zhang, S. C. Wong, C. K. Tse and Q. Chen, "Design for Efficiency Optimization and Voltage Controllability of Series–Series Compensated Inductive Power Transfer Systems," in *IEEE Trans. on Power Electronics*, vol. 29, no. 1, pp. 191-200, Jan. 2014.

[76] A. Esser, H.-C. Skudelny, H. C. Skundenly, and H.-C. Skudelny, "A New Approach to Power Supplies for Robots," *IEEE Trans. on Industry Applications.*, vol. 27, no. 5, pp. 872–875, 1991.

[77] R. C. Fernandes and A. A. de Oliveira, "Theoretical bifurcation boundaries for Wireless Power Transfer converters," *in Proc. IEEE Brazilian Power Electronics Conference and 1st Southern Power Electronics Conference*, Fortaleza, 2015, pp. 1-4.

[78] Chwei-Sen Wang, G. A. Covic and O. H. Stielau, "General stability criterions for zero phase angle controlled loosely coupled inductive power transfer systems," in *Proc. Annual Conference of the IEEE Industrial Electronics Society,* Denver, CO, 2001, pp. 1049-1054 vol.2.

[79] S. Chopra and P. Bauer, "Analysis and design considerations for a contactless power transfer system," in *2011 IEEE 33rd International Telecommunications Energy Conference (INTELEC)*, 2011, pp. 1–6.

[80] R. L. Steigerwald, "A comparison of half-bridge resonant converter topologies," in *IEEE Transactions on Power Electronics*, vol. 3, no. 2, pp. 174-182, Apr 1988.

[81] G. B. Joung and B. H. Cho, "An energy transmission system for an artificial heart using leakage inductance compensation of transcutaneous transformer," *IEEE Trans. on Power Electronics*, vol. 13, no. 6, pp. 1013–1022, 1998.

[82] V. Vorperian, "Simplified analysis of PWM converters using model of PWM switch. Continuous conduction mode," in *IEEE Trans. on Aerospace and*

Electronic Systems, vol. 26, no. 3, pp. 490-496, May 1990.

[83] L. Boylestad, Robert, Introducción al análisis de circuitos. *México : Prentice-Hall, 2011*.

[84] E. Waffenschmidt and T. Staring, "Limitation of inductive power transfer for consumer applications," in *Proc. European Conference on Power Electronics and Applications,* Barcelona, 2009, pp. 1-10..

[85] N. A. Keeling, G. A. Covic, and J. T. Boys, "A unity-power-factor IPT pickup for high-power applications," in *IEEE Transactions on Industrial Electronics*, 2010, vol. 57, no. 2, pp. 744–751.

[86] D. G. Galbraith, M. Soma, and R. L. White, "A Wide-Band Efficient Inductive Transdermal Power and Data Link with Coupling Insensitive Gain," *IEEE Trans. Biomedical Engineering*, vol. BME-34, no. 4, pp. 265–275, 1987.

[87] C. Fernandez, O. Garcia, R. Prieto, J. A. Cobos and J. Uceda, "Overview of different alternatives for the contact-less transmission of energy," in *Proc. IEEE Annual Conference of the Industrial Electronics Society,* 2002, pp. 1318-1323 vol.2.

[88] Y. H. Chao, J. J. Shieh, C. T. Pan, W. C. Shen and M. P. Chen, "A Primary-Side Control Strategy for Series-Parallel Loosely Coupled Inductive Power Transfer Systems," in *Proc. IEEE Conference on Industrial Electronics and Applications*, Harbin, 2007, pp. 2322-2327..

[89] Y. H. Chao, J. J. Shieh, C. T. Pan and W. C. Shen, "A Closed-form Oriented Compensator Analysis for Series-parallel Loosely Coupled Inductive Power Transfer Systems," *in Proc. IEEE Power Electronics Specialists Conference*, Orlando, FL, 2007, pp. 1215-1220.

[90] M. W. Baker and R. Sarpeshkar, "Feedback analysis and design of RF power links for low-power bionic systems," *IEEE Trans. Biomedical Circuits Systems*, vol. 1, no. 1, pp. 28–38, 2007.

[91] H. L. Li, A. P. Hu, G. A. Covic and C. S. Tang, "Optimal coupling condition of IPT system for achieving maximum power transfer," in *Electronics Letters*, vol.

45, no. 1, pp. 76-77, January 1 2009.

[92] R. Bosshard, J. W. Kolar and B. Wunsch, "Control method for Inductive Power Transfer with high partial-load efficiency and resonance tracking," in *Proc. International Power Electronics Conference*, Hiroshima, 2014, pp. 2167-2174.

[93] R. Bosshard, U. Badstübner, J. W. Kolar and I. Stevanović, "Comparative evaluation of control methods for Inductive Power Transfer," in *Proc. International Conference on Renewable Energy Research and Applications*, Nagasaki, 2012, pp. 1-6.

[94] H. A. Wheeler, "Simple Inductance Formulas for Radio Coils," in *Proceedings of the Institute of Radio Engineers*, vol. 16, no. 10, pp. 1398-1400, Oct. 1928.

[95] H. A. Wheeler, "Inductance formulas for circular and square coils," in *Proceedings of the IEEE*, vol. 70, no. 12, pp. 1449-1450, Dec. 1982.

[96] S. S. Mohan, M. del Mar Hershenson, S. P. Boyd and T. H. Lee, "Simple accurate expressions for planar spiral inductances," in *IEEE Journal of Solid-State Circuits*, vol. 34, no. 10, pp. 1419-1424, Oct 1999.

[97] Bryan Esteban, "Development of Mutual Inductance Formula for Misaligned Planar Circular Spiral Coils," M.Sc. Thesis, University of Windsor, Canada, 2014.

[98] C. L. W. Sonntag, E. A. Lomonova and J. L. Duarte, "Implementation of the Neumann formula for calculating the mutual inductance between planar PCB inductors," in *IEEE International Conference on Electrical Machines,* Vilamoura, 2008, pp. 1-6.

[99] K. Fotopoulou and B. W. Flynn, "Wireless power transfer in loosely coupled links: Coil misalignment model," *IEEE Trans. on Magnetics*, vol. 47, no. 2 PART 2, pp. 416–430, 2011.

[100] P. E. K. Donaldson, "Frequency-hopping in R. F. energy-transfer links," *Electron. Wirel. World,* pp. 24–26.

[101] Q. C. Q. Chen, S. C. W. S. C. Wong, C. K. Tse, and X. R. X. Ruan, "Analysis,

design and control of a transcutaneous power regulator for artificial heart," in *Proc. IEEE Power Electron. Spec. Conf.*, vol. 3, no. 1, pp. 23–31, 2008.

[102] C. M. Zierhofer and E. S. Hochmair, "High-efficiency coupling-insensitive transcutaneous power and data transmission via an inductive link," in *IEEE Trans. on Biomedical Engineering*, vol. 37, no. 7, pp. 716-722, July 1990.

[103] B. L. Cannon, J. F. Hoburg, D. D. Stancil, and S. C. Goldstein, "Magnetic Resonant Coupling As a Potential Means for Wireless Power Transfer to Multiple Small Receivers," *IEEE Trans. on Power Electron.*, vol. 24, no. 7, pp. 1819-1825, 2009.

[104] T. Imura and Y. Hori, "Maximizing air gap and efficiency of magnetic resonant coupling for wireless power transfer using equivalent circuit and Neumann formula," *IEEE Trans. on Industrial Electronics*, vol. 58, no. 10, pp. 4746-4752, 2011.

[105] S. Cheon, Y. H. Kim, S. Y. Kang, M. L. Lee, J. M. Lee, and T. Zyung, "Circuit-model-based analysis of a wireless energy-transfer system via coupled magnetic resonances," *IEEE Trans. on Industrial Electronics*, vol. 58, no. 7, pp. 2906-2914, 2011.

[106] W. Q. Niu, J. X. Chu, W. Gu and A. D. Shen, "Exact Analysis of Frequency Splitting Phenomena of Contactless Power Transfer Systems," in *IEEE Trans. on Circuits and Systems I: Regular Papers*, vol. 60, no. 6, pp. 1670-1677, June 2013.

[107] S. C. Tang, S. Y. Hui, and H. S. H. Chung, "Characterization of coreless printed circuit board (PCB) transformers," *IEEE Trans. on Power Electronics*, vol. 15, no. 6, pp. 1275–1282, 2000.

[108] S. C. Tang, S. Y. Hui, and H. S. H. Chung, "A low-profile low-power converter with coreless PCB isolation transformer," *IEEE Trans. on Power Electronics*, vol. 16, no. 3, pp. 311–316, 2001.

[109] U. M. Jow and M. Ghovanloo, "Design and optimization of printed spiral coils for efficient inductive power transmission," in *Proc. IEEE International*

Conference on Electronics, Circuits, and Systems, 2007, pp. 70–73.

[110] U. M. Jow and M. Ghovanloo, "Optimization of Data Coils in a Multiband Wireless Link for Neuroprosthetic Implantable Devices," in *IEEE Trans. on Biomedical Circuits and Systems*, vol. 4, no. 5, pp. 301-310, Oct. 2010.

[111] U. M. Jow and M. Ghovanloo, "Modeling and Optimization of Printed Spiral Coils in Air, Saline, and Muscle Tissue Environments," in *IEEE Trans. on Biomedical Circuits and Systems*, vol. 3, no. 5, pp. 339-347, Oct. 2009.

[112] M. W. Coffey, "Mutual inductance of superconducting thin films," *Jornal of Applied Physics*, vol. 89, no. 10, pp. 5570–5577, 2001.

[113] A. E. Ruehli, G. Antonini and L. Jiang, "Skin-effect model for round wires in PEEC," in *Proc. IEEE International Symposium on Electromagnetic Compatibility,* Rome, 2012, pp. 1-6..

[114] P. Meyer and Y. Perriard, "Skin and proximity effects for coreless transformers," in *Proc. IEEE International Conference on Electrical Machines and Systems*, Beijing, 2011, pp. 1-5.

[115] M. Bartoli, A. Reatti and M. K. Kazimierczuk, "High-frequency models of ferrite core inductors," in *Proc. IEEE International Conference on Industrial Electronics, Control and Instrumentation,* Bologna, 1994, pp. 1670-1675 vol.3.

[116] S. Mei and Y. I. Ismail, "Modeling skin and proximity effects with reduced realizable RL circuits," in *IEEE Transactions on Very Large Scale Integration (VLSI) Systems*, 2004, vol. 12, no. 4, pp. 437–447.

[117] J. Mühlethaler, J. W. Kolar and A. Ecklebe, "Loss modeling of inductive components employed in power electronic systems," in *Proc. IEEE 8th International Conference on Power Electronics and ECCE Asia,* Jeju, 2011, pp. 945-952.

[118] R. Bosshard, J. W. Kolar, J. Mühlethaler, I. Stevanović, B. Wunsch, and F. Canales, "Modeling and η - α-pareto optimization of inductive power transfer coils for electric vehicles," *IEEE Journal of Emerging and Selected Topics in Power Electronics, vol. 3, no. 1, pp. 50-64, March 2015.*.

[119] C. R. Sullivan, "Optimal choice for number of strands in a litz-wire transformer winding," *IEEE Trans. on Power Electronics*, vol. 14, no. 2, pp. 283–291, 1999.

[120] J. M. Miller and A. Daga, "Elements of Wireless Power Transfer Essential to High Power Charging of Heavy Duty Vehicles," *IEEE Trans. on Transportation Electrifications*, vol. 1, no. 1, pp. 26–39.

[121] M. Hediehloo and M. Akhbari, "New approach in design of planar coil of induction cooker based on skin and proximity effects analysis," in *Proc. IEEE International Conference on Industrial Technology,* Gippsland, VIC, 2009, pp. 1-6.

[122] C. R. Sullivan and R. Y. Zhang, "Simplified design method for litz wire," in *Proc. IEEE Applied Power Electronics Conference and Exposition*, Fort Worth, TX, 2014, pp. 2667-2674.

[123] C. R. Sullivan, "Cost-constrained selection of strand diameter and number in a litz-wire transformer winding," *IEEE Trans. on Power Electronics*, vol. 16, no. 2, pp. 281–288, 2001.

[124] R. Bosshard, J. W. Kolar and B. Wunsch, "Accurate finite-element modeling and experimental verification of inductive power transfer coil design," *in Proc. IEEE Applied Power Electronics Conference and Exposition*, Fort Worth, TX, 2014, pp. 1648-1653.

[125] J. Kim *et al*., "Coil Design and Shielding Methods for a Magnetic Resonant Wireless Power Transfer System," in *Proc. of the IEEE*, vol. 101, no. 6, pp. 1332-1342, June 2013.

[126] TDK Ferrites Datasheet. https://product.tdk.com/info/en/catalog/datasheets/ferrite_mn-zn_material_characteristics_en.pdf

[127] SAE TIR J2954Wireless Power Transfer for Light-Duty Plug-In/ Electric Vehicles, 2016.

[128] Q. Inc., "Qualcomm Halo wireless electric vehicle charging: No fuss, just wireless; wireless charging for electric vehicles," *QUALCOMM Inc., San Diego,*

CA, USA, Broch., 2011.

[129] Y. Gao, A. Ginart, K. B. Farley and Z. T. H. Tse, "Misalignment effect on efficiency of wireless power transfer for electric vehicles," *in Proc. IEEE Applied Power Electronics Conference and Exposition*, Long Beach, CA, 2016, pp. 3526-3528.

[130] X. Zhang, Z. Yuan, Q. Yang, Y. Li, J. Zhu and Y. Li, "Coil Design and Efficiency Analysis for Dynamic Wireless Charging System for Electric Vehicles," in *IEEE Trans. on Magnetics*, vol. 52, no. 7, pp. 1-4, July 2016.

[131] U. K. Madawala, M. Neath, and D. J. Thrimawithana, "A power-frequency controller for bidirectional inductive power transfer systems," *IEEE Trans. on Industrial Electronics*, vol. 60, no. 1, pp. 310-317, 2013.

[132] C. Buccella, C. Cecati, H. Latafat, P. Pepe and K. Razi, "Linearization of LLC resonant converter model based on extended describing function concept," in *Proc. IEEE International Workshop on Intelligent Energy Systems,* Vienna, 2013, pp. 131-136.

[133] A. Nejadpak and F. Tahami, "Stabilizing Controller Design for Quasi-Resonant Converters Described by a Class of Piecewise Linear Models," *IEEE Trans. on Circuits and Systems I: Regular Papers*, vol. 61, no. 1, pp. 312-323, Jan. 2014.

[134] S. Tian, F. C. Lee and Q. Li, "Equivalent circuit modeling of LLC resonant converter," *in Proc. IEEE Applied Power Electronics Conference and Exposition*, Long Beach, CA, 2016, pp. 1608-1615.

[135] H. Hao, G. A. Covic, and J. T. Boys, "An Approximate Dynamic Model of LC-T Based Inductive Power Transfer Power Supplies," *IEEE Trans. on Power Electronics*, vol. 29, no. 10, pp. 5554–5567, 2014.

[136] E. X. Yang, F. C. Lee and M. M. Jovanovic, "Small-signal modeling of series and parallel resonant converters," in *Proc. IEEE Applied Power Electronics Conference and Exposition,* Boston, MA, 1992, pp. 785-792.

[137] C. H. Chang, C. A. Cheng, and H. L. Cheng, "Modeling and design of the LLC resonant converter used as a solar-array simulator," *IEEE Journal of Emerging*

and Selected Topics in Power Electronics, 2014, vol. 2, no. 4, pp. 833–841.

[138] C. Buccella, C. Cecat, H. L. C., P. Pepe, and K. Razi, "Observer-Based Control of LLC DC/DC Resonant Converter Using Extended Describing Functions," *IEEE Trans. on Power Electronics*, vol. 30, no. 10, pp. 5881–5891, 2015.

[139] K. Song, C. Zhu, K. E. Koh, D. Kobayashi, T. Imura and Y. Hori, "Modeling and design of dynamic wireless power transfer system for EV applications," in *Proc. Annual Conference of the IEEE,Industrial Electronics Society,* Yokohama, 2015, pp. 005229-005234.

[140] Z. U. Zahid, Z. Dalala and J. S. J. Lai, "Small-signal modeling of series-series compensated induction power transfer system," in *Proc. IEEE Applied Power Electronics Conference and Exposition,* Fort Worth, TX, 2014, pp. 2847-2853.

[141] L. Junwei, C. Y. Chung and H. L. Chan, "Design and implementation of high power closed-loop AC-DC resonant converter for wireless power transfer," in *Proc. IEEE Workshop on Control and Modeling for Power Electronics*, Santander, 2014, pp. 1-8

[142] Z. U. Zahid *et al*., "Modeling and Control of Series–Series Compensated Inductive Power Transfer System," *IEEE Journal of Emerging and Selected Topics in Power Electronics*, vol. 3, no. 1, pp. 111-123, March 2015.

[143] H. Maki, Y. Yonezawa, E. Harada and I. Ninomiya, "An implantable telemetry system powered by a capacitor having high capacitance," in *Proc. Annual IEEE International Conference of the Engineering in Medicine and Biology Society, 1998.*, Hong Kong, 1998, pp. 1943-1946 vol.4.

[144] P. Si, A. P. Hu, S. Malpas and D. Budgett, "Switching Frequency Analysis of Dynamically Detuned ICPT Power Pick-ups," in *Proc. International Conference on Power System Technology*, Chongqing, 2006, pp. 1-8.

[145] P. Si, A. P. Hu, S. Malpas and D. Budgett, "A Frequency Control Method for Regulating Wireless Power to Implantable Devices," *IEEE Trans. on Biomedical Circuits and Systems*, vol. 2, no. 1, pp. 22-29, March 2008.

[146] R. Mecke and C. Rathge, "High frequency resonant inverter for contactless

energy transmission over large air gap," in *Proc. IEEE Power Electronics Specialists Conference,* 2004, pp. 1737-1743.

[147] J. M. Burdío, L. A. Barragán, F. Monterde, D. Navarro, and J. Acero, "Asymmetrical voltage-cancellation control for full-bridge series resonant inverters," *IEEE Trans. on Power Electron.*, vol. 19, no. 2, pp. 461–469, 2004.

[148] Z. U. Zahid *et al.*, "Modeling and Control of Series–Series Compensated Inductive Power Transfer System," *IEEE Journal of Emerging and Selected Topics in Power Electronics*, vol. 3, no. 1, pp. 111-123, March 2015..

[149] L. Grajales and F. C. Lee, "Control system design and small-signal analysis of a phase-shift-controlled series-resonant inverter for induction heating," in *Proc. IEEE Power Electronics Specialists Conference,* Atlanta, GA, 1995, pp. 450-456 vol.1.

[150] L. A. Barragán, J. M. Burdío, J. I. Artigas, D. Navarro, J. Acero, and D. Puyal, "Efficiency optimization in ZVS series resonant inverters with asymmetrical voltage-cancellation control," *IEEE Trans. on Power Electronics*, vol. 20, no. 5, pp. 1036-1044, 2005.

[151] B. Sharp and H. Wu, "Asymmetrical Voltage-Cancellation control for LCL resonant converters in Inductive Power Transfer systems," in *Proc. IEEE Applied Power Electronics Conference and Exposition*, Orlando, FL, 2012, pp. 661-666.

[152] S. Bai, Z. Pantic and S. Lukic, "A comparison study of control strategies for ZVS resonant converters," in *Proc. Annual Conference on IEEE Industrial Electronics Society*, Glendale, AZ, 2010, pp. 256-262.

[153] A. Khaligh and Z. Li, "Battery, ultracapacitor, fuel cell, and hybrid energy storage systems for electric, hybrid electric, fuel cell, and plug-in hybrid electric vehicles: State of the art," *IEEE Trans. on Vehicular Technology*, vol. 59, no. 6, pp. 2806–2814, 2010.

[154] J. Deng, S. Li, S. Hu, C. Mi, and R. Ma, "Design methodology of LLC resonant converters for electric vehicle battery chargers," *IEEE Trans. on Vehicular*

Technology, vol. 63, no. 4, pp. 1581–1592.

[155] Y.-C. Hsieh and C.-S. Huang, "Li-ion battery charger based on digitally controlled phase-shifted full-bridge converter," *IET Power Electronics*, vol. 4, no. 2, p. 242, 2011.

[156] Weixiang Shen, Thanh Tu Vo and A. Kapoor, "Charging algorithms of lithium-ion batteries: An overview," in *Proc. IEEE Conference on Industrial Electronics and Applications*, Singapore, 2012, pp. 1567-1572.

[157] M. Chen and G. A. Rincon-Mora, "Accurate, Compact, and Power-Efficient Li-Ion Battery Charger Circuit," *IEEE Trans. on Circuits and Systems II: Express Briefs*, vol. 53, no. 11, pp. 1180-1184, Nov. 2006.

[158] "Charging Lithium-Ion Batteries." Available: http://batteryuniversity.com/learn/article/charging_lithium_ion_batteries

[159] S. Dearborn. (2006, March 2). *Developing Affordable Mixed-Signal Power Systems for Battery Charger Applications* [online]. Available:www.electronicdesign.com/energy/develop-affordable-mixed-signal-battery-charger-design.

[160] A. Affanni, A. Bellini, G. Franceschini, P. Guglielmi, and C. Tassoni, "Battery choice and management for new-generation electric vehicles," *IEEE Trans. on Industrial Electronics*, vol. 52, no. 5, pp. 1343–1349, 2005.

[161] F. Marra, G. Y. Yang, C. Træholt, E. Larsen, C. N. Rasmussen and S. You, "Demand profile study of battery electric vehicle under different charging options," *in Proc. IEEE Power and Energy Society General Meeting*, San Diego, CA, 2012, pp. 1-7.

[162] J. M. Burdio, F. Canales, P. M. Barbosa and F. C. Lee, "Comparison study of fixed-frequency control strategies for ZVS DC/DC series resonant converters," in *Proc. IEEE Power Electronics Specialists Conference,* Vancouver, BC, 2001, pp. 427-432 vol. 1.

[163] Shuo Wang and D. Dorrell, "Review of wireless charging coupler for electric vehicles," in *Proc. Annual Conference of the IEEE Industrial Electronics*

Society, , Vienna, 2013, pp. 7274-7279.

[164] H. Jiang, P. Brazis, M. Tabaddor and J. Bablo, "Safety considerations of wireless charger for electric vehicles — A review paper," in *Proc. IEEE Symposium on Product Compliance Engineering* Portland, OR, 2012, pp. 1-6.

[165] Ieee C95.1-2005, *IEEE Standard for Safety Levels With Respect to Human Exposure to Radio Frequency Electromagnetic Fields, 3 kHz to 300 GHz*, vol. 2005, no. April. 2006.

[166] I. C. on N.-I. R. Protection, "Guidelines for limiting exposure to time-varying electric, magnetic, and electromagnetic fields (up to 300 GHz). International Commission on Non-Ionizing Radiation Protection," *Heal. Phys*, vol. 74, no. 4, pp. 494-522, 1998.

[167] F. Musavi and W. Eberle, "Overview of wireless power transfer technologies for electric vehicle battery charging," *IET Power Electronics*, vol. 7, no. 1, pp. 60–66, 2014.

[168] S. Y. R. Hui, Z. Wenxing, and C. K. Lee, "A critical review of recent progress in mid-range wireless power transfer," *IEEE Trans. on Power Electronics*, vol. 29, no. 9, pp. 4500-4511, 2014.

[169] J. H. and O. C. M. Ibrahim, L. Pichon, L. Bernard, A. Razek, "Advanced Modeling of a 2-kW Series–Series Resonating Inductive Charger for Real Electric Vehicle," *IEEE Trans. on Vehicular Technology*, vol. 64, no. 2, pp. 421-430.

[170] H. Kronmuller, *Handbook of Magnetism and Advanced Magnetic Materials*. 2007.

[171] F. Musavi, W. Eberle and W. G. Dunford, "A High-Performance Single-Phase Bridgeless Interleaved PFC Converter for Plug-in Hybrid Electric Vehicle Battery Chargers," in *IEEE Trans. on Industry Applications*, vol. 47, no. 4, pp. 1833-1843, July-Aug. 2011.

[172] F. Y. Lin, G. A. Covic, and J. T. Boys, "Evaluation of Magnetic Pad Sizes and Topologies for Electric Vehicle Charging," *IEEE Trans. on Power Electronics*,

vol. 30, no. 11, pp. 6391-6407, 2015.

Appendix A

Output Power of an SS-RIPT Link Fed from a Voltage Source

Consider the equivalent circuit of a SS resonant inductive link, shown in Figure A.1.
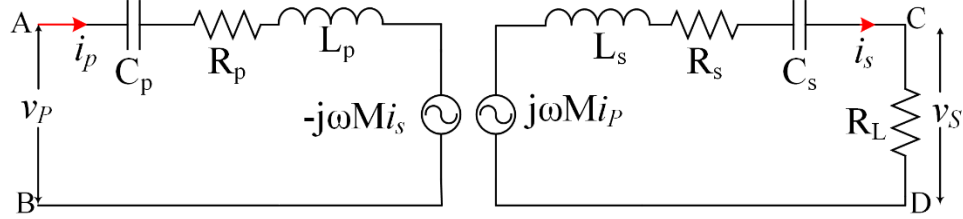

Figure A. 1 Equivalent circuit of SS-RIPT link

If control is applied to maintain primary voltage v_P constant and allow primary current i_P to vary as load varies, then power transfer capability of an SS-RIPT link can be derived as follows. Consider the equivalent circuit of an SS-RIPT link referred to primary side as shown in Figure A.1.
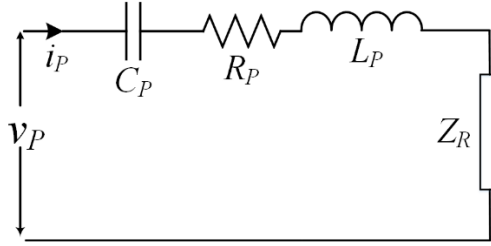
Figure A. 2 Equivalent circuit of SS-RIPT link referred to primary

Here, Z_R is secondary impedance reflected to primary side and is given by:

$$Z_R = \frac{\omega^2 M^2}{j\omega L_S + R_S + R_L + \frac{1}{j\omega C_S}} \tag{A.1}$$

If the system operates at a nominal angular frequency ω_o such that both the primary and secondary coil are tuned to this frequency then Z_R is purely resistive and is given by:

$$Z_R = \frac{\omega_o^2 M^2}{(R_S + R_L)^2}(R_S + R_L) \tag{A.2}$$

The power transferred from the primary to the secondary is the reflected resistance multiplied by the square of primary current (RMS value). Primary current in terms of primary voltage is given by:

$$I_{Prms} = \left(\frac{V_{Prms}}{R_P + \frac{\omega_o^2 M^2}{(R_S+R_L)^2}(R_S+R_L)} \right) \tag{A.3}$$

Therefore power transferred to the load at resonant condition, in terms of primary voltage, can be given by:

$$P_{Lv} = I_{Prms}^2 Z_R$$

$$\triangleq \frac{V_{Prms}^2 \omega_o^2 M^2 R_L}{R_P^2(R_S+R_L)^2 + \omega_o^4 M^4 + 2R_P(R_S+R_L)\omega_o^2 M^2} \tag{A.4}$$

A. Optimal Condition for Maximum Power transfer to load w.r.t. Mutual Inductance M:

By solving $\frac{\partial P_{Lv}}{\partial M} = 0$, the maximum power transferred to the load P_{Lvmax_M} and the optimal value of mutual inductance M_{ovmax} at which it occurs can be obtained as

$$P_{Lvmax\_M} = \frac{R_L V_{Prms}^2}{4\omega_o^2 M_{ovmax}^2} \tag{A.5}$$

$$M_{ovmax} = \frac{\sqrt{R_P(R_S+R_L)}}{\omega_o} \tag{A.6}$$

B. Optimal Condition for Maximum Power transfer to load w.r.t. load resistance R$_L$:

By solving $\frac{\partial P_{Lv}}{\partial R_L} = 0$, the maximum power transferred to the load P_{Lvmax_RL} and the optimal value of load resistance R_{Lvmax} at which it occurs is obtained as

$$P_{Lvmax\_RL} = \frac{V_{Prms}^2 \omega_o^2 M^2}{4 R_{Lvmax} R_P^2} \tag{A.7}$$

$$R_{Lvmax} = \frac{R_P R_S + \omega_o^2 M^2}{R_P} \tag{A.8}$$

Efficiency of an SS-RIPT Link Fed from a Voltage Source

From Figure A.1, one can write,

$$\eta = \frac{I_{Srms}^2}{I_{Prms}^2} \frac{R_L}{(Primary\ Resistance + reflected\ resistance)} \tag{A.9}$$

Here,

$$\left| \frac{I_{Srms}}{I_{Prms}} \right| = \frac{\omega_o M}{R_S + R_L} \tag{A.10}$$

Putting the value of primary resistance, reflected resistance, and eq. (A.10) into eq. (A.9), the efficiency of an SS-RIPT link can be rewritten as

$$\eta = \frac{R_L}{(R_S+R_L)(1+\frac{R_P R_S + R_P R_L}{M^2 \omega_o^2})} \tag{A.11}$$

From (A.11), one can observe that the efficiency is independent of input voltage and input current, and is a function of the physical parameters of the windings and operating resonant frequency. It should be noted that eq. (A.11) is valid for air-cored coils. In case of the SS-RIPT link where core material is present, eq. (A.11) can be used by assuming the core loss to be negligible.

A. Optimal Conditions for Maximum Efficiency with respect to Mutual Inductance

From (A.11), the range of optimal values of mutual inductance for maximum efficiency can be calculated as obtained in (A.12). The corresponding maximum value of efficiency is given in (A.13).

$$M_{\eta max} \gg \sqrt{\frac{R_P(R_S+R_L)}{\omega_o^2}} \tag{A.12}$$

$$\eta_{max} = \frac{R_L}{R_S+R_L} \tag{A.13}$$

From (A.13), one can observe that maximum value of efficiency is independent of either mutual inductance or resonant frequency and only depends upon winding resistance and load resistance. It can be observed that for zero secondary resistance, maximum efficiency can reach 100%. Therefore, winding resistance should kept as low as possible.

B. Optimal Condition for Maximum Efficiency with respect to Load, R_L

By solving $\frac{\partial \eta}{\partial R_L} = 0$, the maximum efficiency η_{max_RL} and optimal value of load resistance $R_{L\eta max}$ at which it occurs is obtained as

$$\eta_{max\_RL} = \frac{\omega_o^2 M^2}{R_P R_S \left(1+\frac{R_{L\eta max}}{R_S}\right)^2} \tag{A.14}$$

$$R_{L\eta max} = R_S \sqrt{\frac{\omega_o^2 M^2}{R_P R_S} + 1} \tag{A.15}$$

Appendix B

Explanation for Negative Mutual Inductance and Null in Coupling Profile

It can be observed in plots shown in Figure 2.16 and Figure 2.19 that for increasing misalignment, mutual inductance becomes zero at particular misalignment and past zero points, is getting negative. The existence of null in coupling profile has been explained very well in the literature for identically sized (symmetrical) coil pair. Null exists in the coupling profile due to a mechanism called flux cancellation [49]. To understand the concept of flux cancellation, consider the Figure B.1 shown below.

(a)$\phi_b > \phi_t$ (b)$\phi_b = \phi_t$

(a)$\phi_b < \phi_t$
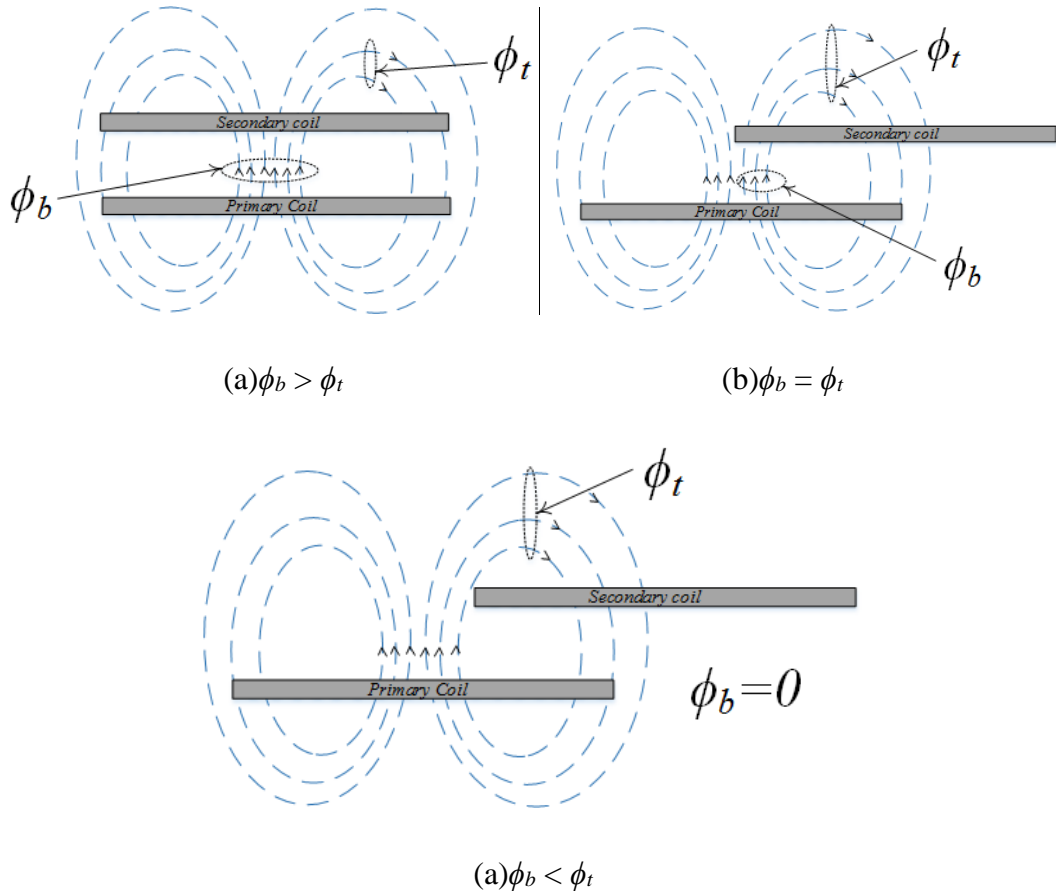
Figure B. 1 Concept of flux cancellation

In Figure B. 1, ϕ_b represents the amount of flux entering the secondary coil from the bottom and ϕ_t accounts for the amount of flux entering the secondary coil from the top. Under perfect alignment and up to certain extent of misalignment ϕ_b is always greater than ϕ_t for such case value of mutual inductance is always positive.

At certain value of misalignment ϕ_b can become equal to ϕ_t therefore they cancel each other out. For such cases value of mutual inductance become zero or '*null*'. This phenomena when $\phi_b = \phi_t$ is known as 'flux cancellation'. It has been reported in [57],[39], [58], [61], [62], [172] that this null exist at same value of misalignment distance (equal to 70% of coil's central diameter or 40% of pad diameter) irrespective of coil separation. However, this may be true only for identically sized coil-pair, i.e. symmetrical coil-pair. For unsymmetrical coil-pairs this position of the null changes with changing air-gap. To illustrate this point mutual inductance of P-S$_1$ and P-S$_4$ for misalignment at various air-gap have been plotted in Figure B. 2.
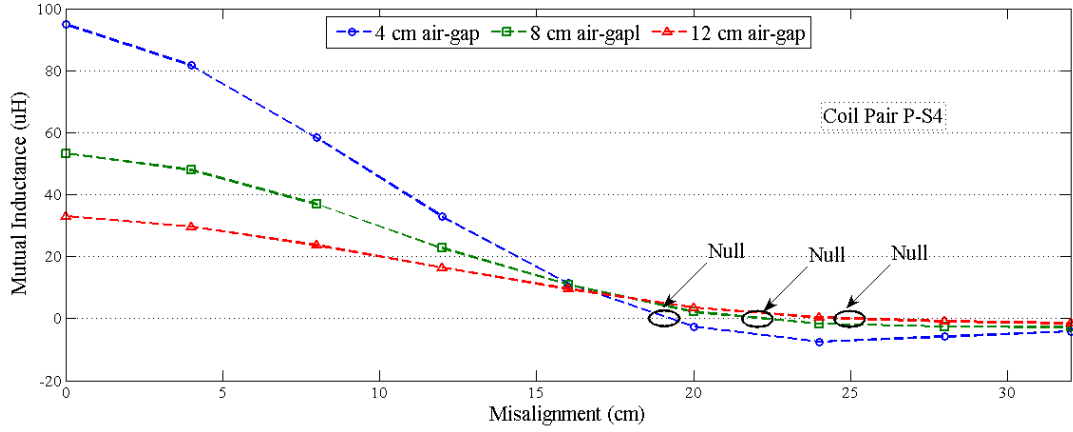
(a) Mutual inductance of P-S$_4$ under misalignment at different air-gap
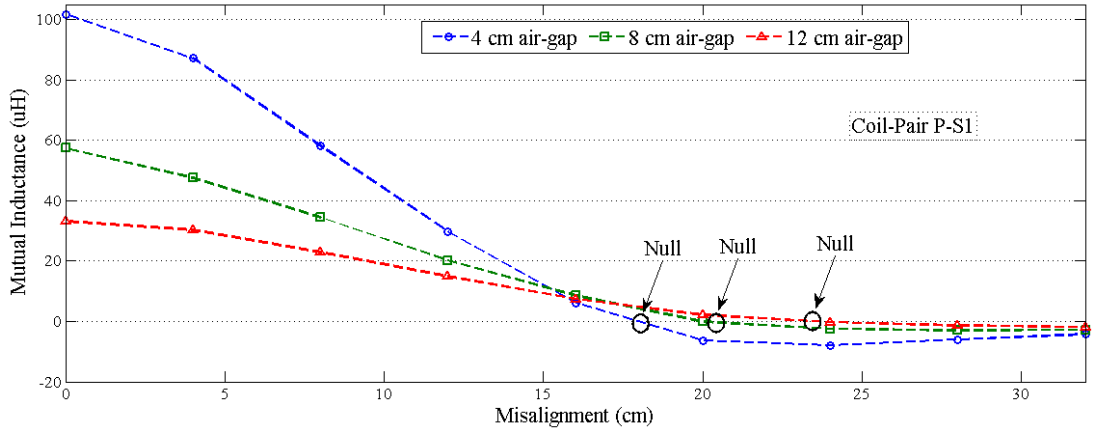
(b) Mutual inductance of P-S$_1$ under misalignment at different air-gap

Figure B. 2 Existence of null in unsymmetrical coil pair

In Figure B.2, it can be observed that position of *null* shifts with decreasing air-gap for the coil-pair P-S$_1$ and P-S$_4$.

At misalignment past the *null* point, ϕ_b becomes zero or less than ϕ_t. For such condition, value of mutual inductance becomes negative. This negative value of mutual inductance can be seen in FEA results for coil-pair P-S$_4$ as shown in Figure B.3. It should be noted that the negative mutual inductance reaches a minimum and then tapers off to zero as the misalignment distance is increased further.
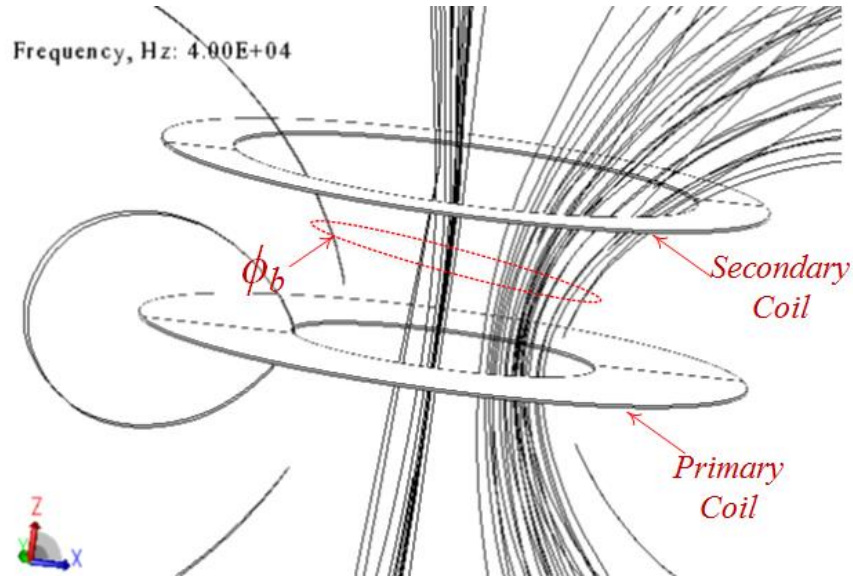
(a) 3-D view of flux lines at misalignment =0 cm and air-gap =8 cm
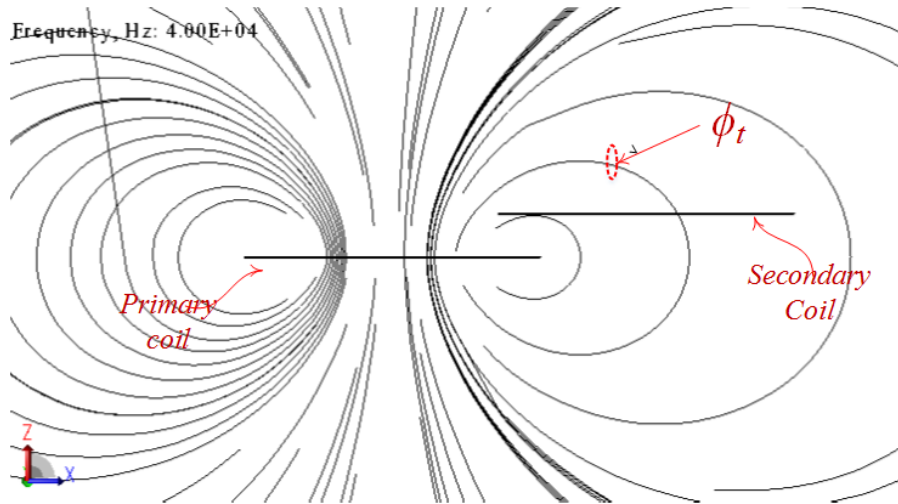
(b) Front view of flux lines at misalignment =25 cm and air-gap =4cm

Figure B. 3 Flux lines distribution for mutual inductance measurements on P-S$_4$

From Figure B. 3 one can observe that perfectly aligned condition almost all the flux enters the secondary from the bottom. Therefore, mutual inductance is positive and has

the maximum value at that air-gap. At misalignment of 25 cm, no flux enter from the bottom and coupling is due to flux entering the secondary coil from the top surface. Therefore, mutual inductance is negative.

Appendix C

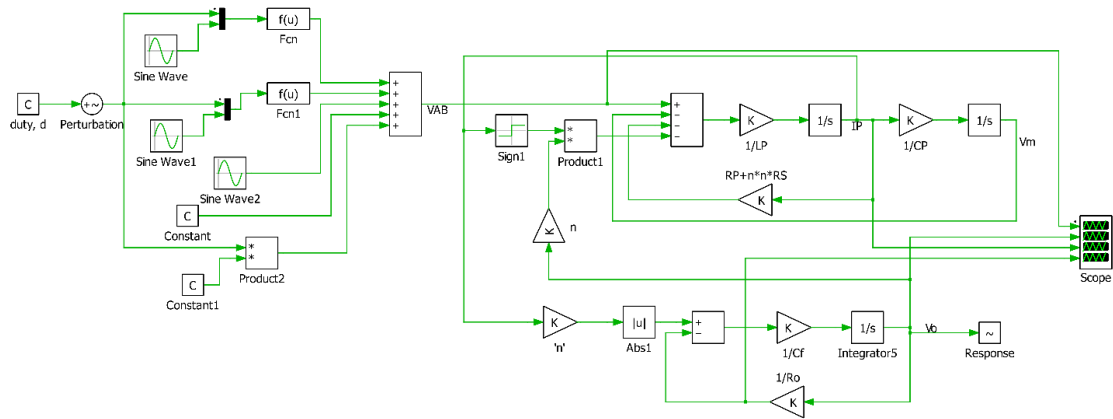## PLECS Simulation Circuits

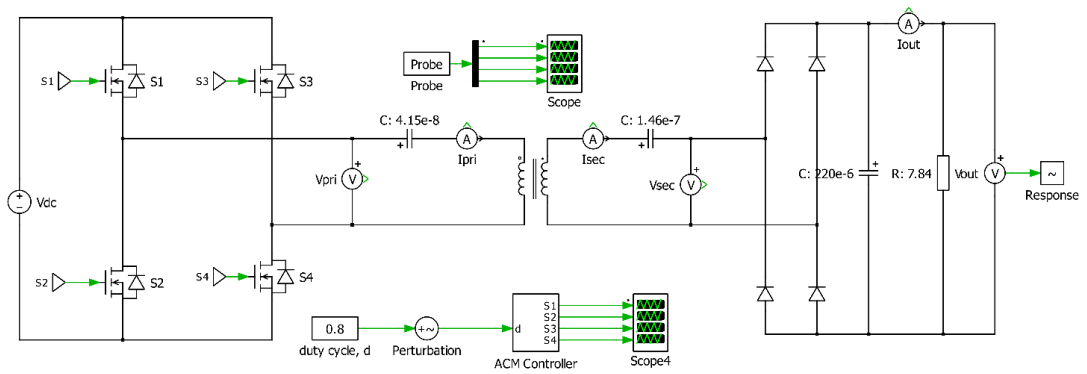Figure C. 1 Circuit diagram of reduced dynamic model developed in PLECS 3.7.5

Figure C. 2 Circuit diagram of open loop full model developed in PLECS 3.7.5

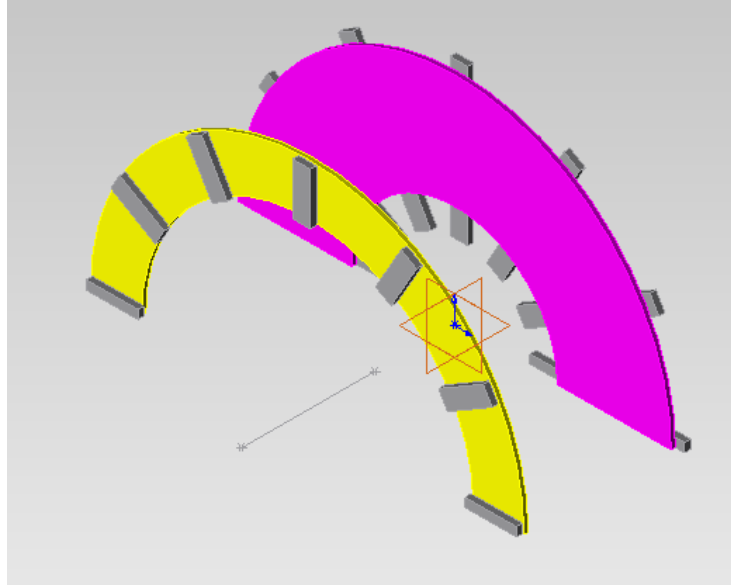# Appendix D

FEA Models for Iterations Mentioned in Table 6.1

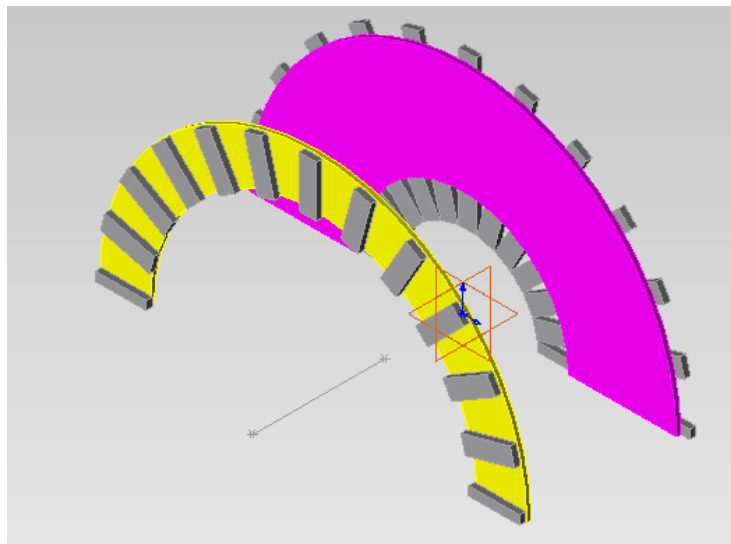Figure D. 1 Model Created For Iteration I: $\theta_P = \theta_S = 30°$, N_P=26, NS=11, L_{fP} =166.5mm, L_{fS} =55.5mm

Figure D. 2 Model Created For Iteration II: $\theta_P = \theta_S = 15°$, N_P=24.2, NS=10.6, L_{fP} =166.5mm, L_{fS} =55.5mm
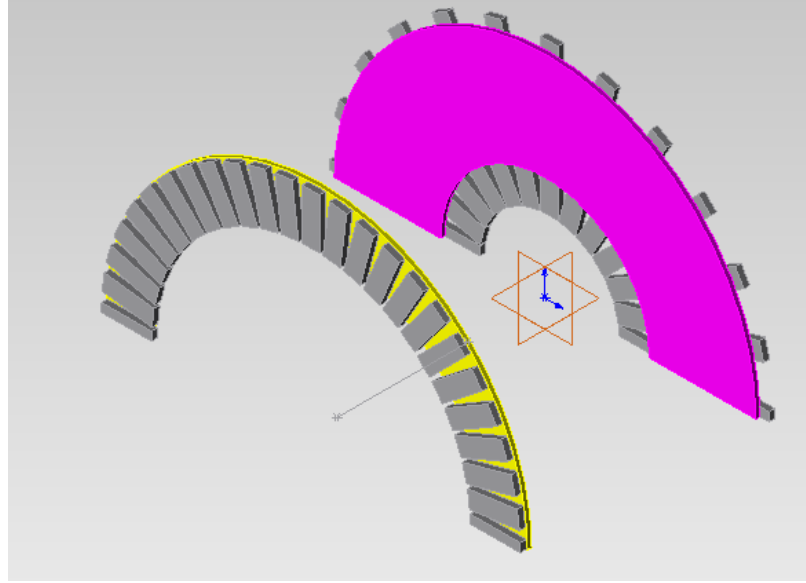
Figure D. 3 Model Created For Iteration III: $\theta_P = \theta_S = 7.5°$, N_P=23.6, NS=10, L_{fP} =166.5mm, L_{fS} =55.5mm

Curriculum Vitae

Kunwar Aditya

Born May 1, 1987

Indian Citizen

kunwar.aditya@uoit.net

Education

Sept 2014 –Sept 2016: Teaching assistant and Ph.D. student at the University Of Ontario Institute Of Technology, Oshawa, ON, Canada.

Sept 2013 - Aug 2014: Ph.D. student at Concordia University, Montreal, QC, Canada.

July 2010 - June 2012: M.Tech. Indian Institute of Technology (Banaras Hindu University), Varanasi, India

July 2005 - June 2009: B.E. Bharati Vidyapeeth University College of Engineering, Pune, India.